

# Magnetic and transport properties of rare-earth titanate thin films and heterostructures

## Thèse de doctorat de l'Université Paris-Saclay

École doctorale n° 564, physique de l'Ile-de-France (PIF)  
Spécialité de doctorat : Physique  
Unité de recherche : Université Paris-Saclay, CNRS, Thales, Unité mixte  
de physique CNRS/Thales, 91767, Palaiseau, France.  
Référent : Faculté des sciences d'Orsay

Thèse présentée et soutenue à Palaiseau, le 15 juillet 2020, par

**Raphaël AESCHLIMANN**

### Composition du jury:

<b>Marc Gabay</b>	Président
Professeur, Université Paris-Saclay (Laboratoire de Physique des Solides (LPS))	
<b>Stefania Pizzini</b>	Rapportrice & Examinatrice
Directrice de recherche, CNRS (Institut Néel, Université Grenoble Alpes)	
<b>Wilfrid Prellier</b>	Rapporteur & Examinateur
Directeur de recherche, CNRS, ENSICAEN (CRISMAT)	
<b>Ralph Claessen</b>	Examinateur
Professeur, University of Würzburg (EP-4)	
<b>Cinthia Piamonteze</b>	Examinatrice
Scientifique permanente, Paul Scherer Institut (Swiss Light Source (SLS): XTreme beamline)	
<b>Manuel Bibes</b>	Directeur
Directeur de recherche, CNRS (Unité Mixte de Physique CNRS/Thales, UMR 137)	
<b>Agnes Barthelemy</b>	Invité
Professeure, Université Paris-Saclay (Unité Mixte de Physique CNRS/Thales, UMR 137)	
<b>Jacobo Santamaria</b>	Invité
Professeur, Universidad Complutense de Madrid (UCM)	

# Synthèse de la présente thèse

Au cours de cette thèse nous allons étudier les titanates de terre rare, leur propriétés et leur utilisation dans les système 2D d'électrons. Cette famille de matériaux fait partie de la plus large famille des oxydes de métaux de transition. Ces derniers présentent une grande variété de propriétés allant de la supraconductivité au magnétisme en passant par la ferroélectricité et la multiferroïcité. Une couche conductrice peut apparaître à interface entre deux isolants comme entre  $\text{LaAlO}_3$  (LAO) et  $\text{SrTiO}_3$  (STO). Dans ce cas de figure comme dans le nôtre les matériaux en questions sont des oxydes perovskites.

Cette structure cristalline est composée de cations positionnés au centre (sites A) et aux coins (sites B) de la maille cristalline. Les cations des sites A sont habituellement de valence 2 ou 3+ alors que les sites B sont habituellement des métaux de transition de valence 3 ou 4+. Chaque métal de transition se trouve lui même au centre d'un octaèdre d'ions oxygène de valence 2-.

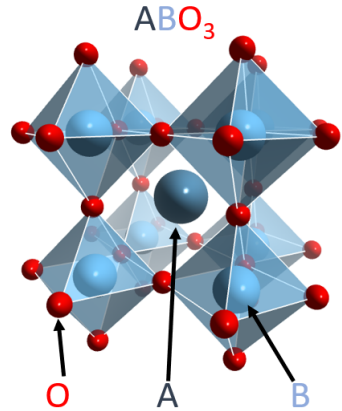


Figure 1: Maille cristalline de la structure pérovskite cubique.

Cette structure cubique est en réalité relativement rare car elle s'accorde aux contraintes en développant différentes déformations. Les cages d'octaèdre d'oxygène peuvent subir des rotations le long de différents axes que ce soit en phase ou anti-phase. Elles peuvent également subir des déformations de type Jahn-Teller. D'autre part, les sites A peuvent adopter des modes de déplacement antipolaire qui résultent en un changement d'environnement électrostatique pour les sites B. Certains de ces modes sont représentés dans la Fig. 2.

## Rotations and « Jahn Teller effect »

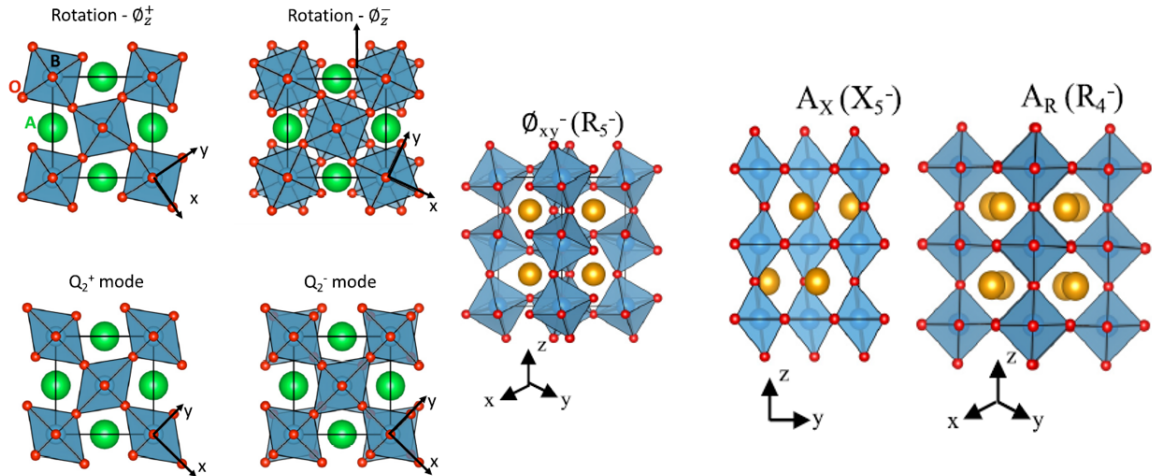


Figure 2: Schéma de la structure pérovskite cubique déformée par les modes: (a)  $\Phi_z^- (R_5^-)$ , (b)  $A_X (X_5^-)$ , (c)  $A_R (R_4^-)$ , (d)  $\Phi_z^+ (M_2^+)$  ou  $Q_2^+ (M_3^+)$ .

## Système d'électron bidimensionnel

Ces oxydes ont comme nous l'avons dit, une très grande variété de propriétés physiques mais certaines propriétés absentes des matériaux individuels émergent lors de la réalisation d'interfaces. L'exemple de LAO/STO a été largement étudié.

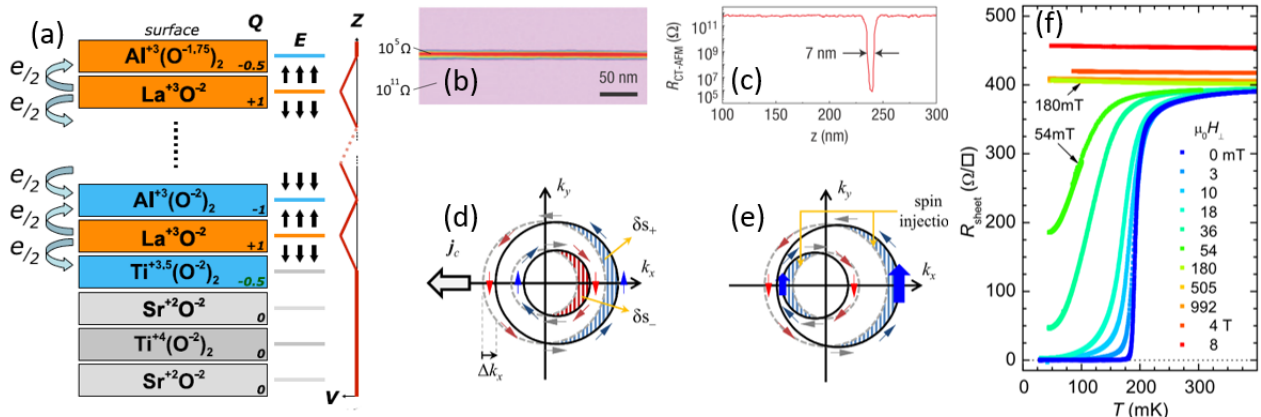


Figure 3: (a) Schéma de la "catastrophe polaire" créée par la discontinuité de polarité à l'interface LAO/STO où se crée le système d'électrons bidimensionnel. (b) Scan CT-AFM d'une interface LAO/STO. (c) Profil de conductivité de l'interface obtenu au CT-AFM. (d) Représentation de l'effet Edelstein (EE). Quand un courant de charge est injecté selon l'axe  $x$ , l'accumulation de spin entre les deux surfaces non équivalentes ce qui résulte en un courant de spin selon  $y$ . (e) Représentation de l'effet Edelstein inverse (IEE). Quand un courant de spin est injecté perpendiculairement au système d'électron 2D, il entraîne un déplacement des surfaces de Fermi des bandes de Rashba dans l'espace des impulsions. Ce déplacement résulte en un courant net de charge perpendiculaire au courant de spin[1]. (f) Résistance de surface d'un échantillon de 8 u.c. en fonction de  $T$  pour différents champs magnétiques perpendiculaires à l'interface. Adapté de [2].

A cette interface un transfert de charge du LAO vers le STO se produit dans le but de compenser la discontinuité de polarité comme montré Fig. 3 (a). Ce dernier a pour conséquence la création d'une zone métallique à l'interface de ces deux isolants comme montré en CT-AFM, cf Fig. 3 (b). Cette zone de conduction a comme propriété un fort effet Rashba résultant en une conversion spin/charge efficace via les effets Edelstein et Edelstein inverse, Fig. 3 (c,d). En addition, elle possède une phase supraconductrice à basse température, Fig. 3 (e).

Sachant que toutes ces propriétés découlent de l'association de simple isolant de bande, il est raisonnable de se demander quel résultat nous pourrions obtenir en utilisant des matériaux plus complexes. C'est ici que les titanates de terre-rare entrent en scène. En effet ces d'oxydes pérovskites ont la particularité d'être à la fois des isolants fortement corrélés, dits insolants de Mott, et de posséder un ordre ferrimagnétique pour certains membres de la famille.

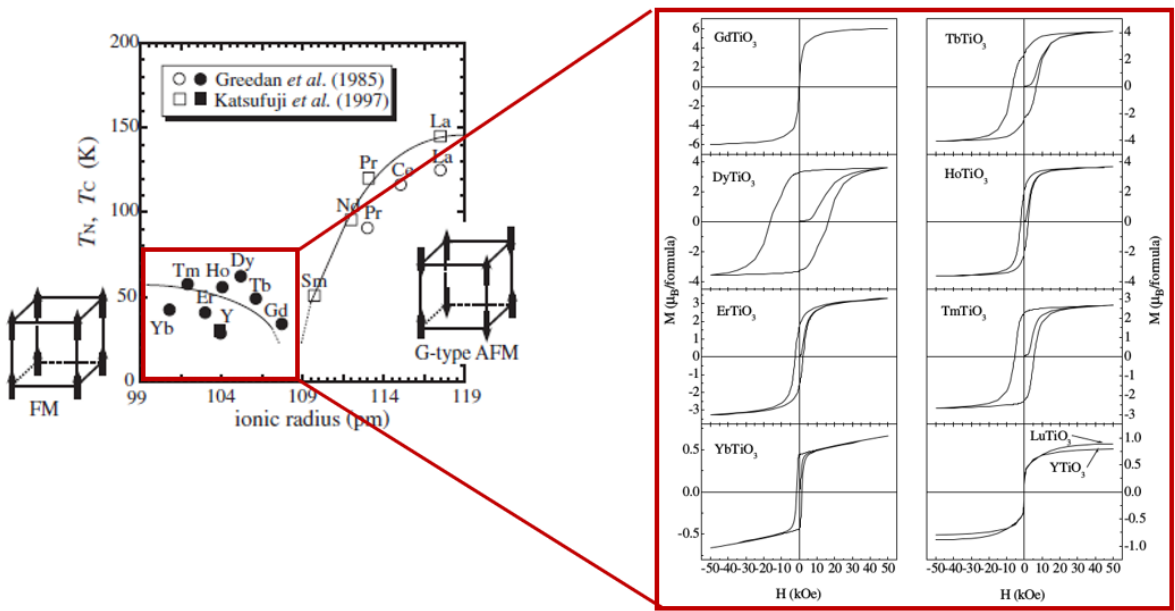


Figure 4: Diagramme de phase des titanates de terre rare (les températures viennent d'échantillons massifs). Adapté de [3]. Cycle d'hysteresis magnétique (magnétisation vs champ magnétique) obtenu à l'aide d'un magnétomètre SQUID sur des échantillons massifs à 5 K. Adapté de [4].

Les titanates de terre-rare se divisent entre des isolants antiferromagnétiques et ferrimagnétiques. Les données présentées dans la Fig. 4 correspondent à des échantillons massifs. On peut voir dans la Fig. 4 (b) que les propriétés magnétiques de la partie ferrimagnétique présentent déjà une grande variété. Malgré tout, les travaux sur ces matériaux en couche mince sont rares et ce sont principalement concentrés sur YTiO<sub>3</sub> (YTO) et GdT<sub>3</sub>O<sub>3</sub> (GTO) que cela soit en ablation laser pulsée (PLD) ou épitaxie par jets moléculaire (MBE).

## Motivation pour cette thèse

1. Comme nous l'avons dit l'étude des titanates de terre-rare ferrimagnétique et spécialement sous la forme de couche mince constitue encore un domaine à explorer. C'est pour cela que nous allons établir dans un premier temps les conditions de croissance en PLD des titanates ferrimagnétiques pour lesquels les études ont manqué. C'est pour cela que nous avons voulu optimiser dans un premier temps DyTiO<sub>3</sub> (DTO) qui contrairement à YTO et GTO possède un fort champ coercitif et un important moment à rémanence.
2. La physique des titanates de terre-rare ferrimagnétiques reste encore à explorer. C'est ce que nous nous sommes atteler à faire en mesurant leur propriétés magnétiques, structurale ainsi que leurs configurations électroniques.
3. Le manque d'une étude portant sur la valence des éléments de ces matériaux nous a poussé à réaliser une étude de ces derniers par analyses spectroscopiques (spectroscopie photoélectronique X et spectroscopie par absorption de rayon X).
4. Comme nous l'avons dit, les titanates possèdent une riche physique due à leur nature d'isolant de Mott et leur utilisation dans des systèmes d'électrons bidimensionnels pourrait donner lieu à de nouvelle propriétés absentes des systèmes plus classiques. C'est pour cela que nous nous sommes fixé pour but de réaliser de telles interfaces à l'aide DTO et STO.

## Croissance des titanates de terres rares

Nous avons commencé optimiser les conditions de croissance de la titanate DyTiO<sub>3</sub>, sur laquelle nous allons concentrer nos études dans un premier temps. Due à la structure électronique du titane, sa forme ionique la plus stable est le Ti<sup>4+</sup>; cependant la plupart des titanates de terre rare possède un titane 3+. La conséquence de ceci est la grande difficulté à stabiliser la phase pérovskite de ces oxydes. Pour pallier à ce problème nous avons développé une méthode de croissance par déposition par ablation laser pulsée (PLD) en atmosphère d'argon pauvre en oxygène et une croissance à haute température (900°C). Dans ces conditions nous avons obtenu une série en épaisseur d'échantillons de phase purement pérovskite, Fig 5.

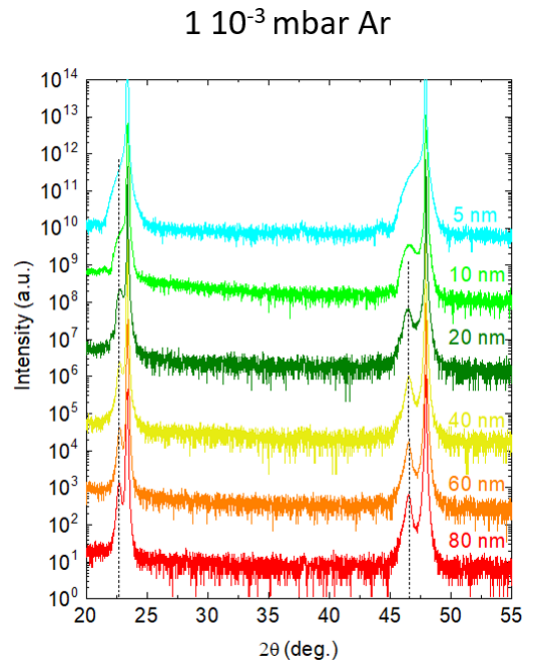


Figure 5: Scan  $2\theta - \omega$  obtenu en diffraction X sur des échantillons de DyTiO<sub>3</sub> de différentes épaisseurs fait sous  $1.10^{-3}$  mbar d'argon à 900 °C.

Lors de la caractérisation magnétique de cette série d'échantillons (par magnétomètre SQUID), nous avons remarqué que ces propriétés évoluent clairement en fonction de l'épaisseur.

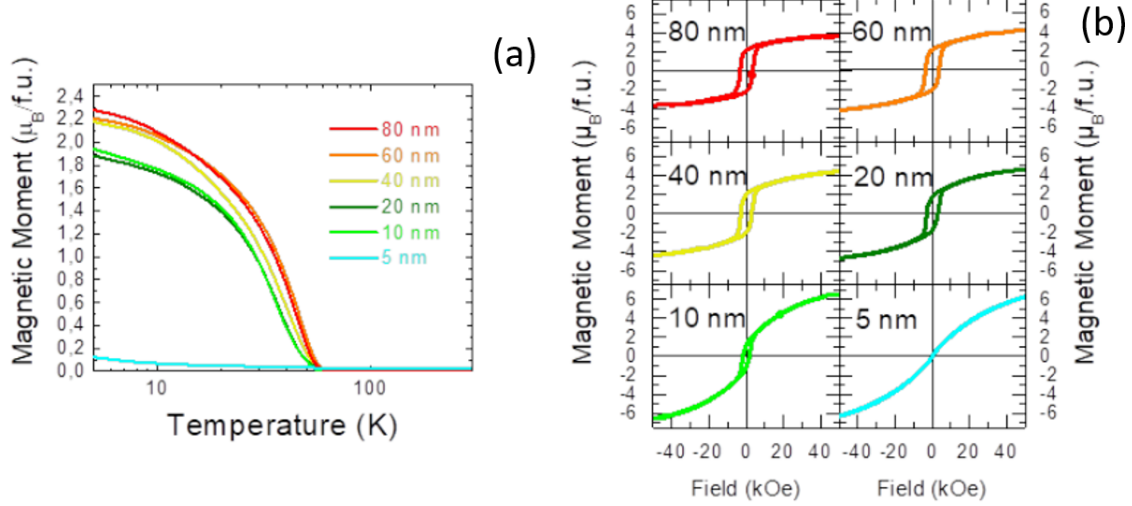


Figure 6: Étude en épaisseur en SQUID pour des échantillons élaborés à 900 ° C sous  $10^{-3}$  mbar d'argon : (a) moment magnétique en fonction de la température sous un champ de 100 Oe (b) moment magnétique en fonction du champ magnétique à 10 K.

Ce comportement voit les propriétés ferrimagnétiques se dégrader quand l'épaisseur diminue, comme mis en évidence avec l'évolution de l'aimantation rémanente, Fig. 6 (a). Ce comportement est cohérent avec la présence d'une couche morte non magnétique. Cependant, si nous regardons la forme des cycles d'hystérésis magnétiques, Fig. 6 (b), nous observons une augmentation de l'aimantation à saturation indiquant un comportement paramagnétique qui se développe (en proportion) par rapport à la partie ferrimagnétique de la couche mince. Nous avons donc soupçonné la présence d'une couche paramagnétique dans notre film ferrimagnétique mais dont la contribution est forte à saturation. C'est pour cela que nous l'avons baptisé "couche morte-vivante" ("living-dead layer").

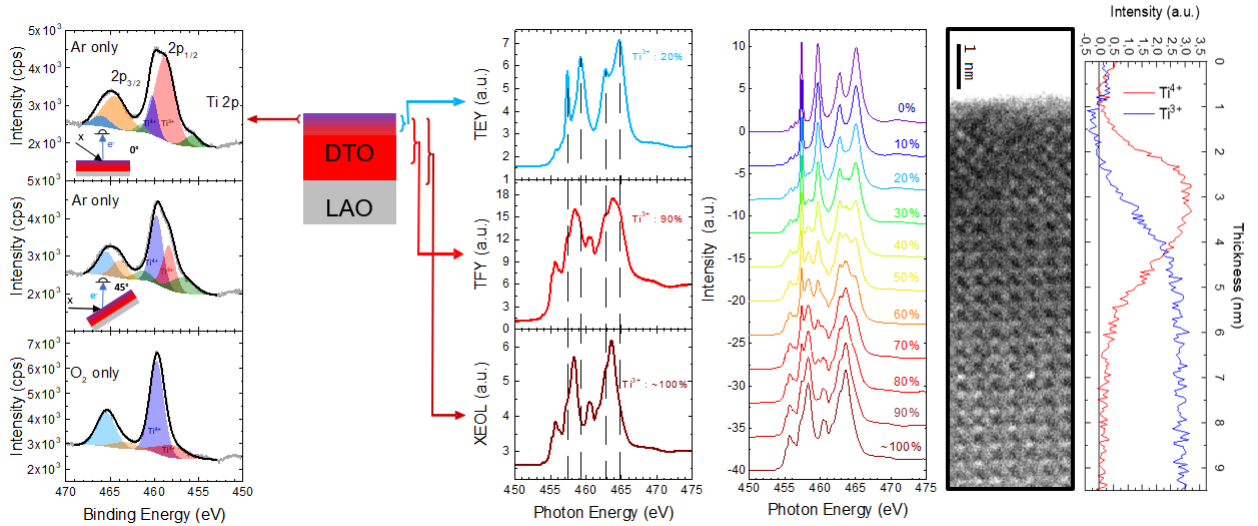


Figure 7: (ac) XPS spectra of the Ti 2p core levels in 20 nm DTO films grown in Ar (a,b) and in oxygen (c), at normal emission (a,c) and a 45 ° emission (b). (df) XAS at the Ti L<sub>3,2</sub> edge at room temperature in a 80 nm DTO film grown in pure Ar, collected in TEY mode (d), TFY mode (e), and XEOL mode (f). The dotted lines guide the eye to the position of the four main peaks present in (d). (g) Linear combinations of XAS spectra between a reference Ti<sup>4+</sup> spectrum and a reference Ti<sup>3+</sup> spectrum (see text for details). Percentage refers to Ti<sup>3+</sup> fraction. (h) Profil EELS de la valence du titane dans une couche de DTO.

A l'aide d'une grande variété de techniques spectroscopiques (XPS, XAS, EELS), nous avons établi la présence d'une couche de 5 nm, dont l'épaisseur ne semble pas dépendre de l'épaisseur totale, où la valence du titane est 4+ au lieu de la valeur nominale de 3+. Cette couche de  $Ti^{4+}$  nous permet d'expliquer l'origine de la couche paramagnétique. En effet les deux sont reliée par l'ordre ferrimagnétique de  $DyTiO_3$ . Dans le cas de  $Ti^{4+}$  l'absence d'électron  $d$  empêche le couplage avec le  $Dy^{3+}$  qui alors se comporte en paramagnétique ( $10.6 \mu_B$ ).

## Moment orbital au seuil $L_{2,3}$ du titane

En transposant les conditions de croissance établie pour  $DyTiO_3$  aux autres titanates, nous avons réussi à faire croître des échantillons de bonne qualités de  $YTiO_3$ ,  $TmTiO_3$  et  $GdTIO_3$ . Durant l'analyse spectrale des spectres de XAS pour l'analyse de la couche morte-vivante, nous avons aussi étudié le spectre du dichroïsme magnétique circulaire de rayon X (XMCD). Cette technique nous permet d'étudier les propriétés magnétiques mais aussi l'état quantique sondé. En effet grâce aux règles de sommes nous pouvons obtenir le moment orbital et de spin des états 3d correspondants aux seuils  $L_{2,3}$  dans le spectre. D'après ces règles on s'attend à avoir une intégrale au post-seuil nul car le moment orbital attendu porté par le titane est nul.

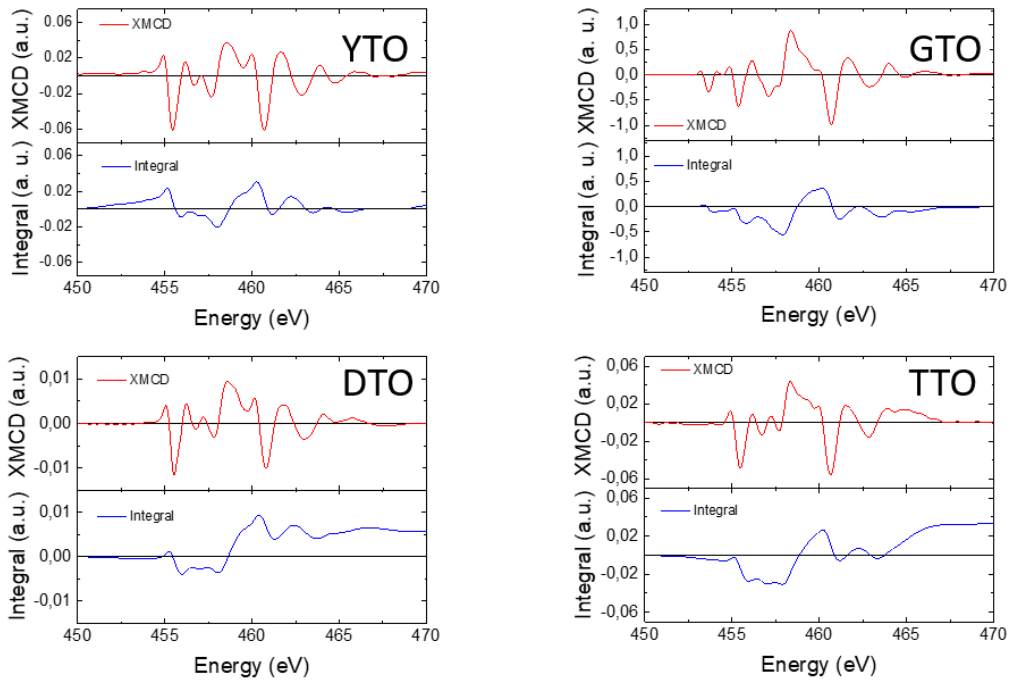


Figure 8: Signaux XMCD et leur intégrale pour des échantillons épais ( $t \simeq 80$  nm) de YTO, GTO, DTO et  $TmTiO_3$  (TTO).

Cependant, on voit ici Fig. 8 que certaines titanates ont une intégrale de l'XMCD, au seuil  $L_{2,3}$  du Ti, non nul et cette propriété semble corrélée à la non-colinéarité de la structure magnétique des matériaux en question. Nous avons proposé une explication basée sur un effet topologique de la structure magnétique qui induit un moment orbital sans faire intervenir le couplage spin orbite.

# Incorporation de $\text{DyTiO}_3$ dans un système d'électrons bidimensionnel

Après avoir étudié les propriétés des titanates prises individuellement, nous nous sommes intéressés à leur intégration dans des systèmes bidimensionnel d'électron. Pour élaborer une interface de DTO/STO nous avons d'abord dû résoudre le problème d'obtenir un film de STO d'excellente qualité et à la surface bien définie. Après avoir optimisé STO et l'avoir combiné à une couche de DTO, nous avons mesuré les propriétés de transport de l'interface et observé un comportement métallique ainsi que des effets de localisations à basse température, comme observé sur la Fig. 9.

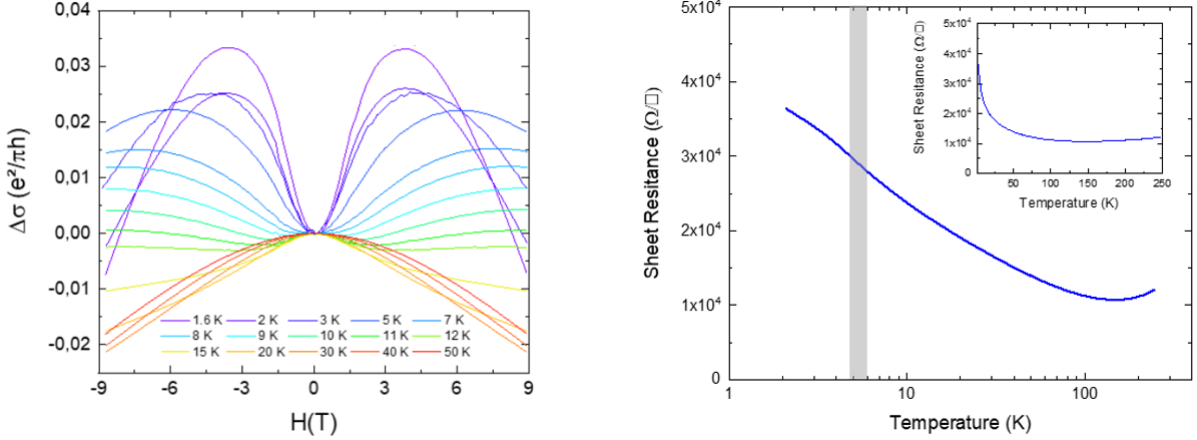


Figure 9: Échantillon de LAO (20 nm)/DTO (10 nm)/STO (5 nm)//LSAT. Magneto-conductance en fonction du champ magnétique à des températures allant de 1,6 K à 50 K. (b) Résistance de surface en fonction de la température

Le comportement de la conductivité en fonction du champ magnétique et à différentes températures apparaît riche et complexe. Nous avons ajusté ces données à l'aide d'un modèle qualitatif pour rendre compte de ces changements de régime. Ce modèle de magnetoconductivité fait intervenir un effet Kondo à basse température, des effets de localisation et d'anti-localisation faible ainsi qu'une composante Lorentzienne en  $B^2$ .

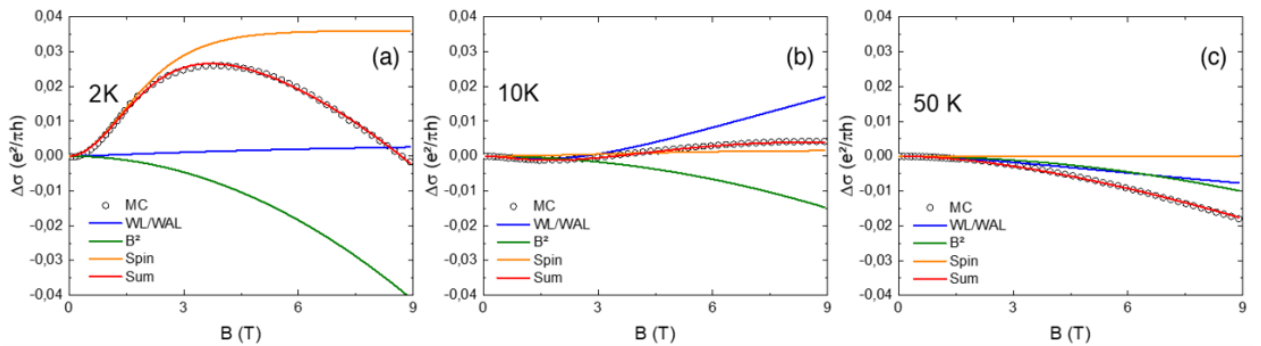


Figure 10: (a) Magneto-conductivité (point creux) ajustée par le modèle complet (en rouge) ainsi que l'antilocalisation et localisation faible (en bleu), la magnetoconductivité de Lorentz (en vert) et l'effet Kondo (en orange) à 2 K (a), 10 K (b) et 50 K (c).

En observant les Fig. 10 (a-c) on peut distinguer trois régimes de conduction. Une à très basse température 2K où l'effet Kondo domine, une à basse température où les effets de localisation et anti-localisation faible dominent et finalement un régime quasi métallique où le régime de Lorentz est pondéré par une localisation faible persistante.

Il est néanmoins nécessaire de garder à l'esprit que ce modèle est qualitatif et ne nous a servi qu'à montrer la présence de magnétisme (Kondo), de couplage spin-orbite (anti-localisation faible). Cela nous montre que nous avons réussi à obtenir un gaz d'électron ferromagnétique dans lequel nous retrouvons l'effet du couplage spin-orbite du dysprosium.

# Résumé

Les oxydes de métaux de transitions possèdent une large gamme de fonctionnalités (supraconductivité, magnétisme, ferroélectricité, multiferroicité) découlant de l'interaction d'effets structuraux et de corrélations fortes. De plus, des travaux récents ont mis en lumière une physique propre à leurs interfaces, incluant de la supraconductivité ainsi que de la conductivité classique dans le système bidimensionnel (2DES) créé à l'interface de deux isolants de bande,  $\text{LaAlO}_3$  et  $\text{SrTiO}_3$ . Malgré cela pour couvrir l'immense potentiel des interfaces d'oxydes et leur phases électroniques sans précédent, il est nécessaire de combiner des oxydes plus fortement corrélés. Cette thèse à la croisée des chemins entre la physique des électrons fortement corrélés, du magnétisme et de la spintronique a pour but de combiner les instabilités magnétique et électronique pour créer de nouvelles phases électronique contrôlable par stimulus externe. Pour cela nous nous sommes intéressés à la famille relativement inexplorée des titanates de terres rares dont l'ordre magnétique ferro ou antiferro est contrôlé par la taille de la terre rare. Contrairement aux travaux existants, nous nous sommes concentrés sur les membres ferrimagnétiques de la famille et leur intégration dans des 2DES. Cette thèse se développera autour de deux axes principaux. Dans un premier temps nous avons étudié plusieurs membres de la famille des titanates de terres rares sous la forme de couches minces épitaxiées. Nous avons aussi mis en évidence la présence d'une couche morte magnétiquement active à la surface de ces échantillons et expliqué sa présence par une suroxydation des ions titane de la surface. Nous avons aussi étudié la présence inattendue d'un moment orbital porté par le titane dans certains des composés étudiés et l'avons corrélé à leur structure magnétique non-colinéaire en conjonction avec un gradient structural observé en microscopie électronique en transmission.

Dans un second temps nous avons combiné  $\text{DyTiO}_3$  avec  $\text{SrTiO}_3$  pour obtenir une interface conductrice possédant des propriétés de magnetotransport complexes que nous avons interprété avec l'aide d'un modèle faisant intervenir le couplage spin-orbite ainsi qu'un magnétisme induit.

# Abstract

Transition metal oxides possess a broad range of functionalities (superconductivity, magnetism, ferroelectricity, multiferroicity) stemming from the interplay between structural effects and electronic correlations. Recent work has revealed exciting physics at their interfaces, including conductivity and superconductivity in the two-dimensional electron system (2DES) that forms at the interface between two band insulators,  $\text{LaAlO}_3$  and  $\text{SrTiO}_3$ . However, to embrace the immense potential of oxide interfaces and unveil unprecedented electronic phases, combining insulators with stronger electronic correlations is necessary. At the crossroad between strongly correlated electron physics, magnetism and spintronics, the present thesis project aims to harness electronic and magnetic instabilities in correlated oxides to craft new electronic phases controllable by external stimuli. We investigated rare-earth titanates  $\text{RTiO}_3$ , a relatively unexplored family of Mott insulating perovskites with a crossover between antiferromagnetic and ferromagnetic orders upon changing the rare-earth size. Contrary to most previous works, we focused on ferromagnetic compounds, and their integration in 2DES. The thesis developed along two main axes. First, we explored several members of the rare-earth titanates family in epitaxial thin film form. We highlighted the presence of a magnetically active dead layer at the surface of thin films and established its origin as due to the overoxidation of titanium ions. We also studied the presence of an unexpected orbital moment carried by the titanium in some compounds, and discussed it in the light of the non-collinear spin arrangement promoted by the rare-earth orbital moment and of a structural gradient evidenced by transmission electron microscopy. In a second stage, we combined  $\text{DyTiO}_3$  with  $\text{SrTiO}_3$  to stabilize a conducting interface with puzzling magneto-transport properties that we interpreted with a model involving spin-orbit coupling as well as induced magnetism.

# Acknowledgement

First, I would like to thank the two reviewers Wilfrid Prellier and Stefania Pizzini for reviewing this manuscript. I'm also very grateful to Ralph Claessen and Cinthia Piamonteze for accepting to be a part of this committee, and for the collaborations I had the chance to establish with them. I would like to thank Professor Claessen for welcoming me in his team in Würzburg and helping me deepen my understanding of rare-earth titanates by working with Philipp Scheiderer and Michael Sing. I also loved to work with Cinthia Piamonteze at the SLS synchrotron. You taught me so much about synchrotron techniques and you have always been available to help me with my numerous questions. I am also grateful to Marc Gabay for accepting to be a part of this committee and his insights on transport. I am glad to have Agnes Barthelemy and Jacobo Santamaria as guests in this committee and for the fruitful discussions, I had the chance to have with you in the laboratory.

In général, I would like to show my gratitude to all the people I had the chance to collaborate with. In addition to the collaboration with Cinthia Piamonteze in SLS, I would like to thank Sergio Valencia, Florin Radu, Chen Luo from BESSY II and Fadi Choueikani as well as Philippe Ohresser from Soleil. Thanks Alexandre Gloter and Léo Cambou for their beautiful TEM images and analysis presented in this thesis, as well as the pedagogy they demonstrated while explaining the principle of the different TEM techniques.

A special thanks to the two post-docs I had the chance to directly work with. First to Daniele Preziosi who trained me to the arcana of PLD growth. You were a tough teacher but a good one. Ciao Daniele! For the second part of my thesis I had the chance to work with Jin Hong Lee my captain in the MINT warrior even if I never could reach your insane growth rhythm! I also had the chance to work with Julien Varignon our computer experimentalist, who was an indispensable part of our team professionally as well as on a personal level.

Now I would like to thank generally people from the lab for the wonderful work environment they collectively created. From the drinks together with the non-permanent staff, the farewell "pots" in the lab as well as the post defense "pots", the CNRS/Thales lab is really a great place to work at. On a more serious and less alcoholized note, I really enjoyed my stay here and appreciate our discussions, scientific or not. From the philosophic ones with Victor to the political ones with Karim and Olivier and passing by many scientific discussions with Nicolas! I enjoyed all of them. Thanks to everyone for this time, especially the oxide team. Thanks also to the directors, who managed to organize this wonderful environment as well as the administrative staff Anne, Nathalie and Christine.

I shall not forget my friends who supported me during this PhD even in the hard times. I really could not have done it without the parties of the Soviet and the holidays spent with them. The heartfelt discussions with you guys and girls really helped me, especially Hugo. I am waiting the next fondue and/or raclette with l'inutile when the pandemic will be over! Charlotte, if she left the lab and traveled

to the other side of the planet, she stayed a good friend and support through this thesis and after. At least, you will have less occasions to humiliate me at ping-pong! A special thanks to Solene for her help in correcting some of my many typos. For more scientific corrections as well as yet some more typos, I have to thank again the wonderful people of the oxide team. Thanks to Julien Brehin, Lucia Iglesias, Sara Varotto and Jin Hong Lee. I could not have finish the last version of this manuscript, while preparing the *agregation de physique*, without your help.

As it will be strange not to thank them, I am grateful to my parents first for being here but more importantly for raising me and supporting my decisions. Even though these last years have been difficult for us, we made it through.

Finally, I would like to thanks Manuel Bibes my PhD supervisor for all of his wonderful work as a supervisor, by helping me staying focus, organizing my work and helping create fruitful collaborations but he also supported me in the hard time that was my fourth year of PhD. I really think, I could not have hoped for a better supervisor. You supported me, as some other kind of supervisor would not do. Not only for me but, and I think the rest of the team would agree, you always prioritized the wellbeing of the team as the recent confinement illustrated, while maintaining great scientific exigence. Thank you for these four years.

# Contents

<b>1</b>	<b>Perovskite oxides</b>	<b>18</b>
1.1	Presentation . . . . .	18
1.2	Crystal structure . . . . .	18
1.3	Electronic structure . . . . .	20
1.3.1	Crystal field . . . . .	20
1.3.2	Point charge contribution . . . . .	21
1.3.3	Ligand field . . . . .	21
1.3.4	Conclusion . . . . .	22
1.4	Type of correlations . . . . .	22
1.4.1	Tight binding model . . . . .	23
1.4.2	Mott insulator . . . . .	24
1.4.3	Charge transfer insulator . . . . .	26
<b>2</b>	<b>Experimental techniques</b>	<b>29</b>
2.1	Substrates preparation . . . . .	29
2.1.1	SrTiO <sub>3</sub> (STO) . . . . .	30
2.1.2	LaAlO <sub>3</sub> (LAO) . . . . .	30
2.1.3	RScO <sub>3</sub> (R = Dy, Gd, and Nd) (RSO) . . . . .	31
2.1.4	(LaAlO <sub>3</sub> ) <sub>0.3</sub> (Sr <sub>2</sub> TaAlO <sub>6</sub> ) <sub>0.7</sub> La <sub>0.18</sub> Sr <sub>0.82</sub> (Al <sub>0.59</sub> Ta <sub>0.41</sub> )O <sub>3</sub> (LSAT) . . . . .	31
2.2	Sample fabrication . . . . .	33
2.2.1	Pulsed Laser Deposition (PLD) . . . . .	33
2.2.2	In situ monitoring . . . . .	38
2.2.3	Reproducibility of the growth . . . . .	40
2.2.4	Target quality . . . . .	40
2.2.5	Device preparation . . . . .	42
2.3	Structure characterization . . . . .	44
2.3.1	X-Ray diffractometer (XRD) . . . . .	44
2.4	Superconducting Quantum Interference Device (SQUID) . . . . .	47
2.4.1	Principle . . . . .	48
2.4.2	Data analysis . . . . .	48
2.5	X-Rays Photoemission Spectroscopy (XPS) . . . . .	50
2.5.1	Historic perspective and principle . . . . .	50
2.5.2	Theory . . . . .	50
2.5.3	Instrumentation . . . . .	50
2.5.4	Peak analysis . . . . .	52

2.6	X-ray Absorption Spectroscopy (XAS) . . . . .	53
2.6.1	Principle . . . . .	53
2.6.2	Detection modes . . . . .	54
2.6.3	XAS spectra . . . . .	55
2.6.4	XMCD (X-ray Magnetic Circular Dichroism) . . . . .	55
<b>3</b>	<b>Rare-earth titanates: a brief introduction</b>	<b>58</b>
3.1	Presentation . . . . .	58
3.2	Properties . . . . .	58
3.2.1	Structural data . . . . .	58
3.2.2	Magnetic data . . . . .	59
3.3	Spin and orbital order . . . . .	60
3.3.1	Explanation of the rare-earth titanates phase diagram . . . . .	60
3.3.2	Magnetic orders . . . . .	63
3.3.3	Electronic properties . . . . .	66
3.4	State of the art on rare-earth titanate thin films . . . . .	67
3.4.1	Growth of epitaxial thin films . . . . .	67
3.4.2	Heterostructures . . . . .	70
<b>4</b>	<b>Growth of rare-earth titanate thin films</b>	<b>72</b>
4.1	Establishment of the growth conditions . . . . .	72
4.1.1	Growth parameters . . . . .	72
4.1.2	Oxygen vs Argon growth . . . . .	77
4.2	Crystalline orientation . . . . .	78
4.2.1	X-rays diffraction characterization . . . . .	78
4.2.2	Transmission electron microscopy characterization . . . . .	80
4.3	Living Dead Layer in DyTiO <sub>3</sub> . . . . .	82
4.3.1	Thickness dependence of the magnetic properties . . . . .	83
4.3.2	XPS and XAS depth analysis . . . . .	86
4.3.3	Establishment of a link between titanium valence and magnetic properties . . . . .	87
4.3.4	Origin of the "living-dead" layer . . . . .	88
4.3.5	Spatial investigation of the "living-dead" layer . . . . .	89
4.3.6	Resurrection of the "living-dead" layer . . . . .	89
4.4	Growth and properties of other rare earth titanates (GdTIO <sub>3</sub> , YTIO <sub>3</sub> and TmTiO <sub>3</sub> ) . . . . .	91
4.4.1	Structural study . . . . .	91
4.4.2	Valence state . . . . .	91
4.4.3	Magnetic properties . . . . .	93
<b>5</b>	<b>X-ray circular dichroism at the Ti L<sub>3,2</sub> edge in rare-earth titanate thin films</b>	<b>94</b>
5.1	Data analysis and experimental results on DyTiO <sub>3</sub> thin films . . . . .	95
5.1.1	First observation of a non-zero integral . . . . .	97
5.2	Sum rules . . . . .	98
5.2.1	Presentation . . . . .	98
5.2.2	Sum rules development . . . . .	99
5.3	XMCD analysis on GdTIO <sub>3</sub> , YTIO <sub>3</sub> and TmTiO <sub>3</sub> thin films . . . . .	99

5.4	Induced orbital moment in literature . . . . .	102
5.4.1	Chirality induced by symmetry breaking of the magnetic environment . . . . .	102
5.4.2	Perspectives . . . . .	104
<b>6</b>	<b>Toward a 2DES system in rare-earth titanate oxide heterostructures</b>	<b>107</b>
6.1	State of the art on 2DES system in heterostructures . . . . .	107
6.1.1	LaAlO <sub>3</sub> / SrTiO <sub>3</sub> interfaces . . . . .	107
6.1.2	Rare-earth titanate/STO systems . . . . .	110
6.2	Optimization of STO thin films . . . . .	112
6.2.1	Homoepitaxy study . . . . .	112
6.2.2	Growth of Nb:STO on STO . . . . .	113
6.2.3	Growth on LSAT (001) . . . . .	114
6.3	2DES systems . . . . .	115
6.3.1	LSAT//STO/DTO/LAO . . . . .	115
6.3.2	Transport properties . . . . .	116
6.3.3	Magneto-conductivity . . . . .	117



# Chapter 1

## Perovskite oxides

### 1.1 Presentation

### 1.2 Crystal structure

The perovskite structure ( $\text{ABO}_3$ ) constitutes an "ideal" framework for condensed matter physics because of its numerous degrees of freedom. It has been extensively studied for oxides but also in other domains, for example the elaboration of photovoltaic cells [5, 6].

The perovskite structure is described by a cubic unit cell belonging to the  $\text{Pm}\bar{3}m$  space group ( $\text{SrTiO}_3$ ,  $\text{CaTiO}_3$ ,  $\text{LaAlO}_3$  etc). This structure is made of transition metal ions sitting on the corner of the cube (B site), the oxygen ions forming octahedra cage around the B site and an A site at the center of the structure. Even if the cubic structure is the prototypical one, it is actually pretty rare. Indeed, many perovskites allow rotations of the oxygen octahedra, thus providing a huge variety of structures and consequently many different physical properties.

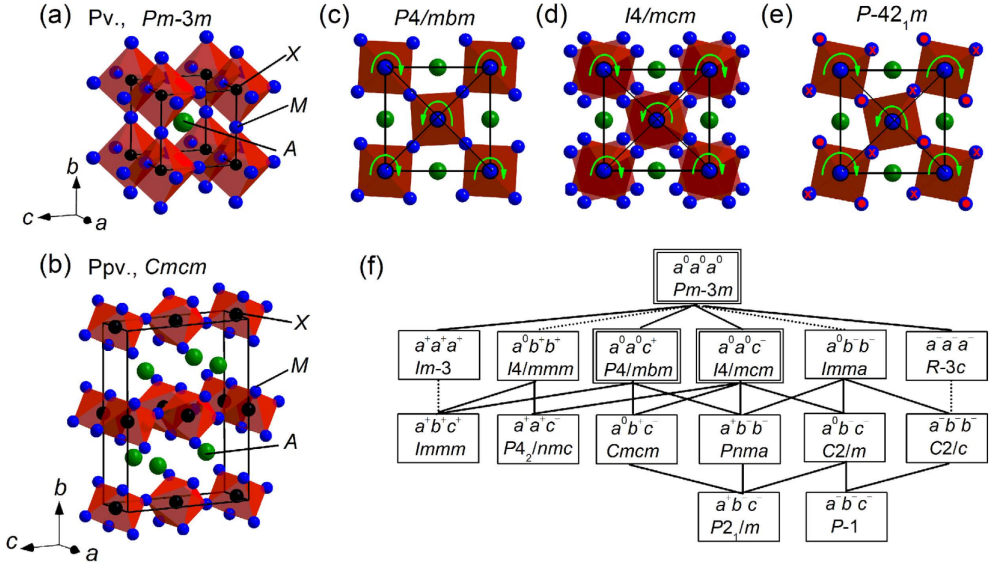


Figure 1.1: Schematic of perovskite structures of different space groups a) Cubic perovskite. b) Anti-phase rotation and in phase rotation respectively along the c and b axis. c) In phase rotation along the c axis d) Anti-phase rotation along the c axis. e) P-421m tetragonal symmetry. f) The supergroup-subgroup relationships among 15 space groups, which are mathematically deduced from the assumption of rigid BO<sub>6</sub> octahedra. The solid and dotted lines represent the second-order and first-order transitions, respectively. The space groups of the crystal structures discussed in this study are identified by double-lined boxes. Adapted from [7]

As one can see in Fig. 1.1 the rotation of the octahedra along different axes control the symmetry of the structure. To represent that we will use the Glazer notation, following the  $(x_i^\pm, x_i^\pm, x_i^\pm)$  format where x is the crystallographic axis and the sign tells us if the rotations are in-phase or anti-phase along the said direction. Of course, those rotations induce changes in lattice constants and result in the instability of the cubic structure.

An easy number we can use to predict the intensity of the deformation is the tolerance factor or Goldschmidt factor  $t = \frac{r_A + r_O}{\sqrt{2}(r_B + r_O)}$  where  $r_A$ ,  $r_B$  and  $r_O$  are the ionic radius of the perovskite species. According to this ratio we can predict the resulting structure as shown on Fig. 1.2:

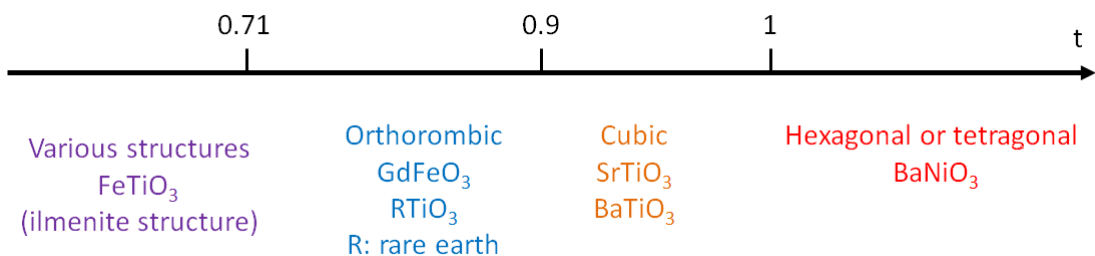


Figure 1.2: Evolution of the perovskite structure according to the tolerance factor [7]

Indeed, a tolerance factor of 1 corresponds to the perfect cubic structure that does not allow any deformation.

## 1.3 Electronic structure

In perovskites the electronic structure is mainly controlled by the different deformations of the crystal structure and the filling of the valence shell of the B site. Indeed, near the Fermi level lie the 2p levels of oxygen and 3d (or 4d) levels of the site B transition metal. Usually the valence shell of the A site lies much lower than the other two. Thus we only have to consider the filling and electronic environment of those levels.

### 1.3.1 Crystal field

Focusing on the 3d levels, we can decompose them on the basis  $|xz\rangle$   $|yz\rangle$   $|xy\rangle$   $|z^2\rangle$   $|x^2 - y^2\rangle$  when applying the observables  $L$  and  $S$

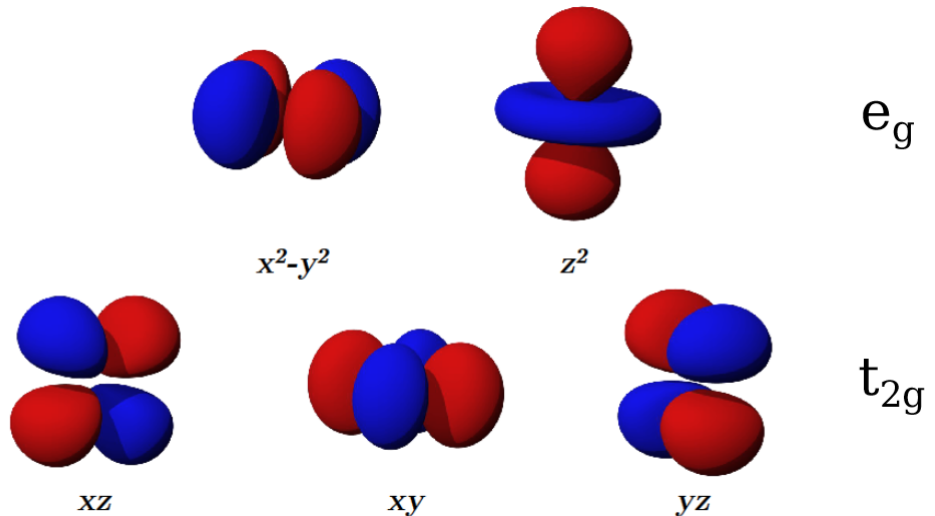


Figure 1.3: Schematic representation of the 3d orbitals

In the same way, the 2p orbitals of the oxygen are to be decomposed in  $|x\rangle$   $|y\rangle$   $|z\rangle$

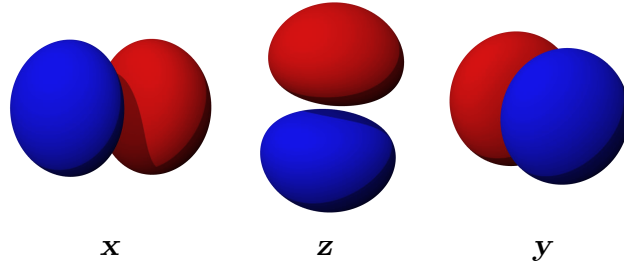


Figure 1.4: Schematic representation of the 2p orbitals

For these two classes of orbitals, we notice the clear anisotropy of these states. They will thus be affected by the shape of their environment and in particular by the repartition of charges around them.

### 1.3.2 Point charge contribution

To take into account this anisotropy we use, in first approximation, the so called point charge model, where the electrostatic environment is modeled by point charges in space for the sake of simplification. Indeed some of 3d orbitals in Fig. 1.3 points toward the 2p of Fig. 1.4, those orbitals are grouped in the  $e_g$  doublet and the other in the  $t_{2g}$  triplet. Consequently, the  $e_g$  group is more destabilized than the  $t_{2g}$  compared to the free ion picture. It thus lifts the degeneracy of the 3d level by an energy of  $\Delta_{CF}$ .

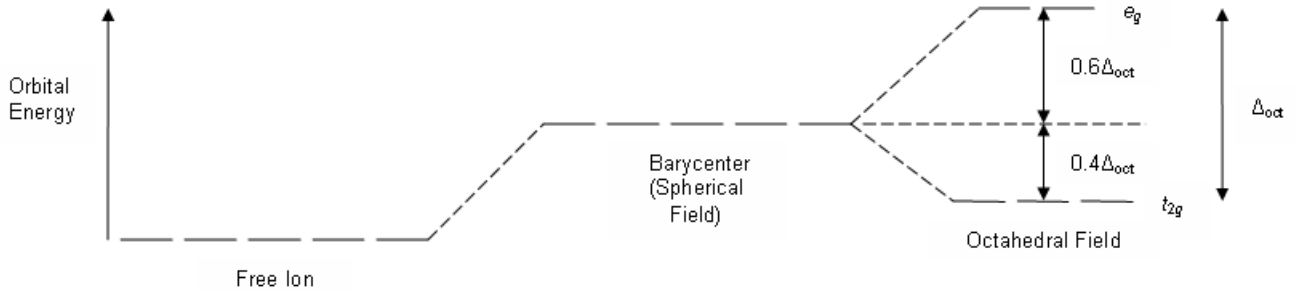


Figure 1.5: Schematic representation of the 3d energy levels in different given electrostatic environment

By taking as a reference the spherical field the  $t_{2g}$  are stabilized by  $0.4\Delta_{CF}$  and the  $e_g$  destabilized by  $0.6 \Delta_{CF}$ . This contribution is known as the point charge contribution.

### 1.3.3 Ligand field

Another effect to take into account is the hybridization between the 3d and 2p orbitals. In addition to the electrostatic contribution, the hybridization creates bonding and anti-bonding states. This effect scales with the overlapping of 3d and 2p and adds up to the effect of the electrostatic repulsion.

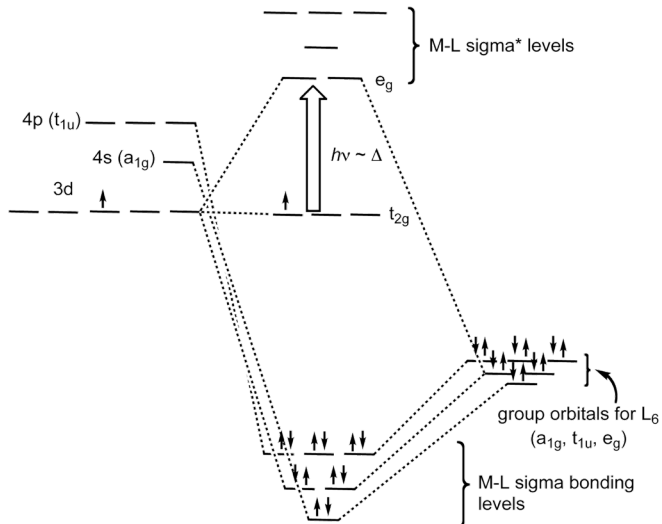


Figure 1.6: Schematic representation of the effect of the ligand field on the electronic state

The  $e_g$  orbital hybridizes to the 2p via  $\sigma$  bonds whereas for the  $t_{2g}$  it is through the weaker  $\pi$  bonds, see Fig. 1.7. Thus, it leads to a similar hierarchy between the states. In first approximation,

we can treat the physics of the  $3d$  levels in the same way as in the point charge picture but while keeping in mind that the resulting states are linear combinations of  $p$  and  $d$  characters.

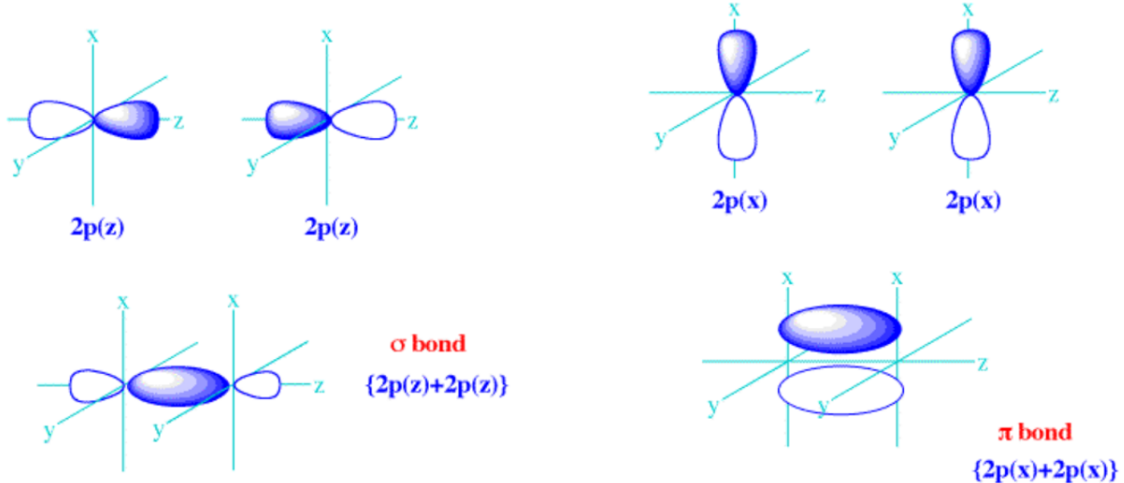


Figure 1.7: Schematic representation the  $\pi$  and  $\sigma$  bonds. REVOIR

### 1.3.4 Conclusion

The point charge contribution is dominant in the ionic picture where the overlap between TM and ligand is weak and neglecting the hybridization is justified. This description is mostly sufficient to understand the observed lift of degeneracy.

However, in most cases the covalent character is predominant, in this case the  $t_{2g}$  states can no longer be considered as purely  $3d$  but as linear combination of the two (*cf* section 1.4.3). The covalent character of the bond depends on the type of ligand and TM. As the size of  $d$  and  $p$  orbitals increase (respectively  $3d < 4d < 5d$  and  $O < S < Se < Te$ ) the overlapping become more efficient and the covalent character and  $\Delta_{CF}$  increase. The filling of  $3d$  levels lowers them and brings them closer to the  $p$  band.

Even if in general the covalency contribution is larger, the resulting states are treated as point charge contribution because of its simplicity of use and the similar end-result.

In oxides ([8] p44) the electrostatic repulsion is still important and the  $t_{2g}$  and  $e_g$  are mostly of  $3d$  character (see section 1.4.2).

## 1.4 Type of correlations

In this section, we will unfold the various physical models needed to understand the physics of our systems. We will be particularly careful to highlight all approximations and limitations to those models for the sake of precision.

One of the simplest models we can use in condensed matter physics is the tight binding model. This model describes **non-interacting** electrons in an infinite and **static** crystal by considering that the solution to the crystal Hamiltonian can be written as a **linear combination** of atomic wave function. Those three hypotheses are at the basis of the Linear Combination of Atomic Orbital (LCAO) method

developed by Robert Mulliken and Fredrich Hund in 1928 [9] and refined in 1955 [10]. This model has been adapted for solid physics use by changing the formalism and introducing the Bloch wave as a solution of the Hamiltonian,

$$\mathcal{H} = \mathcal{H}_{at} + \Delta U(r) \quad (1.1)$$

where  $\mathcal{H}_{at}$  is the atomic Hamiltonian and  $\Delta U(r)$  the term needed to take into account the periodic potential of the crystal.

#### 1.4.1 Tight binding model

This model is called tight binding model because the electrons are tightly bound to the atomic sites<sup>1</sup>. As a result, the solution is quite similar to atomic orbitals and interactions are considered to be small.

Compared to the more general LCAO treatment here two of the three Hamiltonian matrix elements can be neglected. Both on-site interaction with the neighboring potentials and overlap of the wave functions are considered small compared to the tunneling between sites through the periodic potential (hopping matrix element).

In the simple case of a lattice of non-degenerate electron levels on each site separated by the same distance, the Hamiltonian is written as following in second quantification,

$$\mathcal{H} = -t \sum_{\langle ij \rangle, \sigma} c_{i\sigma}^\dagger c_{j\sigma} \quad (1.2)$$

where  $c_{i\sigma}^\dagger$ ,  $c_{j\sigma}$  are the creation and annihilation operators of electrons at the site  $i$  with a spin  $\sigma$  and  $t$  is the hopping matrix element or hopping integral<sup>2</sup>.

The Fourier transform of Eq. 1.2 in the reciprocal space yields:

$$\mathcal{H} = \sum_{\mathbf{k}, \sigma} \epsilon(\mathbf{k}) c_{\mathbf{k}\sigma}^\dagger c_{\mathbf{k}\sigma} \quad (1.3)$$

By using a Bloch wave function to solve the Eq. 1.3, we obtain the following the eigenvalues corresponding to the energy of the each  $|\mathbf{k}\rangle$  states

$$\epsilon(\mathbf{k}) = -2t(\cos(k_x) + \cos(k_y) + \cos(k_z)) \quad (1.4)$$

From this result, we derive the band theory where the interactions between atomic levels give rise to a continuum of states called band. Eq. (1.4) describes the dispersion relation of free electrons inside a cubic 3D lattice. Of course, the free electron model is extremely limited:

1. It does not explain properly why some materials are insulating or metallic and describe very poorly the optical spectra of solids.

---

<sup>1</sup>This can be really confusing to a lot of people expecting the bonding between sites to be tight.

<sup>2</sup>Note that in Eq. 1.2 all matrix elements are equal irrespective of the  $(i, j)$  couple and only the nearest neighbors are considered. If necessary, we can avoid those simplifications and still solve the system. It would only make the development a little bit more complex.

2. It also does not take into account the electron-electron interaction, which is key to understand the new materials from the end of the XXth century (such as the cuprates).
3. Finally, by considering, the ions still (adiabatic approximation), it puts aside the physics of phonons *de facto*.

Actually the free electrons model is only fully suited to describe alkali metals (Li, Na, K, Rb, Ce and Fr) because of their simplicity in terms of band structure.

However, in most of the cases the dispersion relations are much more complex. We have to take into account the fact that all directions are not equivalent, electronic interactions are playing a role and band-band interactions also exist. This results an anisotropic dispersion relation and an highly complex density of states (DOS), as seen in Fig.1.8.

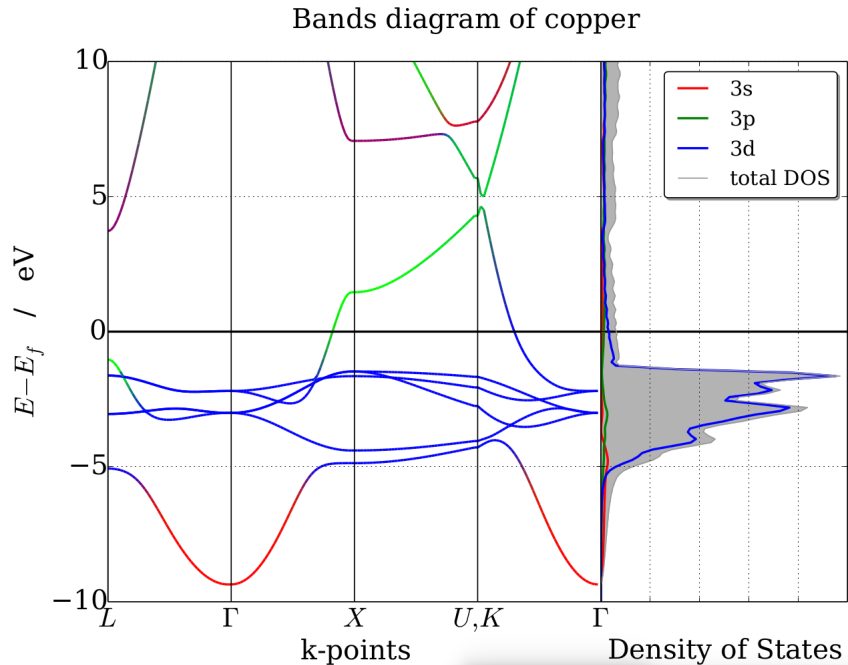


Figure 1.8: Dispersion relation and density of state of Cu

#### 1.4.2 Mott insulator

To further complexify our description, we abandon the ideal gas framework and introduce interactions between electrons. After hopping from the  $i$  to  $j$  sites, the system will present two electrons on the  $j$  site and these two electrons will repeal each other via the Coulomb repulsion. This phenomenon will destabilize the system by an energy usually called  $U$ . Of course, in order to respect the Pauli exclusion principle our non-degenerate orbitals allow only the electrons with opposite spin.

$$d^n d^n \rightarrow d^{n-1} d^{n+1}, \Delta E = U = U_{dd} \quad (1.5)$$

This interaction is described for the full system by the following Hamiltonian:

$$\mathcal{H}_{\text{int}} = U \sum_i n_{i\uparrow} n_{i\downarrow} \quad (1.6)$$

where  $n_{k\sigma} = c_{k\sigma}^\dagger c_{k\sigma}$  is the number operator simply counting the number of electrons on the  $i$  site.

By adding Eq. (1.6) to (1.2) we obtain Eq. (1.7)

$$\mathcal{H} = -t \sum_{\langle ij \rangle, \sigma} c_{i\sigma}^\dagger c_{j\sigma} + U \sum_i n_{i\uparrow} n_{i\downarrow} \quad (1.7)$$

this model is known as the Hubbard model [11].

Excitations such as the ones presented Fig.(1.5) create an electron and a hole that would be able to travel through the crystal and form new bands with a width of  $W = 2zt$  ( $z$  the number of nearest neighbor) but as we saw the creation of such an excitation would cost an energy  $U$ . Thus, the energy gap needed for this excitation is

$$E_g \sim U - W = U - 2zt \quad (1.8)$$

this gap plays a similar role as the one between a full valence band and an empty conduction band in a band insulator.

We can understand that in the case where  $U \geq W$ ,  $E_g \geq 0$  and the gap becomes effective. For example, a system with one electron per site would be insulating whereas in the simple band picture it would have been conducting.

This happens to materials where the bandwidth<sup>3</sup> (i.e.  $t$ ) is small compared to  $U$ . This is what Mott predicted in 1990 [12].

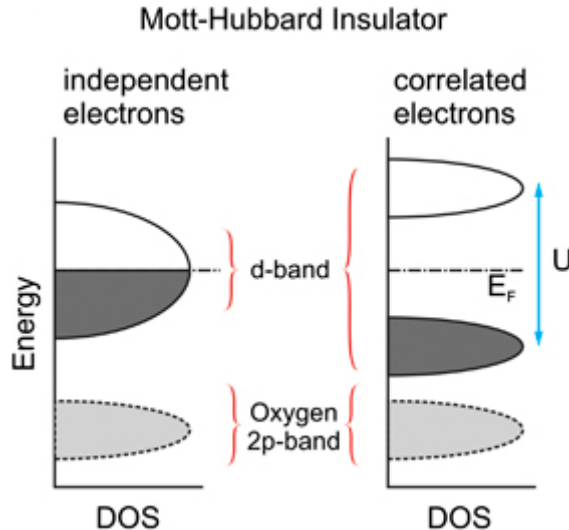


Figure 1.9: Schematic of the splitting of the band in upper and lower Hubbard subbands as a function of the strength of the one-site electron-electron repulsion

Even if the situation looks quite similar to that of band insulators, there is in fact a lot of differences. For example, the gap here has a completely different origin. Instead of the lattice periodicity, it is driven by the electron-electron interaction. Whereas the capacity of band is usually constant and equal to  $2N$  ( $N$  the number of sites), in Mott insulators the capacity of each subband is not constant. If the filling is below  $N$ , the lower Hubbard band could contain less than  $N$  states and the upper one more. This phenomenon is known as the spectral weight transfer or redistribution.

<sup>3</sup>In the early literature, the use of band width was preferred to the one of hopping matrix element.

Even if these subtleties are important, the main points are:

- a gap is opened by electron-electron interaction in a system otherwise supposed to be metallic
- this gap opens through a so-called Mott transition that can be driven by pressure, temperature and change in composition, all acting on the  $U$  parameter
- compounds with half-filled bands are more likely to undergo a Mott transition because in this case the gain in electronic repulsion is the most important

These points are crucial to explain the splitting of the Hubbard bands. However, in perovskite oxides the opening of the gap seems to be driven by structural deformation of the lattice according to a recent study [13, 14]. We will go in more detail about this process in the 3rd chapter dedicated to our main system of interest, here: rare-earth titanates.

### 1.4.3 Charge transfer insulator

In the previous section, we mainly discussed the physics of d electrons but as we have seen in subsection 1.3.1 it would be a mistake to forget the effect of the p electrons from O atoms.

As we saw the overlap between transition metal and oxygen should not be overlooked. It appears in fact quite unlikely that the hopping of d electrons occurs directly between d sites but more through jumps between the p and the d orbitals.

$$d^n p^6 \longrightarrow d^{n+1} p^5, \Delta E = \Delta_{CT} \quad (1.9)$$

where  $\Delta_{CT}$  is the energy needed to promote a p electron to the d band  $\Delta_{CT}(d^0) = \epsilon_p - \epsilon_d$ , here equivalent to the  $E_g$  of Eq. (1.8).

Note that if the d-shell has already one electron  $\Delta_{CT}(d^1) = (\epsilon_p + U_{dd}) - \epsilon_d$ , the corresponding model extends the Hubbard model to jumps between p and d and is therefore known as the p – d model.

$$\mathcal{H} = \epsilon_d \sum d_{i\sigma}^\dagger d_{i\sigma} + \epsilon_p \sum p_{j\sigma}^\dagger p_{j\sigma} + \sum t_{pd,ij} (d_{i\sigma}^\dagger p_{j\sigma} + h.c.) + U_{dd} \sum n_{di\uparrow} n_{di\downarrow} + U_{pp} \sum n_{pj\uparrow} n_{pj\downarrow} + U_{pd} \sum n_{di\uparrow} n_{pj\downarrow} \quad (1.10)$$

where  $\epsilon_d$  and  $\epsilon_p$  are respectively the on-site energy of d and p electrons,  $d_{i\sigma}$   $p_{i\sigma}$  are the creation operators of d and p electrons and  $n_{di\sigma}$   $n_{pj\sigma}$  the corresponding number operators. Finally,  $U_{dd}$ ,  $U_{pp}$  and  $U_{pd}$  are the repulsion energies between d and p electrons or between the two.

Because this model is more detailed than the Hubbard model, one can wonder if it still holds. Since the p – d model corresponds to a decomposition of the hopping processes, we can build an effective dd hopping integral  $t = t_{dd}^{eff} = \frac{t_{pd}^2}{\Delta_{CT}}$  and use the p – d model as the Hubbard model when  $U_{dd} < \Delta_{CT}$ . In these conditions the effect of the p level has little influence on the opening of the gap and on the nature of the d state.

On the contrary if  $U_{dd} \gg \Delta_{CT}$ , when the d band splits, the effective gap is opened between the p band and the upper Hubbard band. At the same time, the lower band doesn't have anymore a pure p or d

character due to the proximity between the lower Hubbard band and the  $p$  band. As a consequence, the smaller (compared to  $U_{dd}$ )  $\Delta_{CT}$  is, the most  $p$  character the valence states are. This type of correlated material is called a charge transfer insulator.

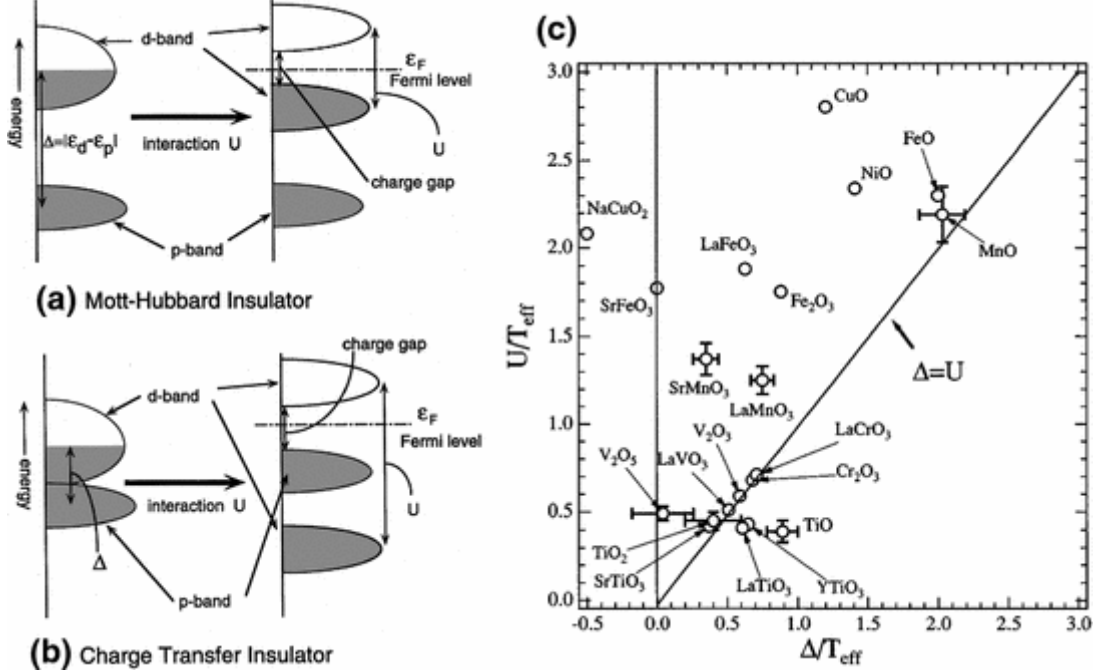


Figure 1.10: (a) Schematic of the band structure of a Mott-Hubbard insulator (b) Schematic of the band structure of a charge transfer insulator (c) Phase diagram of oxides,  $U$  as a function of  $\Delta$  normalized by the hopping matrix element peculiar to each compound. The line  $\Delta = U$  is plotted as the approximated frontier between CT and Mott insulator. Adapted from [15] (a,b) and [16] (c)

The broader  $p - d$  model is used for charge transfer insulator such as NiO and LaMnO<sub>3</sub> and for high-T<sub>C</sub> cuprates where the bond with  $p$  orbitals is thought to be crucial and is still describing Mott insulators. It provides us a more detailed explanation of the physics of correlated materials. In the end, the competition between different parameters can be summarized in the following phase diagram adapted from [17].

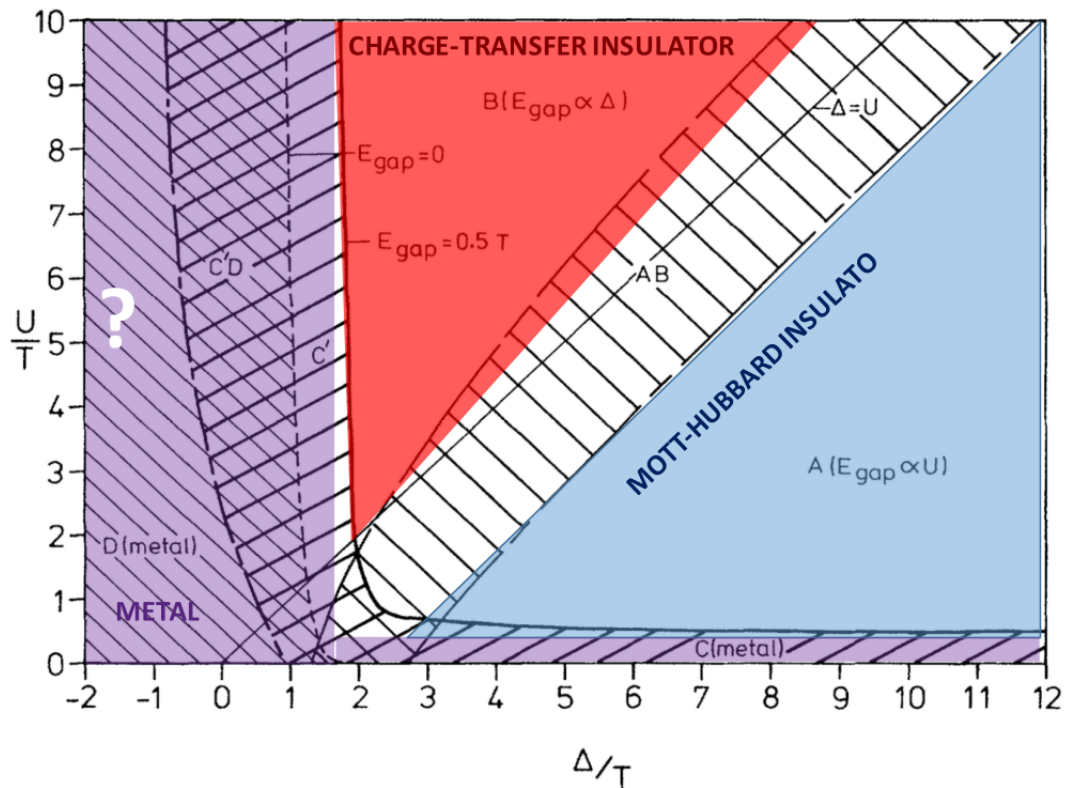


Figure 1.11: Phase diagram of the different states discussed above. Adapted from [17]

# Chapter 2

## Experimental techniques

### 2.1 Substrates preparation

The control of the substrate surface is critical in order to get high quality epitaxial thin films. The first requirement to obtain an atomically flat surface would be to start with one. Indeed, starting with an already atomically flat surface helps to keep a smooth surface after growth and allows access to the step flow regime.

In certain cases, a specific termination of the substrate is required as for LaAlO<sub>3</sub> on SrTiO<sub>3</sub> (001) samples where the TiO<sub>2</sub> termination is needed to obtain the 2DES at the interface.

In the perovskite structure ABO<sub>3</sub> the (001)<sub>pc</sub> oriented surface is either AO or BO<sub>2</sub>. In the as-received substrates, the surface is composed of a mix of AO and BO<sub>2</sub> where no well-defined step can be seen. So they can be only half-unit cell high steps and no apparent order in certain cases, see Fig. 2.1 (a, b). Usually the resulting surface is rougher compared to its treated equivalent.

The following recipes will be mainly extracted from A. Biswas et al., Progress in Surface Science 2017, 92, 117.

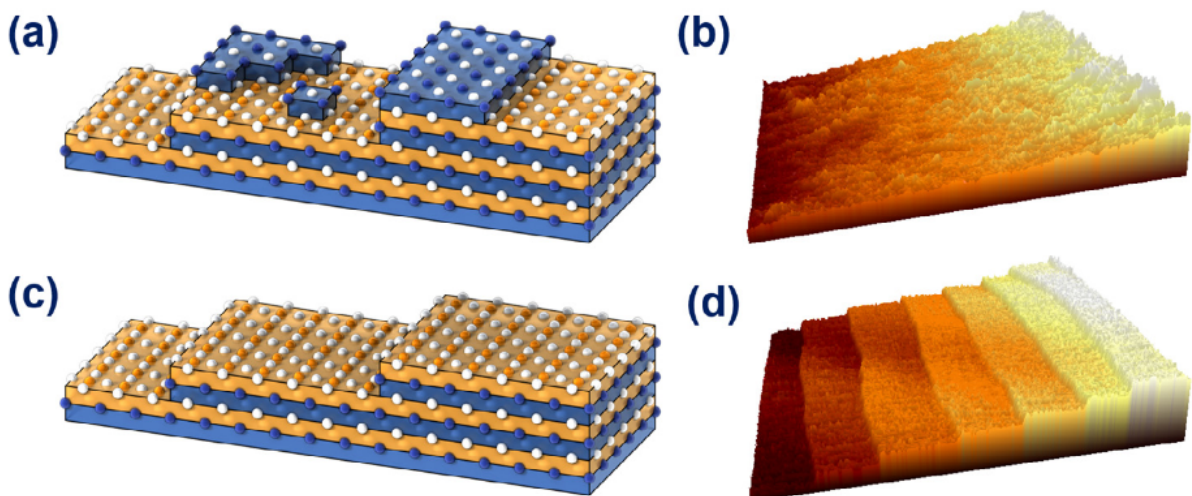


Figure 2.1: Atomic structure and typical AFM topography of: (a)-(b) an as-received surface and (c)-(d) an atomically flat surface. Schematic figures (a) and (c) are reproduced from [18].

**Nota Bene:** In the following recipe, the term "cleaning" refers to a specific procedure where we dip the substrate in isopropanol, dry it with N<sub>2</sub> gun, dip it in acetone then in isopropanol again and

dry it. Of course one shouldn't dry the substrate after acetone to avoid drying marks of the surface. After this first step, we used a Q-tip wrapped in the cleaning tissue dipped in isopropanol and we scrub the surface with it, then we dip it one last time in isopropanol, dry it and observed its surface under the AFM camera lens to check for meso particle or fiber. If the AFM shows no traces of particles the process is over if not we have to start all over again.

### 2.1.1 SrTiO<sub>3</sub> (STO)

STO has a stable perovskite structure and on the electronic structure point of view, it is a band insulator with an indirect band gap of 3.25 eV and a direct one of 3.75 eV. It also has a large dielectric constant of approximately 300 at room temperature.

in plane parameter (Å)	density (g.cm <sup>-3</sup> )	T <sub>C</sub> (K)
3.905	5.175	2080

**Recipe for STO (001):** We start by filling an ultrasonic cleaner and heat it to 60 °C. We fill a borosilicate glass beaker with acetone, and place an out of the box mix-terminated single-side polished (001)- oriented STO single-crystal substrate (25 mm<sup>2</sup> in lateral size, 0.5 mm in thickness with a miscut angle between 0.01° and 0.02°) inside the borosilicate glass beaker. We proceed to sonicate the substrate in acetone for 3 min and dry it using a nitrogen blowgun. We then repeat this procedure but using isopropanol and then deionized water, to ensure that the surface is as clean as possible. Then, we place the clean substrate in a sample holder made of polyvinylidene fluoride, PVDF, with a "dipper" shape (see Fig. 2.17a). It is important to choose a dipper made of a material that sustains the acidic HF solution. We then fill a large borosilicate glass beaker with running deionized water (see Fig. 2.17b). After placing the substrate in the dipper, we fill a beaker, typically made of Polytetrafluoroethylene, PTFE, to about 20 volume, with a buffered hydrofluoric (HF) solution (HF:NH<sub>4</sub>F = 1:7). Then, we submerge the dipper in HF for exactly 30 s and immediately move it into the deionized running water to stop any subsequent chemical reactions. After 2 min, we remove the sample holder from the deionized water, and dry the substrate with a nitrogen blowgun.

30 s in HF pH= 4.5 and annealing at 1000 °C for 2-3 h in O<sub>2</sub> flow. After a second etching the surface is perfectly TiO<sub>2</sub> terminated.

The procedure is thoroughly described and shown in video [19].

### 2.1.2 LaAlO<sub>3</sub> (LAO)

LAO is a rhombohedral perovskite belonging to the space group R̄3c at room temperature. However, it is interesting to notice the presence of a cubic phase at 435 °C with an in-plane parameter of 3.82 .

	In plane parameter (Å)	density (g.cm <sup>-3</sup> )	T <sub>C</sub> (K)
LaAlO <sub>3</sub>	3.787 (3.82 cubic phase > 435 ° C)	6.52	

**Recipe for LAO (001):** LaAlO<sub>3</sub> is one of the easiest substrates to treat in order to obtain a single termination at the surface. After cleaning, we just need to anneal the substrates at 1000° C under O<sub>2</sub> for 3 hours with a ramping speed of 20°C/min.

### 2.1.3 RScO<sub>3</sub> (R = Dy, Gd, and Nd) (RSO)

RSO are orthorhombic perovskite substrates presenting the same GdFeO<sub>3</sub> type distortion as many oxide perovskites that we might grow on top. The RSO family consists of alternately stacked polar RO<sup>+</sup> and ScO<sup>-</sup> layers. The most widely used surface is (110) because of its square structure at the surface  $0.5\sqrt{a^2 + b^2}$

	$0.5\sqrt{a^2 + b^2}$ (Å)	0.5c (Å)	density (g.cm <sup>-3</sup> )
DyScO <sub>3</sub>	3.946	3.952	6.992
TbScO <sub>3</sub>	3.960	3.959	6.749
GdScO <sub>3</sub>	3.970	3.966	6.485
SmScO <sub>3</sub>	3.991	3.983	6.233
NbScO <sub>3</sub>	4.014	4.002	5.958
PrScO <sub>3</sub>	4.028	4.014	5.965

**Recipe for DSO (110):** only annealing at 1047 °C in O<sub>2</sub> or Ar during 30 to 60 min in order to obtain ScO<sub>2</sub><sup>-</sup> but the termination will be DyO<sup>+</sup> if the substrate is left 10h or more [20]. This has been explained by the evaporation of the dysprosium ions and the subsequent migration of these ions to the surface leading to this termination. This phenomenon is due to the weaker nature of the Dy-O bond and end after a prolonged heating to give a ScO<sup>-</sup> surface.

In the rest of the thesis, we heated the DSO at 1000° C for 1h under O<sub>2</sub> in order to obtain the surface. After this treatment, we can soak DSO in NaOH solution in order to dissolve eventual excess Dy at the surface. We reach then perfectly flat surface and ScO<sub>2</sub><sup>-</sup> terminated.

### 2.1.4 (LaAlO<sub>3</sub>)<sub>0.3</sub>(Sr<sub>2</sub>TaAlO<sub>6</sub>)<sub>0.7</sub> La<sub>0.18</sub>Sr<sub>0.82</sub>)(Al<sub>0.59</sub>Ta<sub>0.41</sub>)O<sub>3</sub> (LSAT)

LSAT has a cubic perovskite structure and an in-plane parameter of 3.868 Å for its (001) orientation.

	In plane parameter (Å)	density (g.cm <sup>-3</sup> )	T <sub>C</sub> (K)
(LaAlO <sub>3</sub> ) <sub>0.3</sub> (Sr <sub>2</sub> TaAlO <sub>6</sub> ) <sub>0.7</sub>	3.868	6.74	

To treat this substrate, we have to take into account the high mobility of La ions. Indeed, by simply annealing the LSAT crystal one can observe the formation of islands [21]. Those islands can be removed by sonicating it in deionized water. This leads one to think that these islands are made of SrO because Sr is the only element that forms a complex in water. However, this method leaves behind holes on the surface.

To avoid these islands we place a substrate of LAO on top of the LSAT one to form a La rich gas in the gap between the two as shown in [22] and Fig. 2.2.

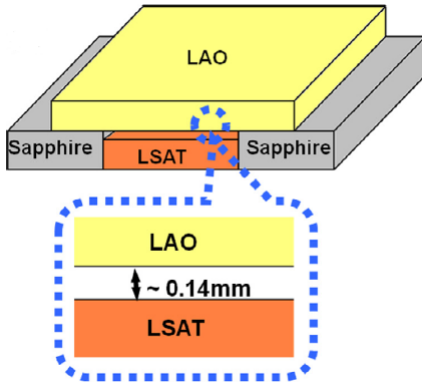


Figure 2.2: Schematic of the setup used to form the La rich gas at the interface. Adapted from [22].

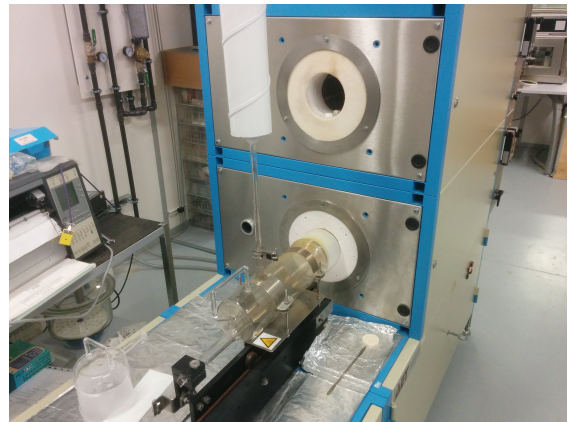


Figure 2.3: Photo the oven setup used in our lab

We reproduce this setup but with mixed results. Even though the steps can be seen, they are still blurred.

Finally, we tried to follow the recipe of V. Leca *et al* [23] based on the treatment of STO. The first step is to soak the substrate in deionized water for 30 min while sonicating. After drying up, we plunged it in aqua regia for 30 seconds to 10 minutes (here we settled on 3 min). Then we annealed the substrates under the same condition as for LAO. But no significant differences has been observed if we soak substrates in aqua regia or not.

Finally, we modified the recipe of [22] and by removing the gap between the LAO and LSAT which actually improved the surface quality.

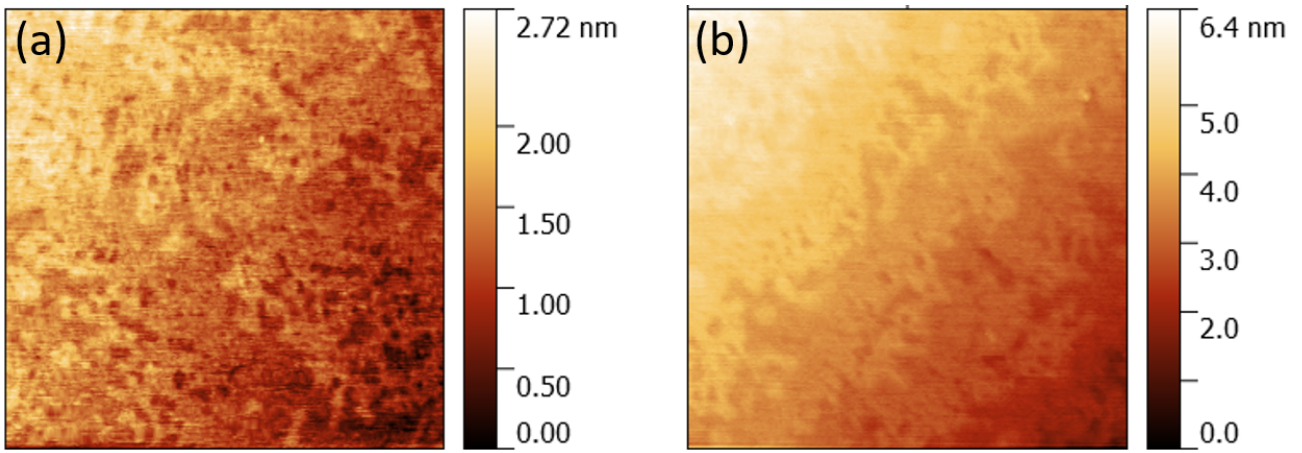


Figure 2.4: (a) AFM scan on LSAT surface after annealing at 1000° C under O<sub>2</sub> with a gap of 0.5 nm between LSAT surface and a LAO substrate (b) AFM scan on LSAT surface in the same condition but with direct contact with LAO.

As we can see from Fig.2.4(a) to Fig.2.4(b), the presence of a LAO substrate increases the flatness of the steps. At the end of this treatment, we obtain substrates suitable for heterostructure growth.

## 2.2 Sample fabrication

### 2.2.1 Pulsed Laser Deposition (PLD)

Pulsed Laser Deposition is a thin film deposition technique such as the Molecular Beam Epitaxy (MBE) and Sputtering deposition. Laser assisted growth has been developed [24] soon after the first lasers in the 60's. However the PLD as we know it, had its first success in the domain of high- $T_C$  superconductor [25] in the 80's.

This technique consists in the ablation of a target material by intense pulses of laser light. A plasma plume is created perpendicularly to the target and condense onto a substrate. There are a lot of parameters to take into account to control the sample quality but we will mainly vary the temperature of the substrate, the fluence of the laser and the background pressure and its composition. The deposition can be divided in three phases:

**Laser/target interaction:** when the laser pulse hits the target, it transfers its energy in the form of heat. Given the short pulse duration this energy is enough to create a plasma on impact Fig.2.5(a). The composition of this plasma at impact depends on the laser (wavelength, duration of the impulsion and repetition rate)[26] and on the target (density, thermal conductivity, absorption coefficient and composition).

**Expansion of the plasma:** after its creation the plasma undergoes an anisotropic expansion in the background gas Fig. 2.5 (b). The anisotropy of the plasma is mainly due to the geometric configuration that makes the main expansion direction perpendicular to the target. In addition, the rotation symmetry around this axis can be broken by the shape of the laser imprint. This effect is known as the flip-over effect [27]. The resulting plasma is what we call a plume. The key parameter to its size and its chemistry is the background pressure in the chamber. One can indeed see its dramatic effect on the size and brightness of the plume. It controls the confinement and thus the kinetic energy of the ionic species in the plasma and most importantly the nature of those species [28]. The pressure will determine if the species moving straight (ballistic regime) or are scattered by the background gas despite the overall impulsion toward the substrate.

**Plume/substrate interaction:** as the species arrive on the substrate, they condense on the substrate Fig.2.5 (d). Depending on the repetition rate, the final kinetic energy and the temperature the growth mode will be different.

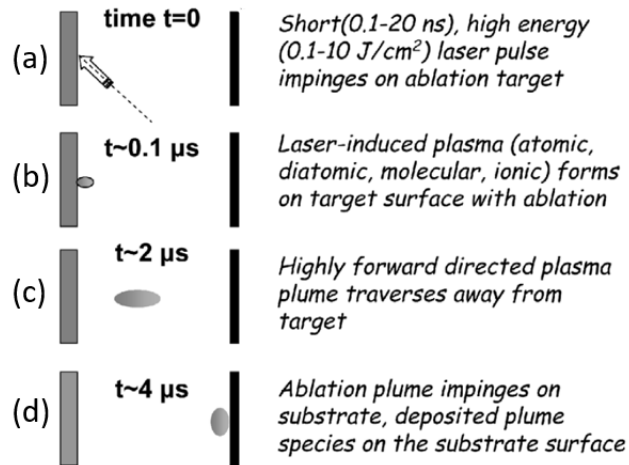


Figure 2.5: Schematic of the deposition process (a) laser impacting the surface (b) creation of the plasma by energy transfer from the light to the target (c) expansion of the plasma in the chamber (d) condensation on the substrate. Adapted from [29] p5.

The parameters controlling those steps will determine which growth mode will occur:

**Step flow growth:** When the steps of the substrate are well defined, the deposited material will diffuse to the edge of steps making them "flow". This growth mode is reached if the substrate has either a high miscut angle of the substrate and/or is at high temperature

**Layer by layer growth:** This mode is the most commonly used because it allows RHEED monitoring as discussed in section 2.2.2. Here islands nucleate on the steps, then added material migrates to the space between island and make them grow. This results in the growth of one unit cell after the other.

**3D growth:** In contrast with the previous mode here islands might nucleate on top of each other and new atoms will not fill the gap. This result in a overall 3D structure with no in plane spacial coherence. It is triggered by a lack of kinetic energy at the surface (namely the temperature of the substrate) or an excess of it in certain cases where the addatoms don't have the time to relax. This growth mode is, of course, incompatible with the growth of sharp interfaces.

## Target preparations

In the present thesis, we used 1-inch targets from Toshima, CrysTec GmbH or  $\pi$ Kem, some polycrystalline. Of course, single crystal targets are better to avoid preferential ablation of certain species which happen more often in polycrystalline ceramic target[30]. Before starting with the deposition, we have to prepare the target by polishing it. This ensures to have the consistent surface across the many growths that we performed. To do so, we polish its surface every 15 growths by using sandpaper and isopropanol and then dry it with a nitrogen gun.

## PLD system

The PLD chamber TURF that I used is a part of a full (ultra high vacuum) UHV system containing two PLD chambers (SURF and TURF) linked to a loadlock, a sputtering chamber and a X-rays Photoemission Spectroscopy system (XPS). This setup allows us to perform measurement and deposit material in a low pressure environment and thus avoiding any contamination or unwanted overoxidation.

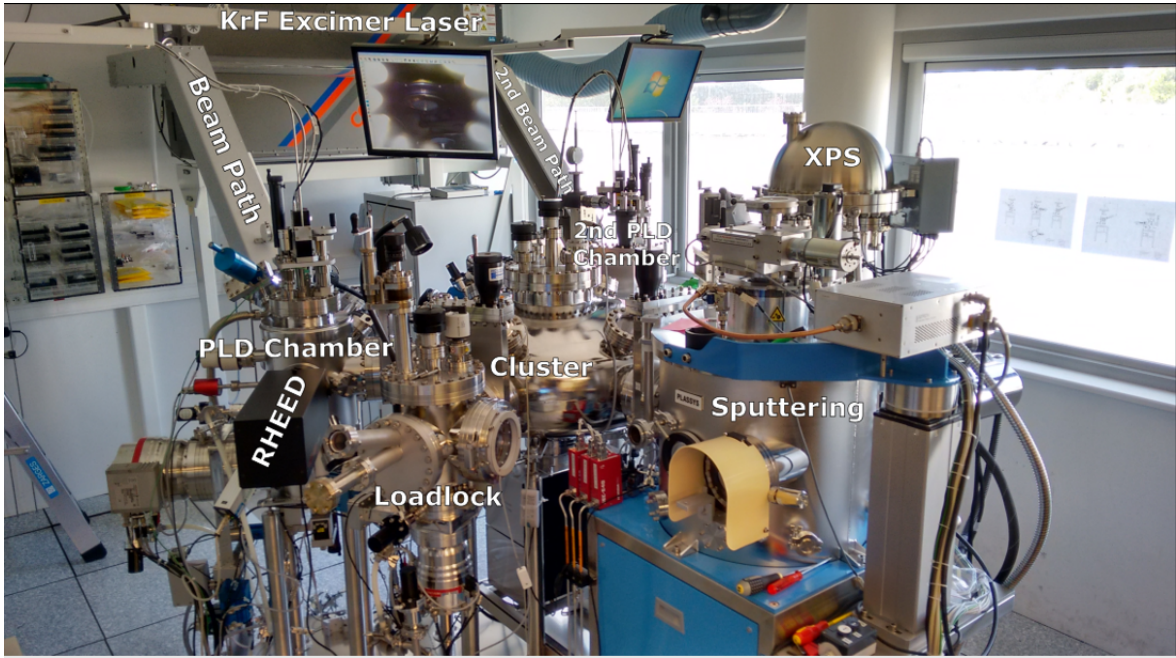


Figure 2.6: Growth and characterization cluster used in the lab, comprising of a central cluster linked to two PLD chambers, an XPS, a sputtering chamber and a loadlock.

### Optical path

The laser used is a KrF excimer laser (Coherent Compex Pro 201F) with a wavelength of 248 nm and pulse duration of 20 ns. The laser beam is generated in a chamber filled with a gas mixture using as active element KrF. By using discharge pins to apply a tension (between 19 and 27 kV), we initiate a transition of 248 nm in the KrF gas. The light emitted during the desexcitation is then amplified in the cavity, the energy of the laser beam is then measured before exiting the cavity. To reduce the energy, we cut the beam by using slits of different sizes (see Fig. 2.7a). Then the beam bounces on a first 45 ° mirror, a splitting mirror and a third and final one (see Fig. 2.7b). The beam is then focused by a pair of lenses and enters the chamber through a quartz porthole (see Fig. 2.7c).

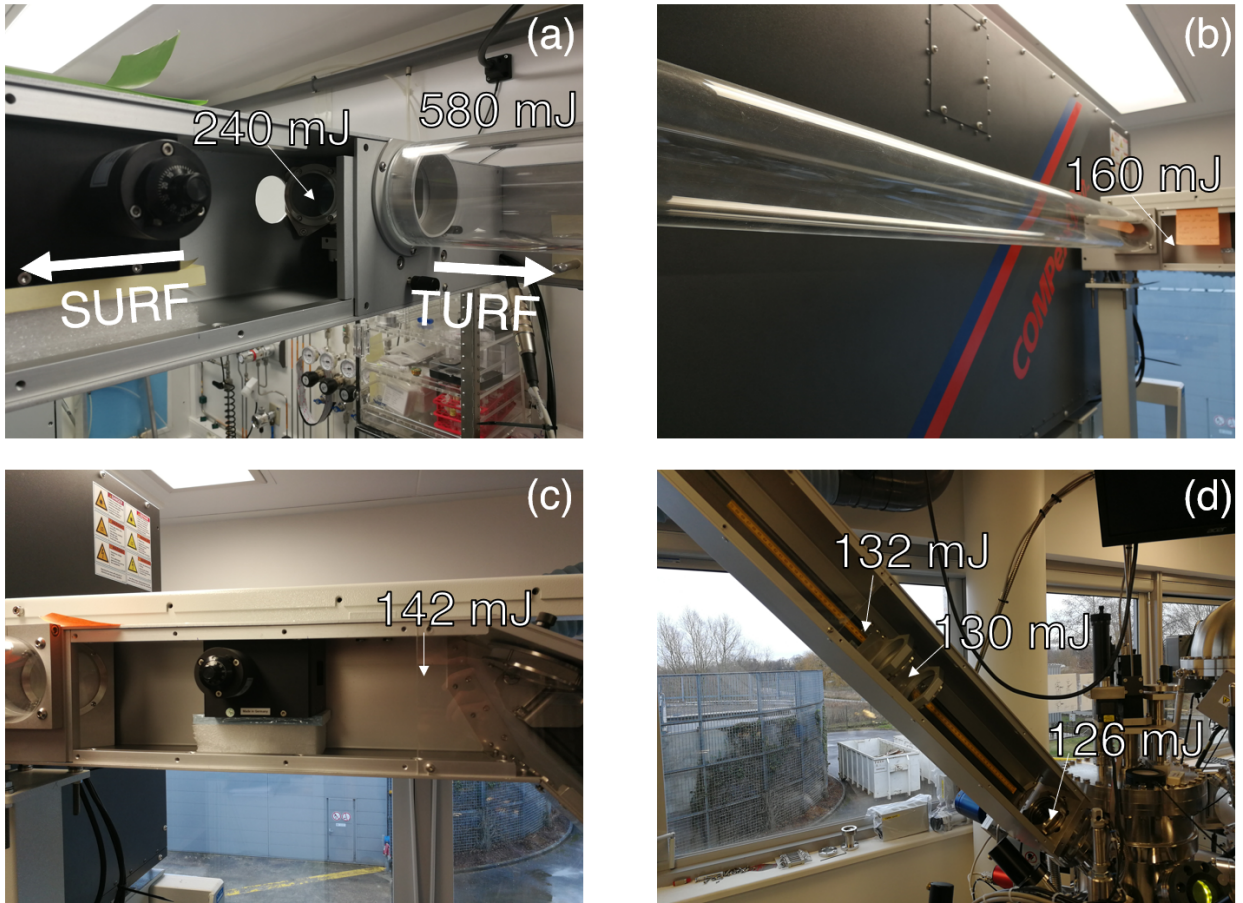


Figure 2.7: Optical path toward the TURF chamber beam path (a) from the laser to the TURF chamber optical path where the energy is first measured before the slit and after the splitting mirror respectively (b) from the splitting mirror to the attenuator, the energy is measured after the  $45^\circ$  mirror (c) from the third to fourth mirror<sup>1</sup>(d) from the fourth mirror to the TURF window. The energy has been measured before and after the first lens and before the window.

Since the optical path is rather long, some energy loss occurs along it. We control the output of the laser via the internal reading of the energy that we talked about earlier. It gives us a huge output compared to the final energy that we have. For example, to get a  $\sim 60$  mJ, when we ask for  $\sim 500$  mJ.

However, it is worth noting that the laser setting may differ from one growth to another, which is a secondary factor.

First the gas premix pressure is decreasing and its composition changes with each growth. This is why we have to regularly replace the gas with a new one. As the gas is getting used up, the voltage that we need to obtain the same energy increases until it can no longer be reached anymore (above 27 kV). On the other side of the spectrum, in order to reach low energy, we can use a variable attenuator (Metrolux ML 2100) to get the very low fluence needed for certain recipes.

During this thesis, we noticed a steady decrease of the gas pressure even when it was not used. After some investigation we discovered a leak of the gas chamber at the level of the discharge pins. Sadly, it could not be fixed without changing the entire chamber. This had the effect, in addition to requiring more frequent refills, to decrease the stability of the beam. Indeed at the beginning of my thesis the usual variation on energy was 0.2 mJ, however at worst it has been up to 10 mJ! It

<sup>1</sup>Note that the attenuator was not in place during the measurement.

represented a real challenge to realize the solid solution thin films which we grew during this PhD but are not included in this manuscript. In the end the gas chamber was changed and the aforementioned problems were fixed. The energy variation even decreased down to 0.1 mJ and we managed to again use the 10 Hz repetition rate which was not reachable due to uncontrolled discharges.

### TURF deposition chamber

The TURF chamber can host a carousel with five targets, that can rotate and toggle to ensure a complete coverage of the target during ablation (Fig. 2.8) and canceling eventual small inhomogeneities in the target. The final spot size of the laser on the target is 2 mm × 5 mm at the focus point of the lenses. This is why we have to keep a fix height of the targets in order to stay in the focal plane. Another important thing to take into account is the state of the mechanism of the carousel. The ball bearing mechanism has to be cleaned approximately once a month. This way, we ensured smooth rotation and avoid jerk motions during deposition that could result in ablating a metallic part of the carousel.

The chamber can reach a pressure between 1 bar and  $5 \times 10^{-9}$  mbar and allows mixing of two gases. We can inject O<sub>2</sub>, N<sub>2</sub> and Ar to control the oxidation chemistry of our films.

The temperature and the ramping speed of the substrate is controlled by a laser diode heater (=910 nm). The big advantage of this type of heating is its reliability compared to the resistive heating, where we can have between 10 and 20 °C of uncertainty. It is also more durable and most important it can reach much higher temperatures, well above 800 °C. In TURF we bring the laser light to the chamber using an optical fiber. It is then coupled to a pyrometer that aims at the backside of the sample, reading the temperature following a two-wavelength blackbody model. This system allows us to get up to 1300 °C at a maximum speed of 50 °C/min.

The sample holder slides inside a sample stage facing the target along a vertical axis. This sample stage is made of the rails for the sample, the shutter and the receiving end of the optic fiber. It can move along the vertical axis, thus allowing us to control the target to substrate distance. The system is also equipped with a sliding shutter that allows us to control the exposition of the substrate. We can also change the position of the shutter relative to the sample stage to exchange sample holder but also to grow a wedge of material. The shutter is made of a simple metallic plate that we used to close the shutter. However the middle part consists of a blade that when grazing to the surface of the sample can move at controlled speed thus creating a gradient of thickness during deposition.

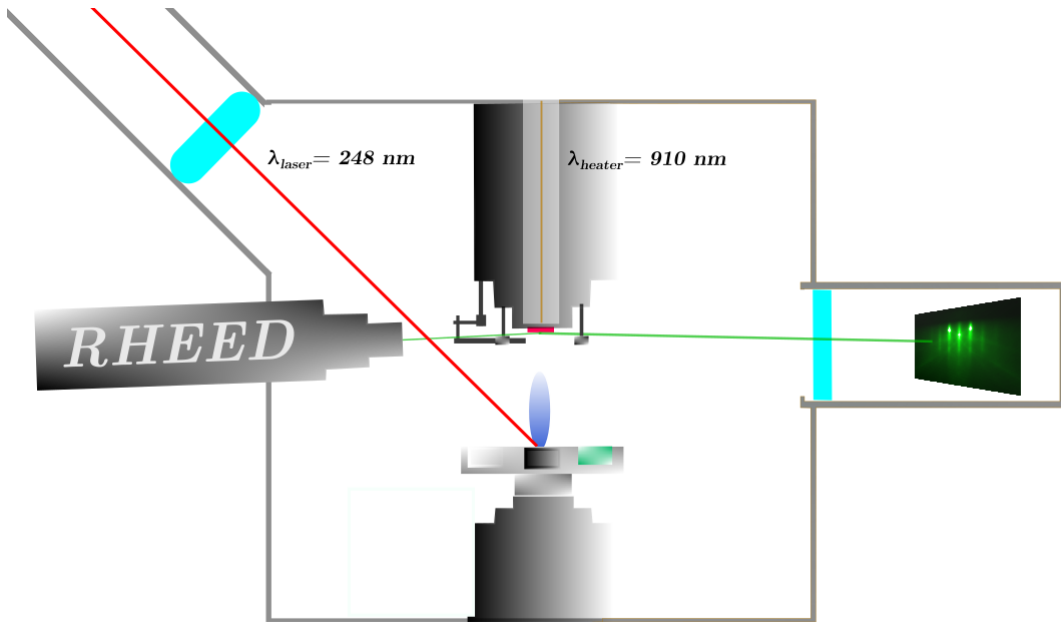


Figure 2.8: Schematic of the TURF deposition chamber composed of: a sample stage, a motorized shutter, a diode laser heater, Horizontal RHEED setup, five targets carousel and using an excimer laser.

Finally, the sample holder can be manually rotated as well as tilted. These settings allow us to get into the diffraction condition of the High Energy Electron Diffraction (RHEED) device.

### 2.2.2 In situ monitoring

As the material is deposited on the substrate, we can monitor it live and in situ via the Reflection of High Energy Electron Diffraction (RHEED). As its name suggests, this technique uses the diffraction of electrons to probe the surface of our sample as it grows. By using electrons, the Bragg condition is reached for lower angles (compared to X-ray diffraction) and probe the very surface (few Angström) of the sample since the wavelength is ten times smaller than with the X-rays. The diffracted electrons are collected on a fluorescent screen, which is recorded by a CCD camera. Our system allows an easy to implement and almost horizontal measurement geometry. At the end of the process, we obtain the intersection of the Ewald sphere and the reciprocal lattice on the screen.

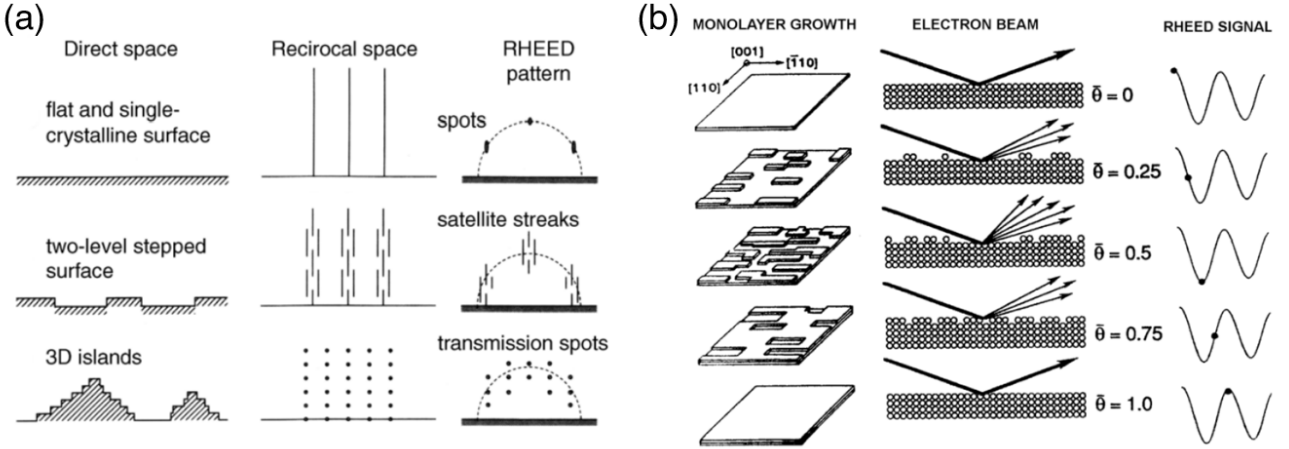


Figure 2.9: (a) Schematic of the structure of the sample in direct space, reciprocal space and the resulting RHEED pattern. Adapted from [31] (b) Schematic linking the oscillation of the RHEED intensity with the completion of a unit cell thus changing the scattering of incident electrons. Adapted from [32]

Since we are probing only the surface, if it is perfectly flat the reciprocal lattice take the form of infinite rods. Thus, we should observe a punctual dot on the screen where the rods intersect the sphere and the screen. However, what we actually see on Fig. 2.10(a), and in most cases, is continuous fringes. This is due to the fact that neither the rods nor the Ewald sphere are of no spatial extension. Indeed, the rods have a certain thickness coming from irregularity on the surface and so does the sphere because of the spatial and energetic dispersion of the incident electrons. The intersection then results in the observed stripes. If the growth mode becomes 3D the rods in reciprocal space will become spotty and the pattern projected on the screen.

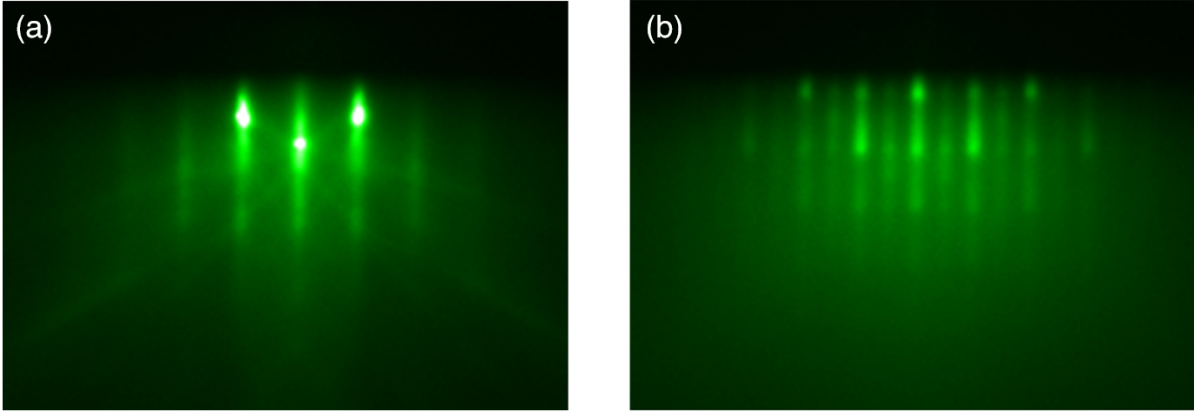


Figure 2.10: RHEED pattern of (a) LAO substrate before deposition and (b) 50 nm thick DyTiO<sub>3</sub>

Each fringe corresponds to a diffraction order thus the space between the fringes gives us the in-plane lattice parameter. We can notice in Fig. 2.10(a) that if the LAO surface is 2D as it should be for a substrate of good quality, for the 50 nm thick DyTiO<sub>3</sub> (DTO) it is no longer the case (Fig. 2.10(b)). The thickness for which we lose the coherence of the surface varies from material to material and growth conditions. When the surface becomes 3D, the transition is somewhat continuous as we can see in Fig. 2.10(b). We observe a mix of points and fringes halfway between the two states. New fringes also appear between the brightest one. They correspond to the orthorhombic nature of DTO unlike the cubic LAO (at the growth temperature). The unit cell is doubled resulting in the interfringe

being halved.

The evolution of the intensity of the fringes is directly linked to the thickness of the film. Indeed, as a unit cell is completed the pattern coherence goes to a minimum at half completion and then increases to completion resulting in oscillations allowing us to measure the thickness of our film to a theoretical atomic precision. Note that this is valid only in a layer-by-layer growth mode. Indeed, at half completion the material is randomly distributed on the surface of the sample, thus explaining the minimum. However, the picture breaks down when we are in the step-flow regime, where the step develops on the surface without the creation of islands and thus no loss of coherence. As a result, the RHEED intensity doesn't change. This regime is obtained under low laser frequency and high temperature as described in [33].

If the growth becomes 3D the diffraction loses coherence and no oscillations are observed. We can understand that by the fact that there is then no particular stage of the growth but only chaotic evolution.

### 2.2.3 Reproducibility of the growth

As most growth techniques, PLD uses a lot of control parameters. This can result in a somewhat chaotic behavior and gives seemingly random fluctuation on the resulting sample. This problem is however not our biggest one. As their name suggests those parameters are supposed to be controlled (temperature, energy, pressure, height etc.) but there is a lot of parameters that we could qualify as hidden. Such parameters could be laser window state, target state, beam path and sample holder state. Those parameters are easily overlooked and can lead to inconsistency in growth series.

### 2.2.4 Target quality

Another key ingredient to obtain high quality sample is the quality of the target we start from. In certain cases as observed in our group for the growth of NdNiO<sub>3</sub> (NNO) [30] the fluctuation observed from samples grown from a non-single phase polycrystalline target are strongly suppressed when we switch to a single-phase monocrystalline target. Polycrystalline targets are made of the monocrystalline domains but often those domains are made of simpler oxides AO, BO<sub>2</sub>, A<sub>2</sub>O<sub>3</sub> (depending on the valence of A and B) or even A<sub>2</sub>B<sub>2</sub>O<sub>7</sub>. Even though the company presents it as ABO<sub>3</sub>. This claim is only "true" relative to the ratio of mass of different atoms (measured by thermogravimetric analysis). The presence of these domains can lead to eventual inhomogeneity if the laser imprint has a size comparable with the inhomogeneity size. The result can be an off stoichiometry of the species sent to the substrate. We actually saw the effect of this as displayed in Fig.2.11.

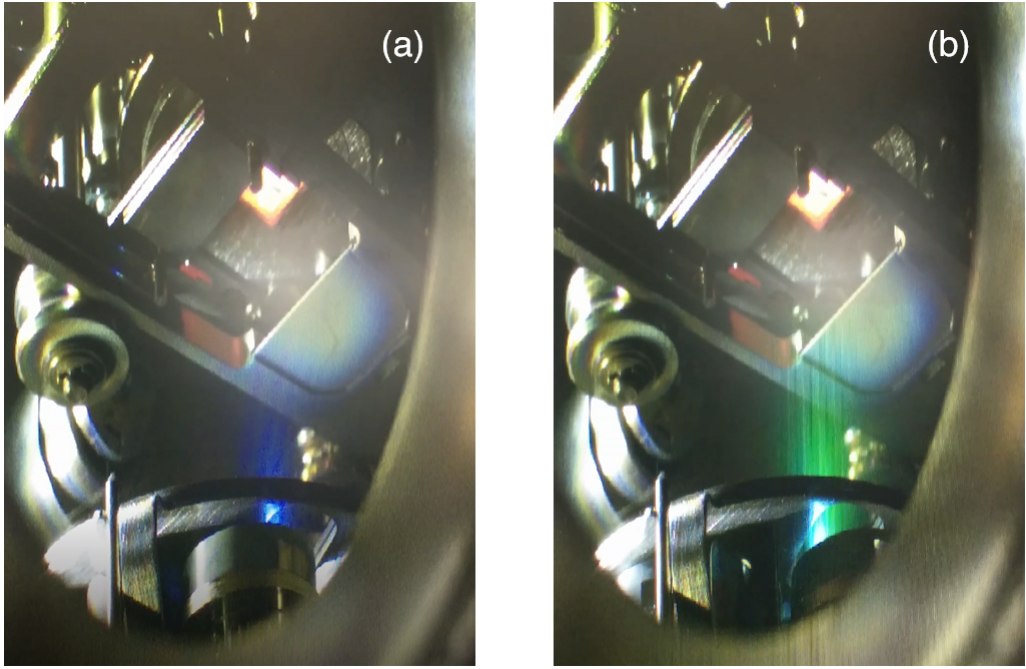


Figure 2.11: Picture of the plasma plume during the deposition. (a) Plume as it should be in the growth conditions of DTO (b) Plume presenting a change of color only when a specific area is ablated.

In Fig. 2.11 we can see a change of color of the plume depending on the area of the target scanned between Fig. 2.11 (a) and (b). This problem has been overcome by increasing the laser energy. Thereafter, the plume appeared blue.

Another effect to take into account is the surface state of the target across different growths. This is why we have to regularly polish our targets.

In certain cases, we can observe preferential ablation of some species. Indeed if ablated at low energy certain NNO targets see the formation of Ni at their surface [30]. In order to check for a similar effect in rare-earth titanate, we took a ablated target of DTO and polish half of its surface. The XRD results can be seen in Fig. 2.12. In Fig. 2.12 (a), we can see that the target is made of  $\text{Dy}_2\text{O}_3$  and  $\text{Dy}_2\text{Ti}_2\text{O}_7$  and not  $\text{DyTiO}_3$ . This fact is really important because most of the materials studied can be found in the form of dense In the case of DTO, there is no sign of preferential ablation (see Fig. 2.12 (b)). If we see shoulders on the peaks (most likely due to the change of structure at the surface when ablated), we don't see any new phases, unlike in [30].

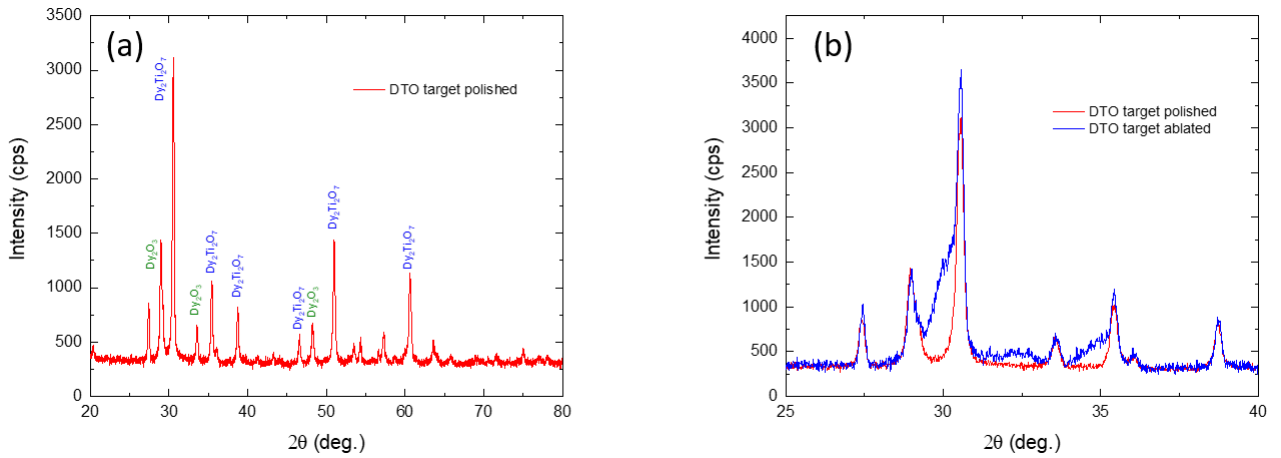


Figure 2.12: (a)  $2\theta - \omega$  XRD scan of DTO target with indexed peaks (b) Zoom on the  $25-40^\circ$  region on polished target and target after ablation.

### 2.2.5 Device preparation

In order to prepare Hall bars we used optical lithography. This technique defines a set motive on a plain plate sample. We first coat our sample with a photoresist that we pattern to our need by shining UV light through a mask thus creating area of different chemical reactivity. By developing the photoresist, we remove a part of it thus creating the desired shape that will protect the sample below. We etch by IBE (Ion Beam Etching) the bare surface, resulting in a patterned thin film.

All the following processes are done in the clean room of our lab, where the atmosphere is controlled. By operating in those conditions, we avoid contamination by dirt and moisture during the lithography procedure and the light is filtered to eliminate UV in order to avoid unwanted reaction of the resists.

#### Resist coating

The first step before the lithography is to prepare a smooth layer of photoresist. To do so we have to start with a clean sample. The usual cleaning treatment seen in section 2.1 is enough to obtain a clean surface as far as optical microscope is concerned.<sup>2</sup> We also dry the sample by putting it 1 minute on a  $90^\circ\text{C}$  hotplate. In order to create a homogeneous thickness of photoresist, we deposit one droplet of it on the sample cooled surface and use a spin-coating machine. As its name suggests this machine spins to spread the resin via the centrifugal force. By controlling the time and speed, we can obtain the desired thickness according to the photoresist specification. Finally, the photoresist must be heated on the hot plate in order to dry and the polymers to reticulate. The coating while supposedly homogeneous might present a thicker edge due to surface tension effects that we can reduce to a minimum by optimizing the parameters seen above.

#### Lithography and development

Depending on whether the photoresist is negative or positive, we want expose to UV light the parts we want to remove or the parts we want to keep. Knowing that, we choose a mask where the motive is either carved out or in. We placed a perfectly cleaned copper mask in contact with the photoresist to avoid shadow effect from distance or particles. We then shine the UV light at an energy of  $\sim 9.81$  mJ in our case with a 3 rays Hg lamp.

<sup>2</sup>Being atomically precise is not needed because of the IBE is not.

The exposition time has to be chosen carefully according to each recipe to achieve sharp motives. We then put the sample in an adapted developer that will selectively dissolve one of the two areas (exposed or not). We then obtain a resist motif protecting the part of the sample we want to conserve after the ion beam etching (IBE).

### **Ion Beam Etching (IBE)**

We use an ion beam of argon to etch the sample until the desired layer is reached. Because of the thick photoresist the sample is expected to be protected under it. To control the advancement of the etching we follow the composition of the etch surface by using a Secondary Ion Mass Spectrometer (SIMS). This spectrometer is working as a mass spectrometer on the secondary ions created by the ablation of the sample. The beam they formed is curved by an electric field according to the ions mass and then analyzed. This technique allows us to follow almost live the evolution of the etched surface and stop it whenever we want.

The IBE machine basically consists of a plasma chamber where the plasma ignites, grid creates a flux by applying a voltage and finally, the ions arrived on a tilting sample stage; as seen on Fig. 2.13.

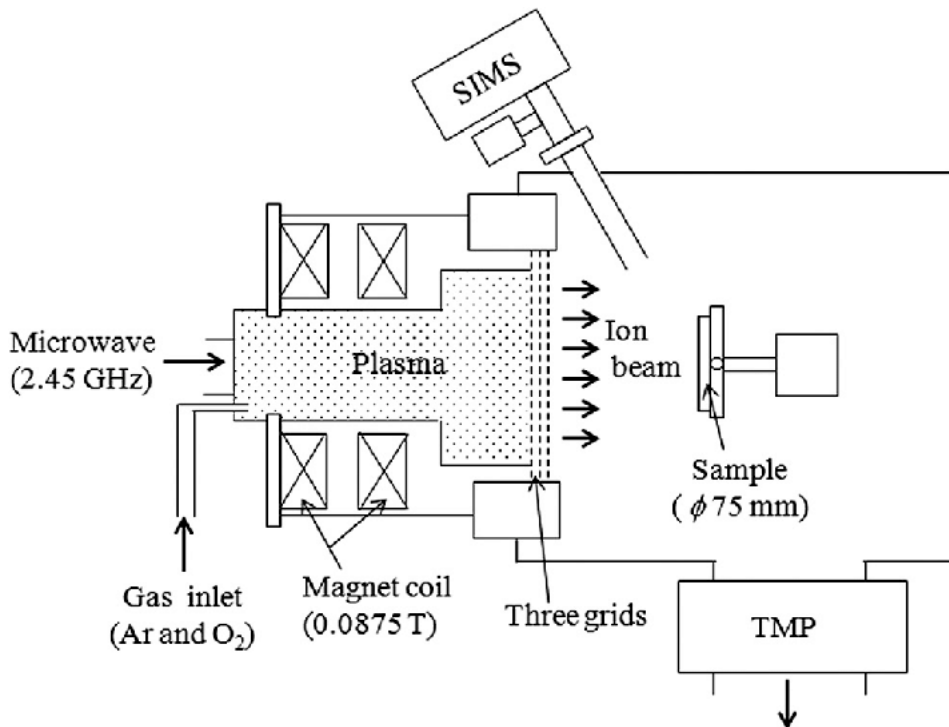


Figure 2.13: Schematic of IBE system equipped with a SIMS

The tilt has to be set to optimize the ablation of the desired material. The sample stage can also rotate in order to suppress eventual anisotropy of the incident beam. Finally, the stage has to be cooled at 5 °C because the heat dissipation caused by the beam can harden the photoresist and make the etching less efficient.

### **Elaboration of electrical contacts**

To design electrical contacts, we follow the same route as described previously. In this case we etch a positive mask of resist and expose a specific part of the sample surface in order to deposit metals

on it by the means of evaporation. Now that the sample is etched as desired, we need to remove the resist that does not serve any purpose anymore. Most of it can be dissolved in acetone and by adding sonication, we ensure that the metal does not redeposit on the sample. This step can be crucial because it can result in full metallic coat of the sample or sample destruction if the sonication is too strong and/or the sample motive are too small (typically below tens of nanometers).

## 2.3 Structure characterization

### 2.3.1 X-Ray diffractometer (XRD)

#### Instrumentation

X-Ray Diffraction (XRD) is used to measure the periodicity of the crystalline lattice by shining X-rays and using their diffraction by the lattice to probe its structure.

In order to analyze the diffraction pattern, we use the well-known Bragg conditions:

$$2dsin(\theta) = n\lambda \quad (2.1)$$

where  $d$  is the distance between the successive crystal planes that we are looking at,  $\theta$  is the incident angle of the beam relative to the plane,  $\lambda$  the wavelength of the X-rays (for us  $1.54056$  , corresponding to the  $K\alpha_1$  of Cu) and  $n$  the order of diffraction.

When this condition is met, the x-rays are diffracted on the selected plane. By scanning the angle space, we can identify the positions corresponding to diffraction condition of the planes. By defining the Ewald sphere as the sphere of  $k = \frac{2\pi}{\lambda}$  radius in the reciprocal space, we understand that the Bragg criteria is met when the sphere intercepts the reciprocal lattice. Thus, by moving detector, source and sample, we can browse the Ewald sphere.

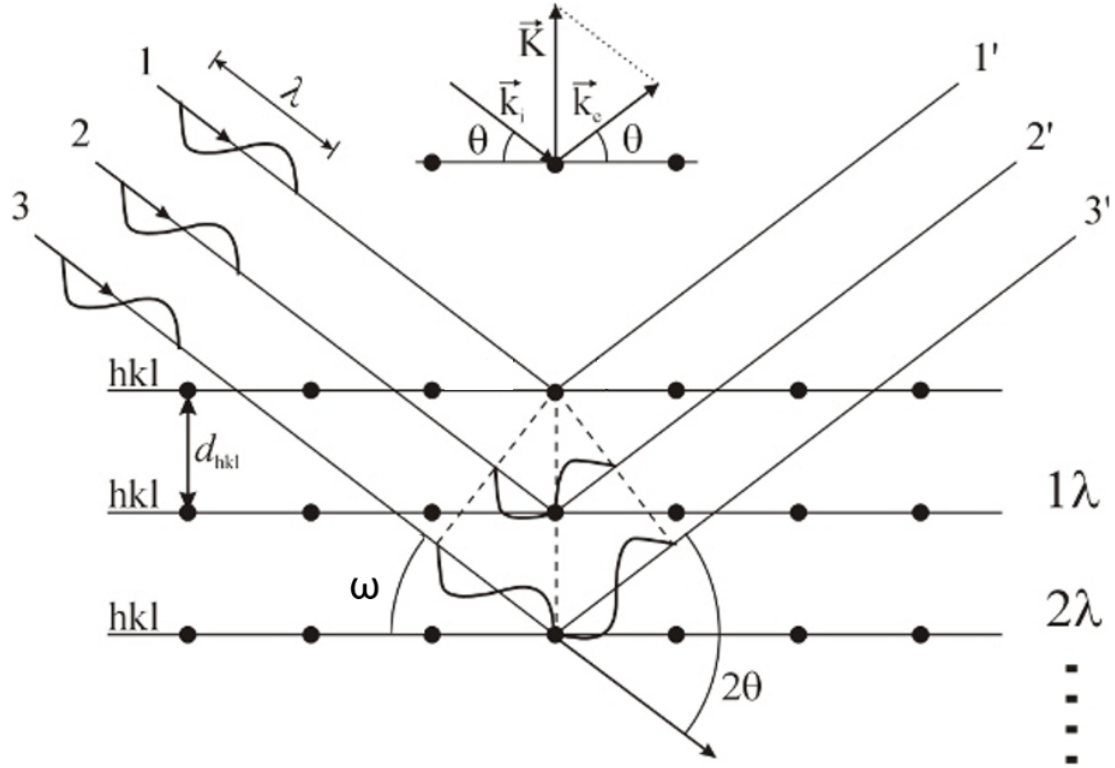


Figure 2.14: Schematic of the diffraction geometry on  $hkl$  planes. The  $n$  indice corresponds to the number of planes crossed by the X-ray beam and result in the corresponding order peak.

For this PhD thesis I mainly used a Panalytical Empyrean X-ray diffractometer here in Fig. 2.14 (a) which presents the following geometry Fig. 2.14 (b) where  $2\theta$  is the angle between the source and the detector,  $\omega$  angle between the sample surface and the incident beam.

The technique allows us to probe the structure along different directions. With this tool we can study the state of the structure, its crystallinity and most importantly identify the phases present in the film.

### **$2\theta - \omega$ scan**

To identify the phases, we usually used a  $2\theta - \omega$  scan. Since the crystalline planes are rarely exactly parallel to the sample surface, there is another angle called  $\delta\omega$  between the sample surface and the crystal plane. A  $2\theta - \omega$  scan is a scan where we vary  $2\theta$  while keeping  $\mathbf{k}_{out} - \mathbf{k}_{in}$  perpendicular to the plane of the sample by keeping  $\omega = \theta + \delta\omega$  constant.

Usually we perform this scan on the plane "parallel" to the surface. This way we measure the out of plane parameter of the substrate and the film at the same time as the two families of planes are expected to be parallel. We typically obtain the following scans:

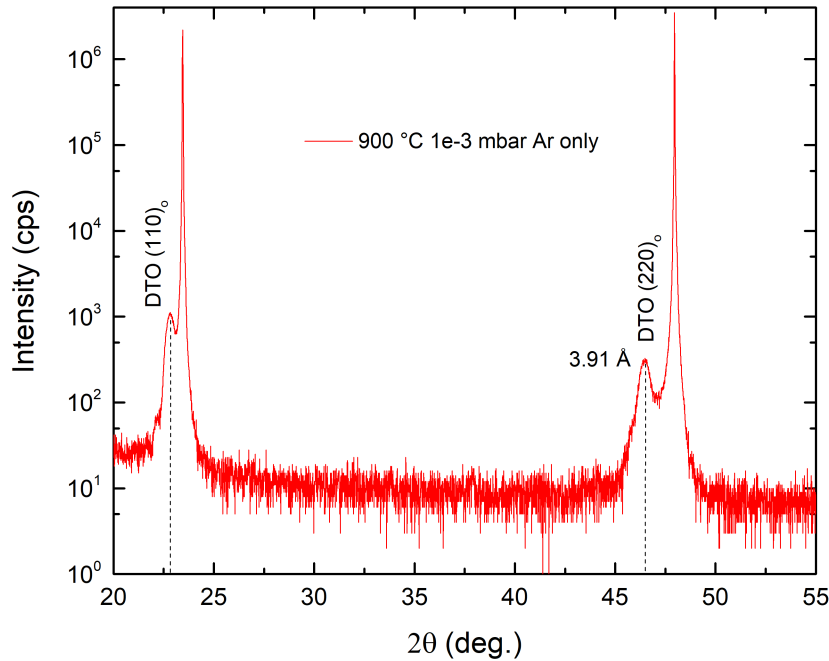


Figure 2.15:  $2\theta-\omega$  scan of 20 nm thick DTO film on LAO(001) substrate

By comparing the obtained peaks and compare their position with the X-rays databases (here we used the ICCD), we can identify the obtain phase.

#### $\omega$ scan or rocking curve

After establishing that we obtained the right phase, we still have to evaluate the crystallinity of the sample. By keeping the angle between source and detector constant and changing  $\omega$  alone around a specific planes, we can visualize the angular dispersion of this family of plane. Thus, the narrower is the resulting peak, the better is the film crystallinity. This is used as a quality test of the grown sample.

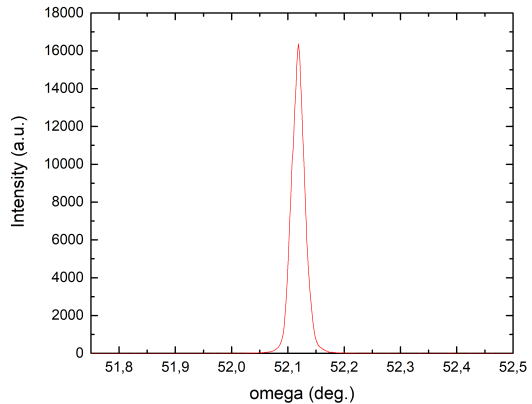


Figure 2.16: Rocking curve on DTO 20 nm thick sample. With a FWHM of  $\Delta\omega = 0.027^\circ$ .

#### Reciprocal Space Map (RSM)

Reciprocal Space Map (RSM) allows us to access several directions in reciprocal space unlike  $2\theta - \omega$  scan. Here we perform a series of 2 theta scans at different omega position. By doing so we can probe two directions of the reciprocal space and obtain information on the different lattice parameters of

our films.

To be didactic we look at the (103) reflection of a cubic lattice. We can justify this choice by the fact that (103) is a widely used diffraction for perovskite because of its relatively high intensity. On the other hand, if the majority of the studied compounds are distorted in some extent (mostly orthorhombic), we can find a set of pseudo cubic parameter for them.

In the Fig. 2.14 we can see that  $\theta_{in} = \pi - \omega$  and  $\theta_{out} = 2\theta - \omega$  Thus the resulting vector  $\mathbf{K}$  is:

$$\mathbf{K} = \begin{pmatrix} k_{out_x} - k_{in_x} \\ k_{out_y} - k_{in_y} \end{pmatrix} = K_0 \begin{pmatrix} \cos(\theta_{out}) - \cos(\theta_{in}) \\ \sin(\theta_{out}) - \sin(\theta_{in}) \end{pmatrix} = K_0 \begin{pmatrix} \cos(2\theta - \omega) - \cos(\omega) \\ \sin(2\theta - \omega) + \sin(\omega) \end{pmatrix} \quad (2.2)$$

With this relationship, we can convert angle into coordinates in the reciprocal space thus we obtain a map of the reciprocal space (RSM).

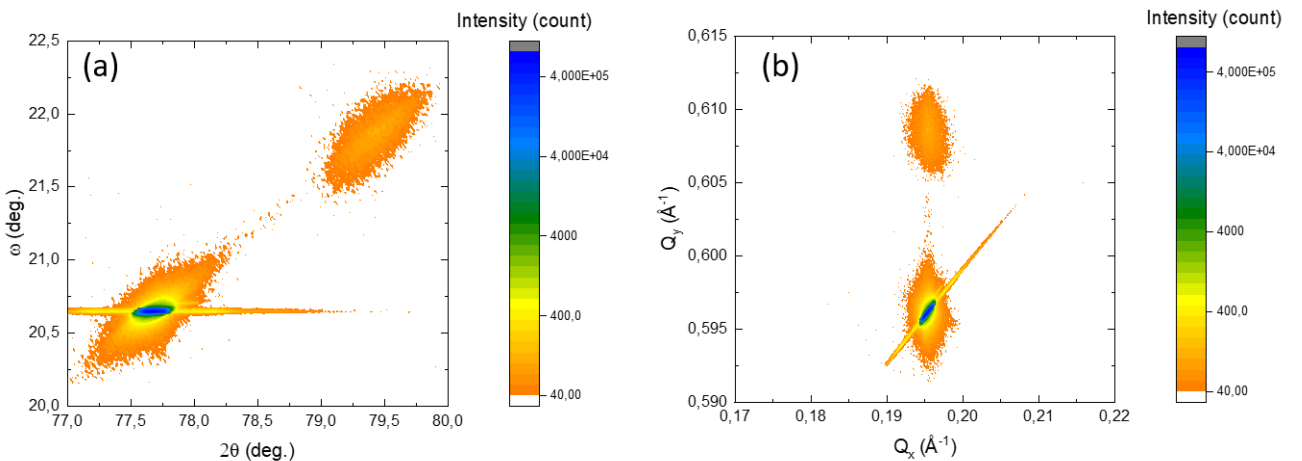


Figure 2.17: DTO sample grown on DSO substrate: a) RSM plotted as a function of  $2\theta$  and  $\omega$  angle b) RSM plotted in k-space (here as a function of  $q_x$  and  $q_y$ )

From this we can extract the lattice parameter along the two directions for our film and substrate by using the fact that  $a_i = \frac{2\pi}{q_i}$ , where  $a_i$  is the lattice parameter along the  $i$  direction and  $q_i$  the corresponding parameter in the reciprocal space.

**Note:** this reasoning is applied to (103) plane and we assumed the lattice to be cubic. However, the method can be generalized to (hkl) plane and not only (h0l) simply by adding a third dimension to the problem.

The advantage of this technique is that it probes two directions of the reciprocal space at the same time and quickly check if our films are strained on the substrate as in Fig. 2.17 (b). It is also noteworthy that RSM can also be used to measure distortion of the structure.

## 2.4 Superconducting Quantum Interference Device (SQUID)

The SQUID is one the most commonly used magnetic characterization tools used in condensed matter laboratories. It allows a relatively simple measurement of the total magnetic moment of a sample at different temperatures and magnetic fields.

### 2.4.1 Principle

As its name suggest the SQUID is a quantum interferometer based on superconductor technology. The actual device consists in a ring of superconductor material, usually pure niobium or a lead alloy with 10% gold or indium, with Josephson junctions in opposite sides through which the current flows, as shown in Fig. 2.18.

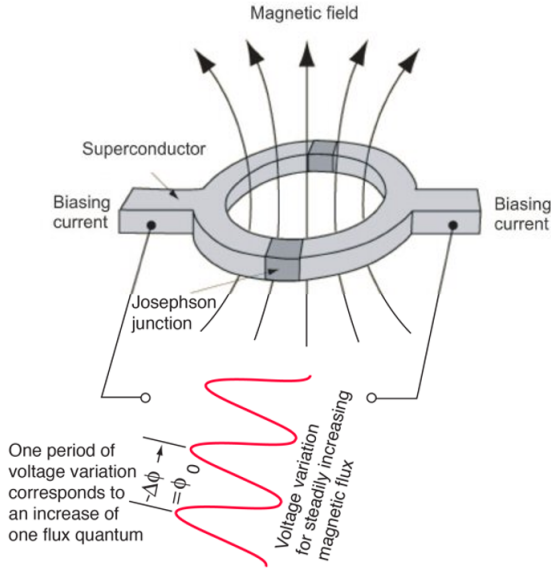


Figure 2.18: Schematic of a simplified SQUID magnetometer.

The current in Josephson junctions is given by  $I(t) = I_c \sin(\Delta\varphi_J(t))$ , with  $\Delta\varphi_J$  the phase difference between the two superconductors forming the junction. Another part of the phase difference is due to magnetic field through the Aharonov-Bohm effect,  $\Delta\varphi_B = \frac{2\pi\Phi}{\Phi_0}$ , where  $\Phi_0 = \frac{\hbar}{2e}$  is the quantum of magnetic flux and  $\Phi$  the actual flux in the SQUID. This flux has to be a multiple of  $\Phi_0$  and the phase has to be continuous inside the loop  $\Delta\varphi_B + 2\Delta\varphi_J = 2\pi n$ , with  $n$  an integer. This results in the response seen in Fig. 2.18  $I(t) = I_c \times (-1)^{n+1} \sin\left(\frac{\pi\Phi}{\Phi_0}\right)$ .

We have thus translated the variations of magnetic flux into an oscillating voltage that can be processed to read flux variation down to one  $\Phi_0$ . In practice the SQUID is not directly exposed to the magnetic field but is instead transported to it via a magnetic transformer.

### 2.4.2 Data analysis

Unlike some more local and element specific techniques that will be discussed later, the SQUID measures the signal from the entire sample (substrate+films), so we must take into account the presence of unwanted signals when processing the data.

A SQUID measures the whole sample, unlike some element specific techniques discussed later, thus we have to take into account the presence of unwanted signals.

Since the substrate is tens of thousand times thicker than the average films, its magnetic properties usually dominates. For example, a ferromagnetic substrate will render any measurement nearly impossible. Even the signal from a paramagnetic one could overshadow the signal of the thin film. This is what prevents us from measuring films on scandate substrates  $R\text{ScO}_3$  ( $R$ : rare earth), which possess free  $R^{3+}$  strong paramagnetic moments. Therefore, most of the substrates used in this Thesis will be diamagnetic (STO, LSAT...).

The magnetic susceptibility  $\chi_M = \frac{\partial M}{\partial H}|_{H=0}$  describes how much the material magnetization reacts to the appearance of a magnetic field. Ferro- or paramagnetic compounds have susceptibilities of  $10 - 100$  and  $10^{-5}$ . Diamagnetism has an opposite sign but is of the same order of magnitude as paramagnetism ( $\chi_M \simeq -10^{-5}$ ). However, diamagnetism does not saturate because it is directly proportional to the applied field, meaning that it may dominate the signal of our film at high field.

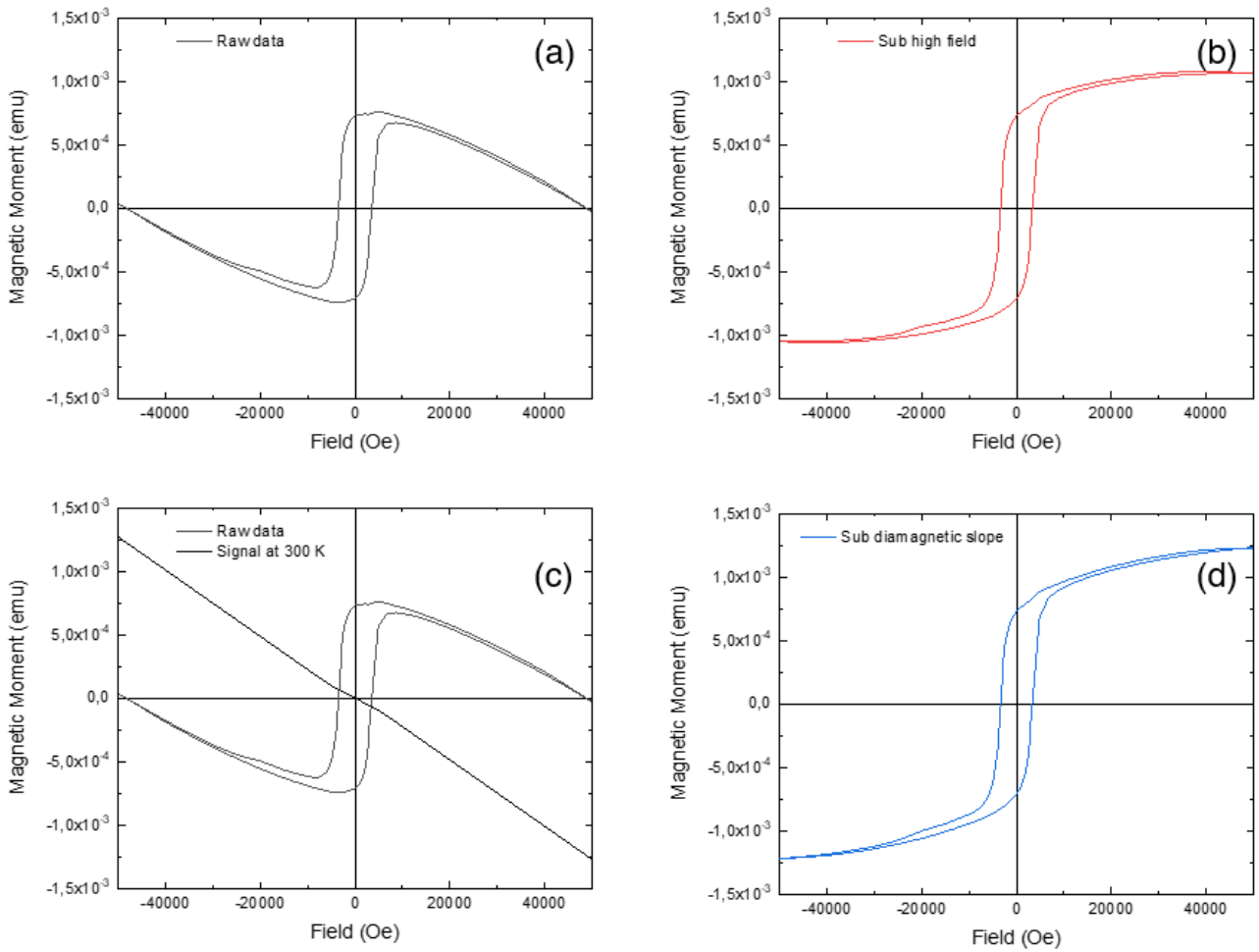


Figure 2.19: SQUID magnetic moment as function of field for a 80 nm DTO thin film on (001) LAO at 10 K (a) Raw data (b) Data after subtraction of the high field slope (extracted from 4 to 5 T) (c) Raw data and diamagnetic signal at 300 K. (d) Data after subtraction of the diamagnetic slope at 300 K.

This is illustrated by the Fig. 2.19 (a), where the "strong" ferrimagnetic signal of 80 nm-DTO thin film is superimposed to the diamagnetic signal from the substrate. In order to correct this effect the classical approach is usually to subtract a slope at high magnetic field. As we can see in Fig. 2.19 (b), the cycle then saturates at high field by construction. However, if this treatment works fine most of the time, it breaks when the sample contains a paramagnetic component. Indeed, since paramagnetic signals only reach saturation at very high fields, using the aforementioned technique will make us lose physical information. To solve this problem, we measure the magnetic signal at 300 K where we expect diamagnetism to dominate because we are well above the Curie temperature (in our case) and that paramagnetic signals are weak. This is illustrated in Fig. 2.19 (c), in which the slope seen in the raw data is mostly explained by the diamagnetic slope (but some of it is not). Thus, by subtracting the diamagnetic slope, we thus obtain the signal shown in Fig. 2.19 (d), in which paramagnetism and ferrimagnetism coexist. Note that we are allowed to do so only because diamagnetism does not depend on the temperature.

## 2.5 X-Rays Photoemission Spectroscopy (XPS)

### 2.5.1 Historic perspective and principle

X-rays Photoemission Spectroscopy (XPS) is a subcategory within the Photoelectron Spectroscopy (PES) technique, which consists of a photon-in (specifically X-Ray photons) and electron-out process with here the photons being specifically X-rays. The photoemission has been first observed by Hertz in 1887 [34] and explained by Einstein in 1905, by introducing the quantized nature of light [35].

### 2.5.2 Theory

The process can be described in three steps [36], first the electron in the initial state (a core level in XPS) is excited to an unoccupied valence state, then the electron travels to the sample surface suffering a series of scattering events; and finally, the electron is emitted from the surface to the vacuum. These steps are useful to decompose the different parts of the process for didactic purposes.

By measuring the kinetic energy of the emitted electrons, we can get the corresponding binding energy of the state we extracted it from.

$$E_{kin} = h\nu - E_{bin} - \Phi$$

where  $E_{kin}$  is the kinetic energy,  $E_{bin}$  is the binding energy,  $\Phi$  is the work function of the instrument and  $h\nu$  is the energy of the X-rays. We can thus access to the density of states of the different core levels of our sample. The resulting lineshape is usually of the Voigt type. The Lorentzian and Gaussian contribution comes from the lifetime of the core level and the Gaussian contribution comes from the instrument. However, some different lineshape might occur in the case of metallic core levels being screened by the valence electrons. This screening result in an asymmetry of the peak described by the Doniach-Šunjić function, giving a typical broadening of the peak at high energies. From the size and shape of the corresponding peaks, one can obtain the chemical composition of a sample as well as the chemical environment of each element.

### 2.5.3 Instrumentation

The measurement system is composed of an X-rays gun (with a Mg and Al sources) that shines on a sample inside an ultra-high vacuum chamber (going to low  $10^{-10}$  mbar). The excited electrons are emitted to the vacuum and collected by a channeltron detector.

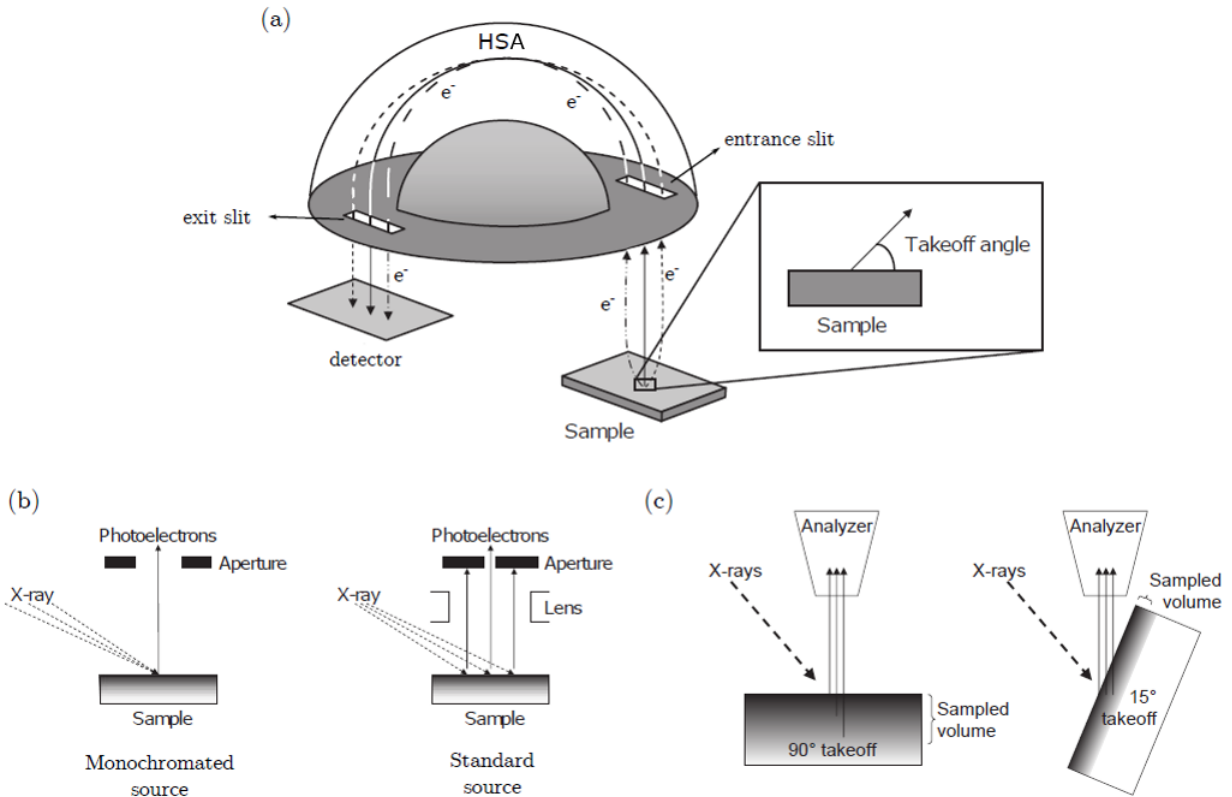


Figure 2.20: X-ray Photoelectron Spectroscopy setup : (a) simplified schematic of the detection process by a HSA (hemispherical sector analyzer).(b) Schematic of the photoemission induced by a monochromated source on the left and non monochromated one on the right. (c) Schematic of the angle dependence of the probing depth. Adapted from [37].

When the X-rays hit the surface, they excite a certain volume of the sample that can be controlled by changing the sample angle, as shown in Fig. 2.20 (c). When the X-rays shine on the sample, we can use a neutralizer (an electron gun) whose will compensate the charge accumulation at the surface of the sample. It mainly occurs in insulating samples, in which the charge compensation through the sample holder is not efficient. The emitted electrons are then selected by an adjustable aperture allowing one to select a certain area of the sample. Because we use a non monochromated source, we have to tune that aperture, Fig. 2.20 (b). The channeltron detector curves the electrons trajectories depending on their energy by applying a voltage between the hemispheres (Fig. 2.20 (a)).

## 2.5.4 Peak analysis

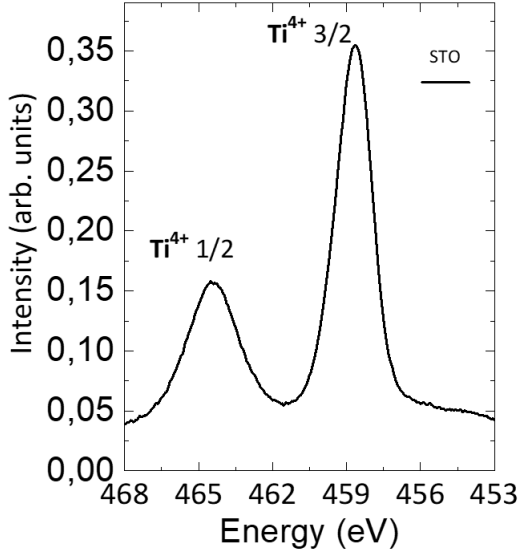


Figure 2.21: XPS spectra of  $\text{Ti}^{4+}$  peaks obtained on STO substrate  $\text{TiO}_2$  terminated by the method described in [19].

In the following analysis, we used the following table Tab. 2.22 for titanium, which was obtained by Mark Biesinger based on different results from the literature [38, 39, 40].

### Peak components

Sometimes an element is present in different environments (oxidation state, chemical environment etc.), which results in a shift in energy and a change of lineshapes (in the case of metals). By fitting the different components of the peak, we can evaluate the proportion of each oxidation states for a given element.

Compound	Ti 2p3/2 (eV)	Std. Dev. (eV)	# of citations	Ti 2p1/2 (eV)	Std. Dev. (eV)	# of citations
Ti(0)	453.86	0.32	8	6.13	0.06	2
Ti(II) Oxide	455.34	0.39	8	5.73	0.15	3
Ti(III) Oxide	457.13	0.35	8	5.60	0.36	3
Ti(IV) Oxide	458.66	0.22	13	5.66	0.08	4

Figure 2.22: XPS titanium peak position, standard deviation and number of article used to obtain the average values present here. Adapted from [38, 39, 40]

By adding those constraints and the one regarding the ratio between 2p 3/2 and 1/2 peaks, we can obtain meaningful fitting of our data, as shown in Fig. 4.16.

## Background subtraction

In order to obtain quantitative data, we need to measure the exact peak area corresponding to each state, so we must subtract the background from the signal. This background comes from excitation of other levels at lower energy.

The question of background subtraction is subject to caution in the scientific community.

Indeed, if it is usually accepted that large band gap materials are better fitted by linear background, in other cases the question is more complicated. We can use a Shirley background, which has the advantage of being an iterative process, therefore, takes into account the peculiar shape of peaks. However, if we try to fit nearby peaks by a single background, we may not take into account the separation of those peaks. In order to fix that we can try to fit each peak with its own background.

Another approach could be to use an universal cross section model, such as the three parameters Toougaard background [41], which aims to represent the average shape of the loss function of the fitted material.

**Note:** The XPS data presented in this thesis will be fitted using CasaXPS software and especially peak specific Shirley background, since we will be measuring a Mott insulator and not a large band insulator.

## 2.6 X-ray Absorption Spectroscopy (XAS)

### 2.6.1 Principle

The X-ray Absorption Spectrometry (XAS) is a spectroscopy technique in which a high density X-rays beam hits on the samples and the signals resulting from its absorption is collected as a function of the energy through various detection modes. Since continuously adjustable and high intensity energy is required, these experiments must be performed in a synchrotron accelerator. Inside electron packs (bunch) are injected and accelerated by electro-magnets. As their trajectory is curved, they emit synchrotron radiation, through the magnetic Bremsstrahlung process to conserve the energy balance. Electrons are used because their relative small mass compared to other particles (like protons), making the process more efficient because the radiation depends in the inverse of the mass of the particle squared.

When absorbed by the sample, these X-rays induce electronic transitions in our material and as the electrons return to their ground state, we can either measure the non absorbed light or the one emitted during the deexcitation process by different detection modes that are detailed in the following sections.

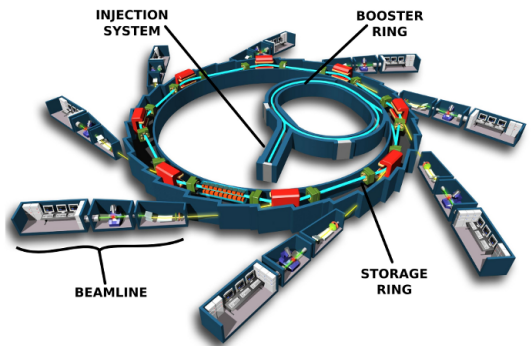


Figure 2.23: Schematic of a synchrotron facility. The electrons are injected through a linear accelerator into a booster ring before the injection into the storage ring. The beamline collects the light radiated by the electrons and polarizes it to the end-station where the experiment is done.

## 2.6.2 Detection modes

### Total Electron Yield (TEY)

In this mode, we do not detect photons but electrons created through the Auger process. Similarly to what happens in XPS, the Auger electrons are created in the sample bulk and are scattered while traveling to the surface, creating secondary electrons on the way through a cascade process. These electrons dominate the TEY signal and are collected through metallic contacts at the sample surface. The probing depth is limited by the scattering process, indeed after a certain number of scattering events the electrons have not enough energy left to overcome the work function of the sample. As a result the probing depth is limited to a few nanometers, 1 to 3 according to [42] and 3 nm in perovskite [43] (here LCMO).

Note that the **Total** in Total electron Yield (TEY) means that we do not select the electrons energy, so this gives us a good measurement of the absorption as a function of the energy.

### Total Fluorescence Yield (TFY)

In this case, we measure photons emitted via a radiative deexcitation process of the electron get back to its ground state. The produced photons leave the sample and are collected by a photodiode. However, precautions have to be taken, since some of the previously mention photoelectrons can escape the sample and reach the diode. To avoid obtaining the TEY signal on the TFY we can place a grid that traps the electrons or simply apply a small magnetic field. Some visible light can also be detected and to avoid that we can either use an X specific diode or a filter such as aluminum foil. Note that this emission is isotropic but the incident angle can still affect the measurement due to the resulting change of probing depth and interaction cross-section. The probing depth of TFY (typically between 10 and 50 nm) is limited by the efficacy of reabsorption in the material.

### X-ray Excited Optical Luminescence (XEOL)

Some of the X-rays are not absorbed and end up being converted into visible light in the substrate. This mechanism is specific to each substrate. The first of these mechanism has been explained for CaF<sub>2</sub> by self-trapped excitons that recombine and produce visible light [44, 45]. However, in our case, we mainly used LaAlO<sub>3</sub> for which the conversion mechanism is still uncertain. According to ref. [46] the visible spectra of LAO is comprised of two broad peaks sitting at 595 and 686 nm. Despite the claim that the crystals are stoichiometric, the peaks are most likely due to defects or phonon relaxation. Consequently, the more efficient the absorption (or thicker the sample), the weaker the XEOL signal is. The intensity of the visible light coming out of the substrate is complementary to the part absorbed by the sample. Obviously, the selected substrate has to be transparent, double side polished and should not contain elements present in the film that we want to measure. By its nature this technique probes the entire sample, but if the film is too thick the transmitted intensity could be too weak and could result in different kind of signal distortion that. We will cover in section 5.1 as we are confronted to it.

We can notice that in XAS we measure the intensity resulting from X-ray absorption but we are not interested in the electron or photon energy. Therefore, this method is the complementary of the XPS (seen in section 2.5), in which a beam of fixed energy is focused on the sample and a spectral

analysis is performed. Here we sweep the energy of the incident beam but measure the resulting intensity indiscriminately, so XAS is measures empty states whereas XPS measures occupied ones.

### 2.6.3 XAS spectra

From these different detection modes, we can obtain element specific spectra at different probing depths. We can thus identify the peaks corresponding to specific transitions and gain information on the element oxidation state and its environment. The simulation of those spectra by multiplet calculation allows us to obtain the underlying electronic structure.

In the rest of this thesis, we will study the  $L_{2,3}$  and  $M_{4,5}$  edges, which correspond to respectively  $2p \rightarrow 3d$  and  $3d \rightarrow 4f$  transitions. They , respectively of particular interest for us because in our perovskites the transition metals and rare earth valence state are respectively  $3d$  and the  $4f$ .

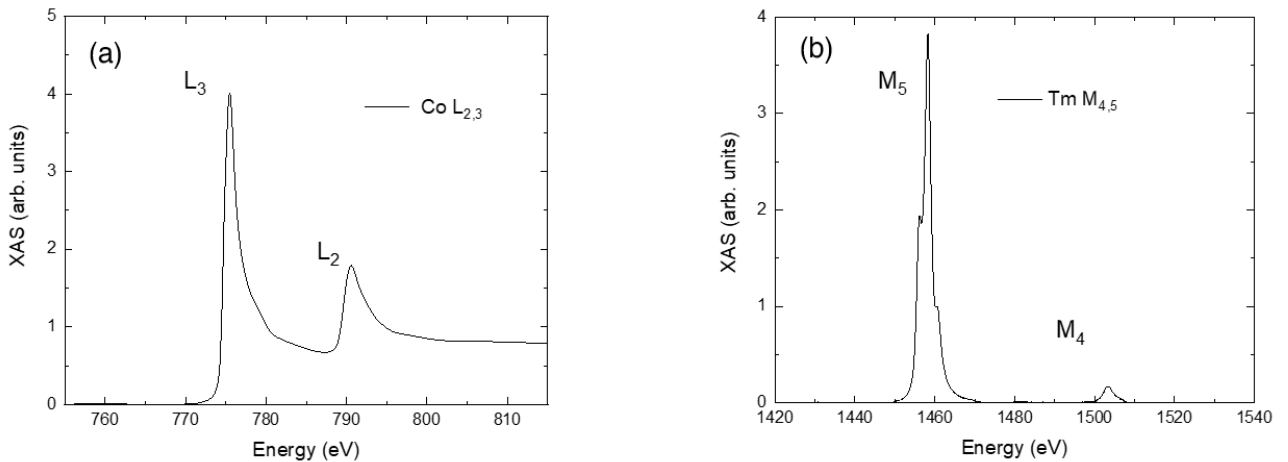


Figure 2.24: Isotropic XAS of the (a)  $L_{3,2}$  edges of Co <sup>3</sup>(b)  $M_{5,4}$  edges of Tm, taken in TFY mode.

In the Fig. 2.24 (a), the  $L_{3,2}$  edge present two peaks corresponding to the transition between  $2p_{\frac{3}{2}} \rightarrow 3d$  ( $L_3$ ) and  $2p_{\frac{1}{2}} \rightarrow 3d$  ( $L_2$ ). Indeed, when a  $p$  electron is promoted it creates a hole that lifts the degeneracy of the  $2p$  state creating  $2p_{\frac{3}{2}}$  and  $2p_{\frac{1}{2}}$  levels, which results in two effective transition energies. This fact stems from the consideration of both possibilities for the hole to be in the final state.

### 2.6.4 XMCD (X-ray Magnetic Circular Dichroism)

The dichroism is a part of a broader class of phenomena where light interacts differently with matter according to polarization or wavelength. Among these, we find birefringence, the Kerr effect, the color dichroism and the polarization dichroism. If these phenomena have various physical explanations, some are set under the same name of dichroism. Coming from the Greek di (two) and khros (color), it has been first used to describe a material which splits a polychromatic beam in two beams of different wavelengths.

Although it does not separate colors, the circular dichroism has taken the same name. It happens when the absorption of a material differs according to the polarization of the light. It has been first described by Aimé Cotton in 1895 [47] (in French). However, the polarization of X-rays remained a challenge for another decade until Charles Glover Barkla *et al.* in 1906 [48]. The first theoretical

<sup>3</sup>Courtesy of Richard Mattana (CNRS Thales)

investigation of the magnetic circular dichroism at the  $M_{2,3}$  edge has been carried out by E. A. Stern *et al.* [49, 50] resp. in 1965 and 1975, respectively. It took another decade for those papers to be noticed and the first try to observe the effect of polarization on absorption started in the early 80's leading to the first observation of the proper X-ray Magnetic Circular Dichroism (XMCD) at the K edge of Co by G. Schütz *et al.* in 1987 [51].

The XMCD is the signal obtained by the subtraction of XAS spectra acquired with opposite circular polarization (left and right). Since the polarized light promotes only certain states more than others, we can use the knowledge of the selection rules [52] to gain information on the final state. As its name suggests, XMCD gives us information on the magnetism of the selected element. Most of the XMCD measurements are performed at the  $L_{3,2}$  (a) and  $M_{4,5}$  edges because their in-depth analysis is allowed by the sum rules (developed in the next section).

We already saw that the XAS spectrum was depending on the "initial state" but it also depends on the final state. As we know the valence band of a magnetic material (here our final state) is divided in two subbands shifted relatively to one another resulting in the predominance of one variety of spins.

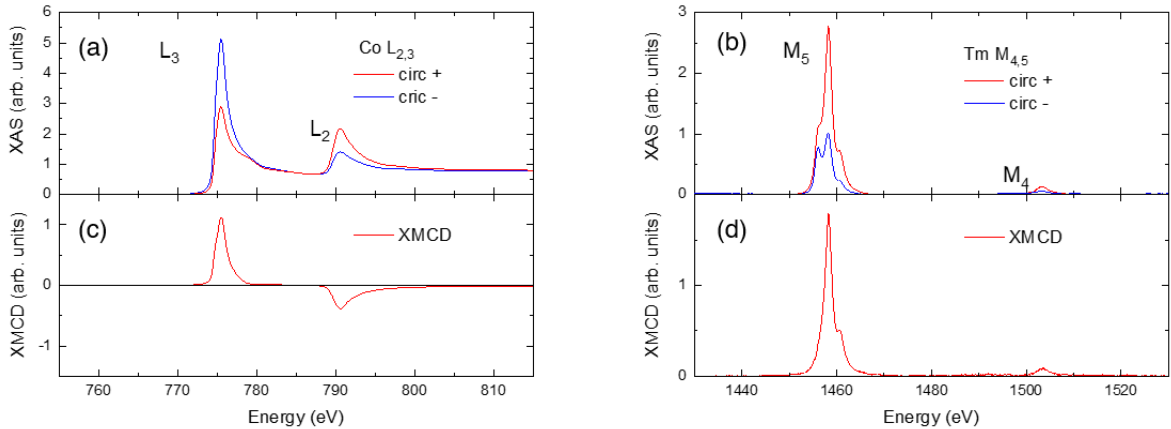


Figure 2.25: XAS and XMCD of the (a) and (c)  $L_{3,2}$  edges of Co. (b) and (d)  $M_{4,5}$  edges of Tm (in  $\text{TmTiO}_3$ ) in TFY at 10 K.

In Fig. 2.25 (a) and (b), we can see respectively the prototypical  $L_{2,3}$  and  $M_{4,5}$  edges at two different polarizations. We obtain the XMCD by subtracting these two signals, Fig. 2.25 (c) and (d).

The non-compensation of the spectra taken with opposite polarization is a consequence of the spin polarization of the valence band due to the ferromagnetic (or ferri-) order being probed by electrons polarized by the light itself polarized. In the following section we will get into more detail about this mechanism.

## XMCD mechanism

Due to the proportionality relationship between the intensity of the different edges and the population of the involved bands, we can use it to access the quantum numbers of the final state.

The physics of XMCD has been explained by the so-called *two-step* model proposed by G. Schültz *et al* also in [51]. In the first step, the electrons are excited by circularly polarized X-ray photon. By conservation of the angular momentum, it is transferred from the incident light to the electrons. At the end of the first step, the electrons are excited but not yet promoted.

During the second step, the electrons get promoted with different probabilities depending on its orbital moment  $l$ . These probabilities are established by the use of the Clebsh-Gordon coefficients. The electrons are now orbitally polarized and the spin-orbit coupling induces a spin polarization as well. As an example, we will take the case of  $2p$  levels split into  $2p_{1/2}$  and  $2p_{3/2}$  excited by a photon with helicity +1. When summing all the possible excitations the spin polarization appears as follow: From  $2p_{1/2}$ , 75 % of electrons have  $m_S = -1/2$  and 25 % of electrons have  $m_S = +1/2$ . From  $2p_{3/2}$  32.5 %, of electrons have  $m_S = -1/2$  and 62.5 % of electrons have  $m_S = +1/2$ .

Note that the overall spin polarization is opposite for the different  $2p$  states, which explains the opposite sign of the two edges in the XMCD. Note that the result is simply opposite if the helicity is instead -1.

With the now excited electrons being spin polarized, they can probe the final states and if they are spin polarized as well, it will finally give rise to a dichroic signal. Of which the exploitation has been described by Stöhr *et al* in [53].

# Chapter 3

## Rare-earth titanates: a brief introduction

### 3.1 Presentation

Among transition-metal perovskites, rare-earth orthorhombic titanates  $\text{RTiO}_3$  ( $\text{R}=\text{La...Lu}$  or  $\text{Y}$ ) emerge as a particularly interesting family of Mott insulators [4, 3, 54, 55]. The most stable valence state of rare-earths (except for Eu and Ce) is  $3+$ , which imposes a  $3+$  valence state to the Ti, that is thus  $3\text{d}^1$  with a spin  $1/2$ . Salient features of  $\text{RTiO}_3$  compounds are the concurrency of ferrimagnetism with an insulating character and the phase transition from ferrimagnetic to antiferromagnetic (G-type) order when going from small ( $\text{La...Sm}$ ) to large rare-earths ( $\text{Gd...Yb}$ ) [4, 54]. This insulating-ferrimagnetic behavior is exceptional among simple perovskites and offers perspectives for engineering novel magnetic states at oxide interfaces [55, 56].

### 3.2 Properties

#### 3.2.1 Structural data

As we discussed in section 1.2, the Goldschmidt tolerance factor  $t$  is crucial in understanding the properties of perovskite oxides and the rare-earth titanates make no exception. As  $t$  decreases, the structure moves away from the cubic structure to an orthorhombic one as the distortions become more important. These distortions are often called of  $\text{GdFeO}_3$  type.

$\text{RTiO}_3$	$a()$	$b()$	$c()$	$V(^3)$	$t$
La	5.633(1)	5.613(2)	7.942(2)	251.1	0.831
Pr	5.555(2)	5.615(1)	7.821(2)	244.0	0.816
Nd	5.524(1)	5.657(1)	7.795(1)	243.6	0.814
Sm	5.467(1)	5.669(1)	7.742(1)	240.0	0.805
Gd	5.402(2)	5.697(2)	7.680(2)	236.4	0.799
Tb	5.384(1)	5.678(1)	7.660(1)	234.2	0.794
Dy	5.363(3)	5.689(2)	7.647(1)	233.3	0.790
Y	5.341(1)	5.686(2)	7.621(1)	231.4	0.786
Ho	5.340(2)	5.689(2)	7.622(1)	231.5	0.786
Er	5.320(3)	5.674(3)	7.609(2)	229.7	0.782
Tm	5.303(1)	5.658(1)	7.597(3)	228.0	0.779
Yb	5.291(1)	5.629(1)	7.595(1)	226.0	0.775
Lu	5.275(1)	5.644(1)	7.581(2)	225.7	0.772

Table 3.1: Structural data of the Rare-Earth titanate family with respectively lattice parameters, unit cell volume and tolerance factor

One can also notice the distortion makes the structure more compact. This fact will prove itself be most relevant in the following section.

### 3.2.2 Magnetic data

Here we present the magnetic properties of the family. As discussed in the introduction of this chapter, it undergoes a magnetic phase transition as the ionic radius decreases.

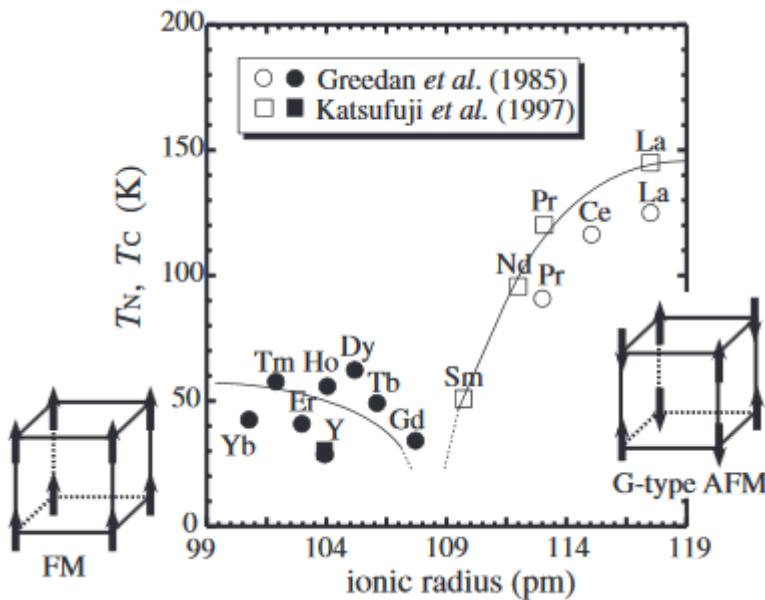


Figure 3.1: Magnetic phase diagram of the rare earth titanates (temperature extracted from bulk samples). Adapted from [3].

$\text{RTiO}_3$	$T_N(\text{K})$	$T_C(\text{K})$
La	140	
Ce	116	
Pr	120	
Nd	110	
Sm	70	
Gd		32
Tb		49
Dy		60
Y		30
Ho		56
Er		42
Tm		68
Yb		36
Lu		40

Table 3.2:  $T_N$  and  $T_C$  of the rare-earth titanates family in Kelvin (K) [4] (dating from 2005).

From the data presented in Tab. 3.2 and Fig. 3.1 and more recent data from [4], we can see that in the AFM region the  $T_N$  is monotonously decreasing. From this we can suppose that the strength of the AFM order is driven by either the compactness of the unit cell and/or the Ti-O-Ti angle. We will see in section 3.3 that the answer is both.

On the ferromagnetic side, the  $T_C$  does not follow a monotonic behavior most likely due to the fact that the filling of the 4f shell of the rare earth has a greater effect on the stability of the magnetic order.

### 3.3 Spin and orbital order

#### 3.3.1 Explanation of the rare-earth titanates phase diagram

Since perovskites are well known for accommodating structural changes, we investigate their effect on the spin and orbital order in order to explain the phase transition from antiferromagnetism to ferromagnetism. To do so, we will be focused on the  $3d^1$  electrons of Ti because they drive the transport and magnetic properties of titanates.

Since the titanium ions are inside oxygen octahedrons, in perovskites, the  $3d$  levels are split into  $t_{2g}$  and  $e_g$  levels by the resulting crystal field. With one electron in the  $t_{2g}$ , we expect titanates to be a textbook example of Jahn-Teller (JT) active systems. However, as shown in [3, 55] JT effect is actually negligible in the explanation of the orbital order. In [55], Varignon *et al* studied via DFT and symmetry-mode analysis the stability of the different distortion modes. All titanates develop antiferrodistortive motions antiphase  $\Phi_{xy}^-$  ( $R_5^-$ ), in-phase  $\Phi_z^+$  ( $M_2^+$ ) corresponding to  $a^-a^-c^0$  and  $a^0a^0c^+$  (in the Glazer notation) rotations respectively. They also exhibit strong antipolar motions of the rare earth through  $A_X$  ( $X_5^-$ ) and  $A_R$  ( $R_4^-$ ) modes. Finally, JT effect is also present through the  $Q_2^+$  ( $M_3^+$ ) mode but it is one to two orders of magnitude lower than the other modes. In order to visualize those different modes, we adapted the figure of [55] where only the mode in question is applied to a cubic structure, in Fig. 3.2 (a-e).

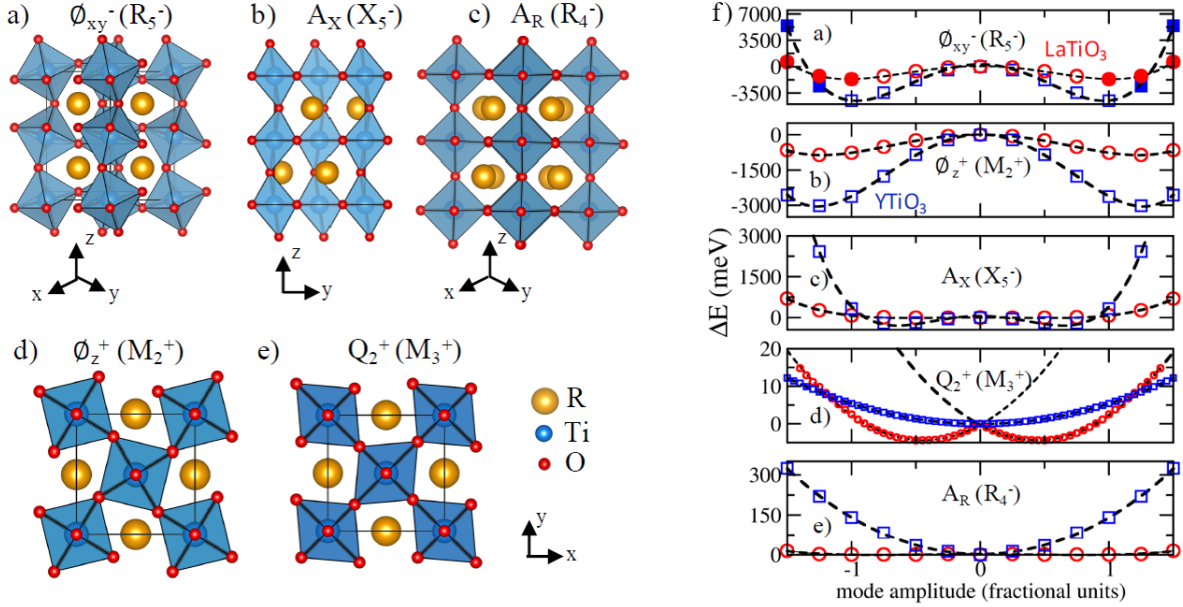


Figure 3.2: Schematic of the cubic perovskite structure distorted by: (a)  $\Phi_{xy}^-$  ( $R_5^-$ ), (b)  $A_X$  ( $X_5^-$ ), (c)  $A_R$  ( $R_4^-$ ), (d)  $\Phi_z^+$  ( $M_2^+$ ) or  $Q_2^+$  ( $M_3^+$ ) modes. In (f): Energy potentials obtain by DFT calculation with respect to the amplitude of distortion (in fractional units) of the different modes appearing in the ground state of  $\text{YTiO}_3$  (blue squares) and  $\text{LaTiO}_3$  (red circles). Filled (unfilled) symbols represent insulating (metallic) solutions. Adapted from [55].

In [55], Varignon *et al* the DFT calculations focused on  $\text{LaTiO}_3$  and  $\text{YTiO}_3$  because they are representative of the two ends of the AFM to FM spectrum. In Fig. 3.2 (f), the potential energies of the five modes are plotted as a function of their amplitude<sup>1</sup>. If the  $\Phi_{xy}^-$ ,  $\Phi_z^+$  and  $A_X$  modes present minima, it is not that clear for  $A_R$  and  $Q_2^+$ . However, as we develop the free energy of the system, we obtain the following, symmetry allowed, trilinear terms:

$$\mathcal{F} \propto a \Phi_{xy}^- \Phi_z^+ A_X + b \Phi_{xy}^- A_X Q_2^+ + c \Phi_z^+ A_X A_R + d A_X A_R Q_2^+. \quad (3.1)$$

According to the first term of Eq. 3.1, the stability of  $\Phi_{xy}^-$  and  $\Phi_z^+$  automatically brings the antipolar motion  $A_X$  irrespectively of its stability. In the same way it follows that the JT distortion  $Q_2^+$  is also stabilized, giving it an improper origin as described in other systems [57, 58, 59, 60] (often multiferroic). In the same way, the third term gives rise to the  $A_R$  antipolar motion. In the fourth and final term, if the  $A_X$  and  $A_R$  antipolar motions do not share the same symmetry, their product  $X_5^- R_4^- = M_3^+$  has the same symmetry as the JT effect. It follows that in the absence of an efficient  $Q_2^+$  distortion, we still have a sizable effective JT motion which control the spin and orbital order.

The change of environment induces a lift of the  $t_{2g}$  degeneracy into three states of mixed  $|d_{xy}\rangle$ ,  $|d_{yz}\rangle$  and  $|d_{xz}\rangle$  nature resulting in a trigonal like splitting as shown in Fig. 3.3 (a).

<sup>1</sup>Note that in [55] the modes are said to be unstable but one should keep in mind that in the DFT theory, one should think relatively to an unperturbed state (aka the cubic structure here). In consequence an unstable solution is a minimum of potential energy for the system where the said solution exists.

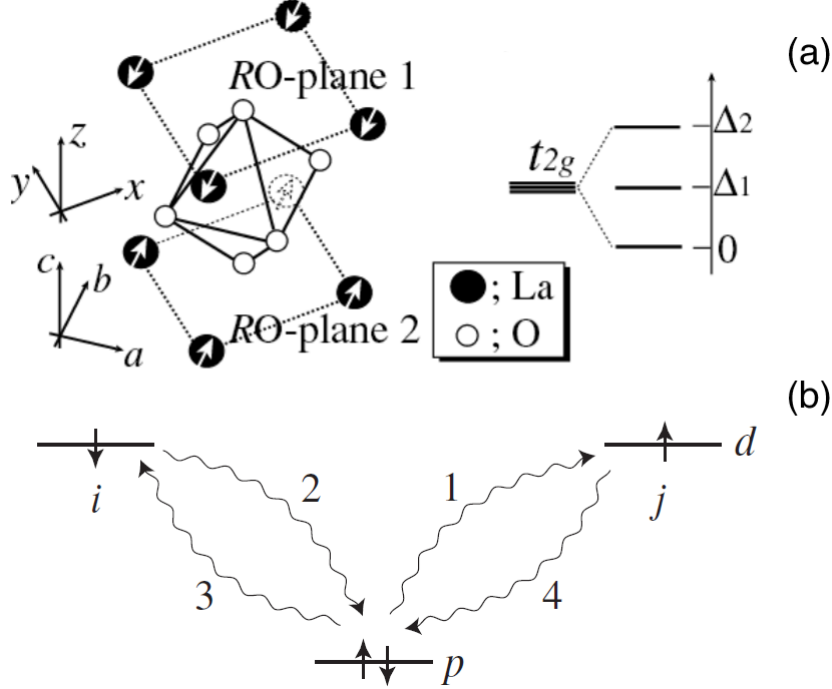


Figure 3.3: (a) Schematic of the  $\text{GdFeO}_3$  distortion and consequent lift of the  $t_{2g}$  degeneracy. Adapted from [3]. (b) Schematic of the superexchange mechanism. Adapted from [8].

In this situation, we obtain a mono occupied state with spin degeneracy. These conditions look like a textbook example of superexchange mechanism. Where  $d$  electrons are interacting with each other through virtual hops via the  $p$  state of the oxygens. The schematic of Fig. 3.3 (b) describes the interaction process between the electrons on the  $i$  and  $j$  sites. Following the Goodenough-Kanamori rules, it appears that the resulting spin orientation is AFM. However, it also appears clear that this mechanism strongly depends on the overlap of the orbitals involved, ie their symmetry.

On the other hand, Varignon *et al* showed that the ground state of the  $d$  electron of YTO and LTO is:

$$|\Psi_{\text{YTiO}_3}\rangle \propto 0.686|d_{xy}\rangle + 0.728(\alpha|d_{xz}\rangle + \beta|d_{yz}\rangle), \quad (3.2)$$

$$|\Psi_{\text{LaTiO}_3}\rangle \propto 0.565|d_{xy}\rangle + 0.825(\alpha|d_{xz}\rangle + \beta|d_{yz}\rangle), \quad (3.3)$$

Where  $\alpha$  and  $\beta$  coefficients as  $\alpha + \beta = 1$ .

Since the  $|d_{xz}\rangle$  and  $|d_{yz}\rangle$  states are facing the  $p$  orbitals, one can easily understand why a strong  $(\alpha|d_{xz}\rangle + \beta|d_{yz}\rangle)$  character is necessary to achieve superexchange and thus to AFM order. According to the calculation of [57], all titanates should be antiferromagnetic if the  $A_R$  were frozen. Indeed, without it the resulting states would always be of  $(\alpha|d_{xz}\rangle + \beta|d_{yz}\rangle)$  character as in Eq. 3.3. Only the inclusion of the  $A_R$  mode can lead to a balanced mix of  $(\alpha|d_{xz}\rangle + \beta|d_{yz}\rangle)$  and  $|d_{xy}\rangle$ , as in Eq. 3.2.

As we have established, the stability of the antipolar modes is a consequence of the intensity of the  $\Phi_{xy}^-$  and  $\Phi_z^+$  rotation motions. Thus, we expect the antipolar modes to scale with the intensity of the rotational mode.

Then, we can understand the transition by the development of the rotation motions as the unit cell compactness increase destroying the AFM order and favoring the direct exchange by closing the distance between the titanium ions, thus creating the FM order.

### 3.3.2 Magnetic orders

Now that we have explained the magnetic transition in the rare-earth titanate family, we will explore in more details the ferrimagnetic part of the phase diagram.

It presents a variety of behaviors as we can see in the Fig. 3.4. It manifests itself by a variation of magnetization at saturation, a remanence and coercive field. Thus, we obtain a good range of softness for insulating magnets.

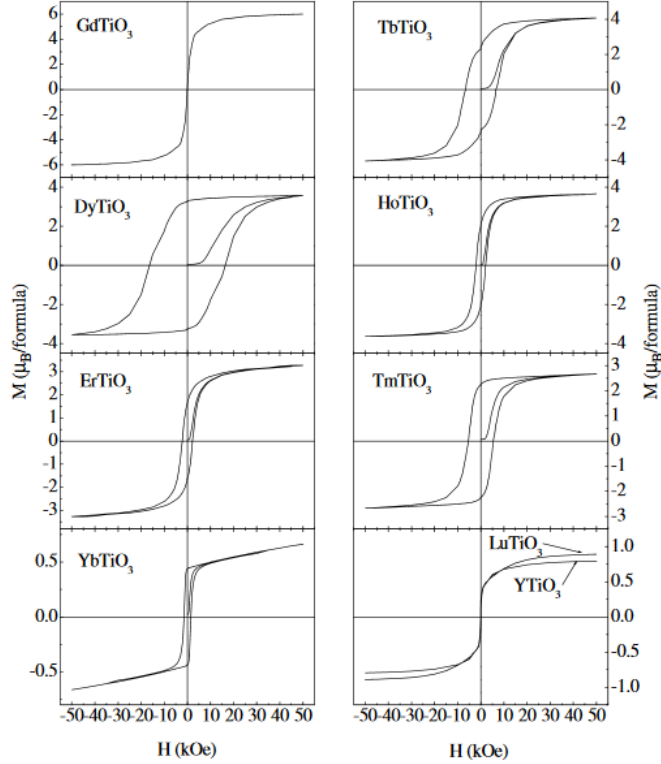


Figure 3.4: Magnetic hysteresis cycle (Magnetization vs Magnetic Field) obtained from SQUID measurements performed on bulk samples of the ferrimagnetic rare-earth titanates at 5 K. Adapted from [4].

Neutron diffraction experiments have investigated the fine magnetic structure of these compounds [61] in the bulk phase. If all of the compounds above have antiferromagnetically arranged sublattices (except LuTiO<sub>3</sub> and YTiO<sub>3</sub>), they present different spin configurations.

In the case of GdTiO<sub>3</sub>, we are in presence of a collinear spin only magnetism. Indeed, the titanium moment is of 1.73  $\mu_B$  and the gadolinium one is 7.94  $\mu_B$  and simply result in a net magnetization of 6  $\mu_B$ . If the configuration of gadolinium is Gd:  $6s^24f^75d^1$  we expect the one of Gd<sup>3+</sup> to be  $6s^04f^7$ . With a half-filled 4f band, we can safely assume the magnetism to be spin only without any orbital moment contribution.

Ion	Electron configuration	LS term of the ground state	calculated $\mu_{eff}$ ( $\mu_B$ )	experimental $\mu_{eff}$ ( $\mu_B$ )
La <sup>3+</sup>	4f <sup>0</sup>	<sup>1</sup> S <sub>0</sub>	0.00	0.00
Ce <sup>3+</sup>	4f <sup>1</sup>	<sup>2</sup> F <sub>5/2</sub>	2.54	2.4
Pr <sup>3+</sup>	4f <sup>2</sup>	<sup>3</sup> H <sub>4</sub>	3.58	3.5
Nd <sup>3+</sup>	4f <sup>3</sup>	<sup>4</sup> I <sub>9/2</sub>	3.62	3.5
Pm <sup>3+</sup>	4f <sup>4</sup>	<sup>5</sup> I <sub>4</sub>	2.68	-
Sm <sup>3+</sup>	4f <sup>5</sup>	<sup>6</sup> H <sub>5/2</sub>	0.84	1.5*
Eu <sup>3+</sup>	4f <sup>6</sup>	<sup>7</sup> F <sub>0</sub>	0.00	3.4*
Gd <sup>3+</sup>	4f <sup>7</sup>	<sup>8</sup> S <sub>7/2</sub>	7.94	8.0
Tb <sup>3+</sup>	4f <sup>8</sup>	<sup>7</sup> F <sub>6</sub>	9.72	9.5
Dy <sup>3+</sup>	4f <sup>9</sup>	<sup>6</sup> H <sub>15/2</sub>	10.63	10.6
Ho <sup>3+</sup>	4f <sup>10</sup>	<sup>5</sup> I <sub>8</sub>	10.60	10.4
Er <sup>3+</sup>	4f <sup>11</sup>	<sup>4</sup> I <sub>15/2</sub>	9.59	9.5
Tm <sup>3+</sup>	4f <sup>12</sup>	<sup>3</sup> H <sub>6</sub>	7.57	7.3
Yb <sup>3+</sup>	4f <sup>13</sup>	<sup>2</sup> F <sub>7/2</sub>	4.54	4.5
Lu <sup>3+</sup>	4f <sup>14</sup>	<sup>1</sup> S <sub>0</sub>	0.00	0.00
Ti <sup>3+</sup>	3d <sup>1</sup>	<sup>2</sup> D <sub>5/2</sub>	1.73	1.6-1.7

Table 3.3: Table of electron configurations and free ion paramagnetic moments of the rare-earths and titanium<sup>2</sup>. Adapted from [62].

The Tab.3.3 shows the magnetic moment calculated from the electronic configuration of the free ions.

The formula used was:

$$\mu = g\sqrt{J(J+1)} \quad (3.4)$$

with 
$$g = \frac{3}{2} + \frac{1}{2} \frac{S(S+1) - L(L+1)}{J(J+1)}$$

It follows from Eq. 3.4 that in the spin only case  $\mu = 2\sqrt{S(S+1)}$ , thus giving us the 7.94  $\mu_B$  of Gd<sup>3+</sup>. However, as soon as we introduce an orbital moment i.e. for the rest of rare-earths (except La and Lu), the picture breaks and simple subtraction are not working anymore. Neither Eq. 3.4 nor the spin only case can explain the magnetic cycles shown in Fig. 3.4.

If we take the example of DyTiO<sub>3</sub>, the material we primarily studied, whereas Dy<sup>3+</sup> have nine electrons on the 4f shell and one on the 3d shell of Ti<sup>3+</sup> it presents a net magnetization of 3.7  $\mu_B$  instead of the 8.9  $\mu_B$  in a collinear spin model. This is partially explained by a complex magnetic structure for DTO described in [61].

---

<sup>2</sup>Note that the Pm<sup>3+</sup> experimental moment is missing because of its radioactive instability. Sm<sup>3+</sup> and Eu<sup>3+</sup> have a greater moment than the one predicted because of Van Vleck paramagnetism. Note also that the titanium value is from a spin only model which is the most common case for transition metal in solids.

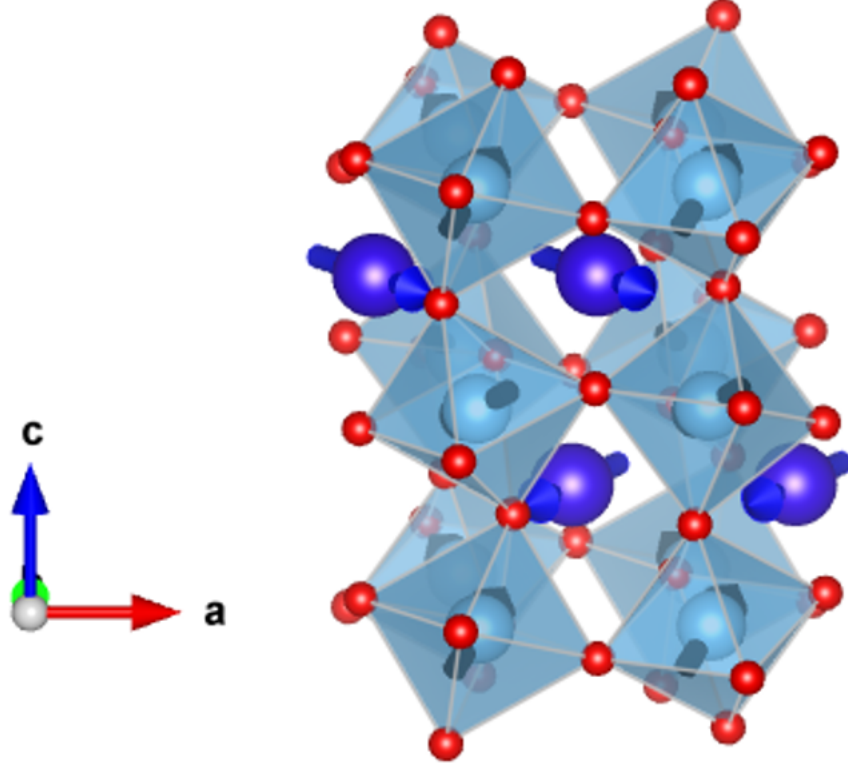


Figure 3.5: Schematic of the structure of the  $\text{DyTiO}_3$  unit cell. The magnetic moment on each site is represented by arrows pointing in the direction established in [54]

The Fig. 3.5 shows us that some components of the magnetization are "lost" on the resulting magnetization. These components correspond to the antiferromagnetic one along the  $b$  axis. According to neutron data DTO the cation spins interact ferromagnetically along the  $a$  and  $c$  axis and antiferromagnetic along  $b$  axis. They are respectively tilted from these axes by  $31^\circ$ ,  $59^\circ$  and  $69^\circ$ . This canting is the result of the Dzyaloshinskii-Moriya interaction (DMI) which rotate the spin along a specific direct and is enhanced by the presence of strong spin-orbit coupling. This structure result in a reduced overall moment.

By using the value of [61]  $9.7 \mu_B$  for  $\text{Dy}^{3+}$  and  $0.9 \mu_B$  for  $\text{Ti}^{3+}$  we obtain,

$$m_{\text{total}} = \frac{\sqrt{2m_{\text{Dy}}^2(\cos(62) + 1)}}{2} - \frac{\sqrt{2m_{\text{Ti}}^2(\cos(62) + 1)}}{2} = 7.53 \mu_B \quad (3.5)$$

If we take into account the  $21^\circ$  tilt from the  $ab$  plane, the existence of which is unsure, the magnetization is reduced to  $7.02 \mu_B$ . However, this magnetization is still almost twice the experimental value. Another explanation for this would be an smaller contribution from  $\text{Dy}^{3+}$  than expected.

The different magnetic structure can be quite difficult to describe and to do so, we use the Bertaut's notation to classify them [63]. The  $F$ -type corresponds to the classic ferromagnetic structure where all spins are collinear but by introducing antiferromagnetic interaction, several configurations are possible.  $A$ -type corresponds to ferromagnetic plans that interact antiferromagnetically along an axis of the magnetic unit cell. This idea can be generalized along any axis for example  $(\frac{1}{2}\frac{1}{2}0)$  and  $(\frac{1}{2}\frac{1}{2}\frac{1}{2})$  (respectively  $C$  and  $G$  type). You can also change the number of planes ferromagnetically interacting, like 2 along  $(11\frac{1}{2})$ . Those configurations are illustrated by Bousquet *et al* in Fig. 3.6

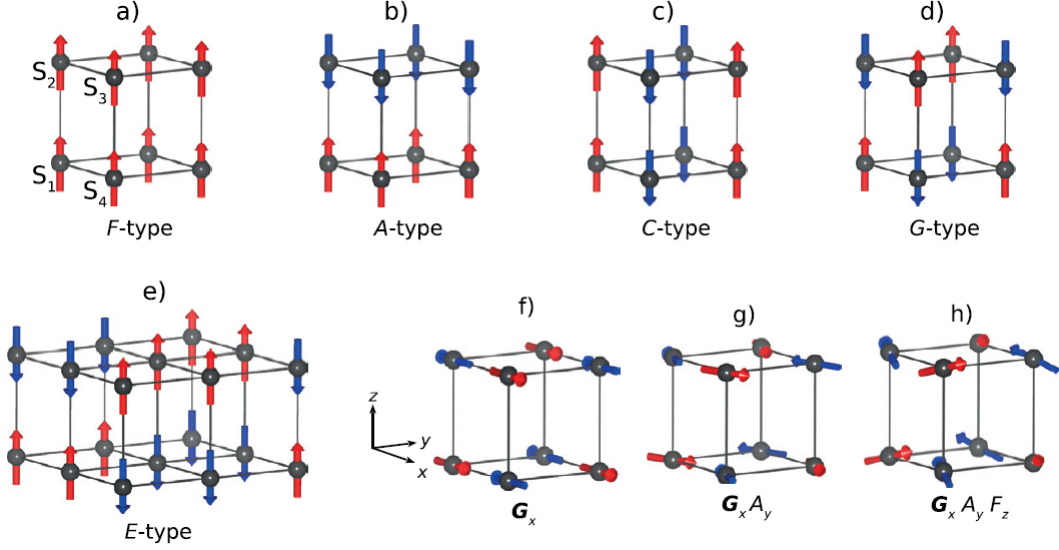


Figure 3.6: Schematic view of (a) *F*-type, (b) *A*-type, (c) *C*-type, (d) *G*-type and (e) *E*-type collinear magnetic orders that can be constructed in cubic perovskites  $\text{ABX}_3$  (for the sake of illustration, spins are directed along the  $z$  axis). (f), (g) and (h) show respectively the  $\mathbf{G}_x$ ,  $\mathbf{G}_x\mathbf{A}_y$  and  $\mathbf{G}_x\mathbf{A}_y\mathbf{F}_z$  non-collinear orders. From [64]

If the spins are not collinear inside a sublattice as it is the case for DTO this configuration can be described as a linear combination of the configurations above along each direction. Orthorhombic perovskites have determined magnetic configurations in order to respect their symmetry.

Irrep.	<i>B</i> -site	<i>A</i> -site	Ext. field
$\Gamma_1^+$	$A_x, G_y, C_z$	$C_z$	
$\Gamma_2^+$	$F_x, C_y, G_z$	$F_x, C_y$	$H_x$
$\Gamma_3^+$	$C_x, F_y, A_z$	$C_x, F_y$	$H_y$
$\Gamma_4^+$	$G_x, A_y, F_z$	$F_z$	$H_z$

Table 3.4: Point-group symmetry properties of some representative orders in orthorhombic  $\text{ABO}_3$  perovskites (Pbnm setting). Adapted from [64].

From Tab. 3.4, we can see that the magnetic structure of DTO corresponds to the point group  $\Gamma_3^+$  according to [61].

### 3.3.3 Electronic properties

As we could expect the Mott gap is changing with the size of the rare earth. Indeed, as we have seen in section 3.3.1 the amplitude of the rotation modes in the structure controls the orbital order and thus the amplitude of the  $t_{2g}$  splitting presented by Mochiziki in [3].

	La	Ce	Pr	Nd	Sm	Gd	Y
Activation energy (eV)	0.01	0.001	0.03	0.03	0.15	0.19	0.22

Table 3.5: Experimental values of activation energy of the different rare-earth titanates in eV. Adapted from [54]

Indeed, the Tab. 3.5 shows an increase of the activation energy (the characteristic energy of the activation of an insulator) as the ion radius decrease, linking the rotation amplitude and gap size. We have to keep in mind that the measured gap is always bigger than what the calculations predict, because the functional calculation have a tendency to underestimate the gap and that the experimental measurements are dependent on the technique used. We can propose a more comprehensive look on the titanate electronic properties in [13, 65, 66, 67, 68, 69].

Note that since  $U \gg \Delta_1$  (typically  $U \simeq$  tens of eV), where  $U^3$  is the Mott splitting discussed in section 1.4.2 and  $\Delta_1$  is the first splitting of the  $t_{2g}$  levels as seen in Fig. 3.3 (a), it means that the effective gap of this compound is  $\Delta_1$ .

We can take for example the case of  $\text{LaTiO}_3$  which has an almost cubic symmetry due to the large size of La, the gap is only of 0.06 eV whereas the  $\text{DyTiO}_3$  gap is of 0.6 eV, thus highlighting the control of the rotation of octahedra over the gap opening. As Varignon, Zunger and Bibes proposed, this mechanism is responsible for the opening of most gaps in oxide perovskite [14].

## 3.4 State of the art on rare-earth titanate thin films

Rare-earth titanates have been first grown in bulk via solid state reaction since the fifties and stabilized during the seventies to the eighties [70, 71, 72]. Following these growths, thorough characterizations have been conducted. First crystalline and magnetic structures by x-ray and neutron diffractions followed by the magnetic and electronic properties. For review papers please refer to the bibliography of [72] and [71] for the bulk samples grown in the fifties. However, most of those resources are quite hard to find online.

The production of thin films of rare-earth titanates have seen a first surge of interest in the 2000s through the work of Ohtomo and Hwang for PLD and the work of Moetakef and Stemmer for Molecular Beam Epitaxy (MBE).

### 3.4.1 Growth of epitaxial thin films

In the early 2000s the group of J-M Triscone [73] (MBE), Ohtomo [74] (PLD) and Mannhart [75] (MBE) grew  $\text{LaTiO}_3$  thin films following the perspectives presented by Tokura in [15], in order to reproduce a cuprate like situation with titanates as a highly correlated metal.

After what we have seen in the previous section, LTO appears as the simplest rare-earth titanate. Indeed, its structure is the closest to cubic, presents a collinear antiferromagnetic structure and does not possess  $4f$  electrons that could complicate the physics of the system. It has also been reported to be easier to grow compared to the other titanates.

In these early works, the focus has been on the transport properties of LTO. By doping it, those groups tried to reach metallicity while reproducing the conditions of the High- $T_C$  cuprates with their  $3d^1$  electron (holes). As we depart from half filling at stoichiometry either by doping by holes or electrons the gap closes as seen in Fig. 3.7.

---

<sup>3</sup> $U$  is actually a effective  $U$  which take into account the Coulomb repulsion and the exchange interaction  $U_{eff} = U - 2J$ .

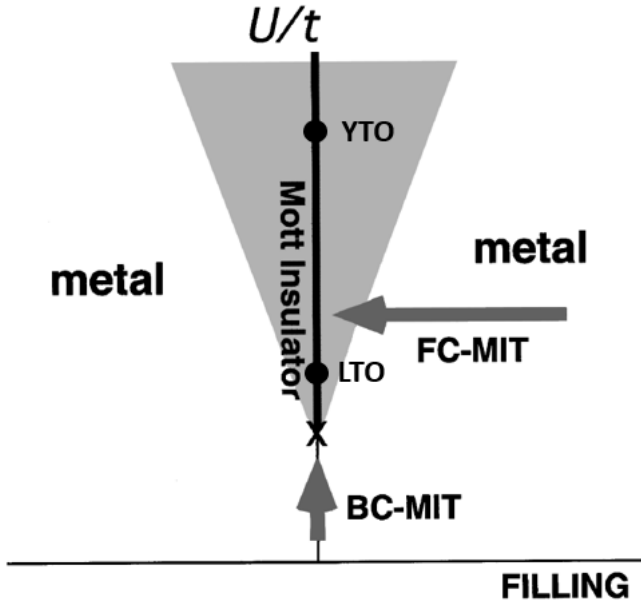


Figure 3.7: Metal-insulator phase diagram presenting  $U/t$  as a function of the  $d$  band filling, according to the Hubbard model. The shaded area corresponds to correlated metals in which carriers are easily localized whereas only the half-filling line corresponds real Mott insulator. As we can see there two ways of obtaining a metal to insulator transition (MIT): either by filling control (FC) as discussed above or by band control (BC). Adapted from [15]

As seen in Fig. 3.7, LTO has also been chosen because of its proximity to the metal to insulator transitions. It is then easier to induce it by lowering and increasing filling of the 3d band [76, 77]. .

As the correlation of the meterial increase (represented by the ratio  $U/t$ ), the range of filling where the phase is insulating increase. The departure from the stoichiometric  $3d^1$  configuration can be done by the overoxydation or reduction of the titanate.

Apart from YTO and LTO, rare earth titanates with  $4f$  electrons, and in particular  $GdTiO_3$ , have also been studied later by the group of Suzanne Stemmer [78]. Those samples have been grown by Molecular Beam Epitaxy using a non-conventional method that in addition to the block-by-block method [79] used in [73], used organic precursors to widen the growth window by self-regulation [80, 81].

However, all those growth methods can not avoid the poor stability of  $Ti^{3+}$ . Thus, they all must be performed under low oxygen pressure and relatively high temperature. We can notice that the works on LTO and YTO before 2010 have studied the off stoichiometric phase (over-oxidized) most likely because of this difficulty. Those early works have been summarized by the following Fig. 3.8.

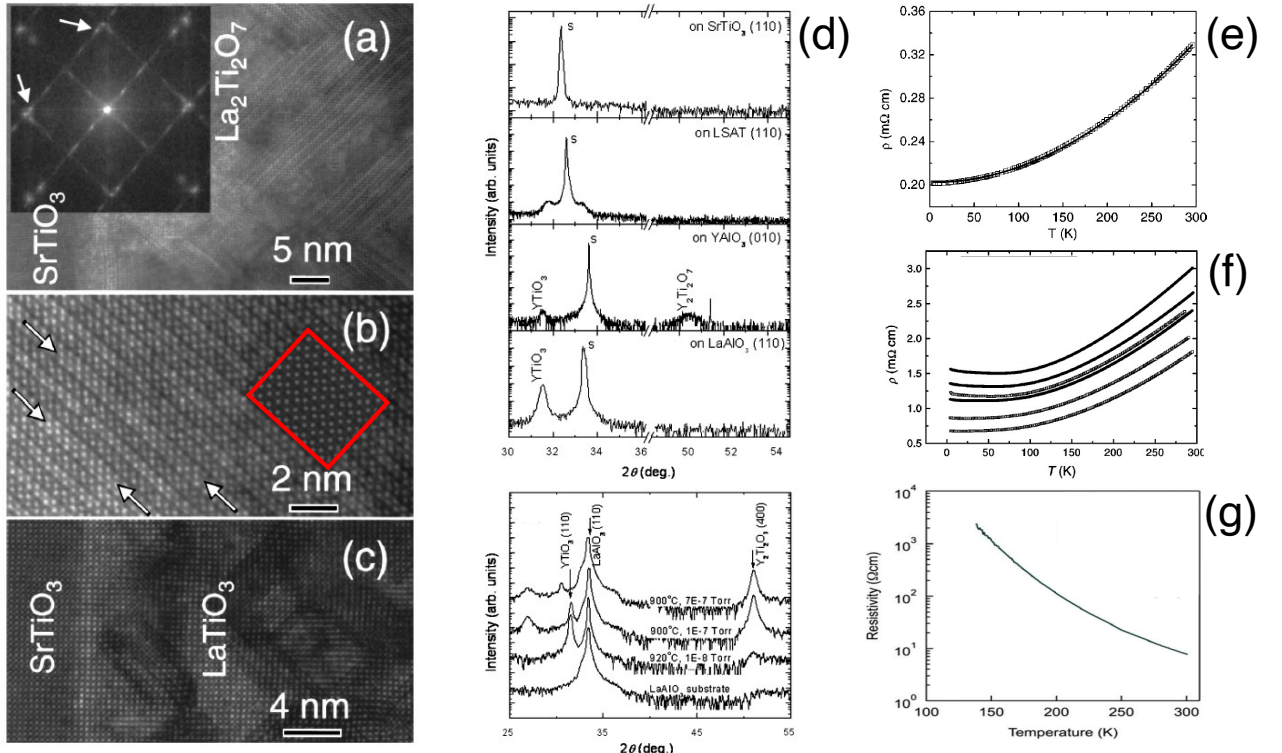


Figure 3.8: Annular dark-field scanning transmission electron microscope images for  $\text{La}_2\text{Ti}_2\text{O}_7$  [(a) and (b)] and  $\text{LaTiO}_3$  (c) grown on  $\text{SrTiO}_3$  (001) substrates. Inset in (a) depicts a Fourier transform of the image, and the arrows indicate the tilting twin microstructure of  $\text{La}_2\text{Ti}_2\text{O}_7$ . Inset in (b) shows a simulated image obtained assuming the bulk structure. Stacking faults in the  $\text{La}_2\text{Ti}_2\text{O}_7$  film are indicated by arrows [74]. (d) X-ray diffraction patterns of  $\text{YTiO}_3$  thin films grown on  $\text{SrTiO}_3$  (110), LSAT (110),  $\text{YAlO}_3$  (010), and  $\text{LaAlO}_3$  (110) single-crystal substrates. X-ray diffraction patterns of  $\text{YTiO}_3$  thin films grown on  $\text{LaAlO}_3$  (110) at different pressure [82]. (e) Resistivity of a 22 nm  $\text{LaTiO}_3$  thin film ( $n = 10^{22} \text{ cm}^{-3}$ ) [73]. (f) Resistivity of  $\text{LaTiO}_{3+\epsilon}$  films grown on  $\text{NdGaO}_3$  (100) (solid symbols) and  $\text{NdGaO}_3$  (110) (open symbols) [75]. (g) Resistivity of an 8 nm  $\text{GdTlO}_3$  grown on LSAT (001) [78].

As mentioned before, stabilizing the perovskite phase proved to be quite challenging as shown in Fig. 3.8 (a,b), where we can observe the formation of the pyrochlore phase instead [74]. However, the perovskite phase is achieved in Fig. 3.8 (c). In the same way the Fig. 3.8 (d) illustrates the difficulty to stabilize YTO on different substrates and the requirement of low oxygen pressure. The resulting transport properties are very interesting in this regard, where Fig. 3.8 (e,f) shows metallic behavior due to doping effect, Fig. 3.8 (g) shows the insulating behavior expected from a Mott material. In all fairness to earlier works, we have to point out the fact that Fig. 3.8 (g) is extracted from [78] in 2012 nearly a decade after the other study presented in this figure. This highlights the huge progress in the growth of rare-earth titanate thin films in the 2010s.

### 3.4.2 Heterostructures

One of the main perks of the rare-earth titanate family lies in their magnetic highly correlated insulator nature. They also possess a perovskite structure as the well-known LAO/STO heterostructure. In those interfaces we have the following stacking sequence of  $(\text{Al}^{3+}\text{O}_2^{2-})^-(\text{La}^{3+}\text{O}^{2-})^+(\text{Ti}^{4+}\text{O}_2^{2-})^0(\text{Sr}^{2+}\text{O}^{2-})^0$  introducing a polar discontinuity at the interface. This discontinuity will create what we call a polar catastrophe in which the potential will build up as the material thickness increases. In order to avoid this, an electronic reconstruction (ER) takes place in which a charge transfer occurs from the top (AlO) layer to the interfacial TiO<sub>2</sub> resulting in  $(\text{Al}^{3+}\text{O}_2^{2-})^{-\frac{1}{2}}\dots(\text{Ti}^{4+}\text{O}_2^{2-})^{-\frac{1}{2}}$ .

However, in the case of RTO/STO (with R: a rare earth) the interface is chemically symmetric  $(\text{Ti}^{3+}\text{O}_2^{2-})^-(\text{R}^{3+}\text{O}^{2-})^+(\text{Ti}^{4+}\text{O}_2^{2-})^0(\text{Sr}^{2+}\text{O}^{2-})^0$ . As shown in Fig. 3.9 the  $(\text{R}^{3+}\text{O}^{2-})^+$  is expected to give  $0.5 e^-$  to the neighboring layer. Several of the groups presented in the previous section have pursued their work towards elaborating heterostructures of this type [83, 84, 85, 86]

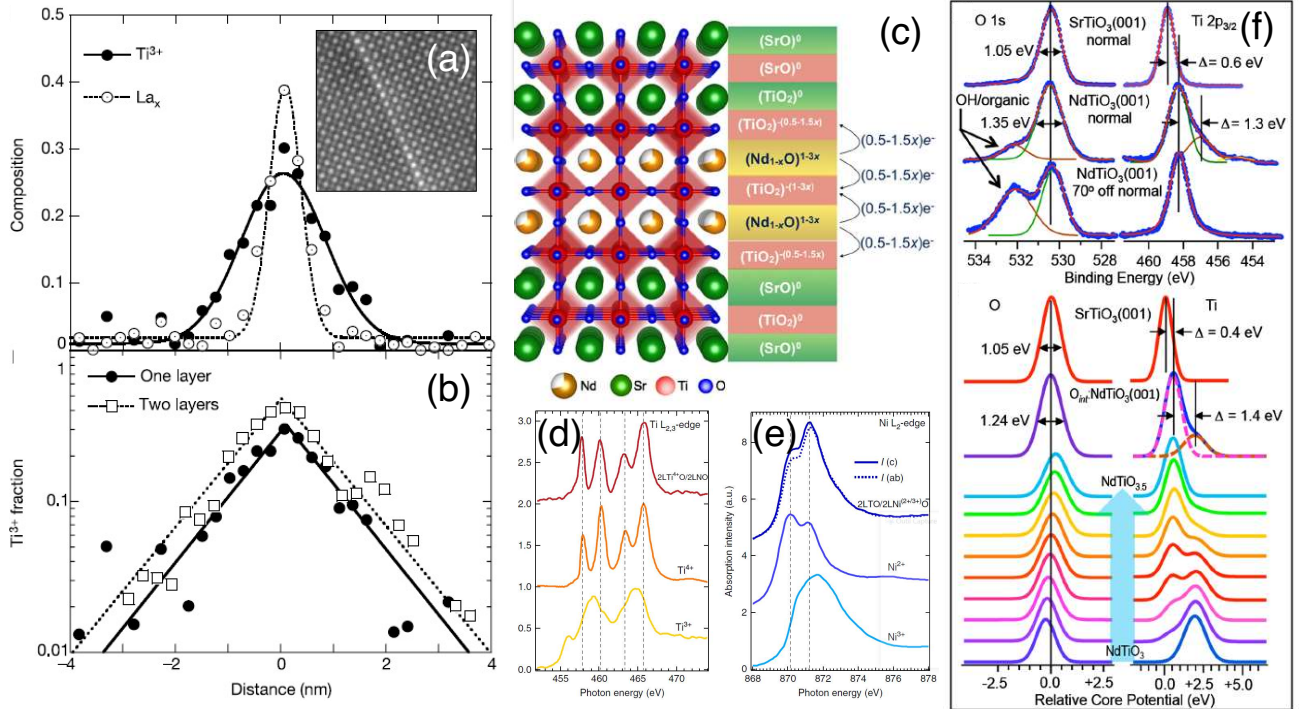


Figure 3.9: (a)  $\text{Ti}^{3+}$  and La compositions obtained by electron energy loss spectroscopy (EELS) at the interface between LTO in lighter color and STO as seen in the inset. (b)  $\text{Ti}^{3+}$  fraction in log scale across a one and two layers of LTO [83].(c) Schematic of an electronic reconstruction for a multilayer of  $\text{Nd}_{1-x}\text{TiO}_3$  sandwiched between layers of STO [84]. XAS spectra (TFY) of (d) Ti  $\text{L}_{2,3}$  edge resp. of LTO/LNO, STO and NTO. (e) Ni  $\text{L}_{2,3}$  edge resp. of LTO/LNO, NiO and LNO [86]. (f) XPS spectra of SrTiO<sub>3</sub> substrate and NdTiO<sub>3</sub> thin film of 10 nm at different collection angles. Simulation of the XPS spectra of NdTiO<sub>3</sub> according to oxygen doping [84].

The 2010s have seen the realization of several bilayer or superlattices and a closer investigation of the valence state of titanium. First Ohtomo team pursued his work on LTO by growing LTO/STO multilayers and investigated the valence of titanium at the interfaces. In Fig. 3.9 (a) they look at a

single unit cell of LTO buried in STO, as shown in the inset, and observe the EELS signal of La and  $Ti^{3+}$ . It is then clear that the  $Ti^{3+}$  is "leaking" from the monolayer to STO, which could indicate a charge transfer. Fig. 3.9 (b) shows exponential decrease of the titanium 3+ away from the LTO regardless of its thickness pointing toward a diffusive effect. In [84], the Jalan team grew NTO/STO interfaces Fig. 3.9 (c) and proposed an electronic reconstruction mechanism in order to explain the observed charge transfer. They also investigated the valence state of titanium by performing XPS on  $NdTiO_3$  thin film of 10 nm on the O 1s and Ti 2p core levels and identified a new component that was not present in the  $SrTiO_3$  reference. They identified it as the signal of  $Ti^{3+}$  and as they change the collection angle; this component disappears and another one grows on the O 1s core level. This points toward an almost pure  $Ti^{4+}$  surface where there are excess oxygens in a specific environment (because of the observed chemical shift at the O 1s levels). This has been verified by simulating those core levels in the case of different oxygen doping levels. However, one can see that even in normal incidence  $NdTiO_3$  titanium is far from being purely 3+. Chakhalian's team [86] also investigated the valence state, this time by performing XAS on their LTO/LNO bilayer at the  $L_{2,3}$  edge of titanium and nickel, respectively Fig. 3.9 (d) and (e). If the mix of states is clear in both transition metals, its origin is not. Indeed, to differentiate charge transfer from oxygen transfer at the interface keeps being a real challenge for the community. Chakhalian's team had the good idea to probe the pre-edge of oxygen to observe hybridization peaks. However, the presence of many components renders this analysis difficult. In the case of RTO/RNO (R: rare-earth) interface keeping the right stoichiometry is extremely challenging because the high oxygen content required for nickelate in contrast with the titanate reduction condition<sup>4</sup>. To avoid that, we have to design specific growing conditions as exposed in the next chapter.

---

<sup>4</sup>Note that differentiating between charge transfer and off-stoichiometry at the interface. One way to find out is to look at the presence of structural defect indicating the off-stoichiometry

# Chapter 4

## Growth of rare-earth titanate thin films

The growth of rare earth titanates constitutes in itself a challenge because of its ionic composition. In the RTO formula R and Ti have an oxidation state of 3+ and O 2- whereas most of the rare earth are stable in the 3+ ionization degree, the Ti<sup>3+</sup> is known to be unstable. The fact that Ti<sup>3+</sup> is one electron away from having its M shell empty and thus to adopt the much more stable electronic configuration of Ar, in the Ti<sup>4+</sup> form. For this reason, the growth of rare earth titanates often leads to the formation of parasitic phases where the titanium is 4+. To avoid this, we need to get the most reducing growth condition possible and minimize the presence of oxygen. In the present chapter, I will be present the optimization of the growth of DyTiO<sub>3</sub>.

### 4.1 Establishment of the growth conditions

#### 4.1.1 Growth parameters

In order to establish the optimal growth conditions, we varied the PLD parameters discussed in section 2.2.1 (temperature, pressure, laser energy and frequency) and characterized the samples by XRD. For that we used the ICDD database and the structure of DTO in [87]

#### Temperature

First, we choose to optimize the temperature growth. In the previous work performed on GTO in our group, Mathieu Grisolia [68, 88] used a temperature of 660 °C but this previous work was done using a less advanced PLD system where the temperature was not as well controlled (resistive heating). During this PhD we used a laser heater that allowed us to reach a maximum substrate temperature of 1300 °C. In the literature, pure phase films of RTO have been obtained at high temperature [78, 73, 74] in PLD as well as in MBE. High temperature allows to stabilize the perovskite phase whereas temperatures below 700 °C will result in a mix of parasitic phases described in [68].

#### Pressure study on different substrates

As we discussed above, the Ti<sup>3+</sup> state is unstable and needs a low oxygen partial pressure. In the previous work the background oxygen pressure is on the 10<sup>-6</sup> mbar range [68] even though this is enough to stabilize the perovskite phase, a more thorough investigation showed that the valence state was still not fully Ti<sup>3+</sup>. Thus, we tried to get to an even lower oxygen partial pressure. Our deposition

chamber can stabilize a pressure of  $4.10^{-7}$  mbar at the growth temperature. Below it the overpressure created by the plume is of the same order of magnitude as the background. We thus scanned a range from  $4.10^{-7}$  mbar to  $1.10^{-5}$  mbar. Since the optimal growth condition could be different from substrate to substrate, we performed this study on SrLaGaO<sub>4</sub> (SLGO), DyScO<sub>3</sub> (DSO), LaAlO<sub>3</sub> (LAO) and SrTiO<sub>3</sub> (STO). To do so we cut the substrates in four ( $2.5 \times 2.5$  mm) and glued them on one sample holder in order to keep the conditions consistent<sup>1</sup>.

### SrLaGaO<sub>4</sub> (SLGO)

We first started to work on SLGO, which has an in-plane lattice parameter of 3.85 . Which correspond to a tensile strain of 0,7 %.

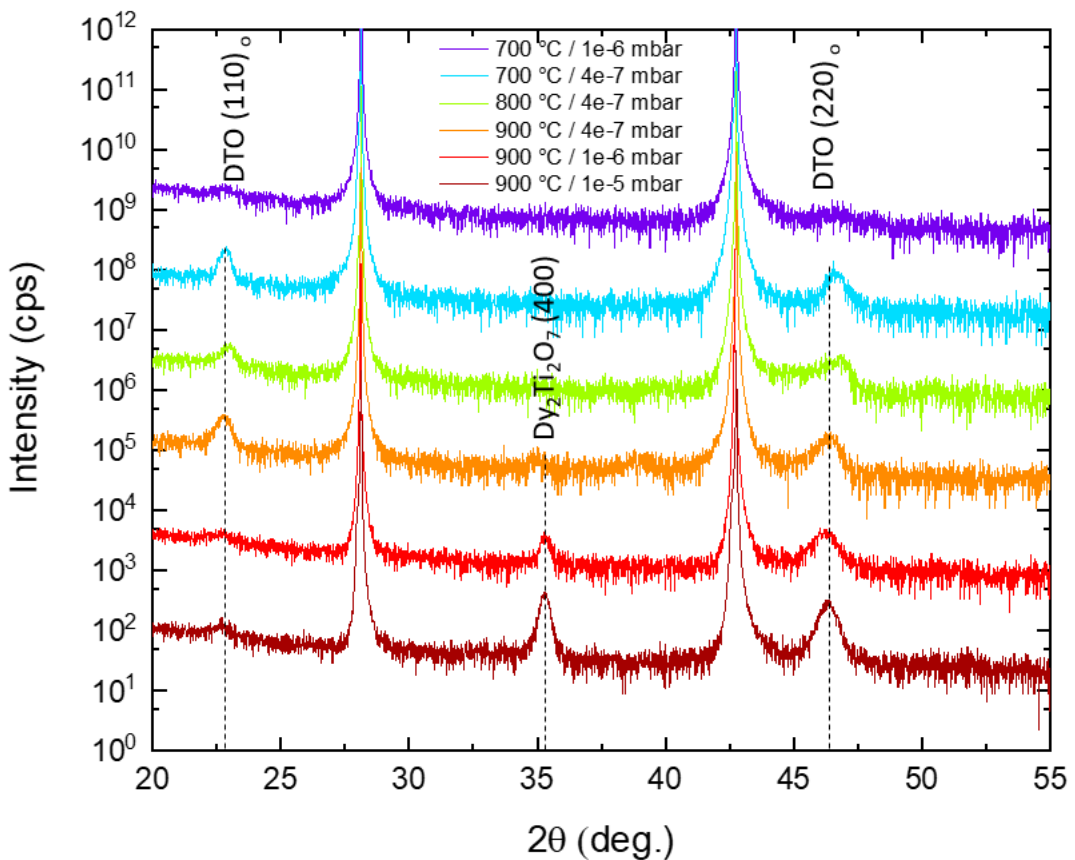


Figure 4.1: Pressure and temperature dependencies of  $2\theta - \omega$  scans of DTO 20 nm films grown on SLGO (001) substrates.

The Fig. 4.1 shows that as the temperature increases the film seems to be more sensitive to oxygen pressure. We see that the parasitic phase identified as Dy<sub>2</sub>Ti<sub>2</sub>O<sub>7</sub> increases in intensity as the oxygen pressure gets higher. At 700 °C, we observe a decrease of the peak's intensity meaning that most of the film is amorphous, thus not diffracting X-Rays. These two behaviors will remain the most relevant guidelines for setting the growth pressure.

From this we can say that DTO grows better at  $900^\circ\text{C} / 4.10^{-7}$  mbar.

---

<sup>1</sup>Note the thin and intense ( $10^4$  times the intensity of the film peak) peaks correspond to the substrate.

## DyScO<sub>3</sub> (DSO)

DSO has an in-plane lattice parameter of 3.94 (leading to a tensile of 1 %). It also has a lower oxygen mobility compare to the other perovskites substrates thanks to its higher distortion [89].

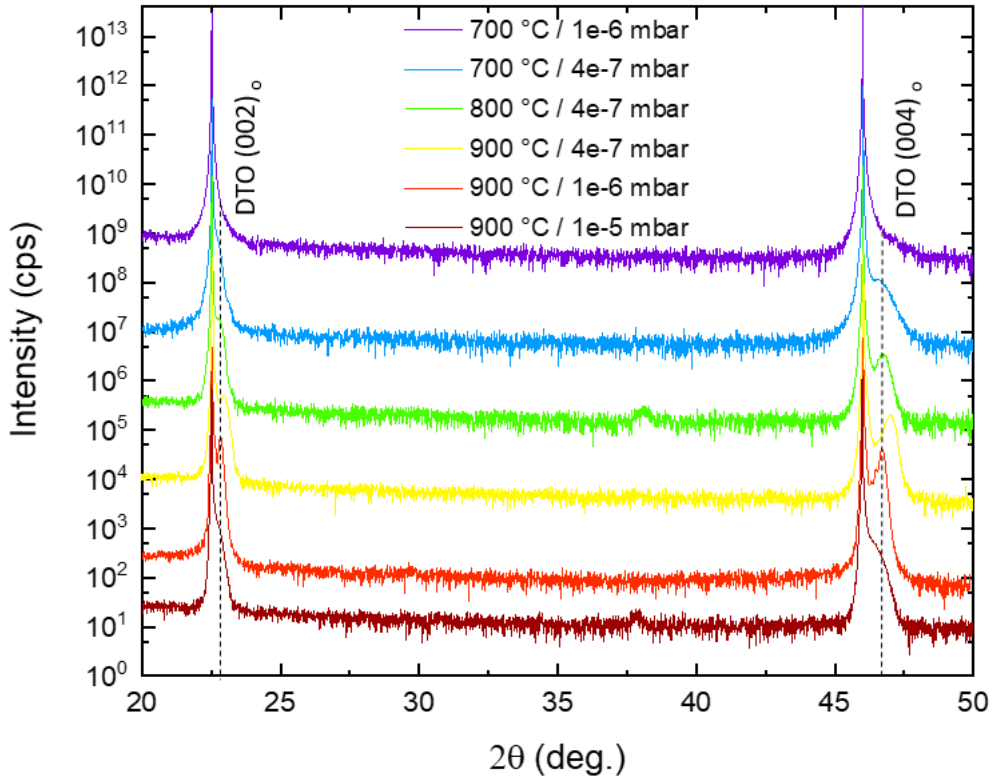


Figure 4.2: Pressure and temperature dependencies of  $2\theta - \omega$  scans of DTO 20 nm films grown on DSO (110) substrates.

Here we can see that no parasitic phase appeared<sup>2</sup> and that the film peak intensity increases as we reduce the oxygen partial pressure in the chamber, this is striking compared to the last two scans ( $1 \times 10^{-6}$  and  $1 \times 10^{-5}$  mbar) at  $900^\circ\text{C}$ . The same goes for when we reduced the temperature at constant pressure ( $4 \times 10^{-7}$  mbar).

## LaAlO<sub>3</sub> (LAO)

In the case of LAO, the window of optimal growth parameters seems to be narrower. Here we clearly need high temperature and low pressure to achieve good sample quality as good growth quality is only achieved at  $900^\circ\text{C}$  and  $4 \times 10^{-7}$  mbar (cf Fig. 4.3).

<sup>2</sup>The small peaks around  $37^\circ$  correspond to silver paste residues because no peak at  $30.6^\circ$  characteristic of the pyrochlore phase can be observed [90]

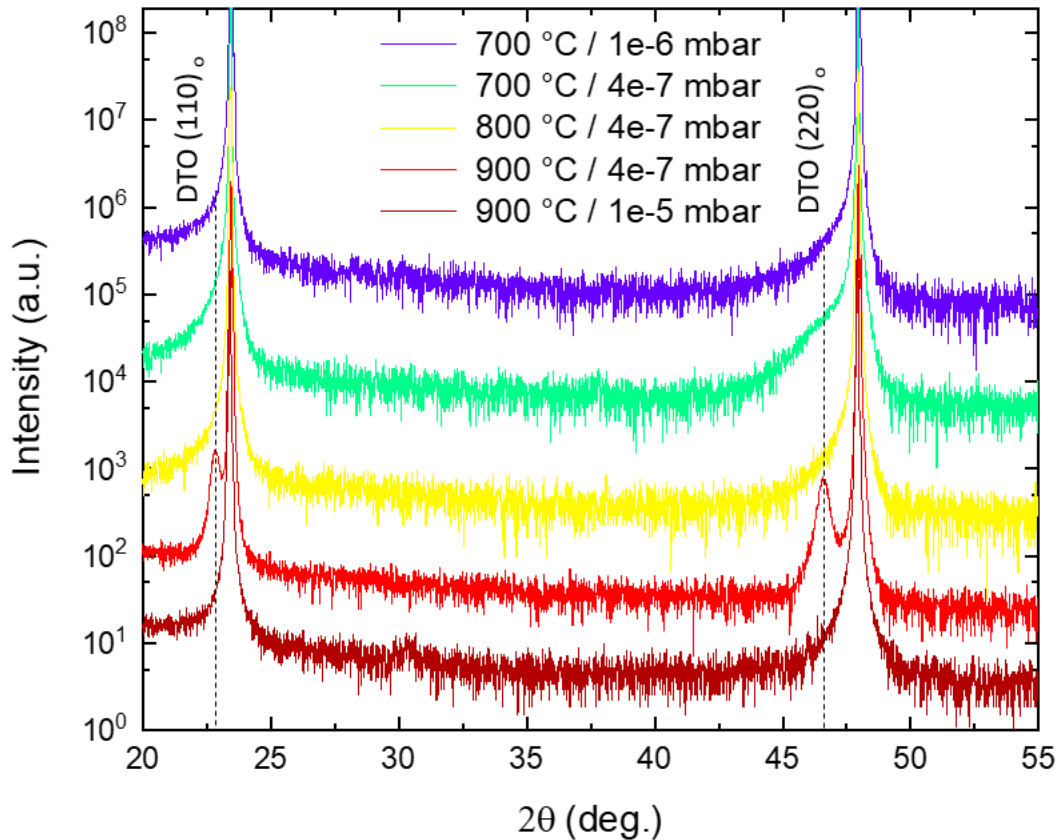


Figure 4.3: Pressure and temperature dependencies of  $2\theta - \omega$  scans of DTO 20 nm films grown on LAO (001) substrates.

### SrTiO<sub>3</sub> (STO)

STO is an interesting case because no growth conditions seem to allow good films, Fig. 4.4.

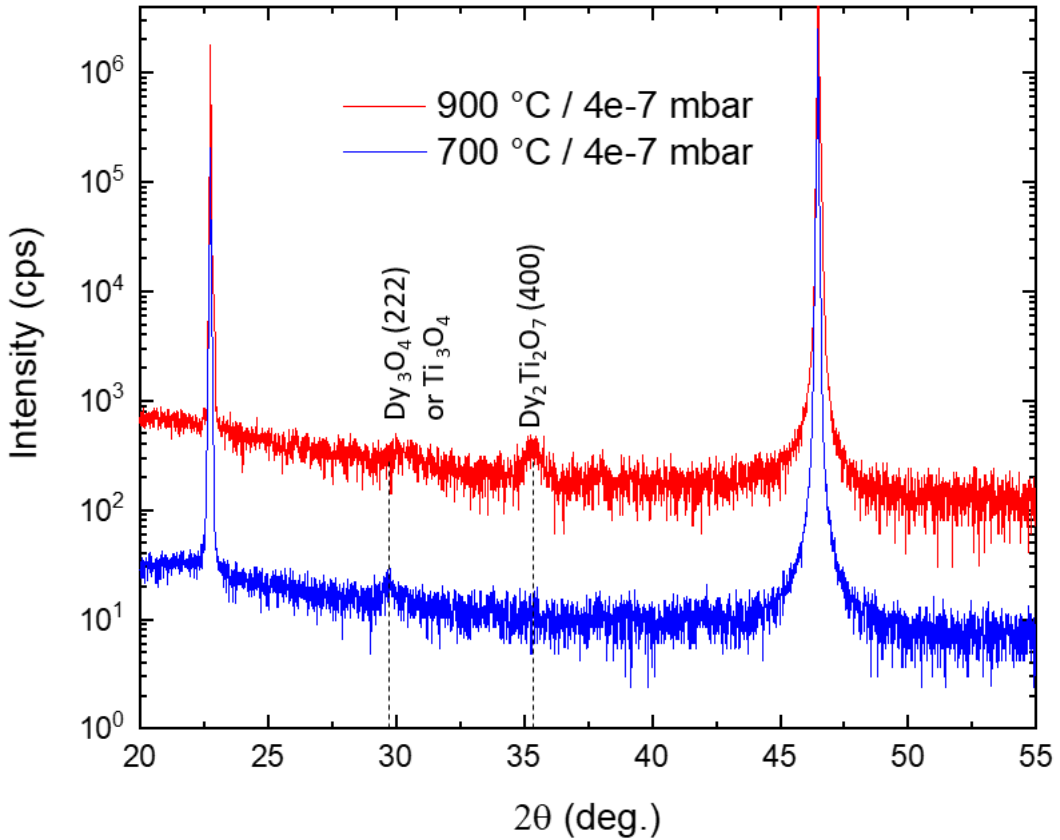


Figure 4.4: Pressure and temperature dependencies of  $2\theta - \omega$  scans of DTO 20 nm films grown on STO (001) substrates.

Even though we see a low intensity parasitic phase peak, the film seems to be amorphous, explaining the absence of real film peak. Those parasitic phases seen in Fig. 4.4 can be identified as  $\text{Dy}_2\text{Ti}_2\text{O}_7$  (at  $35^\circ$ ) and  $\text{X}_3\text{O}_4$  (at  $30^\circ$ ), where X: Dy or Ti. However, all those phases are expected to be paramagnetic or antiferromagnetic. This failure to obtain the perovskite phase might be explained by the commonly known high mobility of oxygen inside STO [89]. This might create an effective excess of oxygen preventing its formation.

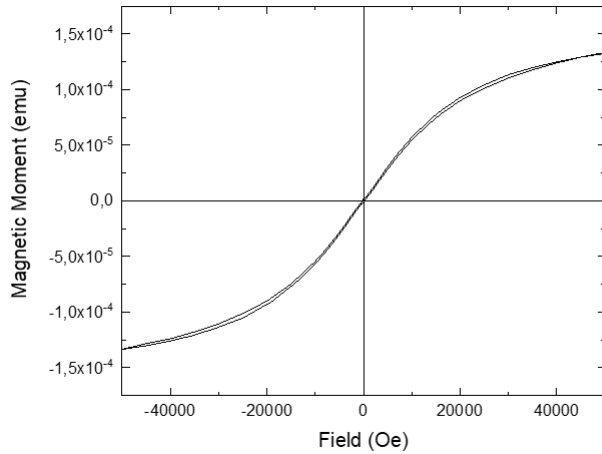


Figure 4.5: Magnetization as a function of field at 10 K of DTO 20 nm thick film grown on STO (001).

The MvH curve of Fig. 4.5 shows only a paramagnetic like a signal with no sign of coercive field nor remnant magnetization. The absence of ferrimagnetism signal thus rules out the possibility of simply

having the film peaks indistinguishable from the substrate peaks, which would not be extravagant given their close lattice parameters. The observed paramagnetic signal most likely comes from the parasitic phases.

## Conclusion

By optimizing the temperature and oxygen pressure during growth, we achieved pure perovskite phase films on different substrates except STO due to the high mobility of the oxygen vacancies. The growth of rare-earth titanate has proved to possess quite a narrow growth window. High temperature and low oxygen pressure are preferable to achieve high-quality films. We extended the phase diagram of [68] to higher temperatures and lower pressures. This allowed us to achieve a better magnetic response and crystalline quality.

### 4.1.2 Oxygen vs Argon growth

We faced the problem that even at the minimal oxygen pressure the magnetic properties of thick samples were not as good as the bulk properties, especially on the point of view of magnetic properties.

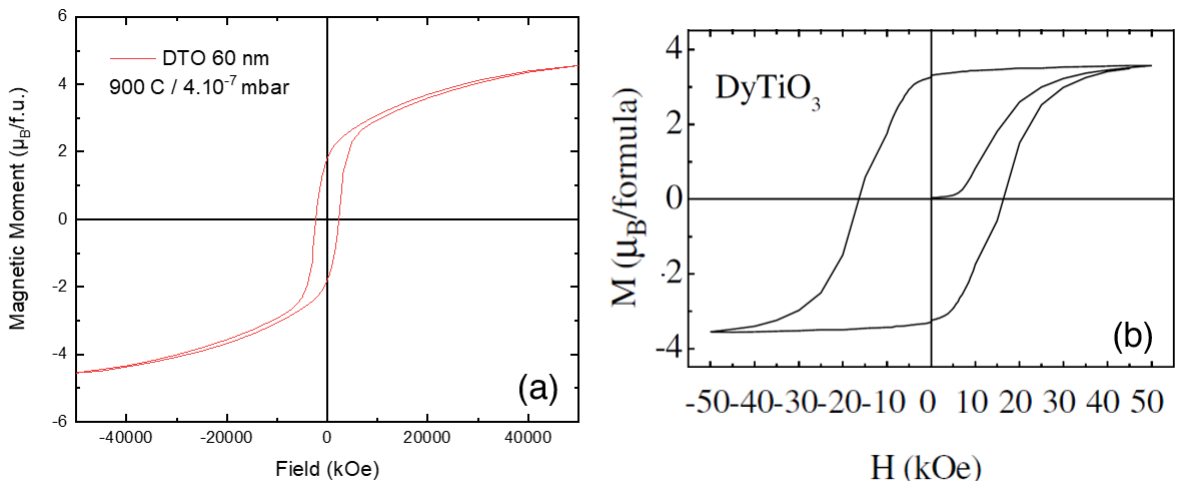


Figure 4.6: Magnetic moment as a function of the field of a DTO (a) 60 nm thin film at 10 K (b) bulk sample 5 K. Adapted from [4].

To overcome this issue, we took a different approach than simply reducing the oxygen pressure in the chamber, since even growing in vacuum does not seem to be enough to make perfect samples. Note that by vacuum, we refer here to a growth without any addition of gas in the chamber and starting from the base pressure of low  $10^{-9}$  mbar, even though the effective pressure during the growth is  $10^{-7}$  mbar.

The goal being to reduce the amount of oxygen or oxidized species reaching the substrate, we opted for the use of argon as background gas (idea from Nicolas Reyren), to confine the plasma while slowing down the lighter elements (namely the oxygen).

If we weren't aware of them at the time, there have been studies analyzing the effect of argon growth on the chemistry of the plume [26, 28, 91].

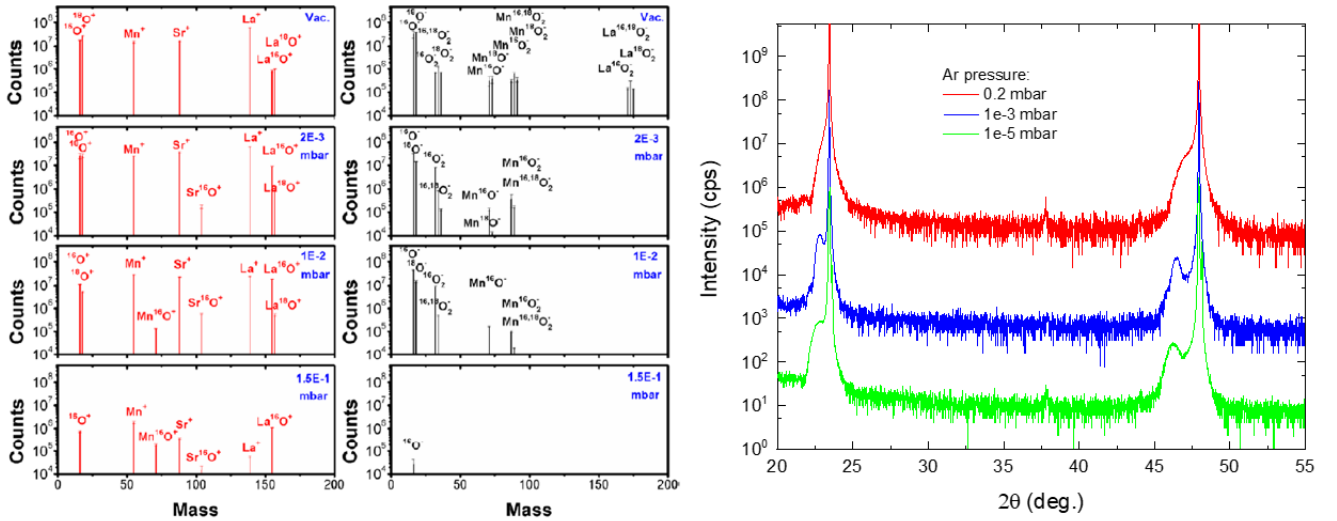


Figure 4.7: (a) Overview of the amounts of the ionic plasma species in laser induced  $\text{La}_{0.6}\text{Sr}_{0.4}\text{Mn}^{16,18}\text{O}_3$  plasmas in vacuum as well as at  $P_{\text{O}_2}$  measured by mass spectroscopy. Adapted from [91]. (b) X-ray  $2\theta$ - $\omega$  scans of DTO samples grown at  $900^\circ\text{C}$  at different argon pressures.

On Fig. 4.7 (a) from [91], we can see the effect of the background gas pressure on the species present in the plume. Positive diionic species are more present as we increase the background pressure but more importantly, the diionic negative species are almost completely suppressed. As Chen explains, it is around  $10^{-3}$ - $10^{-2}$  mbar that we go from a "ballistic" regime, where the mean free path is greater than the target to substrate distance, to a shock-wave regime where the species are slowed down through scattering by background gas. Of course, the bigger the background pressure is, the more efficient the scattering is. At high pressure all species are scattered equally resulting in a congruent transfer. By placing ourselves at the limit between these two regimes, we scatter only the lighter element, namely the oxygens. This strategy actually proved to be more efficient than simply reducing the pressure, as seen in Fig. 4.7 (b).

## 4.2 Crystalline orientation

### 4.2.1 X-rays diffraction characterization

As we presented in section 3.2.1, DTO has an orthorhombic structure with  $a = 5.363$   $b = 5.689$   $c = 7.647$  as lattice parameters. However, the lattice can be approximated in pseudo-cubic notation where  $a_{pc} = b_{pc} = \sqrt{a^2 + b^2} = 3.90$  and  $c_{pc} = c/2 = 3.82$ . There are then two possibilities for the film orientation either the c axis is out of plane as in Fig. 4.8 (a) or in plane (c).

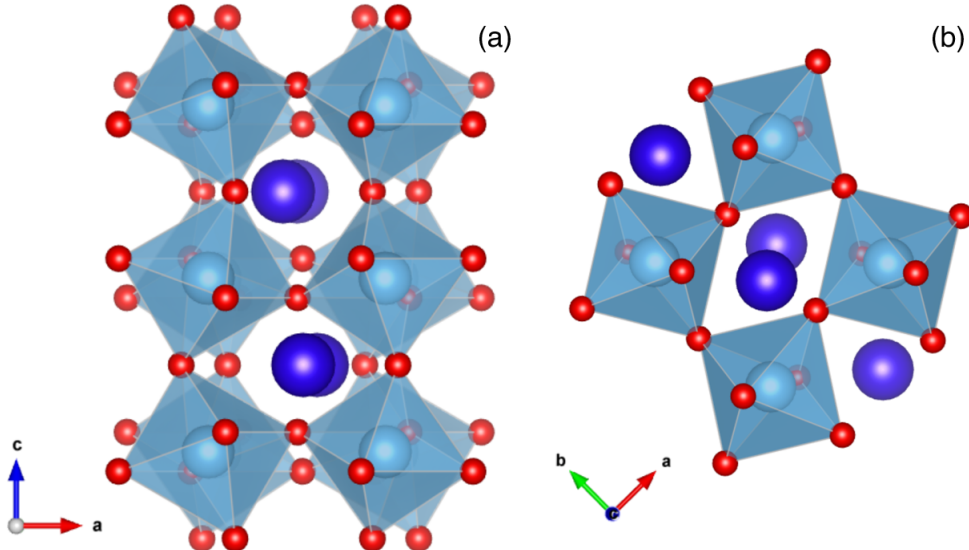


Figure 4.8: (a) Orientation of DTO with the *c* axis out of the substrate plan (b) Orientation of DTO with the *c* axis in the substrate plan.

One of the orientations will be "chosen" depending on the substrate in order to minimize the strain  $\epsilon = \frac{a_{\text{sub}} - a_{\text{film}}}{a_{\text{film}}}$  where  $a_{\text{film}}$  is either 3.82 and 3.89 in order to minimize  $\epsilon$ . Indeed, when we grow on DSO (110) and LAO (001) we can see a change from one configuration to the other ((a) to (b)).

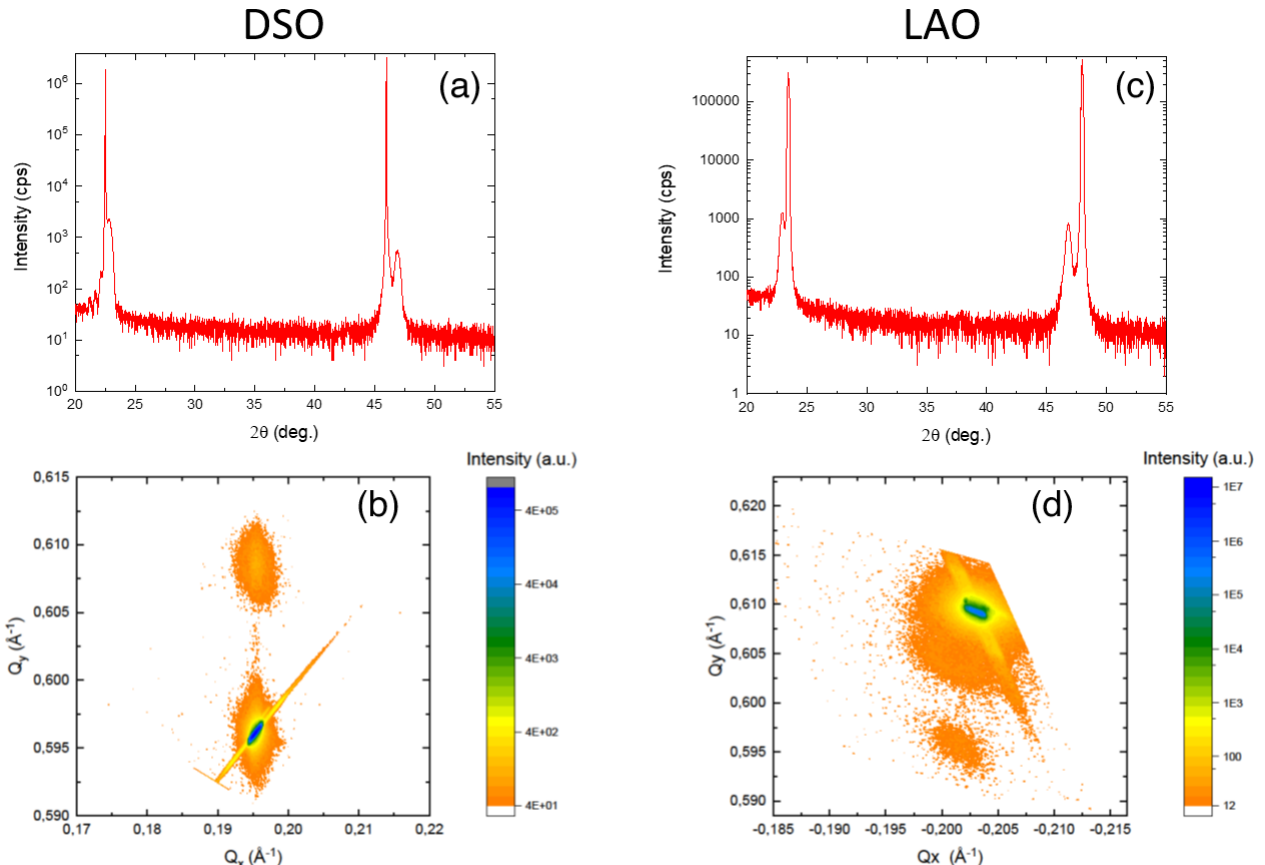


Figure 4.9: (a) X-ray  $2\theta$ - $\omega$  scan (b) RSM of DTO grown on DSO (110) ( $t=40$  nm)(c) X-ray  $2\theta$ - $\omega$  scan (d) RSM of DTO grown on LAO (001) ( $t=32$  nm).

We can see from the Fig. 4.9 (a) to (c) that the film peak is going from right to left from the substrate peak meaning that the strain goes from tensile to compressive. However, the calculations

of the out of plane parameter are consistent with the change of crystal orientation when changing substrate. This is further confirmed by the fact that the RSM Fig. 4.9 (b,d) shows that our film is strained on DSO thus putting aside the possibility of relaxation explaining the out of plane parameter value. The RSM on LAO (001) will be explained in the light of transmission electron microscopy later in section 5.4.2. The existence of two regions with different relaxations results in the presence of the two film peaks observed.

#### 4.2.2 Transmission electron microscopy characterization

In order to have better understanding of the crystalline quality of our films, we performed Transmission Electron Microscopy (TEM) at the Laboratoire de Physique des Solides (LPS) with the help of Alexandre Gloter and his team.

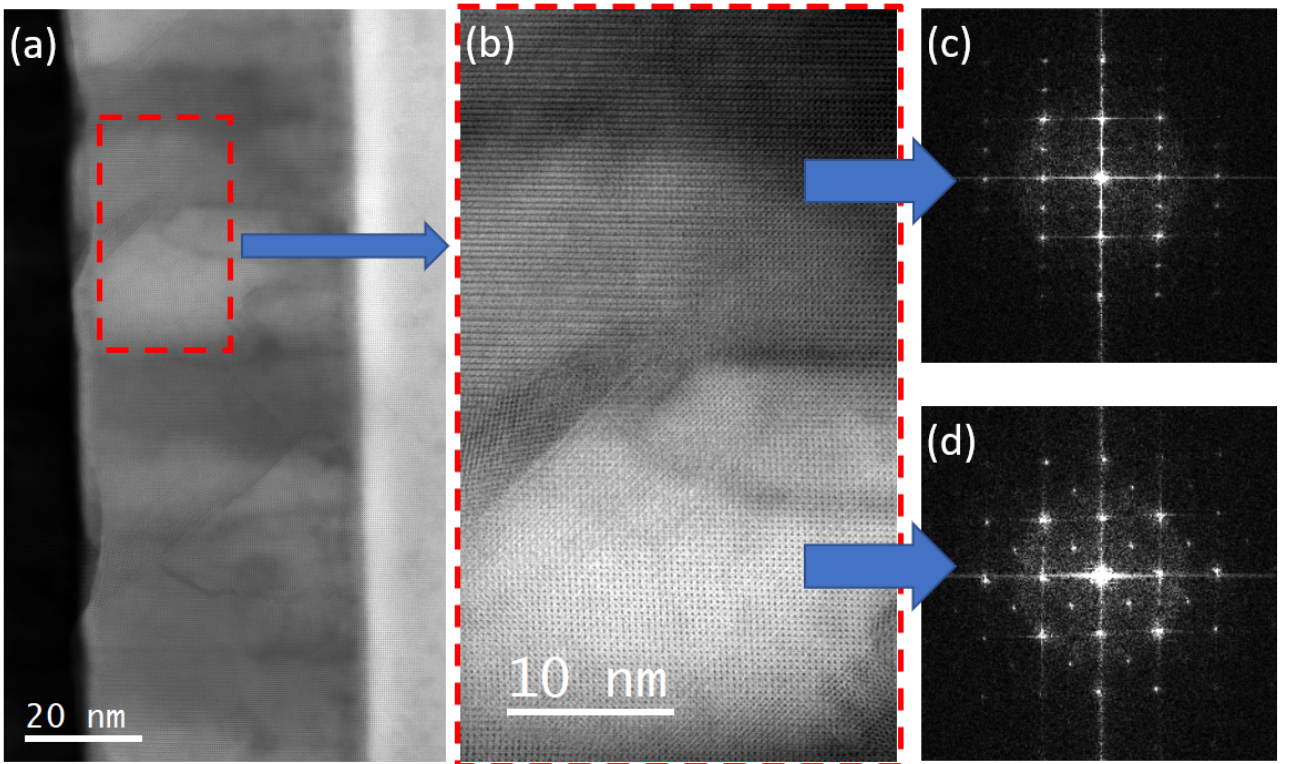


Figure 4.10: (a) Bright field picture of a 50 nm thick DTO film on LAO (001) (b) Zoom on the highlighted region of the previous picture (c) FFT of the upper part of the previous picture (d) FFT of the lower part of the previous picture.

We first noticed the presence of domains in Bright Field (BF) pictures. This detection mode increases the contrast between these regions, as shown in Fig. 4.10 (a), because of its sensibility to lighter elements. We can see in the zoom presented in Fig. 4.10 (b) that these color differences correspond to different orientations. As discussed in the previous section, two growth orientations are possible but since we grow on LAO here, we expect the c axis to be in the plane of the substrate. However, there is no reason to privilege having the c axis in one direction of the substrate plane or the other.

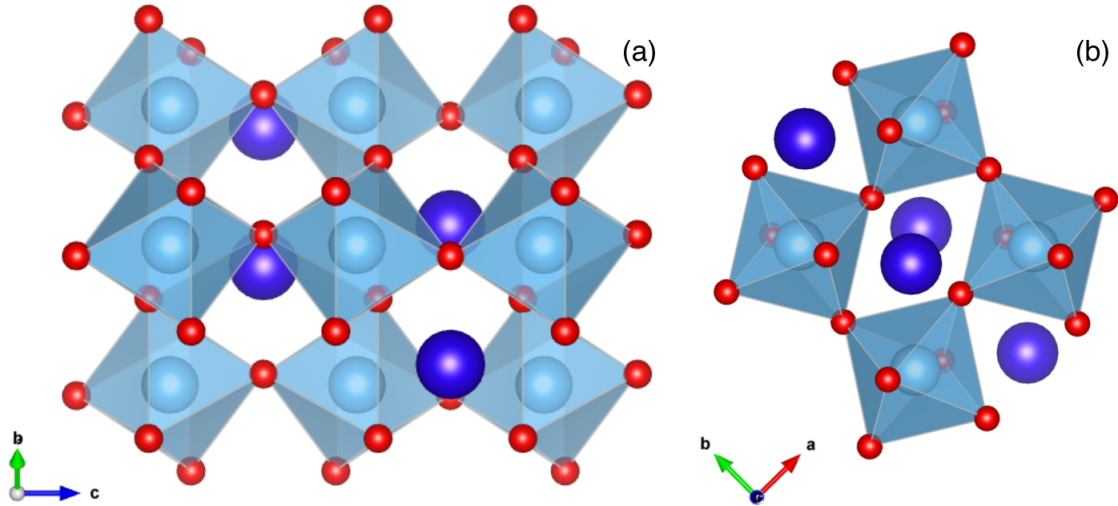


Figure 4.11: Crystal structure of DTO oriented with their *c* axis (a) along the lamella plane (b) perpendicular to the lamella plane.

As illustrated in Fig. 4.11, the *c* axis can either be in the plane of the TEM lamella or perpendicular to it. The top domain on Fig. 4.10 (b) clearly shows columns of atoms (titanium since we are in bright field) perpendicular to the film plane, whereas in the second type of domain those columns are tilted by 45 °. Considering this, we would associate them to the configuration of 4.11 (a) and (b) respectively. This is further confirmed by their Fast Fourier Transform (FFT). In order to understand these patterns, we can simplify the structure of Fig. 4.11 by considering only the titanium ions. The doubling of the periodicity along one direction seen in Fig. 4.10 (c) matches with the fact that true periodicity is reached along [110]<sub>DTO</sub> for twice the distance from which it is along [001]<sub>DTO</sub>. Fig. 4.10 (d) shows secondary periodicity peaks corresponding to the  $\left[\frac{1}{2}00\right]_{\text{DTO}}$  family of vectors.

Finally, we highlighted the presence of these domains by imaging them with intensity based on the characteristics spots associated with both domains as seen in the FFT of Fig. 4.10 (c,d).

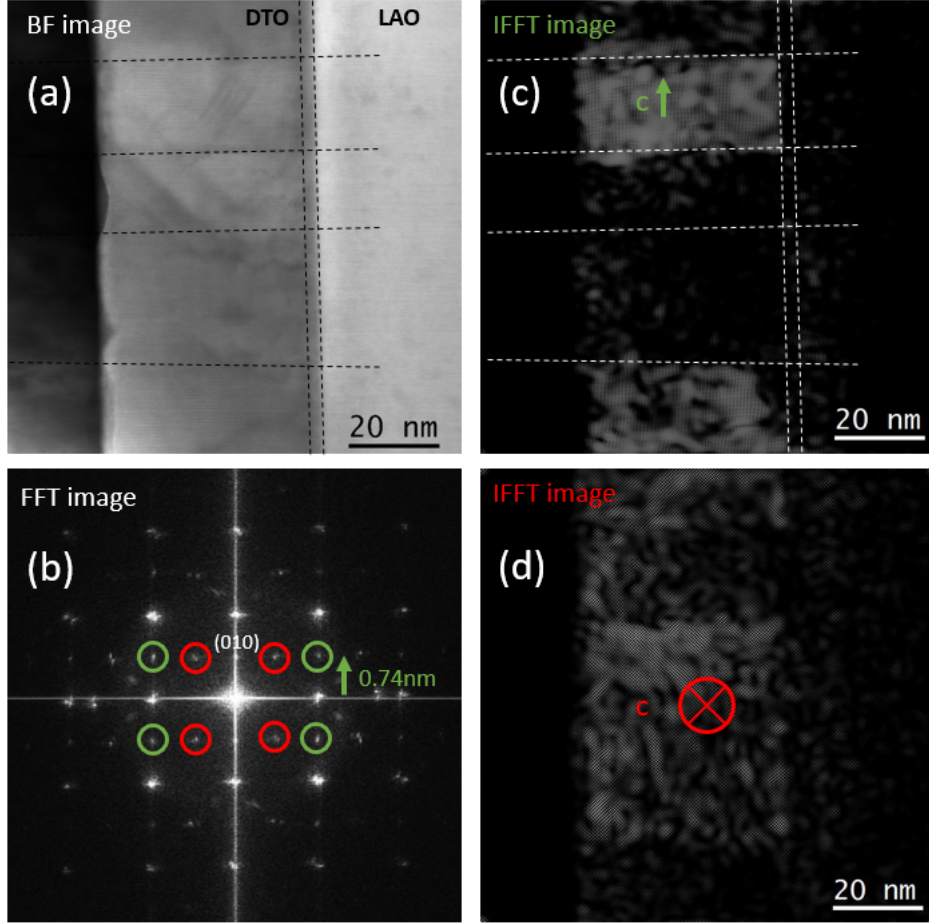


Figure 4.12: (a) Bright field (BF) image of the layer of Pt, DTO and LAO from (left to right and darker to lighter). (b) FFT image of the full DTO layer where the peaks corresponding to the different orientations in red and green. (c) Inverse FFT image obtained by using the peak highted in green corresponding to the c axis in the plane of the picture. (d) Inverse FFT image obtained by using the peak highted in red corresponding to the c axis perpendicular to the plane of the picture.

Here, on a different area we can see the same FFT as before in Fig. 4.10 (c,d). We follow the intensity of the peaks in red and green in Fig. 4.12 (b) which corresponds to the two different orientations. This allows us to produce a map showing the presence of the corresponding structure Fig. 4.12 (c,d), which overlaps well with the contrast from the bright field (BF). With this, we definitively link our two expected orientations with the contrast seen in TEM.

### 4.3 Living Dead Layer in $\text{DyTiO}_3$

During this part of the PhD, we changed the thickness of our films on a broad range using both growth methods established in section 4.1 in order to compare their merits.

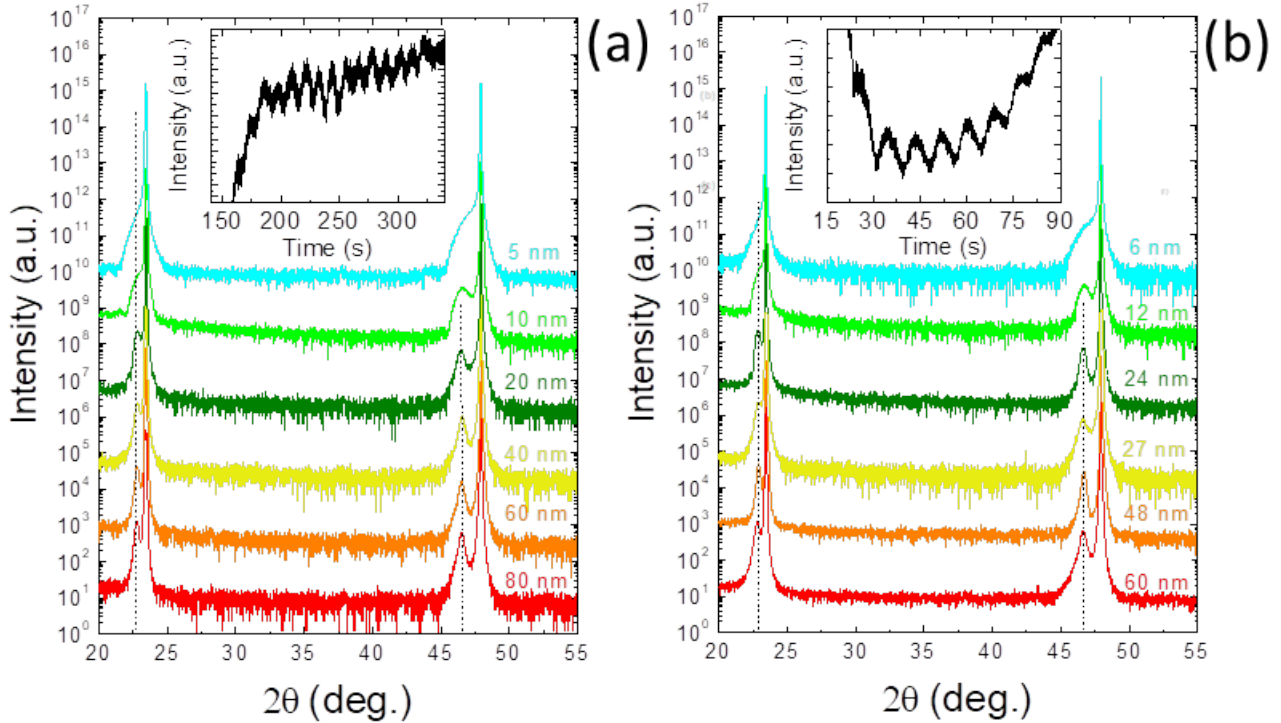


Figure 4.13: XRD thickness study (a) growths with argon at  $1 \times 10^{-3}$  mbar at 900 °C. (b) growths with oxygen at  $4 \times 10^{-7}$  mbar at 900 °C. The insets correspond to the RHEED oscillations obtained at the begin of growths performed in both conditions on LAO.

The sample grown for this study have a thickness varying from 5 to 80 nm and according to the scans, they are free from parasitic phases. Nevertheless, if the scans look rather similar, the Ar growths Fig. 4.13 (a) seems to have a better crystallinity. This difference will be further supported by the measured done in this section.

#### 4.3.1 Thickness dependence of the magnetic properties

While checking the structure of the sample, we measured their magnetic properties by using an MPMS SQUID magnetometer. We measure the magnetization as a function of field Fig. 4.14 (a) and temperature Fig. 4.14 (c). We first noticed that, for the thickest samples, we obtained a magnetic response similar to the bulk DTO Fig. 3.4.

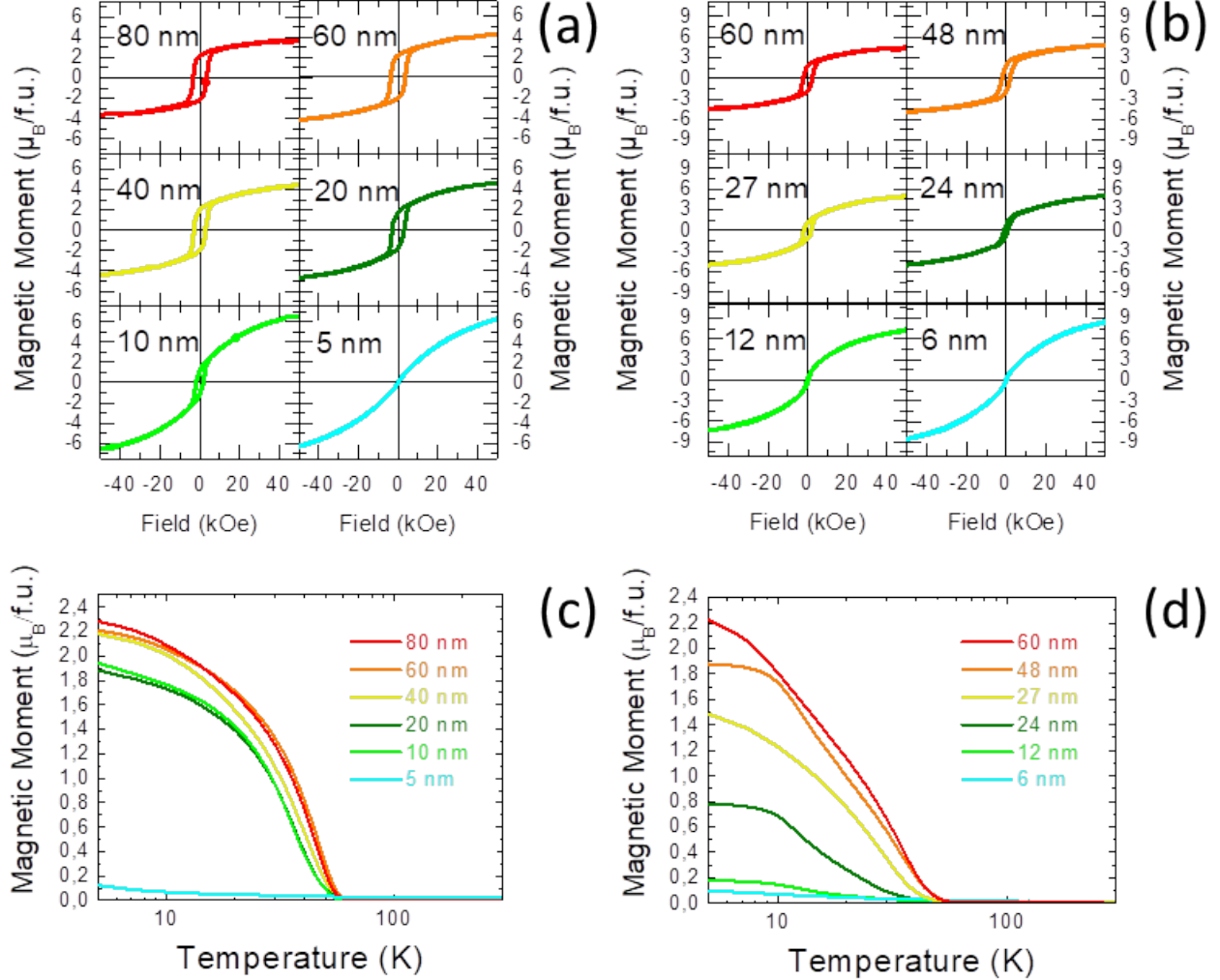


Figure 4.14: SQUID thickness dependence study: (a,c) respectively magnetic moment as a function of the field at 10 K and temperature at 100 Oe of samples grown in  $1 \times 10^{-3}$  mbar of argon (b,d) respectively magnetic moment as a function of the field at 10 K and temperature at 100 Oe of samples grown in  $4 \times 10^{-7}$  mbar of oxygen.

We first see that the improvements due to the use of argon also apply to the magnetic properties ( $T_C$ ,  $M_{\text{sat}}$  and  $H_C$ ). The  $T_C$  is a lot more consistent with the thickness and drops suddenly at what appears to be a critical thickness in the case of growth in argon. Overall, the ferrimagnetic character seems to be stronger in the samples grown in argon<sup>3</sup>.

The hysteresis cycles for both growth conditions show an interesting trend as a function of thickness. The squareness of the cycles decreases in both cases and the general shape seems to tend toward a paramagnetic cycle. Most striking, the  $M_{\text{sat}}$  for the thinner samples get above the nominal value of  $3.7 \mu_B$  up to  $6 \mu_B$ . We attribute this behavior to the emergence of a paramagnetic signal, which develops itself at the expense of the ferrimagnetic phase and has a higher moment.

We summarized the relevant magnetic quantities in the following figure.

<sup>3</sup>The inflection points seen in the Fig. 4.14 (d) should not be consider as such and are in fact sampling artifact

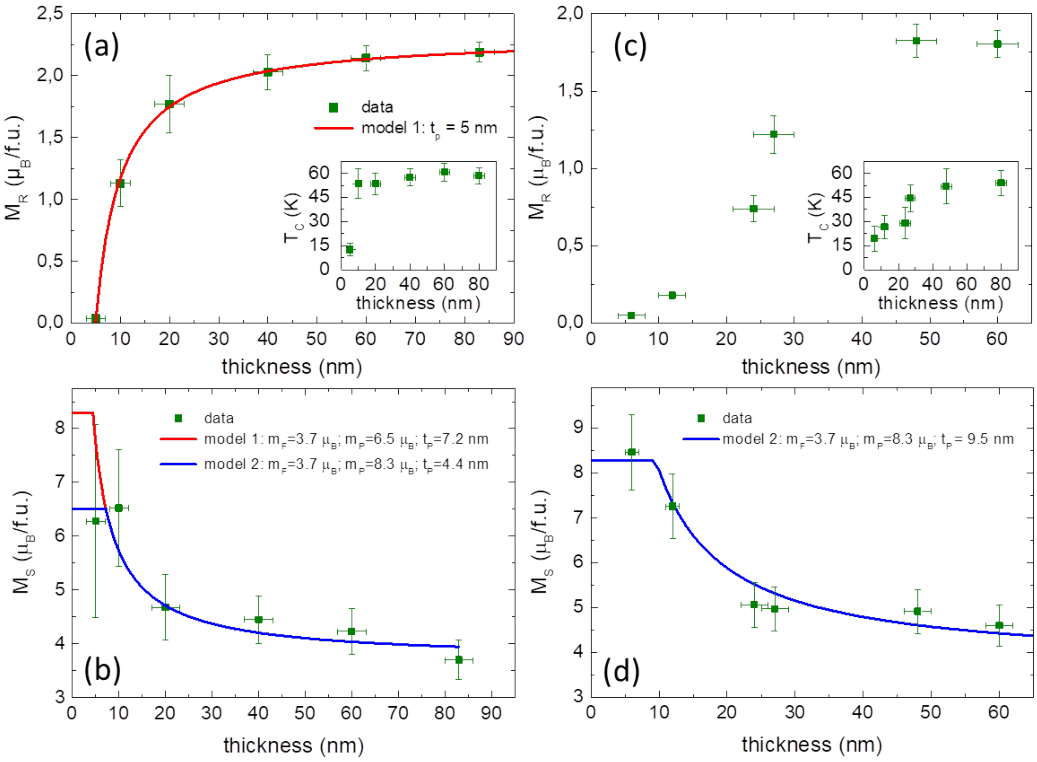


Figure 4.15: SQUID thickness study: (a,c) respectively remnant magnetization and magnetization at saturation as a function of the thickness of samples grown in argon at  $1 \times 10^{-3}$  mbar (b,d) respectively remnant magnetization and magnetization at saturation as a function of the thickness of samples grown in oxygen at  $4 \times 10^{-7}$  mbar.

In Fig. 4.15 (a,c), we see that  $M_R$  and  $M_{\text{sat}}$  seem to follow an inverse law as a function of the thickness. However, if  $M_R$  decreases at lower thickness, the saturation magnetization increase. This behavior is at odds with the situation of ferromagnetic where the decrease of  $M_R$  and  $M_{\text{sat}}$  are concomitant. In classical itinerant ferromagnets or double-exchange systems such as manganites [92], the reduction of the saturation magnetization in ultrathin films has been modeled using the so-called dead-layer picture. In this model, we assume that a non-magnetic layer exists at the interface with the substrate. Since the behavior of  $M_{\text{sat}}$  is incompatible with this picture, we postulate the presence of a nonferromagnetic magnetically active layer what choose to call a "living dead layer". From the shape of the MvH loops and the high saturation magnetization, we can conclude that the living dead layer is paramagnetic with a high paramagnetic moment. To fit the data, we used a simple bilayer model (ferrimagnetic and paramagnetic).

$$M_{\text{total}} = m_{\text{total}} \cdot t = m_P \cdot t_P + m_F \cdot t_F \quad (4.1)$$

$$m_{\text{total}} = \frac{(m_P - m_F)t_P}{t} + m_F \quad (4.2)$$

where  $t = t_P + t_F$  the total thickness,  $t_P$  the thickness of the paramagnetic layer,  $t_F$  the thickness of the ferrimagnetic layer,  $m_F$  the moment per unit volume of the ferrimagnetic layer, and  $m_P$  the moment per unit volume of the paramagnetic layer.

We used the DTO bulk value of  $3.7 \mu_B$ /f.u. [4] for  $m_F$  and focused on the samples grown in pure Ar. Setting  $m_P$  to the maximum magnetization of the thinnest sample ( $m_P \simeq 6.5 \mu_B$ ) and using  $t_P$  as a fitting parameter (model 1) yields a high fit quality ( $\chi^2 = 1 \times 10^{-9}$  and a reduced chi square of 0.43 validating our error bars), with  $t_P = 7.2$  nm, Fig. 4.15 (b). A dead layer thickness of 5 nm is obtained by fitting the remnant magnetization, Fig. 4.15 (a) (since  $m_P = 0 \mu_B$  at zero field). We also performed another fit using  $m_P \simeq 8.7 \mu_B$  because it corresponds to the magnetization obtained for a layer of pure paramagnetic  $Dy^{3+}$  at 5 T and obtained  $t_P = 4.4$  nm. These two thicknesses are respectively the upper and the lower limit for the thickness of this so-called "living-dead" layer. For the  $O_2$  grown films, the fit of  $M_R$  (not shown) is not very good, possibly reflecting a progressive reduction of the anisotropy in the ferrimagnetic layer when decreasing thickness.

We still need to understand the origin of the "living-dead" layer and in order to have a closer insight, we performed x-ray spectroscopy to track composition and valence changes at different depths.

#### 4.3.2 XPS and XAS depth analysis

In this section, we used XPS, XAS in TEY, TFY and XEOL detection modes as ways to probe our sample. With both techniques we can change the probing depth, by changing the collection angle in XPS and by using the different detection modes in XAS.

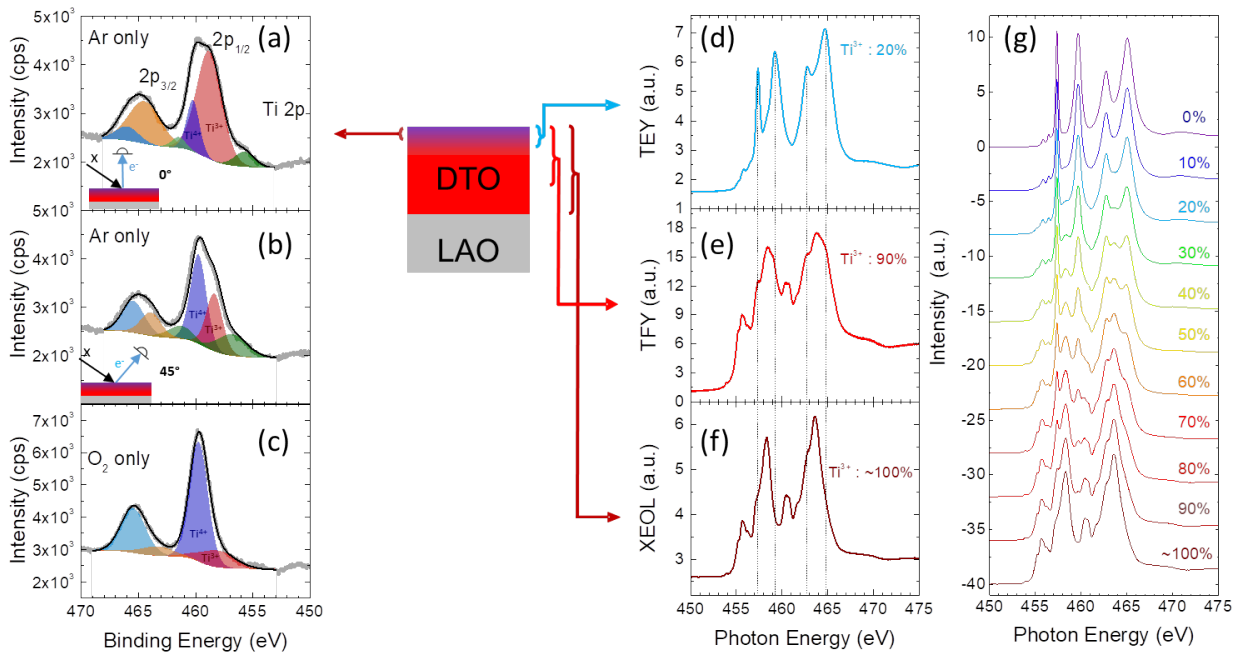


Figure 4.16: (ac) XPS spectra of the Ti 2p core levels in 20 nm DTO films grown in Ar (a,b) and in oxygen (c), at normal emission (a,c) and a 45° emission (b). (df) XAS at the Ti L<sub>3,2</sub> edge at room temperature in a 80 nm DTO film grown in pure Ar, collected in TEY mode (d), TFY mode (e), and XEOL mode (f). The dotted lines guide the eye to the position of the four main peaks present in (d). (g) Linear combinations of XAS spectra between a reference  $Ti^{4+}$  spectrum and a reference  $Ti^{3+}$  spectrum (see text for details). Percentage refers to  $Ti^{3+}$  fraction.

In Fig. 4.16 (a-c), we plot XPS spectra of Ti 2p core levels for two 20 nm samples one grown in argon Fig. 4.16 (a,b) and in oxygen Fig. 4.16 (c). The Ti 2p are divided into  $2p_{1/2}$  and  $2p_{3/2}$  due to spin orbit coupling. However here we see that these peaks contain two main components corresponding to  $Ti^{4+}$  (shaded in blue) and another to  $Ti^{3+}$  (shaded in red) at higher and lower binding

energies, respectively. A third, minor component, possibly corresponding to  $\text{Ti}^{2+}$  (in green) is also visible [39, 40]. By evaluating the area of the fitted peaks, we can obtain the 3+/4+ ratio of the probed part of the film. At normal emission Fig. 4.16 (a), the 3+/4+ ratio is 80:20 and decreases to 39:61 at 45° emission Fig. 4.16 (b). By changing the collection angle, we probe less of the sample, thus this quite surprisingly means that the valence deviation happens at the surface of the sample unlike the classical dead layer. Following [93], we estimate that the equivalent thickness of the  $\text{Ti}^{4+}$  surface layer is about 1.3 nm. Finally, if we look at the sample grown in  $\text{O}_2$ , suggests a larger proportion of  $\text{Ti}^{4+}$  (3+/4+ ratio is  $\simeq 20:80$ ), in line with the more degraded magnetic response of films grown in  $\text{O}_2$  in this thickness range.

More insight into this depth dependence of the Ti valence state is provided by XAS at the  $\text{Ti L}_{3,2}$  edge on an 80 nm film. The TEY, TFY and XEOL respectively probe 2-5 nm, 20-50 nm and the full thickness is probed. The spectrum obtained in TEY the four same features as in  $\text{SrTiO}_3$  [94] (where titanium is 4+), with albeit some noticeable differences in line shape and intensities. We used the TFY to probe deeper into the sample and detect the development of new components seemingly corresponding to lower energy counter-part to the TEY components [95, 96]. We interpret this as the signature of  $\text{Ti}^{3+}$  ions for which XAS features shift to lower photon energies due to the smaller binding to the 2p levels and present a richer multiplet structure due to the splitting of the  $t_{2g}$  and  $e_g$  states, expected for a 3d<sup>1</sup> configuration. Finally, the XEOL spectrum (Fig. 4.16 (f)) suggests the presence of an almost pure 3+ state, [76, 86, 97] very rarely reported in the literature on rare-earth titanates (presumably because most XAS experiments used TEY detection and thus only probed the  $\text{Ti}^{4+}$  rich dead layer at the surface [98]). Finally in Fig. 4.16 (f), we plot linear combinations of a reference spectra of  $\text{Ti}^{4+}$  (from a  $\text{SrTiO}_3$  substrate) and the XEOL spectra used as a  $\text{Ti}^{3+}$  reference. We considered the XEOL signal to correspond to a fully 3+ situation because of the ratio between the "living-dead" layer and the full thickness is 5:80 meaning the XEOL measure in fact 94% of 3+. This overall confirms the existence of a  $\text{Ti}^{4+}$  gradient seen in XPS.

#### 4.3.3 Establishment of a link between titanium valence and magnetic properties

Now that we have seen the presence of a layer of  $\text{Ti}^{4+}$  at the surface we need to formally link it to the so-called "living dead" layer seen in the magnetic data. To achieve this, we mixed the two previous measurements, on the one hand the magnetic measurement as a function of field and on the other hand the element specificity allowed by spectroscopy. For this purpose, we used XRMS (X-ray Resonant Magnetic Scattering), a technique described in section 2.6.4, that allows us to measure dichroism as a function of the field. The measured hysteresis cycles are thus element specific. We measured the dichroism at the titanium  $\text{L}_3$  edge and the dysprosium  $\text{M}_5$  edge.

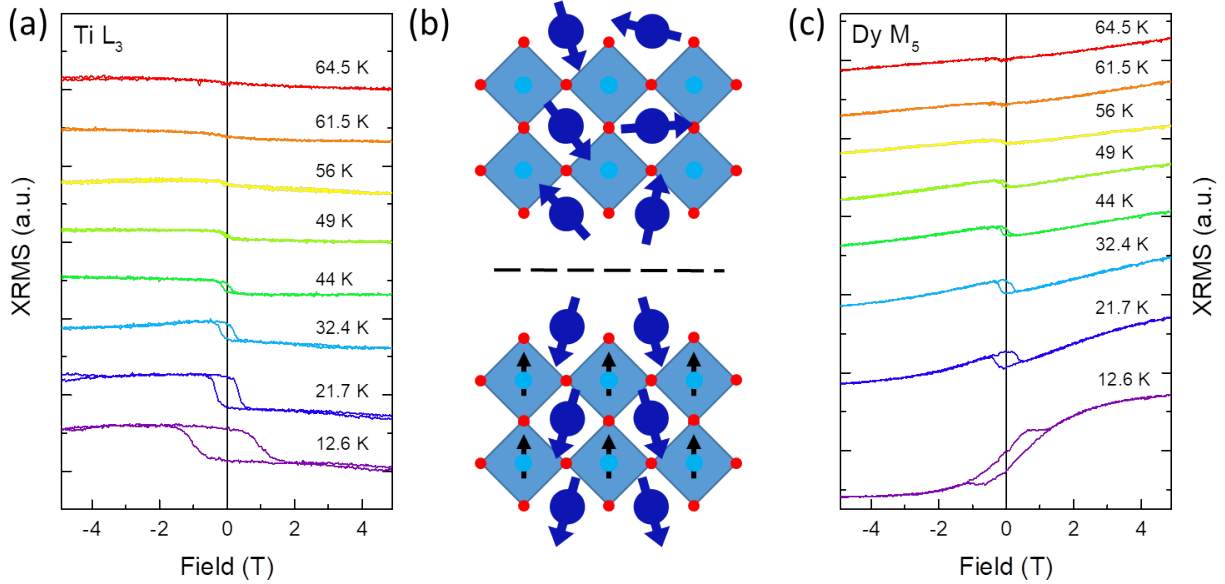


Figure 4.17: (a,c) Magnetic field dependence of the XRMS signal at the Ti L<sub>3</sub> edge (a) and Dy M<sub>5</sub> edge (c), at different temperatures, for an 80 nm DTO film grown in Ar. (b) Sketch of the magnetic order near the surface (top), where Ti is 4+, carries no magnetic moment, and Dy is paramagnetic and deeper in the film (bottom), where Ti is 3+ and the Ti and Dy moments show a canted ferrimagnetic order.

Both elements in Fig. 4.17 (a,c) present a hysteresis cycle at low temperature after a transition around 60 K which agrees with the SQUID data for thick samples. This observation supports the globally ferrimagnetic magnetic order of DyTiO<sub>3</sub> observed in refs [72, 61] (see the bottom sketch in Fig. 4.17 (b)). If the titanium cycle seems to correspond to a purely ferromagnetic response, the one of dysprosium shows a superposition of a ferromagnetic and a paramagnetic response. We can thus assume the paramagnetic signal seen in SQUID comes in fact from Dy<sup>3+</sup> ions that are not coupled to titanium in the layer were the valence is Ti<sup>4+</sup>. Coupling being impossible with a 3d<sup>0</sup>, the dysprosium moments are thus paramagnetic. Supporting the connection between the two phenomena notice that the "living dead" layer is about the sample size as the evaluated thickness of the Ti<sup>4+</sup> surface.

#### 4.3.4 Origin of the "living-dead" layer

Thus, we can with a certain degree of confidence say that the magnetic phenomena observed in section 4.3.1 are in fact due to a titanium valence offset near the surface of the sample. The change of oxidation degree of titanium could be caused by an overoxidation of our sample at the surface. However, the Fig. 4.13 showed no **ordered** parasitic phase can be seen. The oxygen can then come only from the very surface. These oxygens are said to be apical meaning that they sit at the top of the incomplete octahedra (in the case of TiO<sub>2</sub> termination) turning effectively a thickness of two unit cells into Ti<sup>4+</sup> as explained in [76]. Nevertheless, this explanation does not work here since our layer is 6 nm thick. It leaves us with the possibility of a phase with higher oxidation degree for titanium but without spatial coherence. The two main possibilities would be random Ruddlesden-Poppers phase ( $R_{n+1}Ti_{n+1}O_{3n+1}$ ) or the insertion of excess oxygen the tetrahedral interstitial sites [84]. Xu suggests in his work that NbTiO<sub>3</sub> would absorb oxygen until it reaches a composition of NbTiO<sub>3.5</sub> corresponding to fully 4+ titanium, with one oxygen turning two titaniums into 4+.

Calculation in the supplementary material of [84] has shed light on the importance of interstitial oxygens in these system. However, they are far less studied than oxygen vacancies and no direct evidences of their presence exist in the litterature. Nevertheless, the results shown in this PhD work point toward the presence of shear planes host the excess oxygen atoms thank to A. Gloter and L. Cambou.

#### 4.3.5 Spatial investigation of the "living-dead" layer

As a last step of this "living dead" layer study, our collaborators A. Gloter and L. Cambou investigate its spatial distribution directly. In order to do this, we measured Electron Energy Loss Spectroscopy (EELS) spectra in TEM.

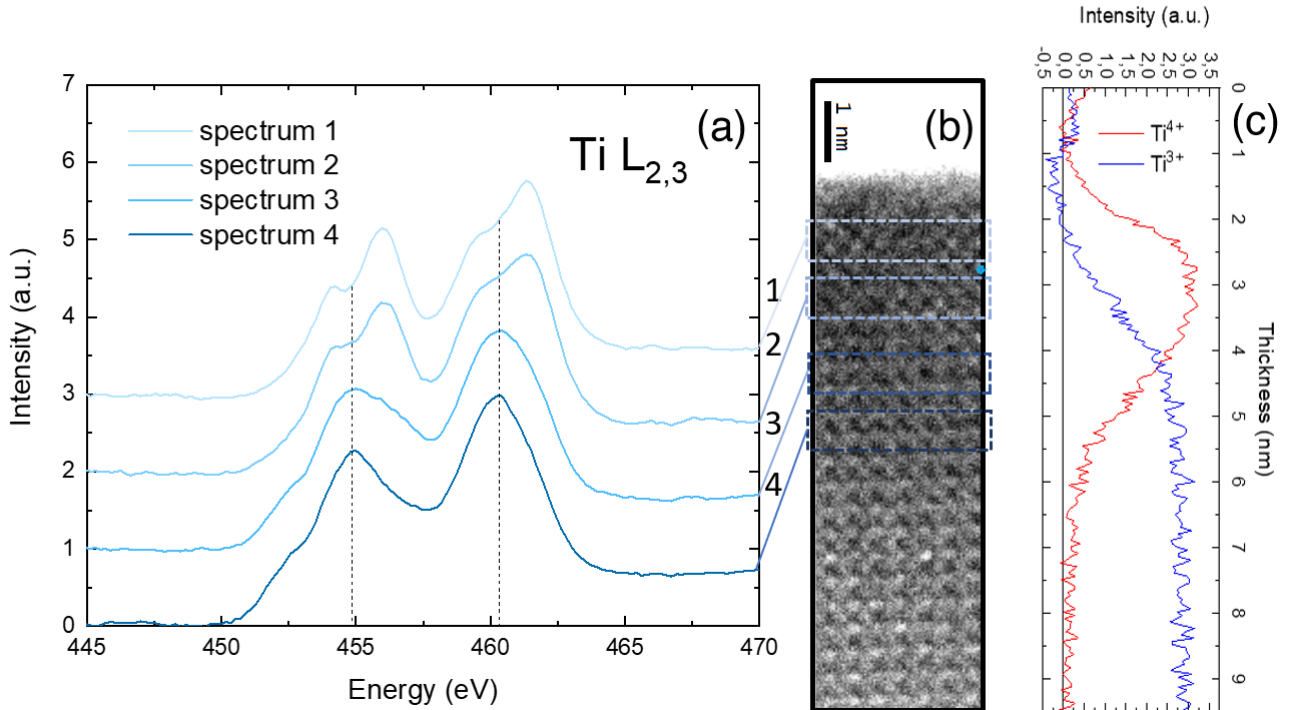


Figure 4.18: (a) EELS spectra at the Ti  $L_{2,3}$  edge on obtained on four different areas shown in the dark field picture (b). (c) Titanium 4+ and 3+ profile obtained by measuring the proportion of purely 4+ and 3+ spectra as function of the distance to the interface.

We measure the EELS spectra at the titanium  $L_{2,3}$  edge on four different regions going away from the interface Fig. 4.18 (b). We see in Fig. 4.18 (a) that the shape of these spectra continuously changes from a spectrum 1 to a spectrum 4 that respectively closely resemble to the TEY and XEOL spectra of Fig. 4.16 (d,f). By quantifying the proportion of these spectra as a function of the thickness, we obtain a  $\text{Ti}^{4+}$  profile that confirms our previous model. Indeed, we obtain an equivalent thickness of "living dead" layer of around 5 nm which properly fits in our error bars, between 4.4 and 7.2 nm for the two sets of parameters of the  $M_S$  and perfectly agree with the  $M_R$  model at  $t_P = 5$  nm.

#### 4.3.6 Resurrection of the "living-dead" layer

Knowing the origin of the living dead layer, two solutions are available to us, first finding even more reducing condition for our growth or a post growth treatment. We found out that the more reducing condition **at the time** (before the development of the argon growth method) was to use the effect of

the background pressure on the plume chemistry. The other option is to cap our samples in reducing condition in order to protect their surface.

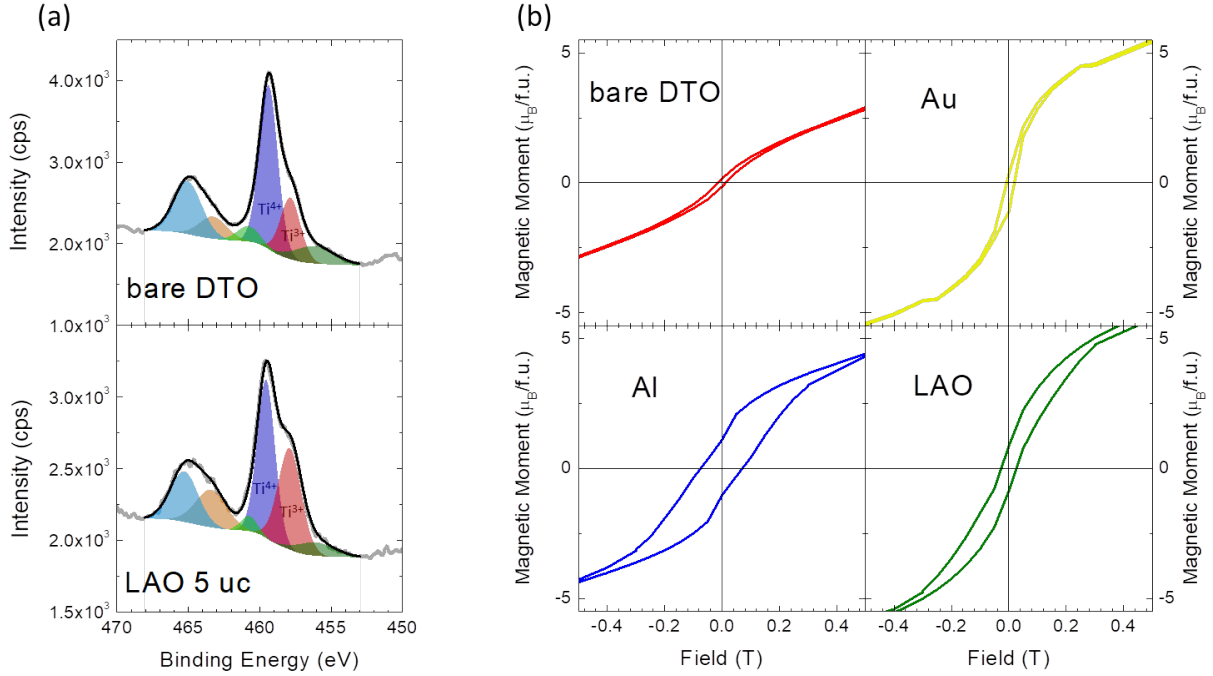


Figure 4.19: (a) XPS spectra of the Ti 2p core levels for a 10 nm DTO film, before (top) and after (bottom) capping with five unit cells of LAO. (b) Magnetic hysteresis cycles at 10 K of 10 nm DTO films uncapped, and capped with different 30 nm-thick materials.

In order to highlight the effect of the capping layers, we started from a DTO film of 10 nm with high Ti<sup>4+</sup>/Ti<sup>3+</sup> ratio. In such a way we hoped to see a more dramatic effect at low field. In Fig. 4.19 (a) we observed the effect of the addition of 5 u.c. of LAO on top of DTO by measuring the Ti 2p levels seen in XPS.

In Fig. 4.19 (a), we compare the XPS response of the DTO film right after growth, and of the very same film after in situ capping. We see that the 3+ components of the titanium 2p levels are enhanced by the addition of 5 u.c. of LAO; we estimate that the 3+/4+ ratio increases from 29:71 to 45:55. To see a clear effect on the magnetic properties, we grew a similar sample with a 30 nm LAO capping layer, and also studied films with 30 nm Au and Al caps. Fig. 4.19 (b) shows a clear improvement of the ferrimagnetic properties of the DTO capped with the reducing materials (LAO and Al), with a much higher remanent magnetization, and a lower magnetization at 5 T. Both Al and LAO are reducing materials and it is thus expected that the excess of oxygen at the interface with DTO will be partially diminished. On the contrary, Au, a noble metal, does not have such a strong effect. These results suggest that a reducing process takes place to restore the right valence state to titanium.

## 4.4 Growth and properties of other rare earth titanates ( $\text{GdTiO}_3$ , $\text{YTiO}_3$ and $\text{TmTiO}_3$ )

After optimizing the PLD growth of DTO films, we transposed those recipes to the growth of other titanates. Under the same conditions, YTO, GTO and TTO films showed similar structural quality comparable to that of DTO films..

### 4.4.1 Structural study

If the RHEED patterns look similar to the one of DTO, the growth speed could vary even at fixed fluence and conditions. This has to be expected because of the variation of target quality (mainly of the density). However, we noticed that the smaller the "rare-earth" radii, the wider the growth window is. The growth of YTO can, for example, be achieved at lower temperature of 700 °C.

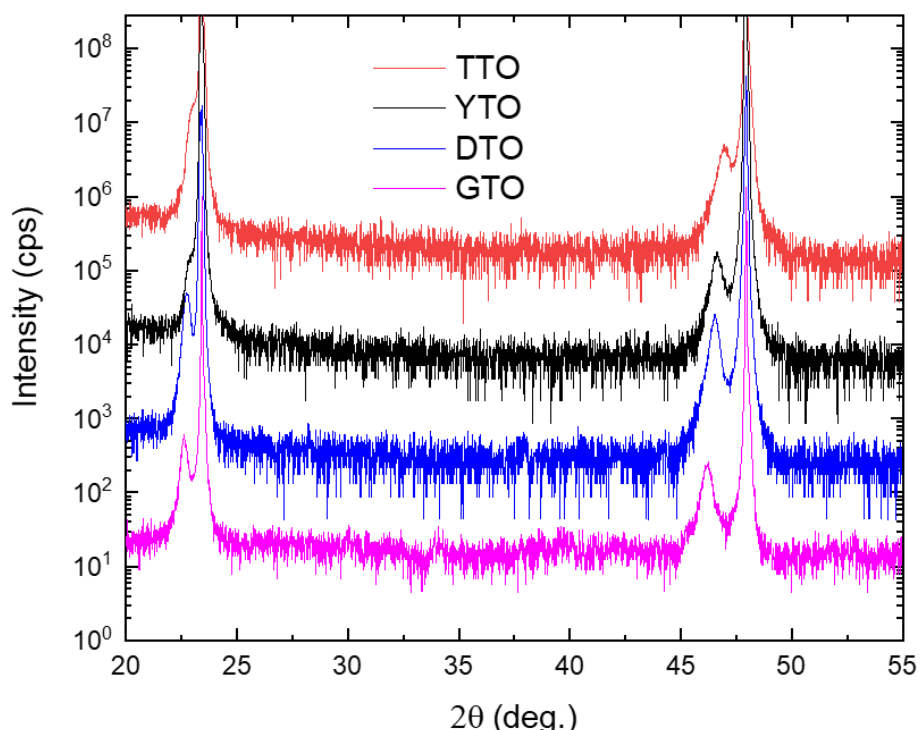


Figure 4.20: XRD  $2\theta - \omega$  scans of GTO, TTO, YTO and DTO samples with thickness ranging from 45 to 55 nm. All samples are grown in  $1 \times 10^{-3}$  mbar of Ar at 900 °C.

The absence of parasitic phase indicates that the growth conditions established before are still valid for the rest of the family.

### 4.4.2 Valence state

If the phase purity is not the same as for DTO, we can nevertheless test the universality of the "living-dead" layer in the rare earth titanates.

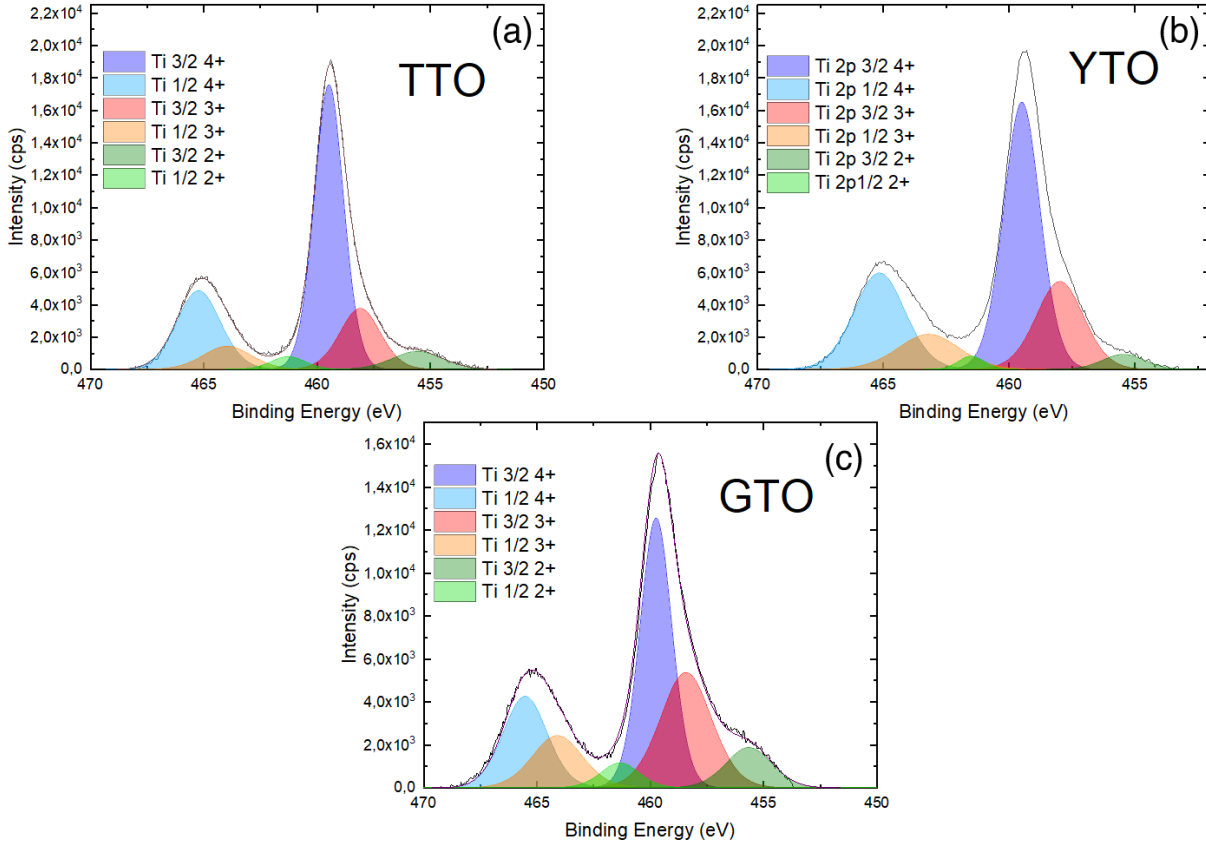


Figure 4.21: XPS titanium 2p core levels of TTO (a), YTO (b) and GTO (c). These films are 10 nm thick and have been grown in  $1 \times 10^{-3}$  mbar of argon at 900 °C.

In Fig. 4.21, we performed the same XPS analysis of the 2p core levels of titanium as in Fig. 4.16. In the same way, we observe the presence of titanium 4+, 3+ and 2+ components following the proportions presented below:

The proportion of different valence states of titanium extracted from the area of the fitted Voigt function. These presented values are the average of the data from Ti 2p 1/2 and 3/2. The results appear similar to the one obtained on DTO. The difference in ratio between TmTiO<sub>3</sub>, YTiO<sub>3</sub> and GdTiO<sub>3</sub> could be explained by variation of the growth condition such as target quality, variation of parameters and the time spent between the end of the growth and the XPS measurement.

	TmTiO <sub>3</sub>	YTiO <sub>3</sub>	GdTiO <sub>3</sub>
4+ (%)	70.05	66.60	52,75
3+ (%)	21.67	16.74	35,26
2+ (%)	8.29	4.50	11.99

Table 4.1: Proportion of different valence states of titanium.

#### 4.4.3 Magnetic properties

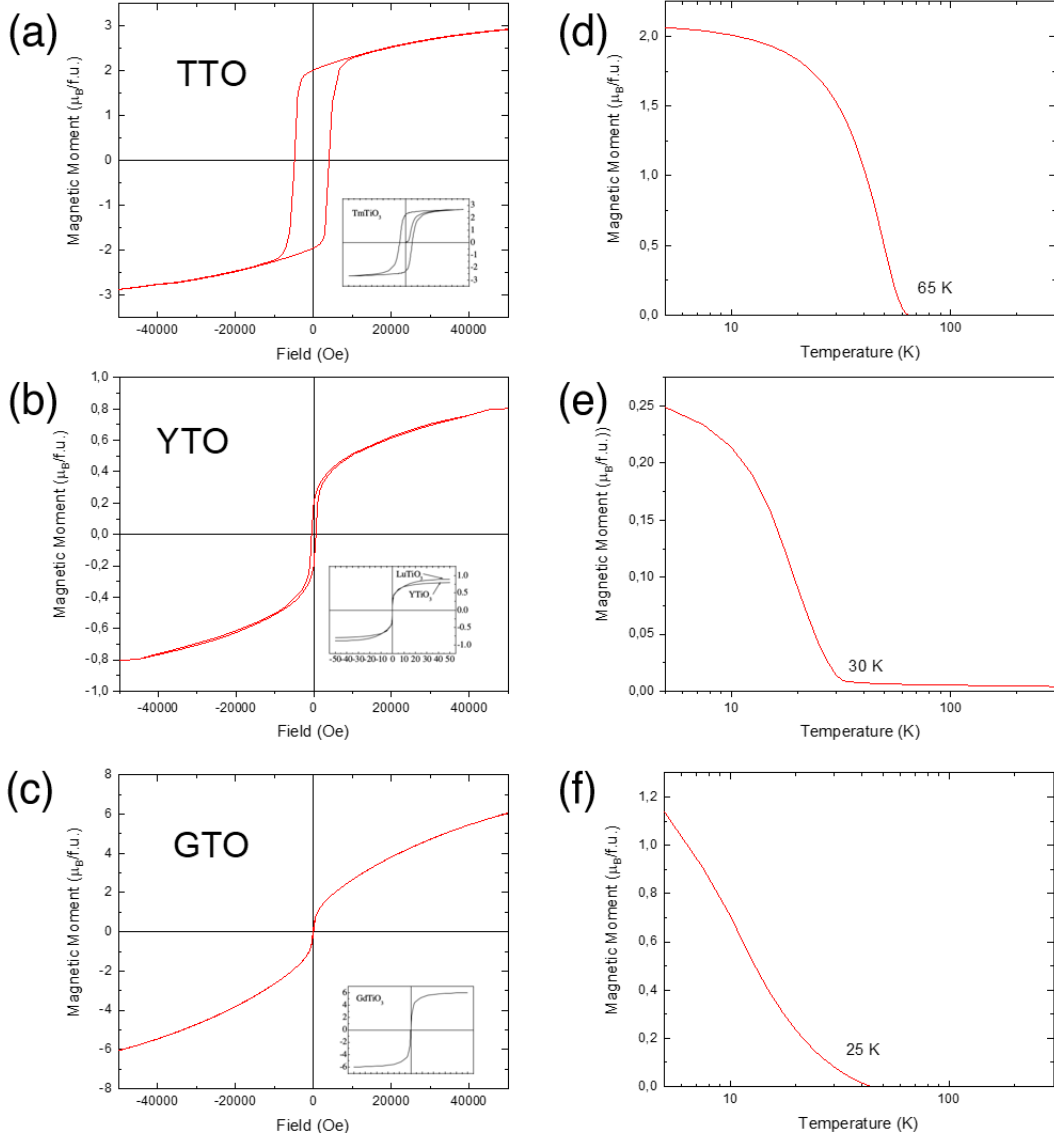


Figure 4.22: Magnetization hysteresis cycles of TTO (a), YTO (b) and GTO (c) obtained at 10 K. Magnetization as a function of temperature of TTO (d), YTO (e) and GTO (f) obtained at 100 Oe. These films are 80 nm thick and have been grown in  $1 \times 10^{-3}$  mbar of argon at 900 °C. For comparison, the insets on each figure present the bulk measurement extracted from [4].

In Fig. 4.22, we can see the magnetization as a function of the field and the temperature of TTO, YTO and GTO. Overall, the magnetic parameters such as  $M_R$ ,  $M_{\text{sat}}$  and  $T_C$  are in good agreement with the bulk sample literature [4]. We can however notice a decrease in the transition temperature of GTO that we impute to the target quality.

## Chapter 5

# X-ray circular dichroism at the Ti L<sub>3,2</sub> edge in rare-earth titanate thin films

In section 4.3.2 we looked at the titanium edge with three detection modes i.e. TEY, TFY and XEOL but we also measured the absorption with two opposite circular polarizations to quantify the X-ray magnetic circular dichroism (XMCD). We obtain a quite intense dichroic signal at the L<sub>2,3</sub> edge which is a rare feature in the literature due to the difficulty in stabilizing the Ti<sup>3+</sup> state.

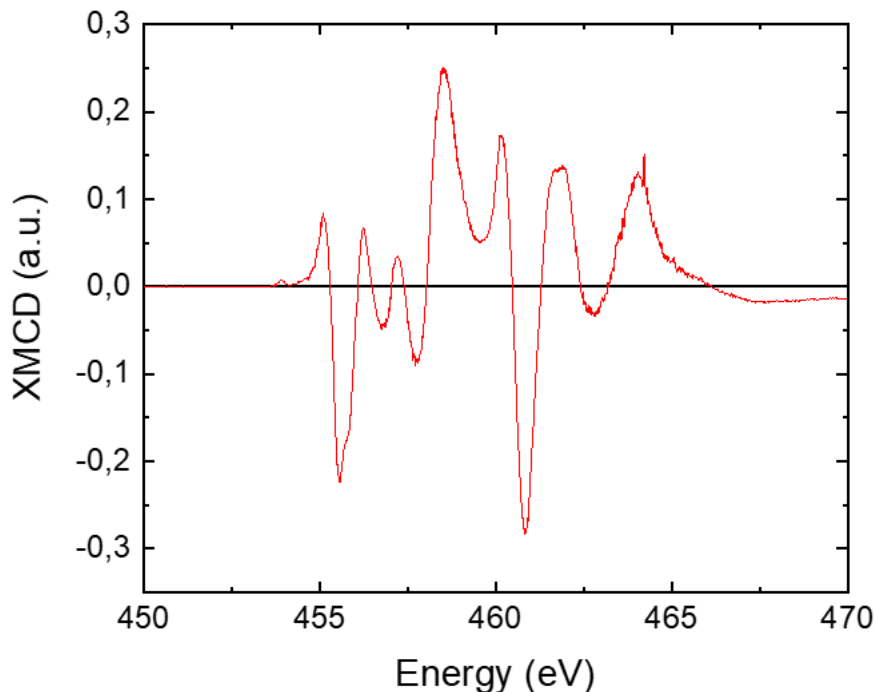


Figure 5.1: XMCD spectrum obtained on DyTiO<sub>3</sub> 80 nm by XEOL.

One of the first XMCD spectrum obtained is presented in Fig. 5.1. We can see a strong dichroic signal of nearly 10 % but one should keep in mind that this signal is almost raw data hence with the visible noise. In the following section, we will present how we refine the data in order to obtain trustworthy physical information.

During the processing of the data we noticed a new feature compared to [99]: the integral of

the XMCD signal of Ti L<sub>2,3</sub> edge does not vanish. As we will explain in the following sections, the existence of a non-zero integral hints at the presence of an unexpected non-zero orbital moment on the titanium. This chapter will explain why we are not expecting titanium to have any orbital moment, the methodology of the analysis of the XAS and XMCD signal, and finally propose some possible mechanism to explain the phenomenon.

## 5.1 Data analysis and experimental results on DyTiO<sub>3</sub> thin films

XAS data has proven to be the most complicated data analysis present in this thesis. As described in section 2.6.4, one can think that an XMCD signal is simply the subtraction of spectra obtained by left and right circularly polarized light but different experimental factors induce a lot of constraints on its analysis.

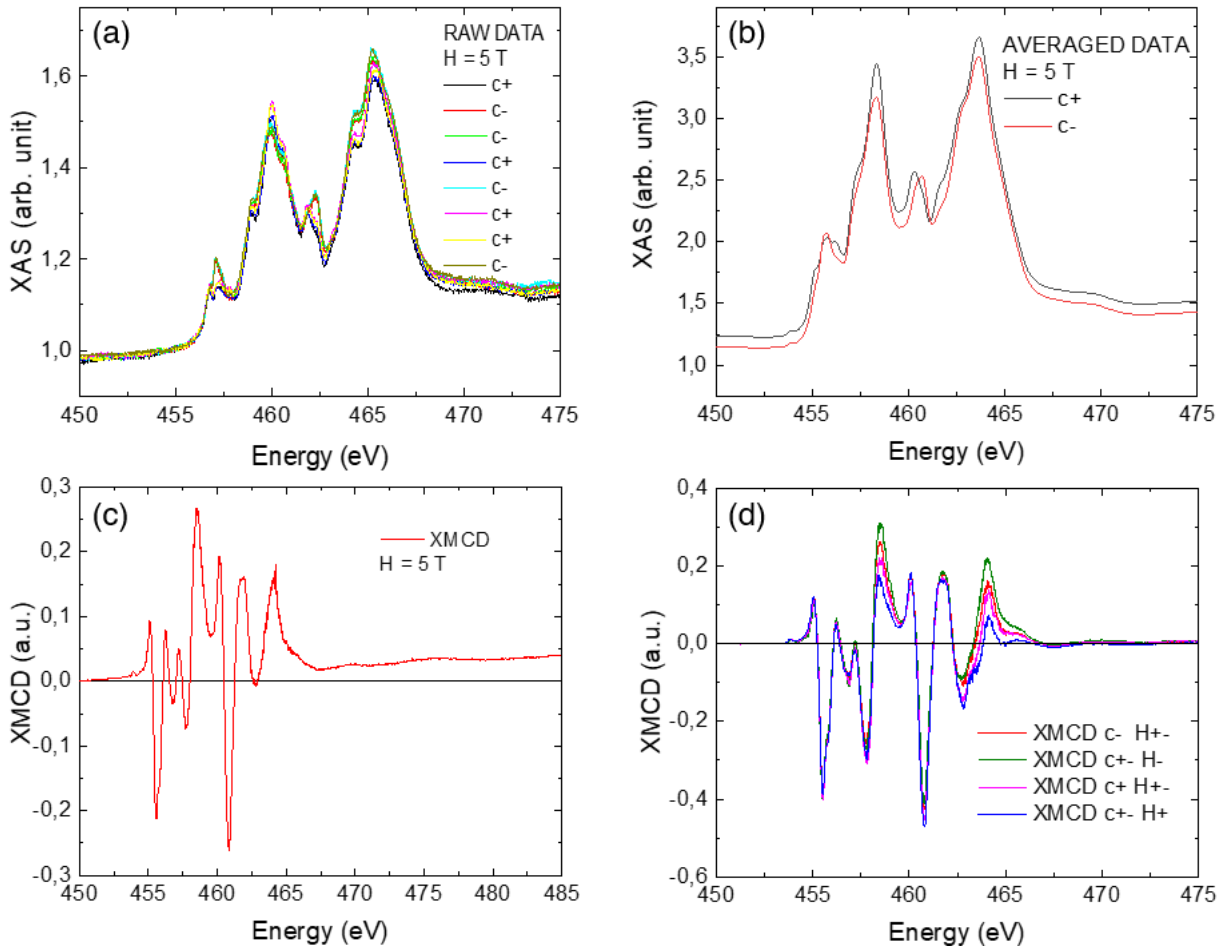


Figure 5.2: Data obtain on DTO: (a) Raw data as measured in TFY at the beamline in the sequence H+c+-+. (b) Average data of the two polarizations. (c) Data shifted to zero at the preedge. (d) XMCD obtained after the subtraction of different set of data. The data in (b-d) have been obtained by XEOL<sup>1</sup>

One of the most common source of error is a fluctuation of the measured intensity around its averaged value Fig. 5.2 (a). This error usually has unknown origin but if stochastic, it can be solved by averaging data.

Since XMCD is expected to be quite small relative to the XAS, small variations on the XAS can

<sup>1</sup>All these data can seem inconsistent but they have been selected to best illustrate the issues encounter during the analysis process. They have been measured at different time, in different beamlines

drastically change the resulting XMCD signal. In order to increase the signal-to-noise ratio, we are bound to measure many consecutive scans and average them thus getting rid of both problems. This is shown in Fig. 5.2 (b), where we see an excellent signal to noise ratio.

One can notice the rigid shift between the two polarizations that we need to set to zero at the pre edge, see Fig. 5.2 (b). This effect is likely due to a non-element specific dichroic effect.

After the pre-edge correction, the post edge of both spectra goes to the same value. Indeed, no dichroic effect should be present at these energies since the background does not correspond to any absorption edge. Thus, there is no risk for us to alter the physical content of the data. On the contrary, applying a multiplicative coefficient to position the pre-edges at the same level will produce a distorted signal strongly affecting the resulting XMCD. The spirit of the following analysis will thus be to interact as little as possible with the data.

We can also sometimes observe a shift in the spectra linearly depending on the energy (or time) resulting in a slope on the XMCD signal, as see Fig. 5.2 (c)<sup>2</sup>. This can be corrected by simply subtracting said slope. This will however introduce data distortion. Fortunately, this effect is likely not physical and comes from experimental errors such as insufficient correction of the linear background from the direct beam signal. This is further supported by the fact that this phenomenon occurs more often in certain beamlines than in others. In the following analysis, we discarded all data-sets that presented this kind of error.

One last problem that could possibly deform our XMCD is the saturation effect present in XEOL signals. Indeed, as we introduced it in section 2.6.2, in XEOL we measure a classical absorption spectra ie where the minimum corresponds to the maximum of absorption. Note that the raw signal is first transformed through a  $-\log(x)$  function. As a result, in thick samples where the absorption is the strongest, small fluctuations near zero transmission get huge when applying the  $-\log(x)$  function, Fig. 5.2 (d). This result in stronger fluctuations at the maxima where the dichroic effect appears (much more visible in the XMCD than the XAS).

In thicker sample, this is even more dramatic and can result in clipping of the signal. This is why we optimized the thickness (moving from 80 nm to 50 nm) in order to find a balance between having enough material to observe a clear  $\text{Ti}^{3+}$  signal while avoiding the aforementioned effects.

---

<sup>2</sup>Note that this data-set corresponds to the one presented in Fig. 5.1 but without the slope correction. This set has not been used in the final result presented later.

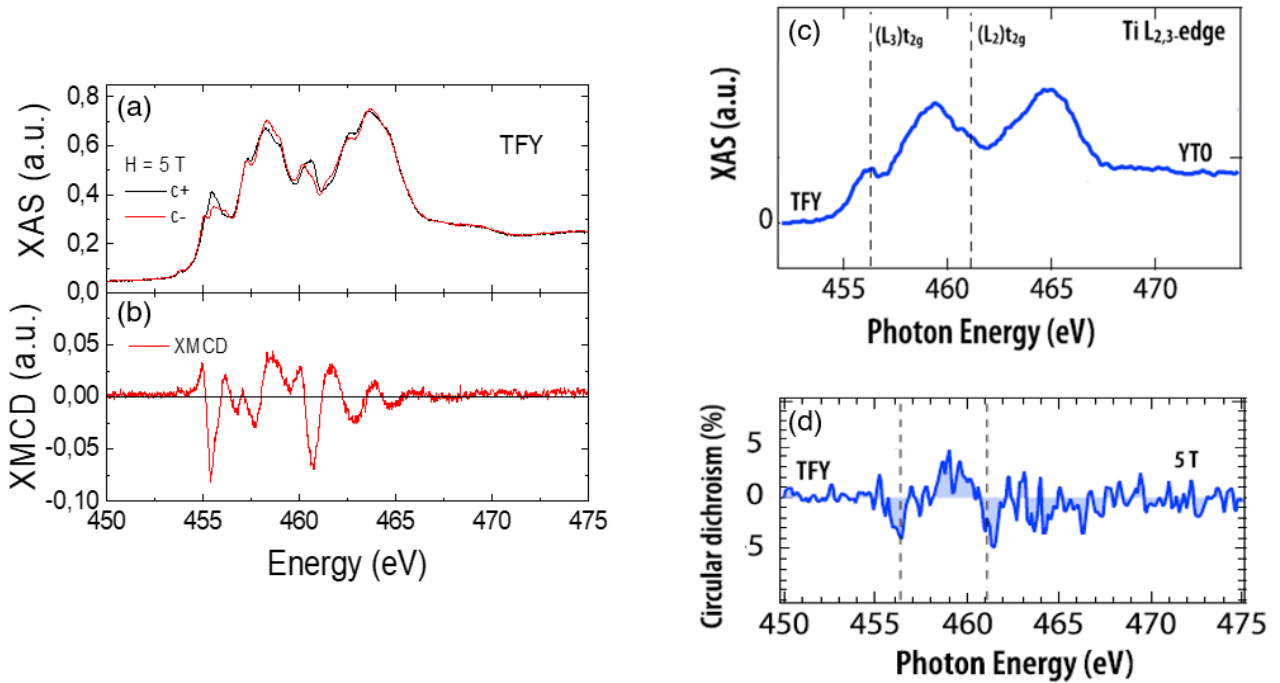


Figure 5.3: Data obtained by TFY on YTO thin films: (a) Treated XAS data  $L_{2,3}$  edges, as measured at 5 T and 20 K. (b) Resulting XMCD signal. (c) Treated XAS data as measured at 5 T and 15 K. (d) XMCD obtained after subtraction. (c,d) adapted from [100].

The compromise is achieved in Fig. 5.3 (a) where we can see that the final signal has a really low noise level resulting in a clear XMCD with clear features, Fig. 5.3 (b). It is worth noting that its intensity reaches 7 % which is stronger than the values obtained in the scarce literature. In Fig. 5.3 (c), we can see that Cao *et al* obtained similar signal as us but with less striking features. This is reflected in Fig. 5.3 (d), where we see similar features. However, we see the signal-to-noise ratio is much stronger in our data, thanks to the optimization of the X-Treme beamline.

### 5.1.1 First observation of a non-zero integral

We obtained the first clear XMCD from the Paul Scherrer Institute synchrotron (SLS) at the X-Treme beamline. We first measured DTO because it was the first titanate optimized in this thesis as well as the one available at the time.

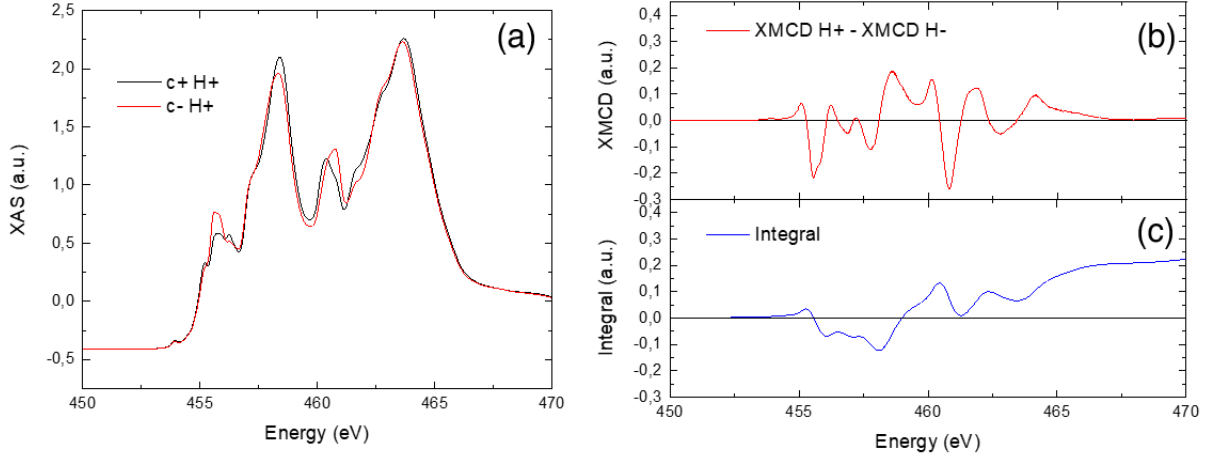


Figure 5.4: Data obtained by XEOL of 80 nm DTO thin film: (a) Fully treated XAS signals at the  $L_{2,3}$  titanium edges. (b) Resulting XMCD signal obtained after averaging over 28 spectra and between the opposite XMCD H+ and XMCD H-. (c) Corresponding integral over the full range of energy.

We applied the data processing explained before and obtained the extremely clean signal in Fig. 5.4 (a). The resulting XMCD is then averaged with its counterpart obtained under negative field to obtain Fig. 5.4 (b). By obtaining such low noise XMCD, we calculated its integral. Indeed, the integral of XMCD signal contains fundamental informations about the state of the element of the measured edge. These can be obtained by applying the so-called sum rules discussed in the following section. Even if the  $L_{2,3}$  edges of titanium are known to be too convoluted to apply reliably the spin sum rule where we need to isolate the two edges, the fact that we obtain a clear no zero integral could indicate the presence of an orbital moment on the titanium. This is unexpected from a transition metal in octahedral coordination where the orbital moment should be quenched.

## 5.2 Sum rules

### 5.2.1 Presentation

As we have seen in the section 2.6.4 the area under each peak gives us information on the population of the different states and their corresponding quantum numbers since, they intervene in the Fermi golden rule controlling the transitions that we measure.

As a reminder the Fermi golden rule determines the probability of transition between two states in quantum mechanics. Applied in particular cases, it results in so-called selection rules parametrized by the appropriate quantum number for the system.

By applying it to the transition induced by X-ray absorption and dichroism, we obtain the famous sum rules developed by Thole in 1992 [101]. They inverse the principle of the Fermi golden rule by giving us access to the quantum number from experimental data. By measuring the integral of each peak, we can access to the relative probability of each of their corresponding transitions.

The sum rules allow us to obtain the quantum numbers  $S_z$  and  $L_z$ , thus we need two equations to obtain the value of those unknowns. For this reason, the sum rules are always applied to two edges of an element split by spin-orbit coupling. This is why they have been developed to be applied to the

$M_{4,5}$  and  $L_{2,3}$  edges. Because the  $L_{2,3}$  edges correspond to  $J = L + S$  and  $L - S$ , we understand why we are able to isolate both numbers.

### 5.2.2 Sum rules development

In [101], Thole applied the Fermi golden rule to the transition the state corresponding to the  $M_{4,5}$  and  $L_{2,3}$  edges. The resulting elements of  $P_q$  of the probability matrix are calculated by using the Wigner-Eckart theorem which, with graphical methods and some approximations (such as the assumed equivalence of the radial part of the wave functions because of the small relativistic correction induced by the spin orbit coupling), result in an expression of the orbital moment as a function of the integral of the different edges and the integral of the isotropic XAS (abbreviated iso XAS). In a second time Carra and Thole have developed the sum rule for the spin moment [102].

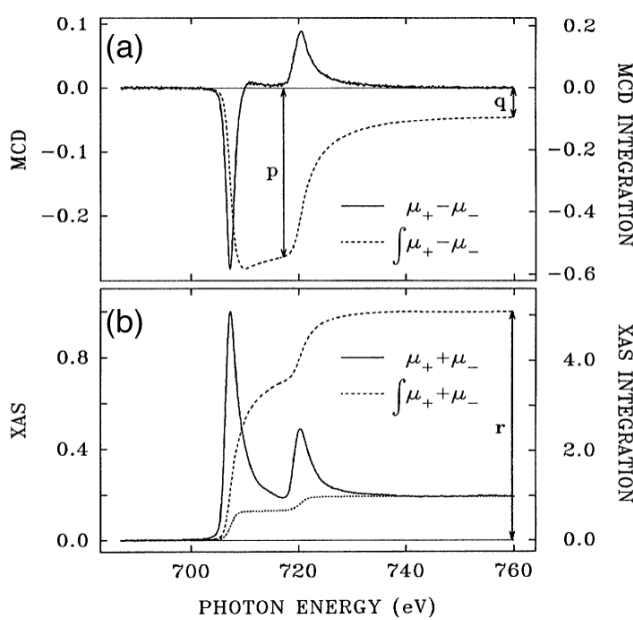


Figure 5.5: (a) XMCD spectra of the  $L_{3,2}$  edge of Co. (b) Iso XAS spectra the  $L_{3,2}$  edge of Co. Adapted from [103]

The expression has been refined in several articles such as [103]. In [103] Chen first experimentally verified the sum rules and defined several integrals label p, q and r which correspond respectively to the integrals of the  $L_3$  edge, the  $L_3$  and  $L_2$  edges of the XMCD and the both edges of the iso XAS, as presented in Fig. 5.5. It results in the following expression for  $m_{orb}$  and  $m_{spin}$ .

$$m_{orb} = -4q \frac{(10 - n_{3d})}{3r} \quad (5.1)$$

$$m_{spin} = -(6p - 2q) \frac{(10 - n_{3d})}{r} \quad (5.2)$$

These expressions are powerful tools to investigate the state of the probed element.

More specifically for our case, we can see that according to Eq. 5.1 the absence of orbital moment implies that  $q$  is null. This means that a non-zero integral of the XMCD indicates a non-zero orbital moment. This is why we are confronted with an unexpected orbital moment at the titanium edge of DyTiO<sub>3</sub> that we will investigate in the following sections.

## 5.3 XMCD analysis on GdT<sub>1-x</sub>Ti<sub>x</sub>O<sub>3</sub>, YT<sub>1-x</sub>Ti<sub>x</sub>O<sub>3</sub> and TmTiO<sub>3</sub> thin films

After the first observation of a non-zero XMCD integral in DTO, we measured the other rare-earth titanate thin films grown during this PhD.

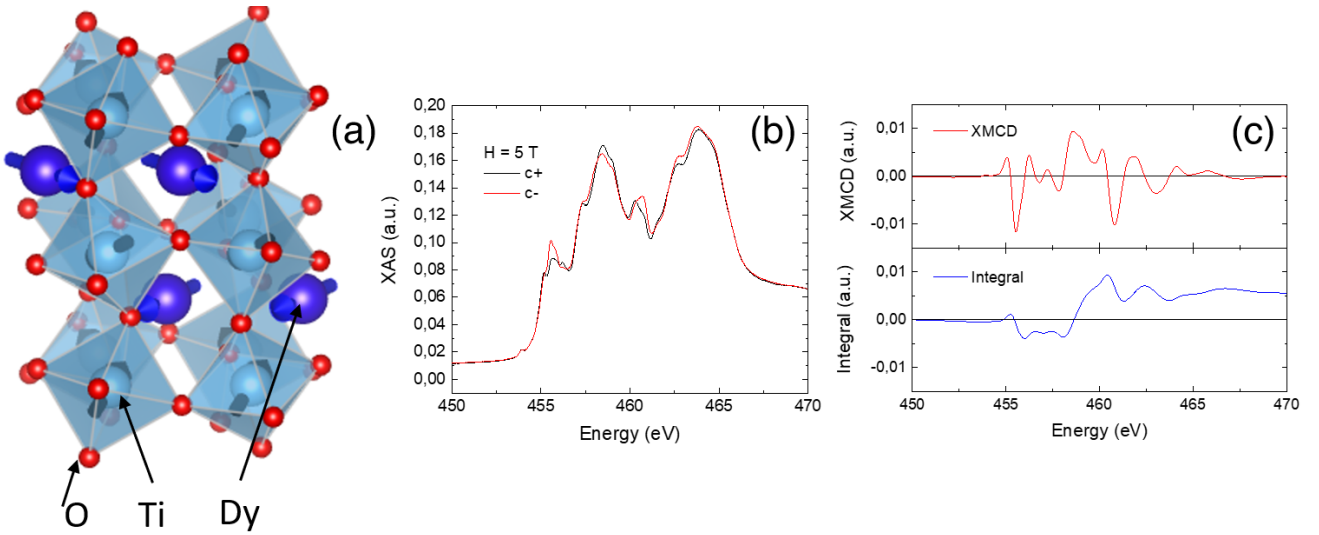


Figure 5.6: (a) Crystal and magnetic structure of  $\text{DyTiO}_3$ . (b) XAS spectra of  $\text{DyTiO}_3$ . (c) XMCD signal of  $\text{DyTiO}_3$  and its integral. (b,c) are obtained in TFY.

We can see in Fig. 5.6 (b,c) that despite more pronounced  $\text{Ti}^{4+}$  features in TFY, the same  $\text{Ti}^{3+}$  features as in the XEOL measurement in Fig. 5.4 (a-c) carry the dichroism. In both cases, it results in a non-zero integral, thus showing the reproducibility of the observation.

Some works [104, 105, 106] have linked the appearance of unexpected orbital moments in magnetic compound to their magnetic structure. Because  $\text{TmTiO}_3$  has a similar magnetic structure as  $\text{DyTiO}_3$ <sup>3</sup>, as we can see in Fig. 5.7 (a), we also investigated this material in order to reproduce the phenomena and eventually invalidate the role of the magnetic structure.

### $\text{TmTiO}_3$

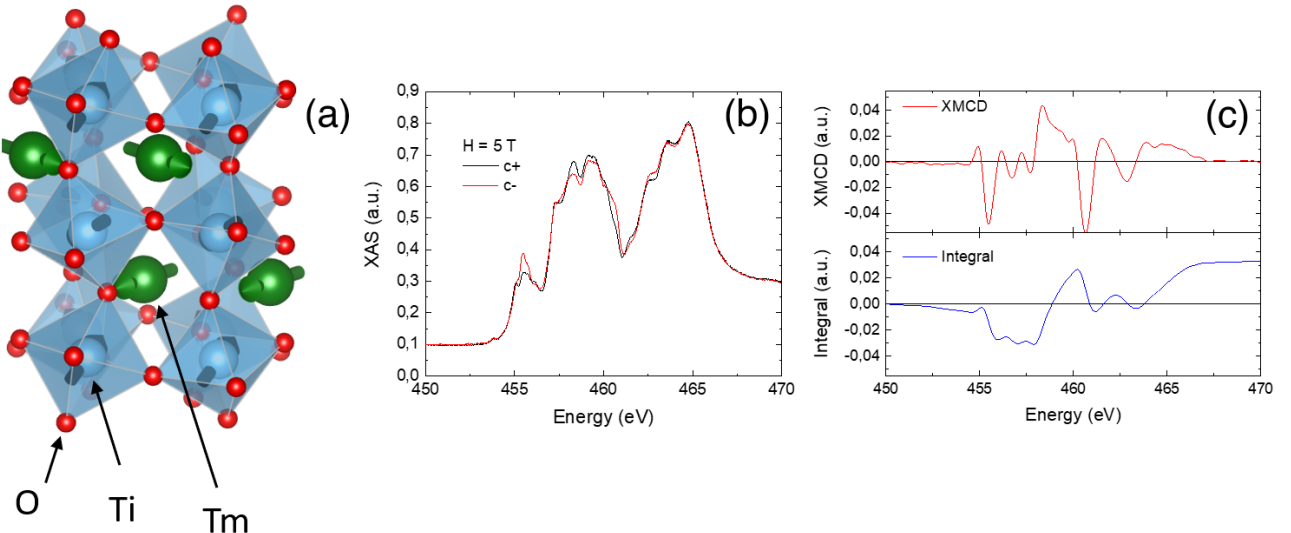


Figure 5.7: (a) Crystal and magnetic structure of  $\text{TmTiO}_3$ . (b) XAS spectra of  $\text{TmTiO}_3$ . (c) XMCD signal of  $\text{TmTiO}_3$  and its integral. (b,c) are obtained in TFY.

<sup>3</sup>Magnetic structure data are extracted from [61] and assigned to their magnetic symmetry group as presented in [64]

If we recognize the same dichroic features as in DTO in Fig. 5.7 (c), there is however significant difference in the line shapes. This points toward a prevalence of  $\text{Ti}^{4+}$  in TTO compared to DTO. The picture portrayed here is coherent with Tab. 4.1 where TTO appears to be the rare earth titanate with the highest  $\text{Ti}^{4+}$  at equivalent growth conditions. Despite all that we obtain a similar behavior from the integral of the XMCD, Fig. 5.7 (c). If this result is not proof of the influence of magnetic configuration, we can look at a titanate with a collinear magnetic order just as  $\text{GdTiO}_3$ , as seen in Fig. 5.8 (a).

### $\text{GdTiO}_3$

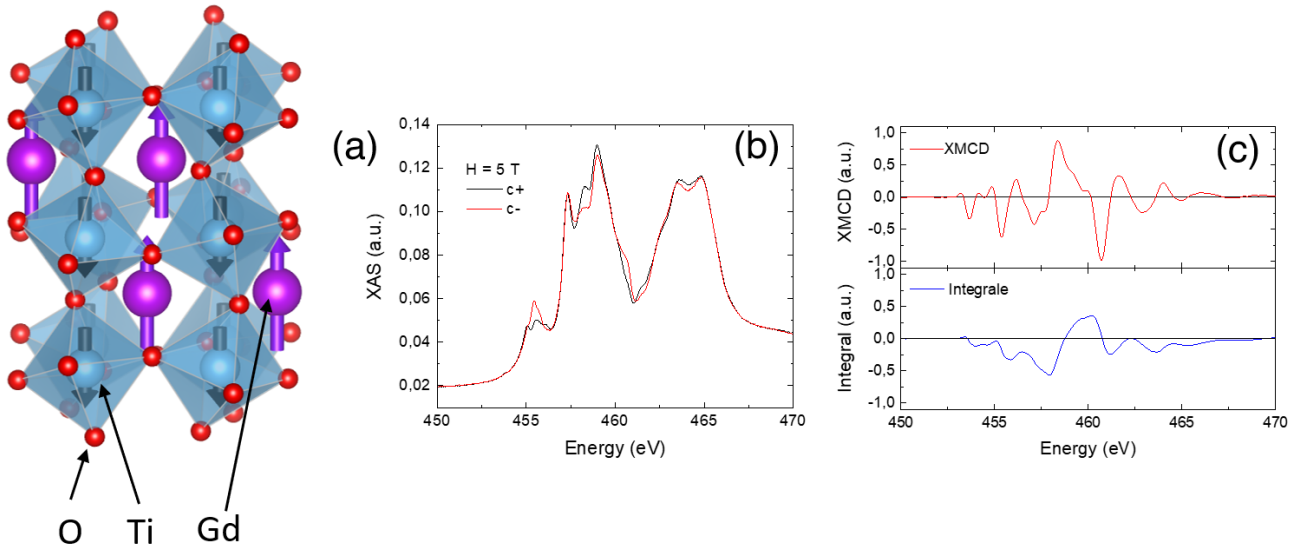


Figure 5.8: (a) Crystal and magnetic structure of  $\text{GdTiO}_3$ . (b) XAS spectra of  $\text{GdTiO}_3$ . (c) XMCD signal of  $\text{GdTiO}_3$  and its integral. (b,c) are obtained in TFY.

Here again we obtain very similar dichroic features seen in the Fig. 5.8 (c). However, the resulting integral clearly converges to zero indicating the absence of orbital moment. In order to confirm this difference observed between the collinear and non-trivial magnetic structure, we investigate the case of  $\text{YTiO}_3$  where the collinearity is ensured by the absence of any moments carried by the Y atoms, see Fig. 5.9 (a).

## YTiO<sub>3</sub>

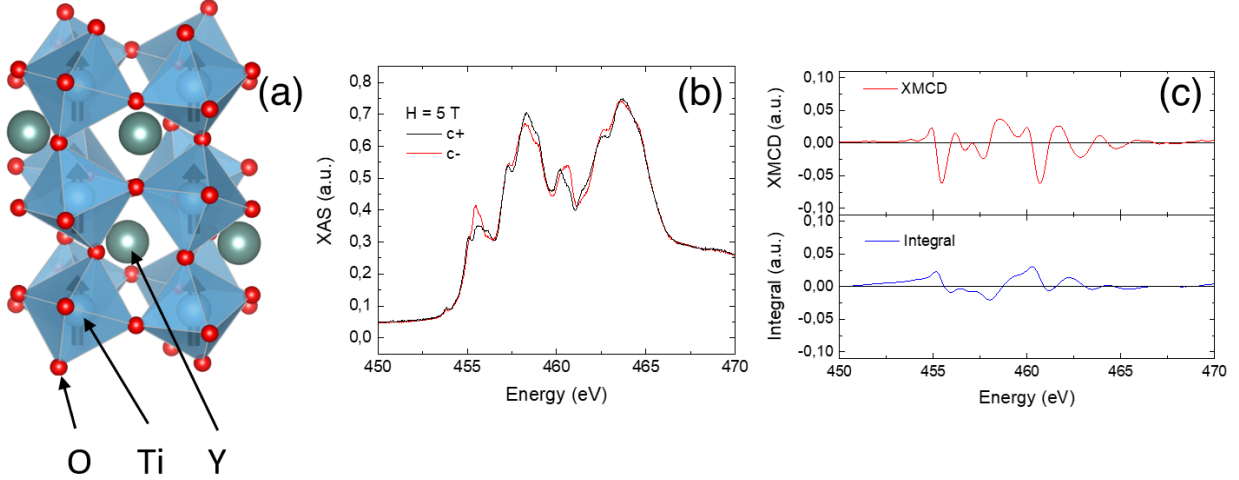


Figure 5.9: (a) Crystal and magnetic structure of YTiO<sub>3</sub>. (b) XAS spectra of YTiO<sub>3</sub>. (c) XMCD signal of YTiO<sub>3</sub> and its integral. (b,c) are obtained in TFY.

Here the shape of the spectrum appears really similar to the one obtained in XEOL detection mode and again the integral converges to zero as in the case of GTO. A clear correlation then emerged, where the presence of a non-collinear magnetic structure seems to be linked to the presence of a non-zero integral.

## 5.4 Induced orbital moment in literature

In this part we will go more in depth about the emergence of an orbital moment created by a non-collinear magnetic structure.

### 5.4.1 Chirality induced by symmetry breaking of the magnetic environment

First, we can ask ourselves why TTO and DTO have non-collinear structures? The obvious difference with GTO and YTO is the presence of an orbital moment carried by their respective rare-earths. Indeed, the canting the Tm and Dy moments can be explained by the Dzyaloshinskii-Moriya interaction (DMI) which is enhanced by the existence of an orbital moment [107, 108, 109]. DMI is well known in the field of chiral magnetic structure such as skyrmions, domain wall etc.

In [106] Dos Santos Dias *et al* propose a model in which an orbital moment could emerge even in the absence of spin-orbit coupling (SOC). They applied density functional theory (DFT) to calculate the orbital moment of spin structures with non-vanishing scalar spin chirality and demonstrate that even in the absence of SOC the orbital moment was still present. They applied this method to skyrmions and showed that a part of the observe magnetic moment was topological in origin.

In order to characterize the magnetic order the scalar spin chirality  $\kappa$  is often used:

$$\kappa = \mathbf{S}_i \cdot (\mathbf{S}_j \times \mathbf{S}_k) \quad (5.3)$$

where  $\mathbf{S}_i$ ,  $\mathbf{S}_j$ ,  $\mathbf{S}_k$  are neighboring spins in the magnetic structure.

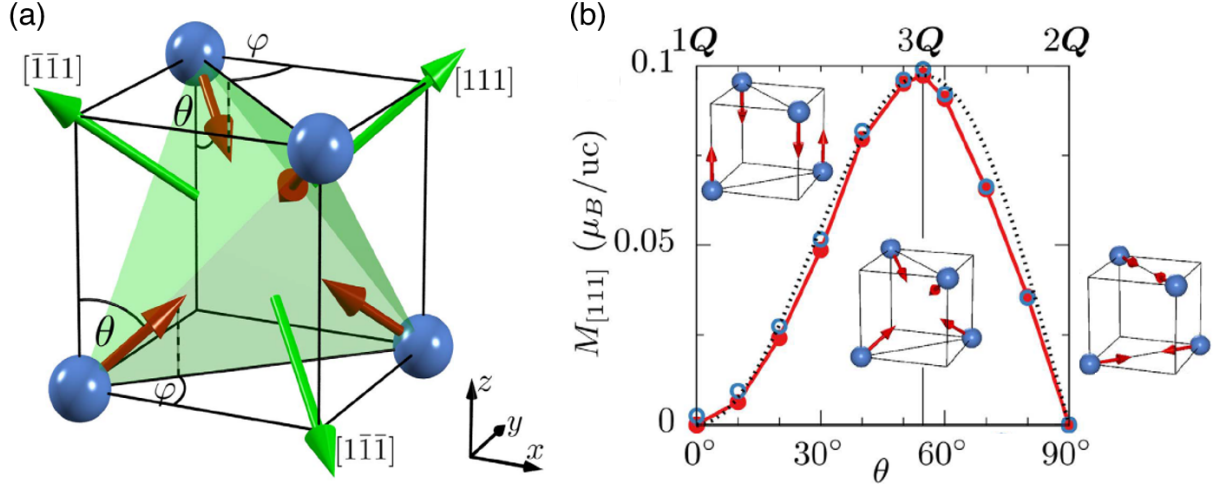


Figure 5.10: (a) Unit cell of face-centered-cubic  $\gamma\text{-Fe}_x\text{Mn}_{1-x}$ . Red arrows indicate the noncoplanar texture of spins pointing towards the center of the transparent green tetrahedron. The faces of the tetrahedron highlight equivalent planes of the undistorted lattice, and green arrows orthogonal to corresponding planes mark the directions [111], [111], and [111], respectively. (b) The [111] component of orbital magnetization and anomalous Hall conductivity as a function of the polar angle  $\theta$ , which characterizes the antiferromagnetic spin texture, for the strain  $\delta = 0.95$  and the concentration  $x = 0.0$ . Spin-orbit coupling was additionally taken into account for the open blue data points. The dotted black line denotes the angular dependence of the spin chirality, Eq. 5.4, and the insets present the multiple-Q structures at  $\theta = 0^\circ$ ,  $54.7^\circ$ , and  $90^\circ$ . Adapted from [105].

In [105], Hanke *et al* studied  $\gamma\text{-FeMn}$  as a prototypical material to explore the topological effects on the orbital moment. In the situation described in Fig. 5.10, we can rewrite Eq. 5.3:

$$\kappa(\theta) \propto \cos \theta \sin \theta \quad (5.4)$$

where,  $\theta$  is the angle define in Fig. 5.10.

From Eq. 5.3, we can see that the spin chirality is non-vanishing only if the spins are not coplanar. As in our case, we can see "similar" structure in the (bc) planes where  $\kappa \simeq 0.47$ . However, as the authors point out the resulting chirality would be equivalent along [111], [-1-11], and [1-1-1]; leading to a null contribution. As a consequence, this tetrahedral symmetry needs to be broken and Hanke *et al* introduce strain in order to do so. Their calculation then leads to a clear but rather small orbital moment as seen in Fig 5.10 (b). The red dots correspond to calculation done without any SOC but its addition seen in the blue hollow dots appears rather insignificant compare to the "topological" effect. We can also see that the orbital moment is maximum when the spins are pointing to the center of the tetrahedron, indicating its clear dependency with the  $\kappa$  value.

We came in contact with the team of Yuriy Mokrousov from Jülich to discuss the possibility of such a phenomenon in our systems. However, since rare-earth titanates are centrosymmetric materials, their spin textures although non-coplanar for e.g. DTO and TTO are not chiral ; the total spin chirality for the whole structure averages to 0. That said, just as in FeMn, if inversion symmetry becomes broken, it is possible that it will lead to the emerge of a topological orbital moment. Although,

the effect is expected to be smaller, because of the smaller non-collinearity in DTO and TTO (in term of angle), it might still be present. As they suggest, the breaking of the symmetry is still needed. As in [105], we can justify it by the presence of a strain gradient which can be expected due to the not negligible strain on LAO (001) ( $\epsilon = 2.9 \%$ ). We will label this hypothesis  $\mathcal{H}1$ .

Another way to break the symmetry is via the presence of the "living-dead" layer discussed in section 4.3. Indeed, one can imagine that the presence of free  $Dy^{3+}$  ions will disturb the magnetic order of the  $Ti^{3+}$  region along the normal to the sample. Breaking this way the symmetry of the magnetic structure. We will label this hypothesis  $\mathcal{H}2$ .

### 5.4.2 Perspectives

Although the origin of the non-zero integral observed remains unclear, we have shown that it seems to be related to the presence of a non-collinear magnetic order. There are however, some experiments we can do to sort out the different hypotheses.

Varying the thickness of our films is our first idea. If we consider a square sample with a surface of  $a^2$  and thickness  $t$ , we can present the contribution of  $\mathcal{H}1$ :

$$C_{\mathcal{H}1} = c_V t a^2 n_V \quad (5.5)$$

where  $C_{\mathcal{H}1}$  is the contribution of  $\mathcal{H}1$  to the observed non-zero integral,  $c_V$  is the volumetric contribution to the non-zero integral due to strain,  $a$  the length of a side of the sample and  $n_V$  the volumetric density of our film because all of it should contribute in the  $\mathcal{H}1$ .

### Elimination of $\mathcal{H}2$

We first notice that in both cases the dependency with thickness is linear. If it does not help us to distinguish between  $\mathcal{H}1$  and  $\mathcal{H}3$ , it allows us to test  $\mathcal{H}2$ . Indeed, we have established that the "living-dead" layer was independent of the thickness of the film. As such, at different thicknesses we expect to obtain the same integral value at the post-edge.

In order to test this, we compare the integrals obtained from TFY and XEOL. As we discussed in section 4.3.2, TFY probes about 50 nm of the sample and XEOL the full thickness of the sample of about 80 nm. Knowing this if either  $\mathcal{H}1$  or  $\mathcal{H}3$  are true, we would expect the signal to be stronger in XEOL than in TFY. By normalizing the integral by the XMCD maximum intensity, we obtain the following integrals.

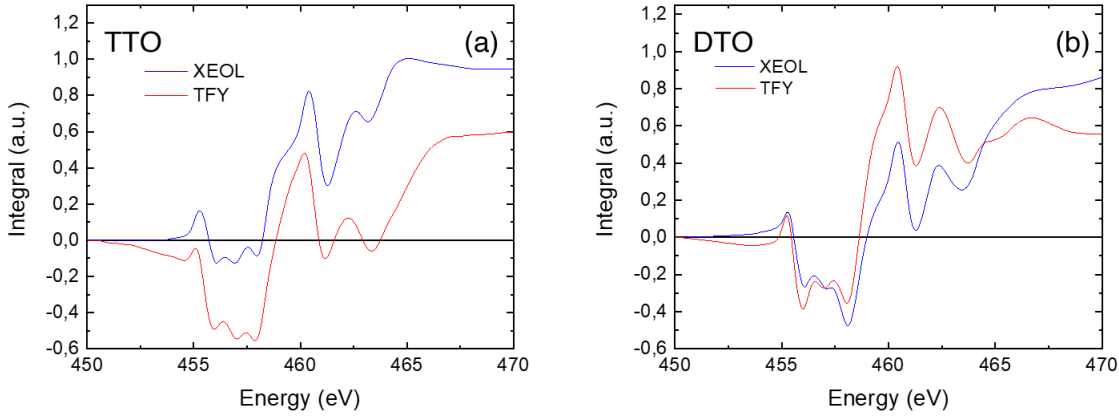


Figure 5.11: (a) Integrals of a  $\text{TmTiO}_3$  80 nm thick film measured in TFY and XEOL. (b) Integrals of a  $\text{DyTiO}_3$  80 nm thick film measured in TFY and XEOL.

For Fig. 5.11, we measure the integral at the post-edge to be 0.596 and 0.944 respectively for TTO. In the case of DTO we obtain 0.5537 and 0.8576. It results in respective ratios of 1.58 and 1.56 that we can compare to the ratio expected from a volumetric dependency of the orbital moment contribution. Knowing that we have a "living-dead" layer of 5 nm (according to EELS, XAS, SQUID and XPS) and that a probing depth of 50 nm for the TFY has been established by the fact that if 90 % of the TFY signal is  $\text{Ti}^{3+}$ , it implies a 50 nm probing depth which itself implies a signal ratio between the XEOL and TFY of 1.6. This result follows closely the value from Fig. 5.11 with an error of 1.27 % to 2.56 % (respectively) which makes sense given the possible errors on the thickness of the sample and the lengths involved in this calculation. This result might allow us to then discard  $\mathcal{H}2$ . However, we should confirm this analysis with samples of different thicknesses measured with the same technique.

### Discussion on $\mathcal{H}1$

We further investigated the structure of the films in TEM and use it to detect an eventual strain gradient.

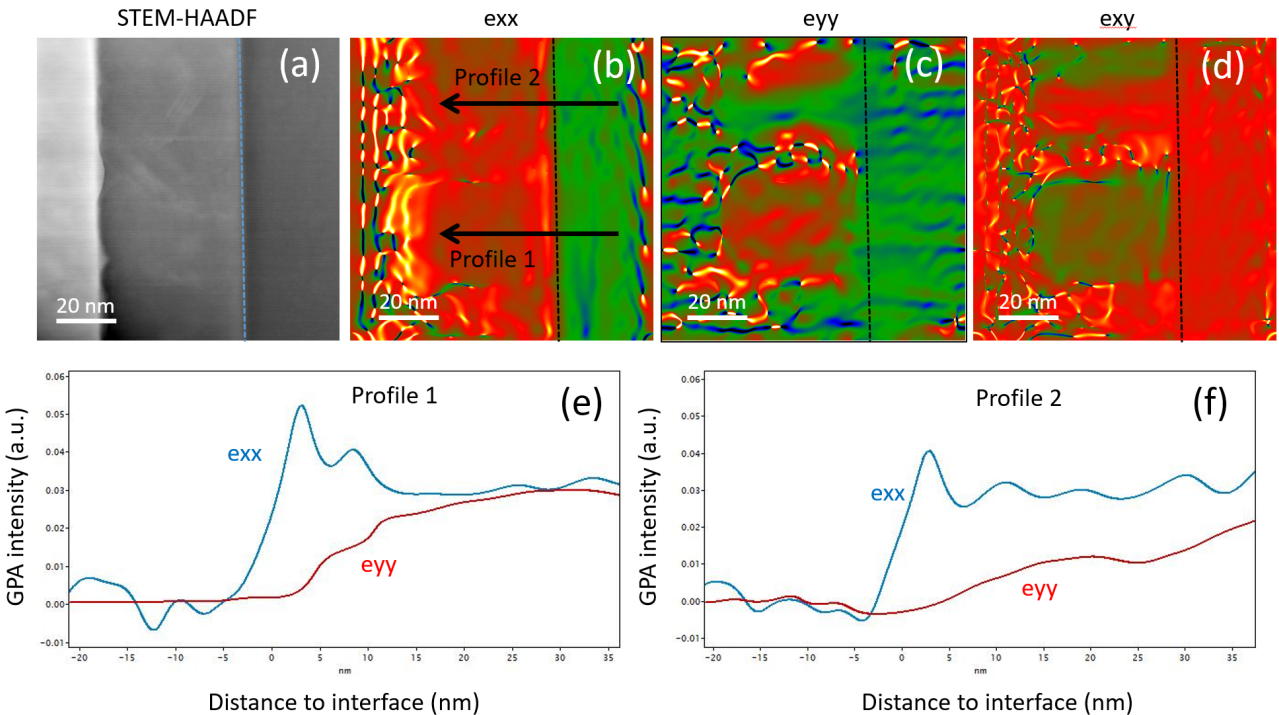


Figure 5.12: (a) STEM-HAADF of DTO ON LAO (b) GPA map of the elongation along the out of plane direction. (c) GPA map of the elongation along the vertical direction of the picture. (d) GPA map of the elongation along the xy direction of the picture. (e) Profile of the GPA map along direction 1. (f) Profile of the GPA map along direction 2.

GPA (geometrical phase analysis) strain mapping [110] has been done based on these HAADF images. The figures are the x and y direction strain maps (exx, eyy) along with the shear strain map (exy). Profiles averaged across the layers are also displayed for two different domain orientations of the film. The profile 1 is obtained across a DTO orientation with a  $[001]_o$  zone axis and the profile 2 is for domain with  $[1-10]_o$  orientation. The references have been set for the LAO substrate. The out-of plane lattice parameter near the interface is always expanded as compared to the substrate. The expansion is of typically 3.5 to 5 % and extends over 5-10 nm in the DTO films. In this area, the in-plane lattice parameter (eyy) has the same value of the substrate indicating a perfectly constrained area. Beyond this strained area, the out-of-plane lattice parameter reduce and reach typically 2-3 % larger of the LAO out-of plane distance. Different relaxations processes are observed for the in-plane distance. Across the profile 1, the in-plane spacing of the DTO is larger and a significant shear is observed. Indeed, for the  $[001]_o$  zone axis of the profile 1, the  $(1-10)_o$  planes of DTO of  $\sim 3.89$  has to match with the LAO pseudo-cubic unit cell (3.79) of the substrate. For the  $[1-10]_o$  zone axis of the profile 2, the DTO (002) plane of 3.81 has a much smaller mismatch with the substrate resulting in the very weak evolution of the in-plane unit cell along the profile 2. This GPA treatment clearly evidences that at the interface with the substrate a compressively strained DTO extend over 5-10 nm. Further away, a relaxation occurs with the presence of domains showing some texture and the presence of shear deformation. The presence of this strain gradient might support  $\mathcal{H}1$  however, some more investigations are needed.

# Chapter 6

## Toward a 2DES system in rare-earth titanate oxide heterostructures

### 6.1 State of the art on 2DES system in heterostructures

If Herbert Kroemer coined the famous phrase that "the interface is the device" when talking about semiconductors interfaces in the field of optoelectronics, it also perfectly applies to oxide interfaces. We briefly introduced oxide heterostructure in section 3.4.2, but only from the structural point of view. Here, we will present the new electronic states appearing at the interfaces.

#### 6.1.1 LaAlO<sub>3</sub> / SrTiO<sub>3</sub> interfaces

LaAlO<sub>3</sub> / SrTiO<sub>3</sub> is the first oxide interface that is expected to come to the mind because it has been the most widely studied, the first to show such a variety of properties and the one that set a framework to study these interfaces. The investigation of high mobility materials has been pushed in the 70s and led to the discovery of the integer [111] and fractional [112] quantum Hall effects in GaAs quantum walls. On the other hand, advances in thin film growth allowed H. Hwang to discover a conducting LaAlO<sub>3</sub> / SrTiO<sub>3</sub> interface [113] in 2004 and paved the way for the field of research. This is remarkable because both STO and LAO are band insulators. A new state appears at the interface because of charge transfer taking place, as described in section 3.4.2. This state is a 2D Electron System of few nanometers thick. Note that sometimes it is called a 2D Electron Gas (2DEG) however, this appellation is somewhat controversial since according to some authors [114], the correlation in those systems would better qualifying them as a 2DEL for 2D Electron Liquid. This is why we will use the more neutral 2DES in the following. After the discovery of Hwang and Ohtomo in 2004 several groups followed this work and explored further the properties of the 2DES.

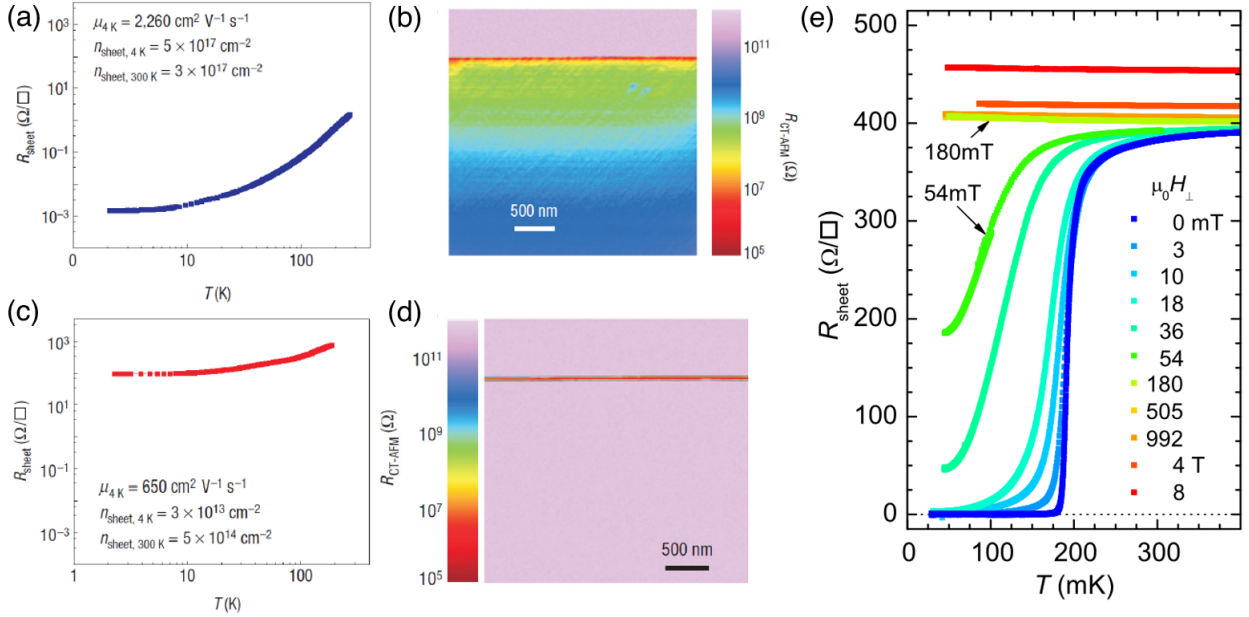


Figure 6.1: Electron profile probed by conductive-tip AFM (CT-AFM), for the unannealed and annealed samples of LAO grown on STO. (a) The sheet resistance as a function of the temperature for the unannealed sample. The 2D carrier concentration  $5 \times 10^{17} \text{ cm}^{-2}$  is unphysically high [113]. (b) The electron profile for the unannealed sample seen under CT-AFM. The electrons are not well confined and spread into the SrTiO<sub>3</sub> bulk. (c) The sheet resistance for the sample annealed at high oxygen partial pressure ( $P(\text{O}_2) = 400 \text{ mbar}$ ) after the growth. (d) The CT-AFM image for the annealed sample. The electrons are confined at the interface with width 7 nm. Adapted from [115]. (e) Sheet resistance of a 8 u.c. sample plotted as a function of  $T$  for magnetic fields applied perpendicular to the interface. Adapted from [2].

Early on, the 2D character of the high mobility conduction was taken with healthy skepticism. Indeed, in some samples the reported carrier density as of the order of  $10^{22} \text{ cm}^{-3}$  and the angular dependence of the quantum oscillation did not correspond to the one expected from a 2D system. In 2006, the evidences of 2D character were obtained [116] and revealed the key role of post annealing to avoid bulk conduction. This is clearly shown in Fig. 6.1 (a-d), Fig. 6.1 (a) display non annealed sample that present the same 3D carrier density for which the character was verified by CT-AFM (b) where the authors observed the conduction properties extending deep into the STO substrate. On the opposite when post annealed in oxygen, thus refilling the oxygen vacancies of STO, the sample shows a carrier density compatible with 2D conduction (c) and only a thin conductive layer (about 7 nm) remains (d). Later superconductivity was observed in these systems [2]. The Fig.6.1 (e) shows a  $T_C \simeq 200 \text{ mK}$  which will turn out to be the range of the rest of the literature on the subject, with a maximum observed  $T_C \simeq 300 \text{ mK}$ . Bulk electron-doped SrTiO<sub>3</sub> also shows superconductivity. It is worth noting that if it presents the typical superconducting dome as a function of carrier doping [117], like for example cuprates, it also has the lowest carrier density of all known superconductors [118].

Another key point of the LAO/STO system is its spin-charge conversion property. We will discuss it in the following figures.

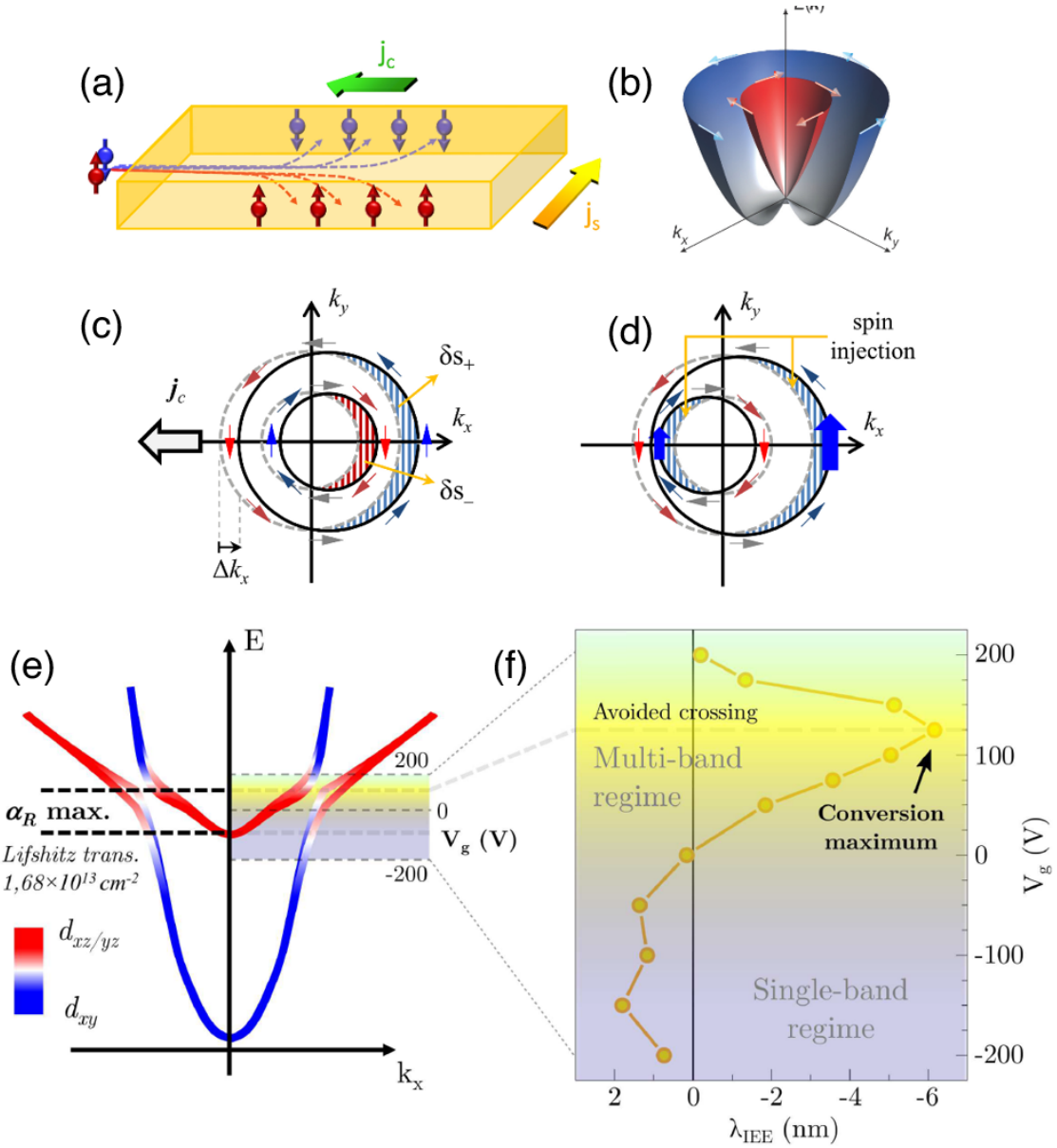


Figure 6.2: (a) Schematic representation of the Spin Hall Effect (SHE), where a current get spin polarized under the effect of a magnetic field in a SOC material. (b) Momentum-dependent spin split Rashba subbands plotted as red and blue parabolic lines in the  $(k_x, k_y)$ -E plot. (c) Representation of the Edelstein Effect (EE). A charge current ( $j_c$ ) injected at the interface along-x induces a shift  $\Delta k_x$  of both Fermi contours, resulting in a spin accumulation polarized along the y-axis due to the inequivalence of the two contours. (d) Representation of the Inverse Edelstein Effect (IEE). When a spin current is injected perpendicularly to the 2DES with the spin polarization along the y-axis, the spin population is altered in the steady state causing a displacement in momentum space of the two in equivalent Fermi surfaces (red and blue lines) by  $\pm \Delta k_x$ . This results in a net charge current generated perpendicularly to the spin current and to its spin polarization [1]. Origin of the spin-to-charge current conversion efficiency maximum. (e) Schematic band structure of the 2DES at the LAO/STO interface. At around  $1.68 \times 10^{13} \text{ cm}^{-2}$  (Lifshitz transition [119]) the heavy  $d_{xz,yz}$  bands start to be occupied. Above that, at the region where the heavy and light bands cross each other, large spin-orbit effects are predicted [120]. The highlighted area represents the expected gate voltage region swept. (f) In this range, the IEE sign change (at  $V_g \simeq 0 \text{ V}$ ) is attributed to the onset of occupation of heavy bands, which contribute with an opposite sign to the overall "effective" Rashba coefficient. The maximum observed at  $V_g = 125 \text{ V}$  is linked to the avoided band crossing region.

The schematic Fig. 6.2 (a) represents the spin Hall effect (SHE) which corresponds to the gen-

eration of a spin current transverse to the applied charge current in a non-magnetic metal with Spin Orbit Coupling (SOC). Conversely, a pure spin current injected into a material with SOC will generate a transverse charge current, through the inverse spin Hall effect (ISHE). Note that this effect appears in bulk as long as the SOC is present. They determine the direction of the currents generated. Another mechanism of spin-charge interconversion exists in systems with Rashba spin-orbit coupling. The Rashba SOC consists of a lift of the spin degeneracy happening when the inversion symmetry is broken either in uniaxial noncentrosymmetric bulk crystals but also in low dimensional systems such as 2DES at a interface that breaks inversion symmetry [121]. The resulting splitted band structure is represented in Fig. 6.2 (b). Taking this splitting into account, the application of a charge current shifts the Fermi contours thus creating a spin density because of the inequivalence of the two contours. Since the  $k_x$  components compensate each other, the result is a spin density along the  $y$  axis. On the other hand, the injection of a spin current creates a excess of one variety of spin. This results in a shift of the contours, creating opposite charge currents which because they do not compensate each other give rise to a net one along the  $x$  axis. These effects are respectively known as the Edelstein effect and the inverse Edelstein effect. These effects unlike the spin Hall effect only take place at the interface where the symmetry is broken and create a spin density in the  $y$  direction. As we have hinted at, LAO/STO interfaces makes good candidate as spin-charge conversion systems. If in Fig. 6.2 (b-d) we presented the simple case of one parabolic band, in reality the electronic structure of STO in LAO/STO system is more complicated. As shown in Fig. 6.2 (e) the band structure of STO presents avoided crossing points between the  $d_{xy}$  band and the heavier  $d_{xz/yz}$  band. By applying a gate voltage, we can shift the Fermi level in order to scan the potential of spin-charge conversion of the different Fermi surfaces. The maximum of conversion efficiency is reached when we are in the multi-band regime. For more details about this, please refer to D. C. Vaz *et al* [122], where by using Al/STO interfaces the authors reached a conversion efficiency of two orders of magnitude superior to the canonical SOC system of Pt.

### 6.1.2 Rare-earth titanate/STO systems

After the rush on LAO/STO interfaces, some groups explored other STO based interfaces, among them rare-earth titanate/STO interfaces. In this case, the 2DES is expected to arise from the fixed charge disparity at the interface. Indeed, if STO is made of alternating neutral  $Ti^{+4}O_2^{-2}$  and  $Sr^{+2}O^{-2}$  layers, rare earth titanates (RTO) are constituted from  $Ti^{+3}O_2^{-2}$  and  $R^{+3}O^{-2}$  respectively charged -1 and +1. Thus, the interface presents a charge discontinuity that could be compensated by a 2DES. In absence of other charge compensation mechanism such as defects, dislocations, interfacial mixing, roughness or nonstoichiometry, we expect a transfer of 0.5  $e$  per u.c. at the interface (see Fig. 3.9 (c)).

These types of interfaces have the particularity to exploit the interplay of Mott insulator and band insulator. We can thus expect to introduce correlations and magnetism in the STO 2DESSs.

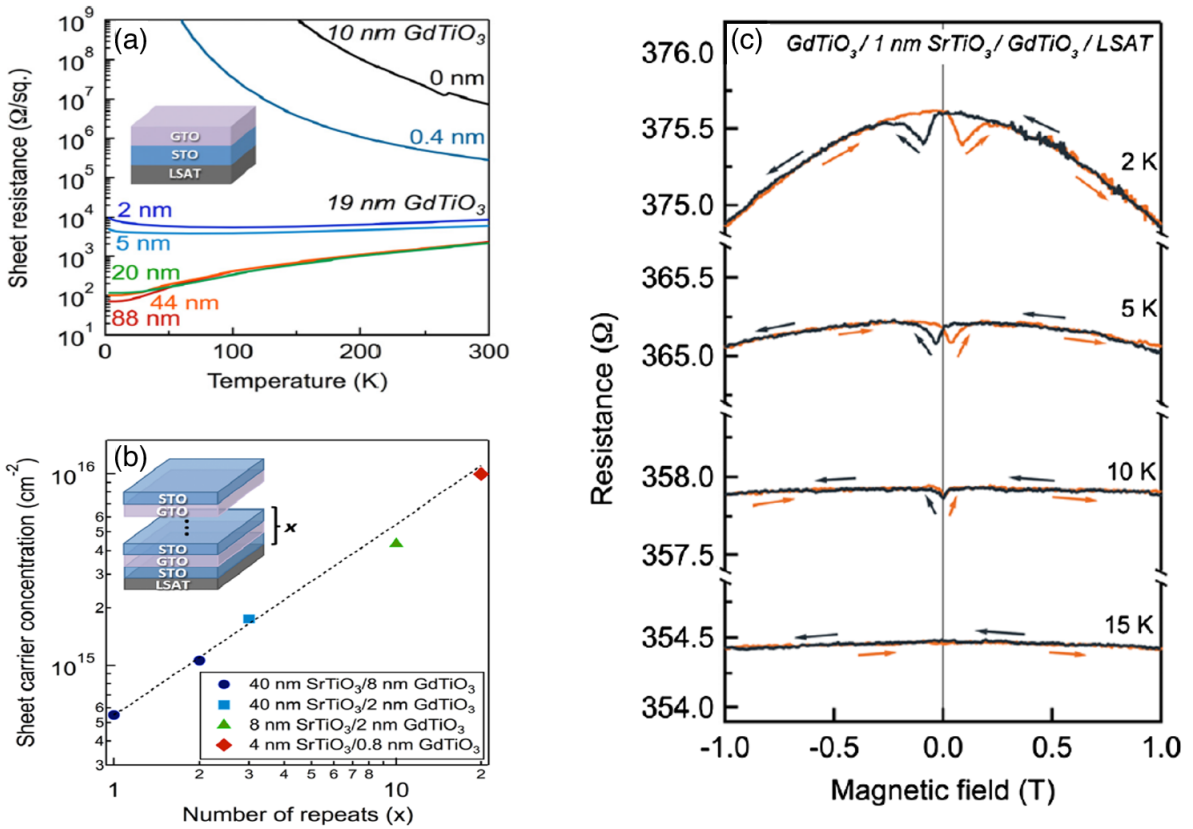


Figure 6.3: (a) Sheet resistance as a function of temperature for GdTiO<sub>3</sub>/SrTiO<sub>3</sub>/LSAT structures with varying SrTiO<sub>3</sub> thicknesses, indicated by the labels. The GdTiO<sub>3</sub> film grown directly on LSAT is labeled 0 nm [56]. (b) Room temperature sheet carrier concentrations of SrTiO<sub>3</sub>/GdTiO<sub>3</sub>/SrTiO<sub>3</sub> multilayers as a function of multilayer repeats (x). The dashed line indicates the expected sheet carrier concentration scaling with number of repeats as calculated from the xij1 sample [56]. (c) Magnetoresistance of a 4 nm GdTiO<sub>3</sub>/1 nm SrTiO<sub>3</sub>/4 nm GdTiO<sub>3</sub>/LSAT heterostructure at 15 K, 10 K, 5 K, and 2 K. Hysteresis appears below approximately 10 K in sweeps with increasing and decreasing B, respectively. Adapted from [123]

Moetakef *et al* in the Stemmer group have performed an extensive study of GdTiO<sub>3</sub>/SrTiO<sub>3</sub> interfaces. As we previously discussed, RTO films must be grown at low oxygen pressure that would reduce a bulk substrate. This is why LSAT is the substrate of choice to grow STO films on top of which one can grow titanates, avoiding the risk of putting them in contact with a huge reservoir of high mobility oxygen vacancies. In addition, LSAT has relatively small lattice mismatch of 0.9 % with STO and is also diamagnetic allowing for magnetic easier characterization. In Fig. 6.3 (a), we can see the appearance of a metallic behavior with the addition of STO. The metallicity increases when the thickness is above 2 nm and reaches saturation above 50 nm. We could first think that this is an effect of oxygen vacancies in STO since the metallic behavior scales with its thickness. However, as the Fig. 6.3 (b) shows the sheet carrier density also scale with the number of repeats of the STO/GTO interface. Still it is worth noting that this interfaces do not have the same thickness of their constituents. If the carriers were purely coming from oxygen vacancies, the second, the fourth and fifth points should have the same sheet carrier density of  $1 \times 10^{15} \text{ cm}^{-2}$ , which is obviously not the case. This shows that, even if there could be some conduction from the STO, there is a clear contribution from conducting interfaces. Fig. 6.3 (c) shows the appearance of negative magnetoresistance and an hysteretic behavior at low temperature. This has been explained in [123] by the influence of the ferrimagnetic layers of GdTiO<sub>3</sub>. However, this picture is uncertain because similar behavior has been observed in strongly

doped STO [123, 124] and that the measured  $T_C \simeq 20$  K of GTO is above the transition temperature seen in Fig. 6.3 (c).

## 6.2 Optimization of STO thin films

As we have shown in the previous section, in order to realize the rare-earth titanate/ STO heterostructure we need to grow STO thin films. In this section, we show the results of our optimization the growth conditions for  $\text{SrTiO}_3$ . As for the growth of LAO/STO interfaces the STO surface need to be extremely well defined and safe from any defects. Indeed, if these conditions are not match the resulting interfaces will be insulating. We have thus to aim at two goals, first we have to make sure than our STO films have as little defects a possible and secondly that these defects do not prevent a metallic regime to exist.

According to Jalan *et al* [81, 80, 125] the obtention of high quality STO requires a low oxygen content. To do so we used the growth condition developed in section 4.1 under argon pressure. All the following optimization has been done by PLD with a monocrystalline target of STO.

### 6.2.1 Homoepitaxy study

The first experimental investigation of the quality of our STO films is done by the growth of homoepitaxial samples. By doing so we can measure the spatial coherence of the STO film with the substrate of the same material. By performing X-ray diffraction, we can observe the presence of Laue oscillations. If usually the presence of Laue oscillations indicates the quality of a film, here it means that we measure a film/substrate interaction, thus showing a different structure and/or composition between the two.

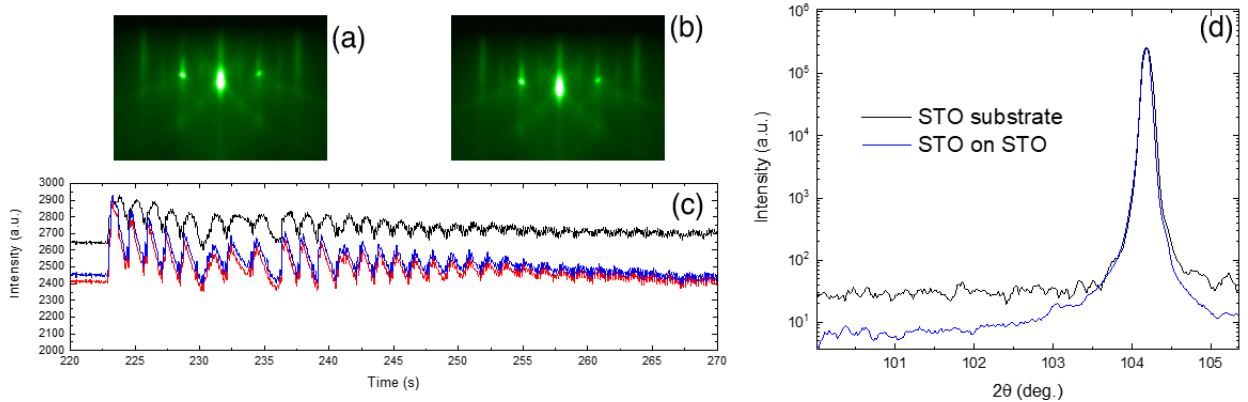


Figure 6.4: RHEED pattern before (a) and after (b) deposition at 1100 °C. (c) RHEED oscillations during the growth (note that the oscillations are recovered by waiting few seconds. (d) X-ray diffraction  $2\theta - \omega$  scan around the (004) substrate peak reflection of a bare  $\text{TiO}_2$  terminated substrate and a homoepitaxied thin film of STO (20 nm).

By using a background pressure of  $1 \times 10^{-3}$  mbar of argon we reached the desired low oxygen content required at the high temperature (1100 °C) to obtain high quality samples. When applying these conditions, we obtain the RHEED patterns of Fig. 6.4 (a,b) respectively before and after the growth. The fact that this remains almost completely unchanged is the sign of the high coherence between substrate and film. The oscillations presented in Fig. 6.4 (c) while decreasing in intensity were quickly recovered by pausing the growth, thus highlighting the effect of the growth dynamics.

Finally, we chose to measure the XRD on the (004) STO peak because of the easier deconvolution at high angle between substrate and film peak. Despite a change in background the peak look exactly the same before and after growth. In addition, no Laue oscillations could be seen indicating the coherence of the film. This is key because the presence of dislocations or non-stoichiometry would result in a difference in density allowing interferences between film and substrate. All of these measurements point toward a fully homoepitaxed and stoichiometric STO film.

### 6.2.2 Growth of Nb:STO on STO

As a more advanced test for the quality of our STO films, we grew Niobium 0.5 % doped STO for which the conduction is expected to be very sensitive to strain and defects. Thus obtaining a conducting sample would be the sign for a good sample quality.

Following the recipe of Kozuka *et al* in [126, 127], we grew a 10 nm thick layer of Nb 0.5 %:SrTiO<sub>3</sub> sandwiched between two 100 nm thick SrTiO<sub>3</sub> layers on a STO substrate.

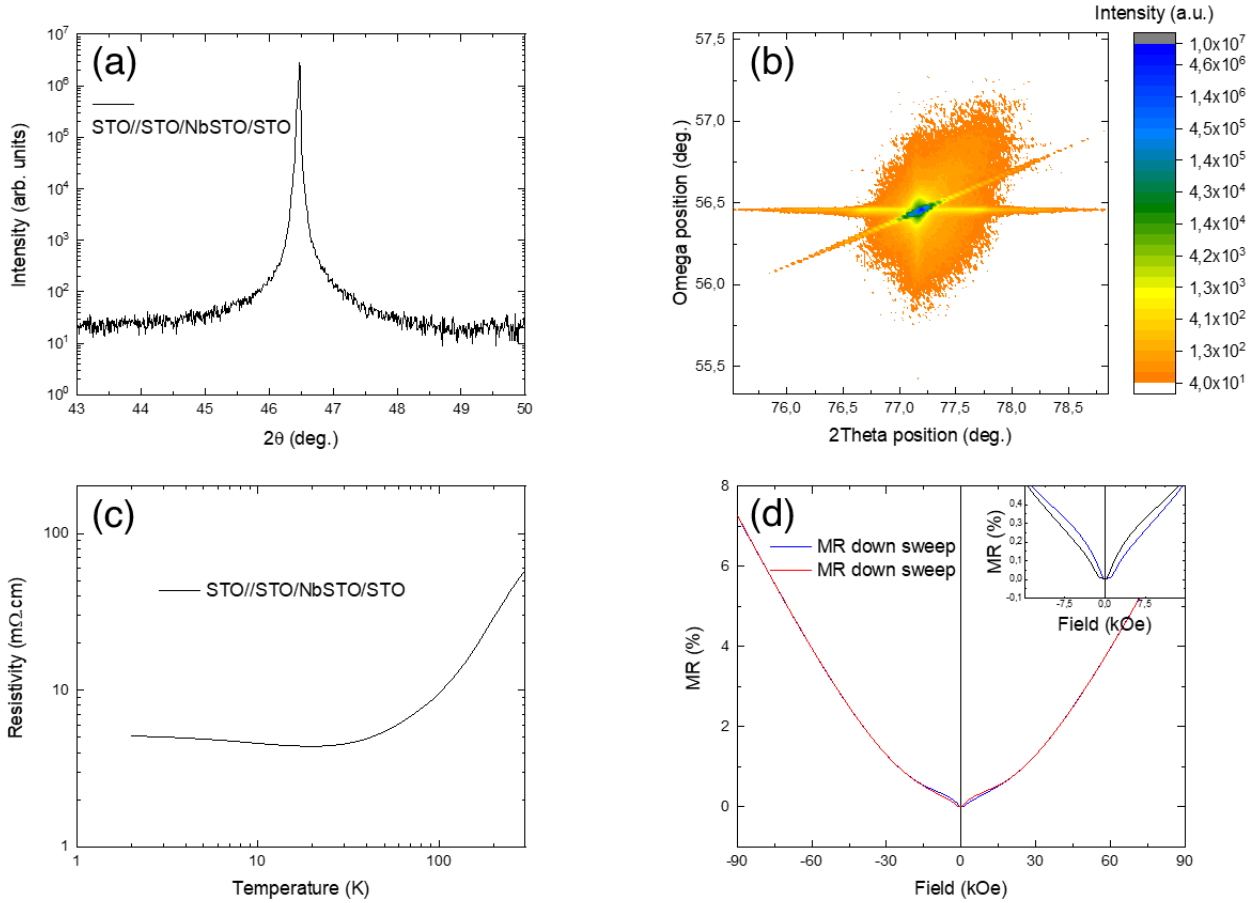


Figure 6.5: (a) X-ray diffraction  $2\theta - \omega$  scan around the (002) reflection of the STO substrate. (b) RSM on the (103) plane. (c) Resistance as a function of temperature at 9 T, Hall effect as a function of Field and Magneto-resistance for Nb 0.5% :STO on STO (001) treated as in [19]. (d) Magneto resistance as a function of the field at 2 K. The inset highlights the hysteresis observed at low field.

We first measured a  $2\theta - \omega$  scan around the (002) plane and could not see any trace of a film peak. In order confirm the result of Fig. 6.5 (a), in (b) we measured the reciprocal space map of the (103) plane showing that our film is fully strained. On the side of the transport in Fig. 6.5 (c), we obtained a metallic behaviour consistent what we expected. We noticed a small upturn at 20 K corresponding to either Kondo or localization effect. The obtained a carrier density at 2 K of  $3.28 \times 10^{20} \text{ cm}^{-3}$

and a mobility of  $526 \text{ cm}^2.\text{V}^{-1}.\text{s}^{-1}$  which closely correspond to the values presented in the literature [126, 127]. In Fig. 6.5 (d) we can see that the magneto resistance of the sample presents the usual quadratic field dependency of metal but what looks like a weak localization effect at low field and low temperature. One can also notice a clear hysteresis at this low fields in the inset. This might be due to the reported magnetism of doped STO as it is reported in the literature [123, 124]. This is supported by the fact that this hysteresis appears only below 10 K as reported in [123].

### 6.2.3 Growth on LSAT (001)

To further check the quality of our growth parameters, we move to LSAT with a misfit of 0.9%, which will introduce disorder to the system. Overall, LSAT is broadly used in the realization of STO based 2DES when the STO is not the substrate itself. Since we needed a smooth substrate, we used the method in section 2.1.4. Despite the misfit, we still manage to observe conduction in our films.

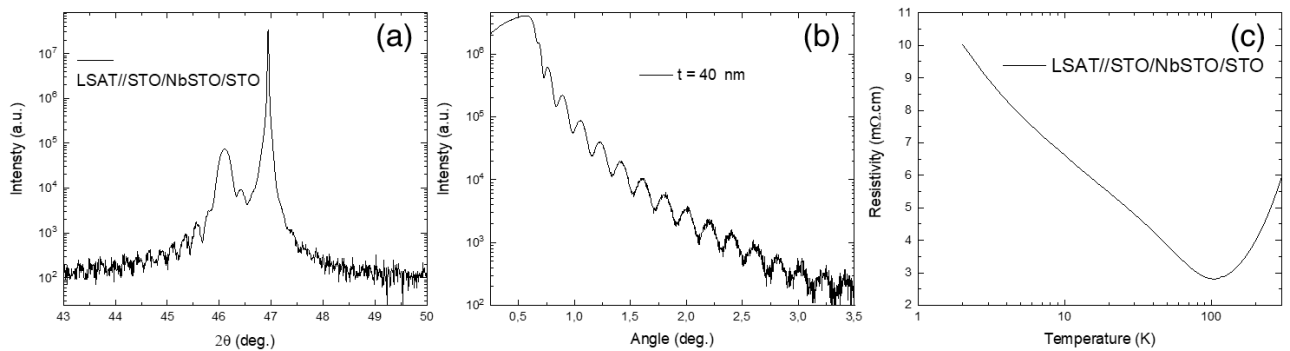


Figure 6.6: (a) X-ray diffraction  $2\theta - \omega$  scan around the (002) reflection of the LSAT substrate. (b) X-ray reflectivity scan. (c) Resistance as a function of temperature. The temperature axis is plotted in log scale.

Since this time the density difference between substrate and film is significant, we can observe Laue fringes in Fig. 6.6 (a). Their fit gives us a thickness of the 40.5 nm which correspond to 100 unit cells. We performed a reflectivity scan on the sample in order confirm that value in Fig. 6.6 (b). It effectively yield to a thickness of 40 nm, coherent with the aimed stack of 10/10/20 nm (resp. STO/NbSTO/STO). Finally, in Fig. 6.6 (c) we measure the resistivity as a function of the temperature and observed a clear metallic behavior between 300 and 100 K. We also observe what appears to be a Kondo effect at low temperature since this behavior seems to be linear when the temperature axis is in log scale. The Kondo effect corresponds to the scattering of electrons on magnetic "impurities" in a metal thus, resulting in a increase of resistivity at low temperature. It was modelized by Jun Kondo in 1964 [128]; in it by summing all scattering events by exchange interactions and considering only the electrons at  $k_B T$  around the Fermi level, he obtained a logarithmic dependence of the temperature.

$$\rho(T) = \rho_0 + aT^2 + c_m \log\left(\frac{\mu}{k_B T}\right) + bT^5 \quad (6.1)$$

where  $\rho_0$  is the residual resistivity and  $a, b, c_m$  and  $\mu$  are constant independent of the temperature. Here the Kondo effect corresponds to the term in  $\log(T)$  whereas the term in  $T^2$  corresponds to the Fermi liquid properties of a metal and the term in  $T^5$  corresponds to the phonon scattering. Thus, at low temperature the Kondo term dominates.

## 6.3 2DES systems

### 6.3.1 LSAT//STO/DTO/LAO

After trying to grow STO on top of LSAT in section 6.2.3, we then grew DTO on top of it and finally used LAO to cap it and prevent further oxidation. We found out that the annealing at high oxygen pressure had a tendency to destroy the magnetic properties of DTO, most likely converting the titanium ions into 4+ or even turn the structure into the pyrochlore phase. However, we have seen that for thin enough STO the annealing was not needed. After some first measurements in fan unpatterned STO/DTO/LAO stack of respectively **5**, **10** and **20** nm, we patterned it into a Hall bar in order to have trustworthy measurement of the carrier density. In order to do so, we used the recipe described in section 2.2.5.

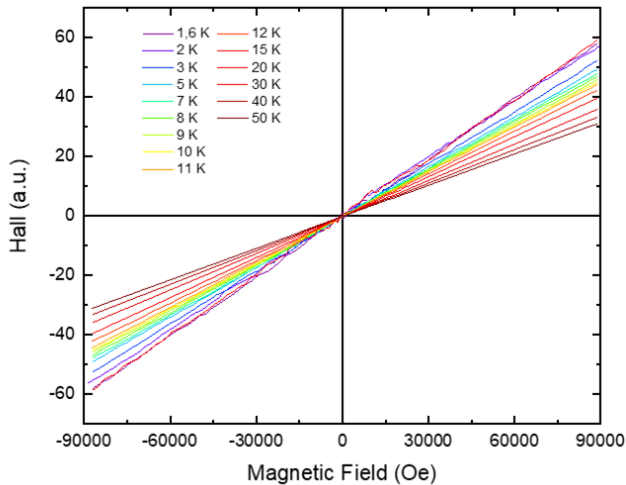


Figure 6.7: Hall measurement as function of field of STO/DTO/LAO multilayer

From Fig. 6.7 we extracted a sheet carrier density ranging from  $1.77 \times 10^{14}$  to  $9.43 \times 10^{13} \text{ cm}^{-2}$  which appears coherent with the idea of a 2DES. Indeed, with a carrier density of  $10^{20} \text{ cm}^{-3}$  this concentration seems incompatible with the hypothesis of a fully doped STO layer. We then are either in a presence of a 2DES or a extremely dilute doping of STO.

### 6.3.2 Transport properties

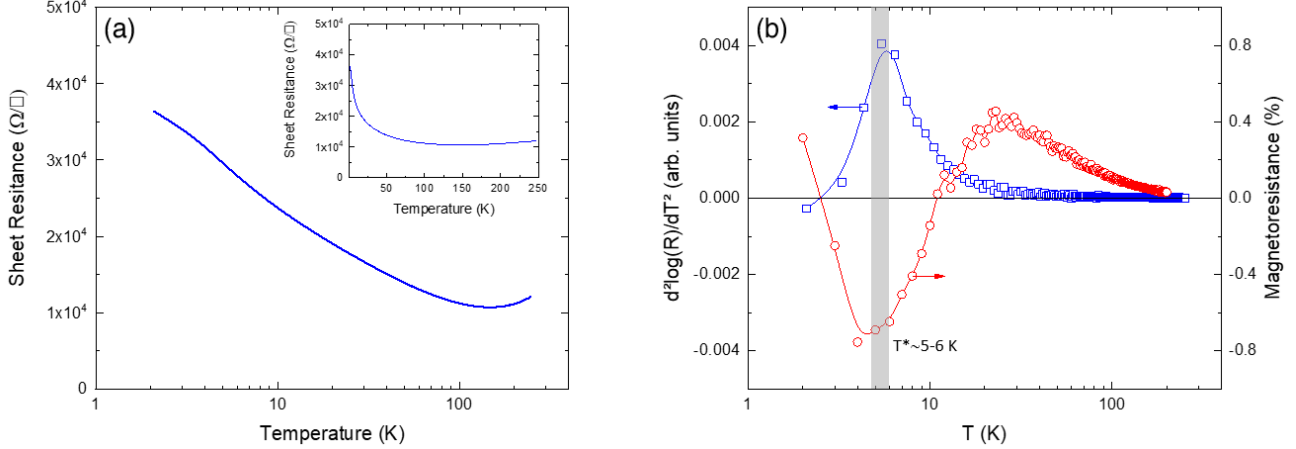


Figure 6.8: (a) Sheet resistance as a function of temperature. (b) Second derivative of the sheet resistance (left axis and blue hollow squares) and the magnetoresistance (right axis and red hollow dots) as function of the temperature. The temperature axis is plotted in log scale for both graphs, except for the inset of (a).

We first measure the sheet resistance as a function of the temperature Fig. 6.8 (a) and as we can see in the inset that the sample presents a metallic behavior until about 100 K where an up turn occurs; sign of a localization of the electrons. When plotting as a function of the log of the temperature, we can notice a seemingly linear behavior at low temperature. It could reflect the presence of a Kondo effect at these temperatures. An inflection seems to be present at 3 K, however this is to take with caution because of the lower effective sampling of the curve at those temperatures. In addition, the temperature fluctuations are stronger at low temperature and their consequences are enhanced by the use of logarithmic scale. Another possibility to take into consideration is the presence of the superposition of different effects. In Fig. 6.8 (b), we plotted the second derivative of the curve and effectively observe a maximum corresponding to the aforementioned inflection. Interestingly, when plotting the magnetoresistance (MR) vs temperature, we see a negative maximum that seems to correspond to the inflection around 5-6 K. We will now analyze the magnetoresistance as function of the field.

### 6.3.3 Magneto-conductivity

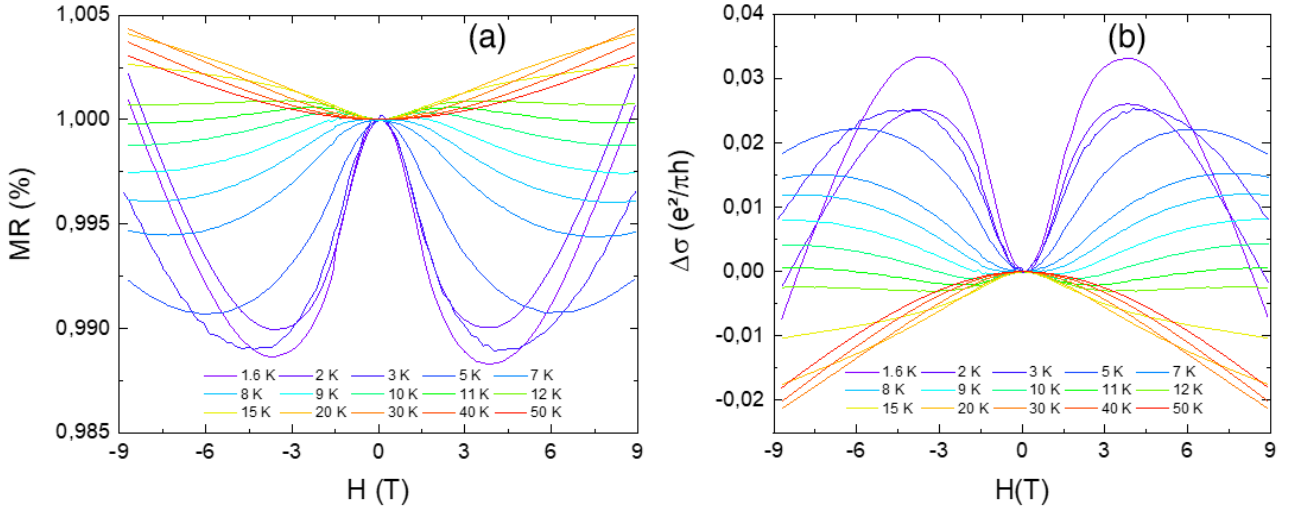


Figure 6.9: (a) Magneto-resistance as a function of field. (b) Magneto-conductance as a function of field. At temperature ranging from 1.6 K to 50 K.

If an apparent classical  $H^2$  behavior (Lorentz magnetoresistance) can be observed in the MR curve displayed in Fig. 6.9 (a) at high temperature, at lower temperature a more complex evolution of the magnetoresistance as a function of the field can be seen. The first striking feature is the negative MR preeminent at the lower temperatures and low field and a positive one at high field. However, it is worth noting that at intermediate temperatures we can see that the previous trend is inverted. A positive MR at low field and negative one at high field is observed at 10 K for example. This led us to believe that this behavior is not the simple superposition of two opposite effects but most likely at least three effects with different temperature dependencies. In order to dress a complete picture of this system, we will investigate different candidates to contribute the MR.

#### Kondo effect

As we previously mentioned the Kondo effect increases the resistance of the material at low temperature. It is the result of the scattering of electrons by magnetic impurities which interact through either paramagnetism or superparamagnetism at low temperature and follow a Brillouin function; seen in section 4.3. As expected the Kondo effect is proportional to the square of the resulting magnetic moment and has a log dependency, as seen experimentally.

$$\rho(H, T) = \rho_{K_0} \left\{ 1 - \ln \left( \frac{T}{T_K} \right) \sqrt{\ln^2 \left( \frac{T}{T_K} \right) + S(S+1)\pi^2} \right\} \left( 1 - B^2 \left[ \frac{g\mu_0\mu_B SH}{k_B(T+T_K)} \right] \right) \quad (6.2)$$

where  $\rho_{K_0}$  is the temperature independent Kondo resistance,  $T_K$  is the characteristic temperature of the Kondo effect,  $k_B$  is the Boltzmann constant,  $\mu_B$  the Bohr magneton,  $S$  the spin of impurities and  $B$  is the Brillouin function, not to confuse with the magnetic induction.

The logarithm temperature dependency Eq 6.2 is derived by the summation of all the scattering events experienced by an electron as explained in [128]. In this article J. Kondo establish the logarithmic variation but the exact form of this expression was refined in [129] by D. R. Hamann who solved the integral equation with the help of the residue theorem. In a second time, we need to modulate the Hamann formula by the spin polarization as it has been done in [130]. The third factor of Eq 6.2

can be understood as such. It varies as the square of the Brillouin function which itself represents the saturation of a magnetic moments population. In [131] Liu *et al* observed similar behaviors and used Eq 6.2 in order to fit it. However, it can not account for the regime observed at intermediate temperatures. As we have said, at 10 K a positive MR can be seen at low field and negative MR one at high field. This is incompatible with the Kondo effect as presented above since it is expect to saturate sooner and act a low field. In this situation, we need to add other low temperature effect in order to account for the experimental data.

## Weak localization and anti-localization

Weak localization (WL), as presented in [132], is a process by which electrons are backscattered by disorder in low dimension systems. From a quantum point of view the electrons interfere constructively with themselves across the different self-intersecting paths they could take.

As a result, they effectively follow a random walk which makes the transport regime diffusive instead of ballistic and thus increasing the resistivity.

As a result their probability density increases where the interference are constructive effectively localizing the electron and thus increasing the resistivity.

Having taken the WL into account, we have to consider its counterpart the weak anti-localization (WAL) in our case. Indeed, WAL takes place when spin orbit coupling (SOC) is present and with DTO based 2DES we can expect a sizable SOC. The SOC breaks the symmetry between the two ways an electron can go through a self-intersecting path. As a result the interference are this time destructive and lead to a decrease of resistivity. Both WL and WAL are described by the Hikami-Larkin-Nagaoka equation [133]:

$$\Delta\sigma = \sigma(H) - \sigma(0) = \frac{e^2}{2\pi^2\hbar} \left[ \ln\left(\frac{H_\phi}{H}\right) - \psi\left(\frac{1}{2} + \frac{H_\phi}{H}\right) \right] + \frac{e^2}{\pi^2\hbar} \left[ \ln\left(\frac{H_{SO} + H_e}{H}\right) - \psi\left(\frac{1}{2} + \frac{H_{SO} + H_e}{H}\right) \right] - \frac{3e^2}{2\pi^2\hbar} \left[ \ln\left(\frac{(4/3)H_{SO} + H_\phi}{H}\right) - \psi\left(\frac{1}{2} + \frac{(4/3)H_{SO} + H_\phi}{H}\right) \right] \quad (6.3)$$

where  $e$  is the elemental charge,  $\hbar$  the Planck constant,  $H_\phi$  is the phase coherence field,  $H_e$  is the elastic characteristic field,  $H_{SO}$  is the spin-orbit characteristic field and  $\psi$  is the digamma function equal to  $\psi(x) = \frac{\partial \ln(\Gamma(x))}{\partial x}$  with  $\Gamma(x)$  the well known gamma function.

We can see that, as expected, the WL and WAL contribution goes to zero as  $H$  do so. If the characteristic fields can be difficult to interpret we can instate manipulate the characteristic length as  $H_i = \frac{\hbar}{4el_i^2}$  or a characteristic time  $\tau_i = \frac{v_F}{l_i} = \frac{(3\pi^2\nu)^{1/3}}{l_i}$  where  $v_F$  is the Fermi speed and  $\nu$  the density of states. It is worth noting that if the weak anti-localization can also give positive magneto-conductivity (MC), we can not get rid of the Kondo effect. If we do so the resulting spin orbit coupling characteristic time would be off by orders of magnitude.

## Final model and fitting

In order to be able to compare the effect presented above, we convert Eq 6.2 into the conductivity contribution of the Kondo effect. This is why we have plotted the conductivity in Fig. 6.9 (b) of our sample.

Eq 6.2 then becomes:

$$\Delta\sigma_{\text{Kondo}}(H, T) = \sigma_{K_0} \frac{B^2 \left[ \frac{g\mu_0\mu_B SH}{k_B(T+T_K)} \right]}{1 - B^2 \left[ \frac{g\mu_0\mu_B SH}{k_B(T+T_K)} \right]} \frac{\sqrt{\ln^2 \left( \frac{T}{T_K} \right) + S(S+1)\pi^2}}{1 - \ln \left( \frac{T}{T_K} \right)} \quad (6.4)$$

Finally, after adding the Lorentz contribution  $-A_k B^2$  to Eq 6.3 and 6.4 we obtain a somewhat complete model of our observed MR.

$$\begin{aligned} \Delta\sigma = \sigma(H) - \sigma(0) = & C \left( \frac{e^2}{2\pi^2\hbar} \left[ \ln \left( \frac{H_\phi}{H} \right) - \psi \left( \frac{1}{2} + \frac{H_\phi}{H} \right) \right] + \frac{e^2}{\pi^2\hbar} \left[ \ln \left( \frac{H_{SO} + H_e}{H} \right) - \psi \left( \frac{1}{2} + \frac{H_{SO} + H_e}{H} \right) \right] \right. \\ & \left. - \frac{3e^2}{2\pi^2\hbar} \left[ \ln \left( \frac{(4/3)H_{SO} + H_\phi}{H} \right) - \psi \left( \frac{1}{2} + \frac{(4/3)H_{SO} + H_\phi}{H} \right) \right] \right) \\ & + \sigma_{K_0} \frac{B^2 \left[ \frac{g\mu_0\mu_B SH}{k_B(T+T_K)} \right]}{1 - B^2 \left[ \frac{g\mu_0\mu_B SH}{k_B(T+T_K)} \right]} \frac{\sqrt{\ln^2 \left( \frac{T}{T_K} \right) + S(S+1)\pi^2}}{1 - \ln \left( \frac{T}{T_K} \right)} - A_k B^2 \quad (6.5) \end{aligned}$$

Now in order to apply it to a fit of our data, we first need to strongly constrain all of our parameters, otherwise the result would be meaningless. Nevertheless, given their high number one should take these results as a qualitative explication of the physics of this system. Indeed we have five parameters to fit  $H_\phi$ ,  $H_e$ ,  $H_{SO}$ ,  $T_K$  and  $S$ . First we can tentatively ascribe  $T_K$  to the maximum of the second derivative of the resistivity in Fig. 6.8 (b), it yields to a temperature of  $6 \pm 0.5$  K.  $\sigma_{K_0}$  depends on the strength of the Kondo effect and can be obtained by fitting the low temperature low field data where only the Kondo effect is expected to play a major role, then we reintroduce the found value to the rest of the calculations.  $A_k$  is proportional to the electron mobility ( $\mu$ ) and can be compared with the expected values. For the weak localization and anti-localization the characteristic fields have been bound by the values in the literature. Finally, the  $C$  factor corresponds to a correction needed to make these effects sizable despite the seemingly activated behavior of the resistivity with temperature. During the fitting process, we mainly used the three temperatures seen in Fig. 6.10, where the different effects appeared the most decoupled. Then, we did an iterative process of using the parameter obtained at one temperature as an indication for other temperature. A last thing that made the fitting easier is the independence from temperature of some of the parameters.

We then proceed to fit our data:

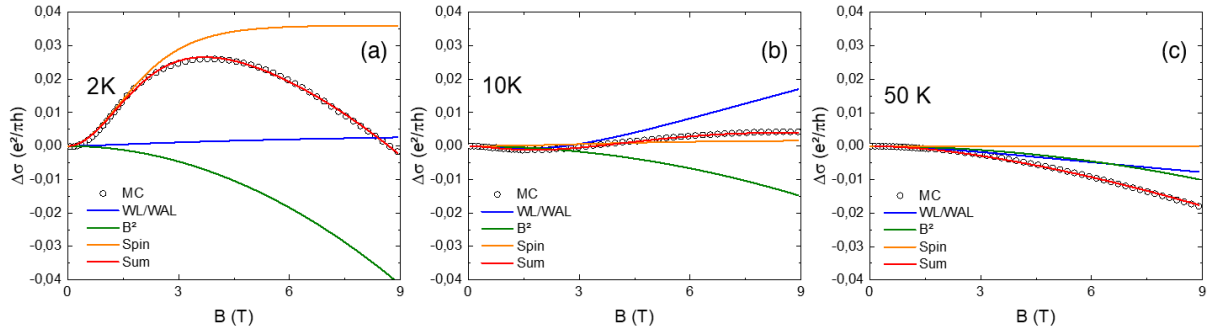


Figure 6.10: (a) Magneto-conductivity (hollow dot) fitted by the complete model (in red) as well as each component WL and WAL (in blue), Lorentz MC (in green) and Kondo effect (in orange) at 2 K (a), 10 K (b) and 50 K (c).

In Fig. 6.10 (a), we can see the superposition of Kondo effect and the Lorenz MC leading to the observed maximum of conductivity before the Lorenz MC lowers it at high field. At 10 K (Fig. 6.10 (b)), we noticed a minimum of conductivity at a non-zero field. Because their expression could not yield to such result, neither the Lorenz MC, the Kondo effect nor a linear combination of the two are enough. This is why, we introduced the weak localization and anti-localization, the combination of which can lead to such behavior. Finally, in Fig. 6.10 (c) we observe a seemingly  $H^2$  behavior with no traces of Kondo at higher temperature. However, the experimental curve could not be properly fit without the addition of WL/WAL effect. This time the WL is dominating.

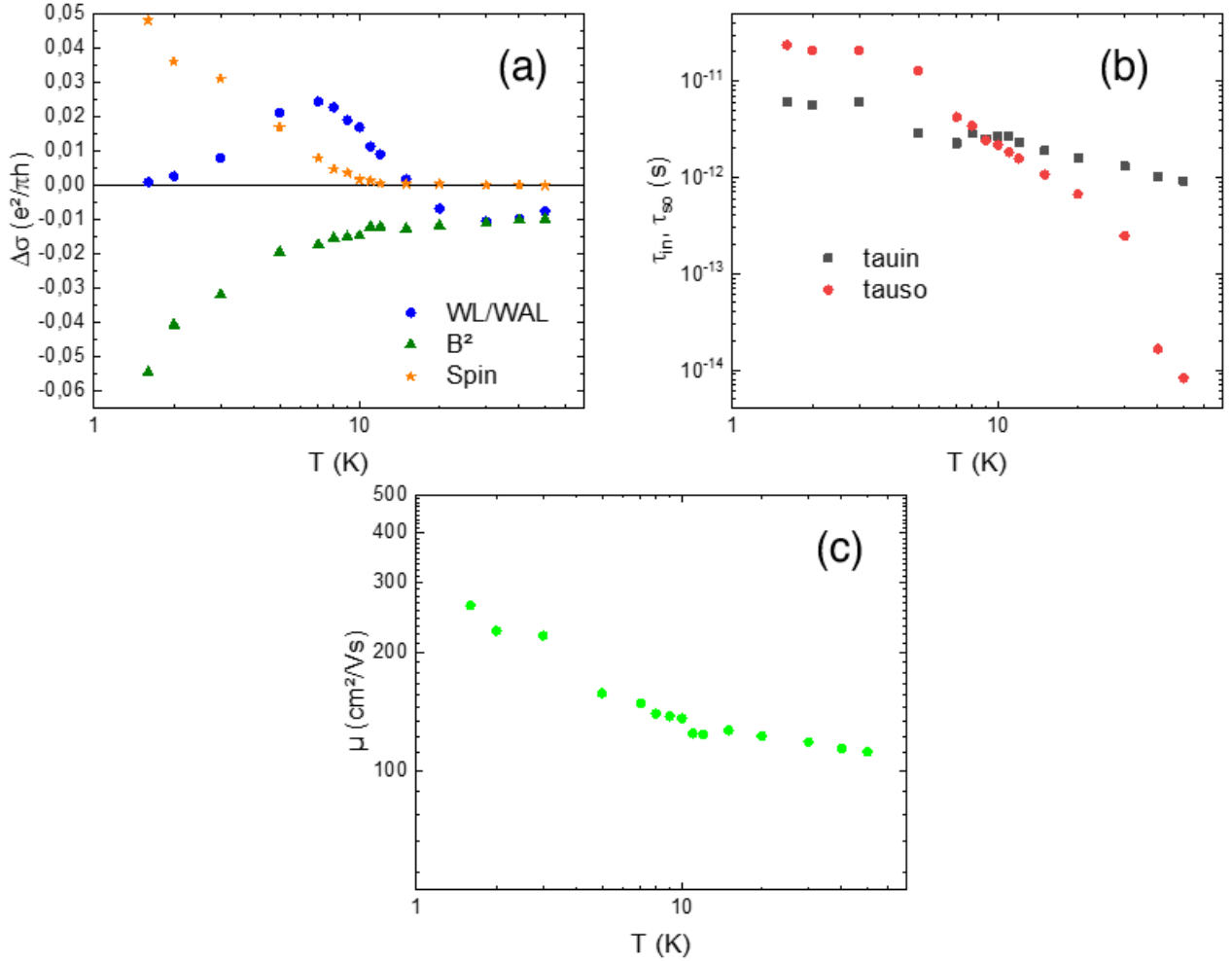


Figure 6.11: (a) Contribution to the magneto-conductivity from WL and WAL (in blue), Lorentz MC (in green) and Kondo effect (in orange) as a function of temperature at 9 T. (b) Characteristic time of inelastic scattering (in black) and spin-orbit coupling (in red). (c) Mobility as a function of temperature extracted from the coefficient of the Lorentz contribution.

By applying this fitting procedure at the other temperatures, we obtain the points of Fig. 6.11. Fig. 6.11 (a) shows us the contributions of each effect to the conductivity. Whereas the Lorentz contribution is monotonic as expected, a weak anti-localization component develops until a maximum around 7 K where the weak localization start dominating even a high field and results in a net negative contribution to the conductivity. This contribution is needed to account for the shape of the seemingly Lorenz contribution above 10 K. This is somewhat at odds with the temperature dependence expected from WL/WAL effects. We can also point that  $\mu$  presented in Fig. 6.11 (c) is weaker than in other oxide 2DESs above 10 K. This might be explained by the limitation of a one band model at these temperatures. The use of two bands might solve this issue and allow us to make the WL vanish; assuming that the mobility of these are different enough to give a non-parabolic result. In Fig. 6.11 (b), we can see the crossover between the characteristic time of inelastic scattering ( $\tau_{in}$ ) and spin-orbit coupling ( $\tau_{SO}$ ). If  $\tau_{SO}$  collapse as expected at higher temperature,  $\tau_{in}$  stays the same order of magnitude, which corroborate what we said earlier. The Kondo effect on its part dominates at low temperature and varies similarly to the behavior observed in Fig. 6.8.

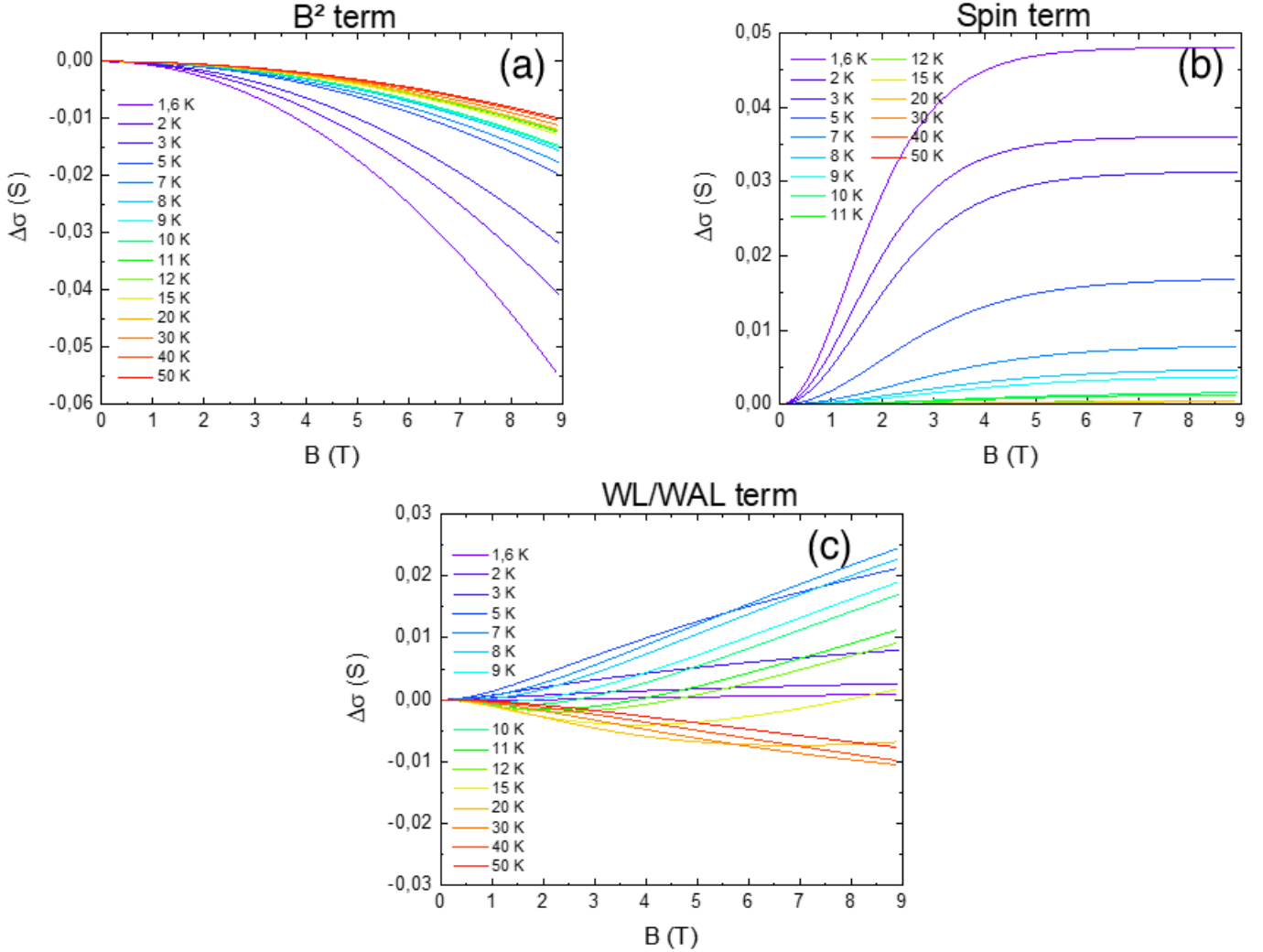


Figure 6.12: (a) Lorentz magneto-conductivity contribution as a function field at different temperature. (b) Kondo effect contribution to magneto-conductivity as a function field at different temperature. (c) Localization effects contribution to magneto-conductivity as a function field at different temperature.

It is also worth noticing that at low temperature , where the Kondo effect dominates Fig. 6.12 (b), the localization effects decrease as seen in Fig. 6.12 (c). This might be explained by the presence of the magnetic field created by the magnetic impurities, which adds a phase that destroys the self-intersecting path responsible for the localization of electrons.

We have to be careful with quantitative interpretations using this toy model. As we have highlighted, the persistence of the localization at higher temperature and the behavior of the mobility tell us that our model need some more refinement. The analysis appears to highlight the presence of magnetism and a spin orbit effect affecting the transport properties, both of which we expected when using DTO in the elaboration of a 2DES. We must however point that the high resistance of our system makes it not well suited to an analysis in a weak localization framework. The analysis should probably be repeated with a different theory, developed for disordered systems where electron-electron interactions are dominant [134]. In addition, it would be important to perform magnetoresistance measurements with the magnetic field in the plane. In the longer term, more efforts should be made to achieve samples with a more metallic character at low temperature, and to perform spin-charge

conversion experiments, to see if the presence of the orbital moment of Dy and Ti, that may survive in the 2DES, would result in an enhanced conversion efficiency.

# Conclusions

In this thesis, we have studied rare-earth titanates thin films from their growth and characterization to their magnetic and transport properties in heterostructures. The focus of this work has been the understanding of the electronic and magnetic state of the rare-earth titanates and their application to 2D electron systems. We grew and optimized a series of titanates such as DyTiO<sub>3</sub>, TmTiO<sub>3</sub>, YTiO<sub>3</sub>, GdTiO<sub>3</sub> and SrTiO<sub>3</sub> in order to develop heterostructures.

We first explained the basis of the physics of perovskite oxides in order to understand the fundamental properties and characteristics of the materials we will study.

To access these, we used a broad range of experimental techniques that we described in the second chapter, going from sample fabrication and classic characterization methods to more advanced ones such as X-Ray absorption spectroscopy.

Having set the basis of both the theory and the experimental techniques, we investigated the specific case of rare-earth titanates. We used the magnetic and structural data to explain the magnetic and transport behavior across the titanate family. During the optimization of DyTiO<sub>3</sub>, we highlighted the difficulties inherent to the growth of rare-earth titanates, which unlike SrTiO<sub>3</sub>, present a Ti<sup>3+</sup> valence state extremely challenging to stabilize. This challenge has been nevertheless overcome by the careful optimization of the growth conditions and the introduction of an argon growth method for our pulsed laser deposited thin films. As we overcame this issue, we evidenced the presence of a magnetically active dead layer (baptized "living-dead" layer) which is linked to the over-oxidation of the sample surface that turns titanium to a 4+ state which then creates a paramagnetic layer of rare-earth moments. The evidence of a paramagnetic layer has been obtained from the thickness dependence of the SQUID magnetic signal. On the other hand, the change of valence at the surface has been observed by both XPS and XAS depth dependent studies. We have found a good correlation between the thicknesses of both of this surface layers indicating their common origin. Capping with a reducing material has proven to help recover the nominal valence state. All these measurements have been reproduced on different titanates (DyTiO<sub>3</sub>, GdTiO<sub>3</sub>, TmTiO<sub>3</sub> and YTiO<sub>3</sub>).

The XAS data obtained in the previous samples revealed a sizable XMCD signal on the titanium L<sub>2,3</sub> edge which led, for some systems, to the observation of a non-zero integral of said signal. This is surprising because the orbital moment of titanium is expected to be quenched and, according to the sum rules, the integral is directly proportional to the orbital moment. Knowing that, we first established a correlation between the non-collinear magnetic structures of some of our compounds and the presence of a non-zero integral. Indeed, the literature suggests that an uncompensated chiral magnetic structure could lead to a "topological" orbital moment. Although the non colinearity of the magnetic structure is evident in DyTiO<sub>3</sub> and TmTiO<sub>3</sub>, the origin of the inversion symmetry breaking necessary to achieve an uncompensated chiral structure remains to elucidate. We proposed several mechanisms, first the breaking of symmetry could happen at the surface where the magnetic order

would be disturbed by the presence of the "living-dead" layer discussed before. Another source could be the domain walls of crystallographic domains or the important strain of 2.9 % from our LAO substrate that could induce strain gradient. We privileged these last two hypotheses because the intensity of the integrals scaled with the probing depth of the different techniques. Indeed, this rules out the first hypothesis because it would not scale with volume. Further experiment still need to be done in order to differentiate between strain gradient or domain wall induced symmetry breaking. Using a substrate like  $\text{KTaO}_3$  should allow for a monodomain growth with a sizable tensile strain of 2.2 %.

In the final chapter of this thesis, we applied the growth methods developed for titanates to the elaboration of rare-earth titanate /  $\text{SrTiO}_3$  interfaces with the goal of obtaining a 2D Electron System (2DES) at this interface. After a quick overview of the literature on  $\text{LaAlO}_3$  /  $\text{SrTiO}_3$  interfaces as well of the rare-earth titanate /  $\text{SrTiO}_3$  interfaces, we optimized the growth of  $\text{SrTiO}_3$  thin film. We first performed homoepitaxial growths of  $\text{SrTiO}_3$  in order to obtain the optimal growth conditions. Then in order to check the strength of said conditions, we transposed it to the growth of Nb0.5%  $\text{SrTiO}_3$  on  $\text{SrTiO}_3$  and LSAT. Since the transport properties of Nb0.5%  $\text{SrTiO}_3$  are tightly bound to the crystallographic quality of the film, the measurement of its metallicity (despite some localization effects at low temperature) indicated our success. Our first samples of STO/DTO interfaces has shown metallicity at room temperature. We then patterned a Hall cross by optical lithography and measured its carrier density of  $\sim 10^{14} \text{ cm}^{-2}$  in line with the one expected from a 2DES. Based on this preliminary result, we have realize STO/DTO/LAO stacks in order to use a symmetric quantum well configuration. When measuring the magnetoresistance as the function of the temperature, we observed a complex behavior that we explained by the competition of several effects acting differently with the temperature. We identified the presence of a weak localization and anti-localization effect at low temperature and a Kondo effect as well as the usual Lorenz contribution, which is dominating at high temperature.

In conclusion, despite the serious difficulty threshold to pass in order to obtain stoichiometric rare-earth titanates, they have proven to be fascinating materials in which the non-collinear magnetism adds new degrees of freedom. Their intrinsic properties and their effect on a 2DES open new perspectives on the elaboration of 2DES. We still need to further investigate the potential presence of an orbital moment in titanates by doing a complete thickness study and grow samples on KTO in order to find a possible origin for this effect. On the 2DES point of view, we still need to improve on the recipe in order to extend the metallic behavior in temperature and improve the mobility by reducing the disorder in our samples.

# Bibliography

- [1] Lesne, E. *Non-Equilibrium Spin Accumulation Phenomena at the LaAlO<sub>3</sub>/SrTiO<sub>3</sub> (001) Quasi-Two-Dimensional Electron System*. Ph.D. thesis, Université Pierre et Marie Curie, France (2015). URL <https://www.theses.fr/191586021>.
- [2] Reyren, N. *et al.* Superconducting Interfaces Between Insulating Oxides. *Science* **317**, 1196–1199 (2007). URL <https://www.sciencemag.org/lookup/doi/10.1126/science.1146006>.
- [3] Mochizuki, M. & Imada, M. G-type Antiferromagnetism and Orbital Ordering due to the Crystal Field from the Rare-Earth Ions Induced by the GdFeO<sub>3</sub>-type Distortion in  $R\text{TiO}_3$  Where  $R = \text{La, Pr, Nd and Sm}$ . *Journal of the Physical Society of Japan* **73**, 1833–1850 (2004). URL <http://journals.jps.jp/doi/10.1143/JPSJ.73.1833>.
- [4] Zhou, H. D. & Goodenough, J. B. Localized or itinerant tio<sub>3</sub> electrons in rtio<sub>3</sub> perovskites. *Journal of Physics: Condensed Matter* **17**, 7395–7406 (2005). URL <http://stacks.iop.org/0953-8984/17/i=46/a=023?key=crossref.96f3571793c6d8cdab2a5aa4707582de>.
- [5] Kojima, A., Teshima, K., Shirai, Y. & Miyasaka, T. Organometal Halide Perovskites as Visible-Light Sensitizers for Photovoltaic Cells. *J. Am. Chem. Soc.* **131**, 6050–6051 (2009). URL <https://pubs.acs.org/doi/10.1021/ja809598r>.
- [6] Tvingstedt, K. *et al.* Radiative efficiency of lead iodide based perovskite solar cells. *Scientific reports* **4** (2014). URL <https://www.nature.com/articles/srep06071>.
- [7] Wang, B. & Ohgushi, K. Post-perovskite Transition in Anti-structure. *Scientific Reports* **6** (2016). URL <http://www.nature.com/articles/srep37896>.
- [8] Khomskii, D. *Transition metal compounds* (Cambridge University Press, 2014). URL [https://books.google.fr/books?id=hEelBAAAQBAJ&printsec=frontcover&source=gbs\\_ge\\_summary\\_r&cad=0#v=onepage&q&f=false](https://books.google.fr/books?id=hEelBAAAQBAJ&printsec=frontcover&source=gbs_ge_summary_r&cad=0#v=onepage&q&f=false).
- [9] Mulliken, R. S. The assignment of quantum numbers for electrons in molecules. ii. correlation of molecular and atomic electron states. *Physical review* **32**, 761 (1928). URL <https://link.aps.org/doi/10.1103/PhysRev.32.186>.
- [10] Mulliken, R. S. Electronic Population Analysis on LCAOMO Molecular Wave Functions. I. *The Journal of Chemical Physics* **23**, 1833–1840 (1955). URL <http://aip.scitation.org/doi/10.1063/1.1740588>.
- [11] Hubbard, J. Electron Correlations in Narrow Energy Bands. *Proceedings of the Royal Society A: Mathematical, Physical and Engineering Sciences* **276**, 238–257 (1963). URL <http://rspa.royalsocietypublishing.org/cgi/doi/10.1098/rspa.1963.0204>.

- [12] Mott, N. F. *Metal-insulator transitions* (Taylor & Francis, London ; New York, 1990), 2nd ed edn.
- [13] Varignon, J., Bibes, M. & Zunger, A. Mott gapping in 3d  $\text{ABO}_3$  perovskites without Mott-Hubbard interelectronic repulsion energy U. *Phys. Rev. B* **100**, 035119 (2019). URL <https://link.aps.org/doi/10.1103/PhysRevB.100.035119>.
- [14] Varignon, J., Bibes, M. & Zunger, A. Origin of band gaps in 3 d perovskite oxides. *Nature Communications* **10**, 1658 (2019). URL <https://www.nature.com/articles/s41467-019-09698-6>. Number: 1 Publisher: Nature Publishing Group.
- [15] Imada, M., Fujimori, A. & Tokura, Y. Metal-insulator transitions. *Reviews of Modern Physics* **70**, 1039 (1998). URL <https://journals.aps.org/rmp/abstract/10.1103/RevModPhys.70.1039>.
- [16] Bocquet, A. E. *et al.* Electronic structure of early 3d -transition-metal oxides by analysis of the 2p core-level photoemission spectra. *Phys. Rev. B* **53**, 1161–1170 (1996). URL <https://link.aps.org/doi/10.1103/PhysRevB.53.1161>.
- [17] Zaanen, J., Sawatzky, G. A. & Allen, J. W. Band gaps and electronic structure of transition-metal compounds. *Physical Review Letters* **55**, 418 (1985). URL <https://journals.aps.org/prl/abstract/10.1103/PhysRevLett.55.418>.
- [18] Kleibeuker, J. E. *et al.* Structure of singly terminated polar  $\text{DyScO}_3$  (110) surfaces. *Physical Review B* **85** (2012). URL <https://link.aps.org/doi/10.1103/PhysRevB.85.165413>.
- [19] Vaz, D. C. *et al.* Growth and Electrostatic/chemical Properties of Metal/ $\text{LaAlO}_3/\text{SrTiO}_3$  Heterostructures. *J Vis Exp* **1** (2018). URL <https://www.jove.com/video/56951/growth-electrostaticchemical-properties-metallaalo3srtio3>.
- [20] Dirsyte, R. *et al.* Thermal-induced change in surface termination of  $\text{DyScO}_3$  (110). *Surface Science* **604**, L55–L58 (2010). URL <http://linkinghub.elsevier.com/retrieve/pii/S0039602810003158>.
- [21] Biswas, A., Yang, C.-H., Ramesh, R. & Jeong, Y. H. Atomically flat single terminated oxide substrate surfaces. *Progress in Surface Science* **92**, 117–141 (2017). URL <http://linkinghub.elsevier.com/retrieve/pii/S0079681617300114>.
- [22] Ngai, J. H. *et al.* Achieving A-Site Termination on  $\text{La}_{0.18}\text{Sr}_{0.82}\text{Al}_{0.59}\text{Ta}_{0.41}\text{O}_3$  Substrates. *Advanced Materials* **22**, 2945–2948 (2010). URL <http://doi.wiley.com/10.1002/adma.200904328>.
- [23] Leca, V., Rijnders, G., Koster, G., Blank, D. H. A. & Rogalla, H. Wet Etching Methods for Perovskite Substrates. *MRS Proceedings* **587** (1999). URL [http://journals.cambridge.org/abstract\\_S1946427400586254](http://journals.cambridge.org/abstract_S1946427400586254).
- [24] Mandani, N. & Nichols, K. G. Laser-evaporated films of  $\text{Al}_2\text{O}_3$  on Si. *Journal of Physics D: Applied Physics* **3**, L7–L9 (1970). URL <https://doi.org/10.1088%2F0022-3727%2F3%2F101>.

- [25] Inam, A. *et al.* Asdeposited high  $T_c$  and  $J_c$  superconducting thin films made at low temperatures. *Applied Physics Letters* **53**, 908–910 (1988). URL <http://aip.scitation.org/doi/10.1063/1.100155>.
- [26] Chen, J. *et al.* Plasma interactions determine the composition in pulsed laser deposited thin films. *Applied Physics Letters* **105**, 114104 (2014). URL <http://aip.scitation.org/doi/10.1063/1.4895788>.
- [27] Ojeda-G-P, A., Schneider, C. W., Döbeli, M., Lippert, T. & Wokaun, A. The flip-over effect in pulsed laser deposition: Is it relevant at high background gas pressures? *Applied Surface Science* **357**, 2055–2062 (2015). URL <http://linkinghub.elsevier.com/retrieve/pii/S0169433215022990>.
- [28] Stender, D. *et al.* Tracing the plasma interactions for pulsed reactive crossed-beam laser ablation. *Journal of Applied Physics* **118**, 165306 (2015). URL <http://aip.scitation.org/doi/10.1063/1.4934553>.
- [29] Eason, R. (ed.) *Pulsed laser deposition of thin films: applications-led growth of functional materials* (Wiley-Interscience, Hoboken, NJ, 2007). OCLC: 249625016.
- [30] Preziosi, D., Sander, A., Barthélémy, A. & Bibes, M. Reproducibility and off-stoichiometry issues in nickelate thin films grown by pulsed laser deposition. *AIP Advances* **7**, 015210 (2017). URL <http://aip.scitation.org/doi/10.1063/1.4975307>.
- [31] Ohring, M. *Materials Science of Thin Films* (Elsevier, 2002). URL <https://linkinghub.elsevier.com/retrieve/pii/B9780125249751X50009>.
- [32] Hasegawa, S. Reflection High-Energy Electron Diffraction. In *Characterization of Materials*, 1–14 (American Cancer Society, 2012). URL <https://onlinelibrary.wiley.com/doi/abs/10.1002/0471266965.com139>.
- [33] Lippmaa, M., Nakagawa, N., Kawasaki, M., Ohashi, S. & Koinuma, H. Growth mode mapping of SrTiO<sub>3</sub> epitaxy. *Appl. Phys. Lett.* **76**, 2439–2441 (2000). URL <https://aip.scitation.org/doi/10.1063/1.126369>. Publisher: American Institute of Physics.
- [34] Hertz, H. Ueber einen Einfluss des ultravioletten Lichtes auf die electrische Entladung. *Annalen der Physik* **267**, 983–1000 (1887). URL <https://onlinelibrary.wiley.com/doi/abs/10.1002/andp.18872670827>.
- [35] Einstein, A. About a heuristic point of view concerning the generation and transformation of light. *AdP* **17**, 132 (1905). URL [http://myweb.rz.uni-augsburg.de/~eckern/adp/history/einstein-papers/1905\\_17\\_132-148.pdf](http://myweb.rz.uni-augsburg.de/~eckern/adp/history/einstein-papers/1905_17_132-148.pdf).
- [36] Alward, J. F. & Fong, C. Y. Theoretical studies on the UV photoemission of CdSe. *J. Phys. C: Solid State Phys.* **8**, 882–894 (1975). URL <http://stacks.iop.org/0022-3719/8/i=6/a=019?key=crossref.74d20d240c21cf0963cb9d146820598>.
- [37] Van der Heide, P. *X-ray photoelectron spectroscopy: an introduction to principles and practices* (Wiley, Hoboken, N.J, 2012). OCLC: ocn744299374.

- [38] Wagner, C. *et al.* Nist standard reference database 20 (2003). URL <http://srdata.nist.gov/xps/>.
- [39] Biesinger, M. C. *et al.* Quantitative chemical state XPS analysis of first row transition metals, oxides and hydroxides. *Journal of Physics: Conference Series* **100**, 012025 (2008). URL <http://stacks.iop.org/1742-6596/100/i=1/a=012025?key=crossref.25e5f253b38ec41c0b11edcf480fa03f>.
- [40] Biesinger, M. C., Lau, L. W., Gerson, A. R. & Smart, R. S. Resolving surface chemical states in XPS analysis of first row transition metals, oxides and hydroxides: Sc, Ti, V, Cu and Zn. *Applied Surface Science* **257**, 887–898 (2010). URL <http://linkinghub.elsevier.com/retrieve/pii/S0169433210010287>.
- [41] Tougaard, S. Universality Classes of Inelastic Electron Scattering Cross-sections. *Surface and Interface Analysis* **25**, 137–154 (1997). URL <https://onlinelibrary.wiley.com/doi/abs/10.1002/%28SICI%291096-9918%28199703%2925%3A3%3C137%3A%3AAID-SIA230%3E3.0.CO%3B2-L>.
- [42] Regan, T. J. *et al.* Chemical effects at metal/oxide interfaces studied by x-ray-absorption spectroscopy. *Phys. Rev. B* **64**, 214422 (2001). URL <https://link.aps.org/doi/10.1103/PhysRevB.64.214422>.
- [43] Ruosi, A. *et al.* Electron sampling depth and saturation effects in perovskite films investigated by soft x-ray absorption spectroscopy. *Phys. Rev. B* **90**, 125120 (2014). URL <https://link.aps.org/doi/10.1103/PhysRevB.90.125120>.
- [44] Bianconi, A., Jackson, D. & Monahan, K. Intrinsic luminescence excitation spectrum and extended x-ray absorption fine structure above the K edge in CaF<sub>2</sub>. *Phys. Rev. B* **17**, 2021–2024 (1978). URL <https://link.aps.org/doi/10.1103/PhysRevB.17.2021>. Publisher: American Physical Society.
- [45] Soderholm, L., Liu, G. K., Antonio, M. R. & Lytle, F. W. X-ray excited optical luminescence (XEOL) detection of x-ray absorption fine structure (XAFS). *The Journal of Chemical Physics* **109**, 6745–6752 (1998). URL <http://aip.scitation.org/doi/10.1063/1.477320>.
- [46] Vaz, C. A. F., Moutafis, C., Buzzi, M. & Raabe, J. X-ray excited optical luminescence of metal oxide single crystals. *Journal of Electron Spectroscopy and Related Phenomena* **189**, 1–4 (2013). URL <http://www.sciencedirect.com/science/article/pii/S0368204813000741>.
- [47] les secrétaires perpétuels, M. Compte rendus hebdomadaires des séances de l'Academie des sciences. *Compte rendus hebdomadaires des séances de l'Academie des sciences* **156** (1896). URL <https://gallica.bnf.fr/ark:/12148/bpt6k32138/f160.image.r=cotton?rk=21459;2>.
- [48] Barkla, C. G. Polarisation in Secondary Rontgen Radiation. *Proceedings of the Royal Society A: Mathematical, Physical and Engineering Sciences* **77**, 247–255 (1906). URL <http://rspa.royalsocietypublishing.org/cgi/doi/10.1098/rspa.1906.0021>.
- [49] Bennett, H. S. & Stern, E. A. Faraday Effect in Solids. *Physical Review* **137**, A448–A461 (1965). URL <https://link.aps.org/doi/10.1103/PhysRev.137.A448>.

- [50] Erskine, J. L. & Stern, E. A. Calculation of the  $m_{2,3}$  magneto-optical absorption spectrum of ferromagnetic nickel. *Physical Review B* **12**, 5016–5024 (1975). URL <https://link.aps.org/doi/10.1103/PhysRevB.12.5016>.
- [51] Schütz, G. *et al.* Absorption of circularly polarized x rays in iron. *Phys. Rev. Lett.* **58**, 737–740 (1987). URL <https://link.aps.org/doi/10.1103/PhysRevLett.58.737>.
- [52] Dirac, P. A. M. & Bohr, N. H. D. The quantum theory of the emission and absorption of radiation. *Proceedings of the Royal Society of London. Series A, Containing Papers of a Mathematical and Physical Character* **114**, 243–265 (1927). URL <https://royalsocietypublishing.org/doi/10.1098/rspa.1927.0039>. Publisher: Royal Society.
- [53] Stöhr, J. Exploring the microscopic origin of magnetic anisotropies with X-ray magnetic circular dichroism (XMCD) spectroscopy. *Journal of Magnetism and Magnetic Materials* **200**, 470–497 (1999). URL <https://linkinghub.elsevier.com/retrieve/pii/S0304885399004072>.
- [54] Greedan, J. E. The rare earth-titanium (III) perovskite oxidesAn isostructural series with a remarkable variation in physical properties. *Journal of the Less Common Metals* **111**, 335–345 (1985). URL <http://www.sciencedirect.com/science/article/pii/0022508885902073>.
- [55] Varignon, J., Grisolia, M. N., Preziosi, D., Ghosez, P. & Bibes, M. Origin of the orbital and spin ordering in rare-earth titanates. *Phys. Rev. B* **96**, 235106 (2017). URL <https://link.aps.org/doi/10.1103/PhysRevB.96.235106>.
- [56] Moetakef, P. *et al.* Electrostatic carrier doping of  $\text{GdTiO}_3/\text{SrTiO}_3$  interfaces. *Appl. Phys. Lett.* **99**, 232116 (2011). URL <http://aip.scitation.org/doi/10.1063/1.3669402>.
- [57] Varignon, J., Bristowe, N. C., Bousquet, E. & Ghosez, P. Coupling and electrical control of structural, orbital and magnetic orders in perovskites. *Sci Rep* **5**, 1–11 (2015). URL <https://www.nature.com/articles/srep15364>.
- [58] Bristowe, N. C., Varignon, J., Fontaine, D., Bousquet, E. & Ghosez, P. Ferromagnetism induced by entangled charge and orbital orderings in ferroelectric titanate perovskites. *Nature Communications* **6** (2015). URL <http://www.nature.com/articles/ncomms7677>.
- [59] Varignon, J., Bristowe, N. C. & Ghosez, P. Electric Field Control of Jahn-Teller Distortions in Bulk Perovskites. *Physical Review Letters* **116** (2016). URL <https://link.aps.org/doi/10.1103/PhysRevLett.116.057602>.
- [60] Varignon, J., Bibes, M. & Zunger, A. Origins versus fingerprints of the Jahn-Teller effect in d -electron A B X 3 perovskites. *Phys. Rev. Research* **1**, 033131 (2019). URL <https://link.aps.org/doi/10.1103/PhysRevResearch.1.033131>.
- [61] Turner, C. W., Collins, M. F. & Greedan, J. E. Magnetic structures of the rare earth orthotitanates  $\text{Rtio}_3$ ; R= Tb, Dy, Tm and Yb. *Journal of Magnetism and Magnetic Materials* **23**, 265–273 (1981). URL <http://www.sciencedirect.com/science/article/pii/0304885381900469>.
- [62] Ashcroft, N. W. & Mermin, N. D. *Solid state physics* (Brooks/Cole Thomson Learning, South Melbourne, 2012), repr edn. OCLC: 935097630.

- [63] Bertaut, E. F., Rado, G. T. & Suhl, H. *Chapter 4: Magnetism. A Treatise on Modern Theory and Material. Vol. 3: Spin Arrangements and Crystal Structure, Domains and Micromagnetics* (New York, 1963). Google-Books-ID: qSi2XwAACAAJ.
- [64] Bousquet, E. & Cano, A. Non-collinear magnetism in multiferroic perovskites. *Journal of Physics: Condensed Matter* **28**, 123001 (2016). URL <http://stacks.iop.org/0953-8984/28/i=12/a=123001?key=crossref>.4543e8245079f6a3459941ba8cdd47ff.
- [65] Arima, T., Tokura, Y. & Torrance, J. B. Variation of optical gaps in perovskite-type 3d transition-metal oxides. *Physical Review B* **48**, 17006–17009 (1993). URL <https://link.aps.org/doi/10.1103/PhysRevB.48.17006>.
- [66] Okimoto, Y., Katsufuji, T., Okada, Y., Arima, T. & Tokura, Y. Optical spectra in (La,Y)TiO<sub>3</sub>: Variation of Mott-Hubbard gap features with change of electron correlation and band filling. *Physical Review B* **51**, 9581–9588 (1995). URL <https://link.aps.org/doi/10.1103/PhysRevB.51.9581>.
- [67] Loa, I. *et al.* Crystal structure and the MottHubbard gap in YTiO<sub>3</sub> at high pressure. *Journal of Physics: Condensed Matter* **23**, 469601 (2011). URL <http://stacks.iop.org/0953-8984/23/i=46/a=469601?key=crossref>.776190649549ffe84a0ea21e0a80fcc9.
- [68] Grisolia, M. N. *et al.* Structural, magnetic, and electronic properties of GdTIO<sub>3</sub> Mott insulator thin films grown by pulsed laser deposition. *Applied Physics Letters* **105**, 172402 (2014). URL <http://aip.scitation.org/doi/10.1063/1.4899277>.
- [69] Bjaalie, L. *et al.* Determination of the Mott-Hubbard gap in GdTIO<sub>3</sub>. *Physical Review B* **92** (2015). URL <https://link.aps.org/doi/10.1103/PhysRevB.92.085111>.
- [70] Ganguly, P., Parkash, O. & Rao, C. N. R. Electron transport and magnetic properties of rareearth orthotitanites and vanadites, LnTiO<sub>3</sub> and LnVO<sub>3</sub>. *physica status solidi (a)* **36**, 669–678 (1976). URL <https://onlinelibrary.wiley.com/doi/10.1002/pssa.2210360227>.
- [71] MacLean, D. A., Ng, H.-N. & Greedan, J. Crystal structures and crystal chemistry of the retio<sub>3</sub> perovskites: RE = La, Nd, Sm, Gd, Y. *Journal of Solid State Chemistry* **30**, 35–44 (1979). URL <https://linkinghub.elsevier.com/retrieve/pii/0022459679901270>.
- [72] Turner, C. W. & Greedan, J. E. Ferrimagnetism in the rare earth titanium (III) oxides, RTiO<sub>3</sub>; R= Gd, Tb, Dy, Ho, Er, Tm. *Journal of Solid State Chemistry* **34**, 207–213 (1980). URL <http://www.sciencedirect.com/science/article/pii/0022459680902236>.
- [73] Gariglio, S., Seo, J. W., Fompeyrine, J., Locquet, J.-P. & Triscone, J.-M. Transport properties in doped Mott insulator epitaxial la<sub>1-y</sub>tio<sub>3+δ</sub> thin films. *Phys. Rev. B* **63**, 161103 (2001). URL <https://link.aps.org/doi/10.1103/PhysRevB.63.161103>.
- [74] Ohtomo, A., Muller, D. A., Grazul, J. L. & Hwang, H. Y. Epitaxial growth and electronic structure of LaTiO<sub>x</sub> films. *Applied Physics Letters* **80**, 3922–3924 (2002). URL <http://aip.scitation.org/doi/10.1063/1.1481767>.
- [75] Schmehl, A., Lichtenberg, F., Bielefeldt, H., Mannhart, J. & Schlom, D. G. Transport properties of LaTiO<sub>3+x</sub> films and heterostructures. *Appl. Phys. Lett.* **82**, 3077–3079 (2003). URL <http://aip.scitation.org/doi/10.1063/1.1572960>.

- [76] Scheiderer, P. *et al.* Tailoring Materials for Mottronics: Excess Oxygen Doping of a Prototypical Mott Insulator. *Advanced Materials* **30**, 1706708 (2018). URL <https://onlinelibrary.wiley.com/doi/abs/10.1002/adma.201706708>.
- [77] Scheiderer, P. *Spectroscopy of Prototypical Thin Film Mott Materials*. Ph.D. thesis, Universität Würzburg, Fakultät für Physik und Astronomie (2019). URL <https://opus.bibliothek.uni-wuerzburg.de/frontdoor/index/index/docId/18635>.
- [78] Moetakef, P. *et al.* Growth and properties of GdTiO<sub>3</sub> films prepared by hybrid molecular beam epitaxy. *Journal of Crystal Growth* **355**, 166–170 (2012). URL <http://linkinghub.elsevier.com/retrieve/pii/S0022024812004721>.
- [79] Locquet, J., Catana, A., Mächler, E., Gerber, C. & Bednorz, J. G. Blockbyblock deposition: A new growth method for complex oxide thin films. *Appl. Phys. Lett.* **64**, 372–374 (1994). URL <http://aip.scitation.org/doi/10.1063/1.111151>.
- [80] Jalan, B., Engel-Herbert, R., Wright, N. J. & Stemmer, S. Growth of high-quality srtio<sub>3</sub> films using a hybrid molecular beam epitaxy approach. *Journal of Vacuum Science & Technology A* **27**, 461–464 (2009). URL <https://avs-scitation-org.proxy.scd.u-psud.fr/doi/10.1116/1.3106610>.
- [81] Jalan, B., Moetakef, P. & Stemmer, S. Molecular beam epitaxy of srtio<sub>3</sub> with a growth window. *Applied Physics Letters* **95**, 032906 (2009). URL <http://aip.scitation.org/doi/10.1063/1.3184767>.
- [82] Chae, S. C. *et al.* Magnetic properties of insulating RTiO<sub>3</sub> thin films. *Journal of Electroceramics* **22**, 216–220 (2009). URL <http://link.springer.com/10.1007/s10832-008-9460-z>.
- [83] Ohtomo, A., Muller, D. A., Grazul, J. L. & Hwang, H. Y. Artificial charge-modulationin atomic-scale perovskite titanate superlattices. *Nature* **419**, 378–380 (2002). URL <http://www.nature.com/articles/nature00977>.
- [84] Xu, P. *et al.* Predictive Control over Charge Density in the Two-Dimensional Electron Gas at the Polar-Nonpolar NdTiO<sub>3</sub> / SrTiO<sub>3</sub> Interface. *Physical Review Letters* **117** (2016). URL <https://link.aps.org/doi/10.1103/PhysRevLett.117.106803>.
- [85] Cao, Y. *et al.* Magnetic Interactions at the Nanoscale in Trilayer Titanates. *Physical Review Letters* **116** (2016). URL <https://link.aps.org/doi/10.1103/PhysRevLett.116.076802>.
- [86] Cao, Y. *et al.* Engineered Mott ground state in a latio<sub>3+δ</sub>/lanio<sub>3</sub> heterostructure. *Nature Communications* **7**, 10418 (2016). URL <http://www.nature.com/doifinder/10.1038/ncomms10418>.
- [87] Yoshii, K. Structure and magnetism of Eu<sub>1-x</sub>DyxTiO<sub>3</sub>. *Journal of Solid State Chemistry* **171**, 345–348 (2003). URL <http://linkinghub.elsevier.com/retrieve/pii/S0022459602002311>.
- [88] Grisolia, M. *Novel interfacial electronic states between correlated insulators*. phdthesis, Université Paris-Saclay (2016). URL <https://tel.archives-ouvertes.fr/tel-01773207>.

- [89] Schneider, C. W. *et al.* The origin of oxygen in oxide thin films: Role of the substrate. *Applied Physics Letters* **97**, 192107 (2010). URL <http://aip.scitation.org/doi/10.1063/1.3515849>.
- [90] Roth, R. S. Pyrochlore-type compounds containing double oxides of trivalent and tetravalent ions. *J. RES. NATL. BUR. STAN.* **56**, 17 (1956). URL [https://nvlpubs.nist.gov/nistpubs/jres/56/jresv56n1p17\\_A1b.pdf](https://nvlpubs.nist.gov/nistpubs/jres/56/jresv56n1p17_A1b.pdf).
- [91] Chen, J. *et al.* Tracing the origin of oxygen for  $\text{La}_{0.6}\text{Sr}_{0.4}\text{MnO}_3$  thin film growth by pulsed laser deposition. *Journal of Physics D: Applied Physics* **49**, 045201 (2016). URL <http://stacks.iop.org/0022-3727/49/i=4/a=045201?key=crossref.a6a5ee0e456c28aea4e805de4c604eae>.
- [92] Bibes, M. *et al.* Surface-induced phase separation in manganites: A microscopic origin for powder magnetoresistance. *Applied Physics Letters* **82**, 928–930 (2003). URL <http://aip.scitation.org/doi/10.1063/1.1543235>.
- [93] Tanuma, S. *et al.* Experimental determination of electron inelastic mean free paths in 13 elemental solids in the 50 to 5000 eV energy range by elastic-peak electron spectroscopy. *Surface and Interface Analysis* **37**, 833–845 (2005). URL <https://onlinelibrary.wiley.com/doi/abs/10.1002/sia.2102>.
- [94] Lesne, E. *et al.* Suppression of the critical thickness threshold for conductivity at the  $\text{LaAlO}_3/\text{SrTiO}_3$  interface. *Nature Communications* **5** (2014). URL <http://www.nature.com/doifinder/10.1038/ncomms5291>.
- [95] Abbate, M. *et al.* Soft-x-ray-absorption studies of the location of extra charges induced by substitution in controlled-valence materials. *Phys. Rev. B* **44**, 5419–5422 (1991). URL <https://link.aps.org/doi/10.1103/PhysRevB.44.5419>.
- [96] Haverkort, M. W. *et al.* Determination of the Orbital Moment and Crystal-Field Splitting in  $\text{LaTiO}_3$ . *Physical Review Letters* **94** (2005). URL <https://link.aps.org/doi/10.1103/PhysRevLett.94.056401>.
- [97] Iga, F. *et al.* Determination of the Orbital Polarization in  $\text{ytio}_3$  by Using Soft X-Ray Linear Dichroism. *Phys. Rev. Lett.* **93**, 257207 (2004). URL <https://link.aps.org/doi/10.1103/PhysRevLett.93.257207>.
- [98] Mizumaki, M. Investigation of the electronic structure in  $\text{eu}_{1-x}\text{dy}_x\text{tio}_3$  by means of soft X-ray absorption spectroscopy. *Solid State Ionics* **172**, 565–568 (2004). URL <http://linkinghub.elsevier.com/retrieve/pii/S0167273804003169>.
- [99] Aeschlimann, R. *et al.* A Living-Dead Magnetic Layer at the Surface of Ferrimagnetic  $\text{DyTiO}_3$  Thin Films. *Advanced Materials* **30**, 1707489 (2018). URL <http://doi.wiley.com/10.1002/adma.201707489>.
- [100] Cao, Y. *et al.* Magnetism and electronic structure of  $\text{YTiO}_3$  thin films. *Applied Physics Letters* **107**, 112401 (2015). URL <http://aip.scitation.org/doi/10.1063/1.4931039>.
- [101] Thole, B. T., Carra, P., Sette, F. & van der Laan, G. X-ray circular dichroism as a probe of orbital magnetization. *Physical Review Letters* **68**, 1943–1946 (1992). URL <https://link.aps.org/doi/10.1103/PhysRevLett.68.1943>.

- [102] Carra, P., Thole, B. T., Altarelli, M. & Wang, X. X-ray circular dichroism and local magnetic fields. *Phys. Rev. Lett.* **70**, 694–697 (1993). URL <https://link.aps.org/doi/10.1103/PhysRevLett.70.694>.
- [103] Chen, C. T. *et al.* Experimental confirmation of the X-ray magnetic circular dichroism sum rules for iron and cobalt. *Physical review letters* **75**, 152 (1995). URL <https://journals.aps.org/prl/abstract/10.1103/PhysRevLett.75.152>.
- [104] Hanke, J.-P. *et al.* Role of Berry phase theory for describing orbital magnetism: From magnetic heterostructures to topological orbital ferromagnets. *Physical Review B* **94** (2016). URL <https://link.aps.org/doi/10.1103/PhysRevB.94.121114>.
- [105] Hanke, J.-P., Freimuth, F., Blügel, S. & Mokrousov, Y. Prototypical topological orbital ferromagnet  $\gamma$ -FeMn. *Scientific Reports* **7**, 41078 (2017). URL <http://www.nature.com/articles/srep41078>.
- [106] dos Santos Dias, M., Bouaziz, J., Bouhassoune, M., Blügel, S. & Lounis, S. Chirality-driven orbital magnetic moments as a new probe for topological magnetic structures. *Nature Communications* **7**, 13613 (2016). URL <http://www.nature.com/doifinder/10.1038/ncomms13613>.
- [107] Dzyaloshinsky, I. A thermodynamic theory of weak ferromagnetism of antiferromagnetics. *Journal of Physics and Chemistry of Solids* **4**, 241–255 (1958). URL <http://www.sciencedirect.com/science/article/pii/0022369758900763>.
- [108] Moriya, T. Anisotropic Superexchange Interaction and Weak Ferromagnetism. *Phys. Rev.* **120**, 91–98 (1960). URL <https://link.aps.org/doi/10.1103/PhysRev.120.91>. Publisher: American Physical Society.
- [109] Treves, D. & Alexander, S. Observation of Antisymmetric Exchange Interaction in Yttrium Orthoferrite. *Journal of Applied Physics* **33**, 1133–1134 (1962). URL <https://aip-scitation-org.proxy.scd.u-psud.fr/doi/10.1063/1.1728631>. Publisher: American Institute of Physics.
- [110] Høtch, M. J., Snoeck, E. & Kilaas, R. Quantitative measurement of displacement and strain fields from HREM micrographs. *Ultramicroscopy* **74**, 131–146 (1998). URL <http://www.sciencedirect.com/science/article/pii/S0304399198000357>.
- [111] von Klitzing, K. The quantized Hall effect (Nobel Lecture) (1985).
- [112] Stormer, H. L. Nobel Lecture: The fractional quantum Hall effect. *Rev. Mod. Phys.* **71**, 875–889 (1999). URL <https://link.aps.org/doi/10.1103/RevModPhys.71.875>.
- [113] Ohtomo, A. & Hwang, H. Y. A high-mobility electron gas at the LaAlO<sub>3</sub>/SrTiO<sub>3</sub> heterointerface. *Nature* **427**, 423–426 (2004). URL <http://www.nature.com/articles/nature02308>.
- [114] Breitschaft, M. *et al.* Two-dimensional electron liquid state at laal<sub>0</sub><sub>3</sub>/sr<sub>2</sub>ti<sub>3</sub> interfaces. *Phys. Rev. B* **81**, 153414 (2010). URL <https://link.aps.org/doi/10.1103/PhysRevB.81.153414>. Publisher: American Physical Society.

- [115] Basletic, M. *et al.* Mapping the spatial distribution of charge carriers in LaAlO<sub>3</sub>/SrTiO<sub>3</sub> heterostructures. *Nature Mater.* **7**, 621–625 (2008). URL <http://www.nature.com/articles/nmat2223>.
- [116] Thiel, S. Tunable Quasi-Two-Dimensional Electron Gases in Oxide Heterostructures. *Science* **313**, 1942–1945 (2006). URL <https://www.sciencemag.org/lookup/doi/10.1126/science.1131091>.
- [117] Schooley, J. F. *et al.* Dependence of the Superconducting Transition Temperature on Carrier Concentration in Semiconducting srtio<sub>3</sub>. *Phys. Rev. Lett.* **14**, 305–307 (1965). URL <https://link.aps.org/doi/10.1103/PhysRevLett.14.305>.
- [118] Lin, X., Zhu, Z., Fauqué, B. & Behnia, K. Fermi Surface of the Most Dilute Superconductor. *Phys. Rev. X* **3**, 021002 (2013). URL <https://link.aps.org/doi/10.1103/PhysRevX.3.021002>.
- [119] Joshua, A., Pecker, S., Ruhman, J., Altman, E. & Ilani, S. A universal critical density underlying the physics of electrons at the LaAlO<sub>3</sub>/SrTiO<sub>3</sub> interface. *Nat Commun* **3**, 1129 (2012). URL <http://www.nature.com/articles/ncomms2116>.
- [120] King, P. D. C. *et al.* Quasiparticle dynamics and spinorbital texture of the srtio<sub>3</sub> two-dimensional electron gas. *Nat Commun* **5**, 1–7 (2014). URL <https://www.nature.com/articles/ncomms4414>.
- [121] Soumyanarayanan, A., Reyren, N., Fert, A. & Panagopoulos, C. Emergent phenomena induced by spinorbit coupling at surfaces and interfaces. *Nature* **539**, 509–517 (2016). URL <https://www.nature.com/articles/nature19820>.
- [122] Vaz, D. C. *et al.* Mapping spincharge conversion to the band structure in a topological oxide two-dimensional electron gas. *Nat. Mater.* **18**, 1187–1193 (2019). URL <http://www.nature.com/articles/s41563-019-0467-4>.
- [123] Moetakef, P. *et al.* Carrier-Controlled Ferromagnetism in SrTiO<sub>3</sub>. *Physical Review X* **2** (2012). URL <https://link.aps.org/doi/10.1103/PhysRevX.2.021014>.
- [124] Middey, S., Meneghini, C. & Ray, S. Evidence of oxygen-vacancy-induced ferromagnetic order in single crystal Mn-doped SrTiO<sub>3</sub>. *Appl. Phys. Lett.* **101**, 042406 (2012). URL <https://aip-scitation-org.proxy.scd.u-psud.fr/doi/full/10.1063/1.4738785>. Publisher: American Institute of Physics.
- [125] Son, J. *et al.* Epitaxial SrTiO<sub>3</sub> films with electron mobilities exceeding 30,000 cm<sup>2</sup> v<sup>-1</sup> s<sup>-1</sup>. *Nature Mater* **9**, 482–484 (2010). URL <http://www.nature.com/articles/nmat2750>.
- [126] Kozuka, Y. *et al.* Enhancing the electron mobility via delta-doping in SrTiO<sub>3</sub>. *Applied Physics Letters* **97**, 222115 (2010). URL <http://aip.scitation.org/doi/10.1063/1.3524198>.
- [127] Kozuka, Y., Hikita, Y., Bell, C. & Hwang, H. Y. Dramatic mobility enhancements in doped SrTiO<sub>3</sub> thin films by defect management. *Applied Physics Letters* **97**, 012107 (2010). URL <http://aip.scitation.org/doi/10.1063/1.3457994>.

- [128] Kondo, J. Resistance Minimum in Dilute Magnetic Alloys. *Progress of Theoretical Physics* **32**, 37–49 (1964). URL <https://academic.oup.com/ptp/article-lookup/doi/10.1143/PTP.32.37>.
- [129] Hamann, D. R. New Solution for Exchange Scattering in Dilute Alloys. *Phys. Rev.* **158**, 570–580 (1967). URL <https://link.aps.org/doi/10.1103/PhysRev.158.570>.
- [130] Felsch, W. & Winzer, K. Magnetoresistivity of (La, Ce)Al<sub>2</sub> alloys. *Solid State Communications* **13**, 569–573 (1973). URL <http://www.sciencedirect.com/science/article/pii/S0038109873800158>.
- [131] Liu, H. *et al.* Observation of the Kondo Effect in Multilayer Single-Crystalline VTe<sub>2</sub> Nanoplates. *Nano Lett.* **19**, 8572–8580 (2019). URL <https://pubs.acs.org/doi/10.1021/acs.nanolett.9b03100>.
- [132] Altshuler, B. L., Khmel'nitzkii, D., Larkin, A. I. & Lee, P. A. Magnetoresistance and Hall effect in a disordered two-dimensional electron gas. *Phys. Rev. B* **22**, 5142–5153 (1980). URL <https://link.aps.org/doi/10.1103/PhysRevB.22.5142>.
- [133] Hikami, S., Larkin, A. I. & Nagaoka, Y. Spin-Orbit Interaction and Magnetoresistance in the Two Dimensional Random System. *Progress of Theoretical Physics* **63**, 707–710 (1980). URL <https://academic.oup.com/ptp/article-lookup/doi/10.1143/PTP.63.707>.
- [134] Lee, P. A. & Ramakrishnan, T. V. Disordered electronic systems. *Rev. Mod. Phys.* **57**, 287–337 (1985). URL <https://link.aps.org/doi/10.1103/RevModPhys.57.287>.

**Titre :** Propriétés magnétique et de transport des couches minces et hétérostructures de titanates de terre rare

**Mots clés :** matériaux corrélés, oxydes, hétérostructures, croissance

**Résumé :** Les oxydes de métaux de transitions possèdent une large gamme de fonctionnalités (superconductivité, magnétisme, ferroélectricité, multiferroicité) découlant de l'interaction d'effets structuraux et de corrélation fortes. De plus, des travaux récents ont mis en lumière une physique propre à leurs interfaces, incluant de la supraconductivité ainsi que de la conductivité classique dans le système bidimensionnel (2DES) créé à l'interface de deux isolants de bande,  $\text{LaAlO}_3$  et  $\text{SrTiO}_3$ . Malgré cela pour couvrir l'immense potentiel des interfaces d'oxydes et leur phases électroniques sans précédent, il est nécessaire de combiner des oxydes plus fortement corrélés. Cette thèse à la croisée des chemins entre la physique des électrons fortement corrélés, du magnétisme et de la spintronique a pour but de combiner les instabilités magnétique et électronique pour créer de nouvelles phases électronique contrôlable par stimulus externe. Pour cela nous nous sommes intéressés à la famille relativement inexplorée des titanates de terres rares dont l'ordre magnétique ferro ou antiferro est contrôlé par la taille de la terre rare. Contrairement aux travaux existants, nous nous

somme concentrés sur les membres ferrimagnétiques de la famille et leur intégration dans des 2DES. Cette thèse se développera autour de deux axes principaux. Dans un premier temps nous avons étudié plusieurs membres de la famille des titanates de terre rare sous la forme de couches minces épitaxiées. Nous avons aussi mis en évidence la présence d'une couche morte magnétiquement active à la surface de ces échantillons et expliqué sa présence par une oxydation des ions titane de la surface. Nous avons aussi étudié la présence inattendu d'un moment orbital porté par le titane dans certains des composés étudiés et l'avons corrélé à leur structure magnétique non-colinéaire. Celle-ci est induite par le moment orbital des terres rares qui en conjonction avec un gradient structural observé en microscopie électronique en transmission.

Dans un second temps nous avons combiné  $\text{DyTiO}_3$  avec  $\text{SrTiO}_3$  pour obtenir une interface conductrice possédant des propriétés de magnetrotransport complexes que nous avons interprété avec l'aide d'un modèle faisant intervenir le couplage spin-orbite ainsi qu'un magnétisme induit.

**Title :** Magnetic and transport properties of rare-earth titanate thin films and heterostructures

**Keywords :** Correlated material, oxides, heterostructures, growth

**Abstract :** Transition metal oxides possess a broad range of functionalities (superconductivity, magnetism, ferroelectricity, multiferroicity) stemming from the interplay between structural effects and electronic correlations. Recent work has revealed exciting physics at their interfaces, including conductivity and superconductivity in the two-dimensional electron system (2DES) that forms at the interface between two band insulators,  $\text{LaAlO}_3$  and  $\text{SrTiO}_3$ . However, to embrace the immense potential of oxide interfaces and unveil unprecedented electronic phases, combining insulators with stronger electronic correlations is necessary. At the crossroad between strongly correlated electron physics, magnetism and spintronics, the present thesis project aimed to harness electronic and magnetic instabilities in correlated oxides to craft new electronic phases controllable by external stimuli. We investigated rare-earth titanates  $\text{RTiO}_3$ , a relatively unexplored family of Mott insulating perovskites with a crossover between antiferromagnetic and ferromagnetic orders

upon changing the rare-earth size. Contrary to most previous works, we focused on ferromagnetic compounds, and their integration in 2DES. The thesis developed along two main axes. First, we explored several members of the rare-earth titanates family in epitaxial thin film form. We highlighted the presence of a magnetically active dead layer at the surface of thin films and established its origin as due to the overoxidation of titanium ions. We also studied the presence of an unexpected orbital moment carried by the titanium in some compounds, and discussed it in the light of the non-collinear spin arrangement promoted by the rare-earth orbital moment and of a structural gradient evidenced by transmission electron microscopy. In a second stage, we combined  $\text{DyTiO}_3$  with  $\text{SrTiO}_3$  to stabilize a conducting interface with puzzling magnetrotransport properties that we interpreted with a model involving spin-orbit coupling as well as induced magnetism.

